Інженерна електрофізика.
Техніка сильних електричних та магнітних полів
Електричні машини та апарати
Електротехнічні комплекси та системи
Електричні станції, мережі і системи
Електричний транспорт

Electrical Engineering & Electromechanics

no. 1, 2022

Table of Contents

M.M. Zablodskiy, V.E. Pliuhin, S.I. Kovalchuk, V.O. Tietieriev

Indirect field-oriented control of twin-screw electromechanical hydrolyzer

Goal. Development of a mathematical model of indirect field-oriented control of a twin-screw electromechanical hydrolyzer.
Methodology*. The paper presents a mathematical model of Indirect field-oriented control of twin-screw electromechanical hydrolyzer. The mathematical model was developed in the MATLAB / Simulink software environment. The determination of the main parameters of a twin-screw electromechanical hydrolyzer was carried out by developing a finite element model in the Comsol Multiphysics software environment.* ***Results****. Based on the results of a mathematical study, graphical dependences of the distribution of magnetic induction in the air gap of a ferromagnetic rotor, a spatial representation of the distribution of magnetic induction on a 3D model of a ferromagnetic rotor of a twin-screw electromechanical hydrolyzer were obtained. The results of finite element modeling were confirmed by a practical study of a mock-up of a ferromagnetic rotor of a twin-screw electromechanical hydrolyzer. By implementing the MATLAB / Simulink model, graphical dependences of the parameters of the ferromagnetic rotor of a twin-screw electromechanical hydrolyzer are obtained under the condition of a stepwise change in the torque and a cyclic change in the angular velocity.* ***Originality****. The paper presents an implementation of the method of indirect field-oriented control for controlling the ferromagnetic rotor of a twin-screw electromechanical hydrolyzer. The work takes into account the complex design of the ferromagnetic rotor of a twin-screw electromechanical hydrolyzer.* ***Practical significance****. The practical implementation of the results of mathematical modeling makes it possible to achieve effective control of a complex electromechanical system, allows further research to maintain the necessary parameters of the technological process and to develop more complex intelligent control systems in the future.* References 19, tables 4, figures 21.
Key words: **Maxwell's equations, field-oriented control, polyfunctional electromechanical converters, hydrolyzer, dissipative energy.**

У статті детально розглянуто конструктивні і електромагнітні особливості нестандартного електромеханічного перетворювача енергії – двошнекового електромеханічного гідролізера. Це технічний пристрій з поліфункціональними властивостями, здатний одночасно нагрівати, диспергувати, транспортувати, перемішувати та піддавати впливу магнітним полем в одному пристрої робочу сировину. Розроблено коло-польові та математичні моделі електромагнітних перехідних процесів цього пристрою. Основні параметри електромеханічної системи визначено шляхом кінцево-елементного моделювання та практичного дослідження феромагнітного ротора. В роботі представлено керування обертовим моментом та кутовою швидкістю феромагнітного ротора двошнекового електромеханічного гідролізера шляхом непрямого полеорієнтованого керування. Шляхом реалізації MATLAB / Simulink моделі отримано графічні залежності основних параметрів феромагнітного ротора за умов ступінчатої зміни обертового моменту та циклічної зміни кутової швидкості. За результатами моделювання помітно доцільність застосування методу непрямого керування з орієнтацією на поле для ефективного керування технологічним процесом двошнекового електромеханічного гідролізера. В порівнянні з розглянутими методами керування, непряме керування з орієнтацією на поле більш просте в проектуванні та реалізації, дозволяє досягти бажаних характеристик та відкриває подальші можливості для дослідження двошнекового електромеханічного гідролізера. Бібл. 19, табл. 4, рис. 21.
Ключові слова: **рівняння Максвелла, непряме керування з орієнтацією на поле, поліфункціональний електромеханічний перетворювач, гідролізер, дисипативна енергія.**

Introduction. Efficient use of energy resources is an important task for today. The development of energy-saving technologies is directly related to increasing the efficiency of individual elements of the system, integrating the functional features of the system in one device and the use of dissipative energy. Since the increase in efficiency, provided that a certain level of system optimization is achieved, is achieved by developing new active and insulating materials, the methods of increasing it are limited. For technological systems that combine the processes of movement, heating and mixing of materials, the method of using dissipative energy should be considered the most effective [1]. Under the conditions of the previously mentioned integration of functional features of the system in one device and the use of dissipative energy, it becomes possible to save resources that under traditional schemes of energy conversion and use were spent, dissipated as heat into the environment.

Within the method of dissipative energy use, a double-screw electromechanical hydrolyzer has been developed for the processing of poultry by-products under the influence of a magnetic field. A double-screw electro-mechanical hydrolyzer is a technical device with poly-functional properties, capable of simultaneously heating, dispersing, transporting, mixing and exposing to a magnetic field in one device. The main working element of the double-screw electromechanical hydrolyzer is a ferromagnetic rotor (Fig. 1). The ferromagnetic rotor simultaneously acts as the rotor of the induction motor, heater, working element and protective shell [2].
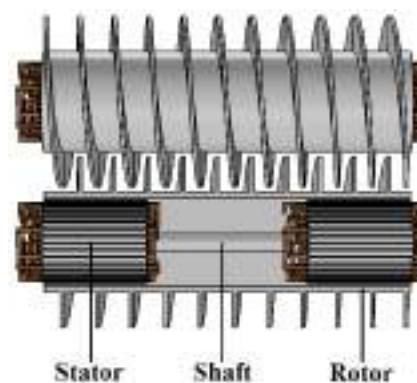

Fig. 1. Ferromagnetic double-screw rotor electromechanical hydrolyzer

The electromagnetic system of a double-screw electromechanical hydrolyzer consists of stators rigidly mounted on a fixed shaft. During the flux of current through the stator windings, they create electromagnetic moments that drive the ferromagnetic rotor.

Since the double-screw electromechanical hydrolyzer is a device that combines several technological processes, it is necessary to ensure effective control of the electromagnetic torque and rotation speed of the ferromagnetic rotor. Obtaining the necessary parameters of speed and torque is possible under the control of the joint operation of two stators, one of which operates in motor mode, the other – in generator mode, but with increasing stiffness of the resulting characteristics significantly reduces the overload capacity of the unit, developing another more effective management method.

Analysis of recent research and publications. Methods of controlling electric machines of alternating current are a difficult task. In the field of highly effective methods of speed and torque control, two methods have become the most widespread – field-oriented control and direct torque control [3-5]. In most cases, these methods are sufficient to meet most industrial needs, but due to the rapid development of digital technologies, more and more research is being conducted in the field of nonlinear control [6]. Recent publications include many works on various methods of controlling electric machines. The control of an induction motor by the method of indirect field-oriented control, considering the influence of perturbations of the rotor resistance, was performed in [3, 7]. The general recommendations for the design of the control system are given in the works, the criteria of stability and the minimum necessary phase conditions for the torque control are indicated, the results of the experimental study of a typical induction motor are presented. In [8], a method of predicted current control with field orientation was described, which was developed for a three-level inverter with a fixed neutral point for controlling a three-phase induction motor. The algorithm for calculating the optimal switching vector was used in the method, the control circuit of the stator voltage, stator current and motor's rotor speed was determined. The simulation results have a slight error when calculating the rotor flux and stator current. Sensorless direct torque control of an induction motor powered by a seven-level inverter using neural networks and fuzzy logic controller is presented in [9], fuzzy PI controller is used to control rotor speed, and artificial neural network is used to stator voltage. The method proposed in this work allows to control the torque, reduce the harmonic distortion of the stator current, improve the dynamic characteristics and reliability of the system. The method of operating cycle control, which is chosen to reduce the pulsation of torque and magnetic flux with direct torque control, is presented in [10]. A new algorithm for accurate selection of active voltage has been developed, the optimal duration of switching on at simultaneous control of stator magnetic flux and electric torque has been determined. According to the results of the study, the presented method provides less pulsations of torque and magnetic flux compared to the traditional method of direct torque control and a model that provides a better model of predicted current control. In [11], a model of predicted torque and magnetic flux based on perturbations was developed; the method of perturbation suppression is improved to ensure compatibility with the theory of finite sets; perturbation is provided for all possible switching states. According to the research

results, this method improves the stability of the response of torque and current, significantly increases the resistance of the system *to changes in the values of the stator and rotor resistance* in comparison with traditional control methods.

The methods presented in [7-11], built on the basis of complex algorithms of neural networks and fuzzy logic, allow to effectively control the parameters of electric machines, however, at the same time, they have certain disadvantages: high complexity of algorithms, a large number of controlled parameters, high design load and the need for a full-fledged system model [12, 13].

The double-screw electromechanical hydrolyzer is a new electric machine and most of its parameters and characteristics still need detailed research. From the existing research, a complete picture of the magnetic field of the ferromagnetic rotor of a double-screw electromechanical hydrolyzer is known [2, 14]. This allows to conclude that for its management it is advisable to use the method of field-oriented control.

The aim of the work is to study the electromagnetic processes in a ferromagnetic rotor of a double-screw electromechanical hydrolyzer and to evaluate the feasibility of using the hydrolyzer indirect field-oriented control method.

Presenting main material. Due to its simplicity, indirect field-oriented control is one of the most effective ways to control an AC machine. For effective control of torque and speed, the stator current components in the model must be separated from the vector magnetic flux of the rotor [15]. Since it is necessary to know the parameters of an electric machine to develop a model of indirect control with field orientation, there is a need to develop a mathematical model of the ferromagnetic rotor of a double-screw electromechanical hydrolyzer, where it is not needed to know these parameters.

Finite element model in the time domain of the study. Due to the need for high accuracy, as well as due to the peculiarities of the design and the need to reduce the time for design, we used the software environment Comsol Multiphysics. The analysis of the electromagnetic field is performed based on the system of Maxwell's equations.

The magnetization of the ferromagnetic rotor is given as the *B-H* curve and is determined from the equation:

$$B = f(|H|)\frac{H}{|H|}. \qquad (1)$$

Multi-turn stator windings are used as a current source in the model (Fig. 2).

In the diagram (Fig. 2) the beginning of the corresponding phases (conductors leave the groove) is marked in capital letters (*A, B, C*) and the end (conductors enter the slot) in small letters (*a, b, c*).

The current density in the winding, A/m²:

$$J_e = \frac{N \cdot I_{coil}}{A} \cdot e_{coil}, \qquad (2)$$

where N – winding turns; A – winding cross-section, m²; I_{coil} – current in stator coil, A; e_{coil} – vector variable (to visualize the direction of winding turns).

The simulation was performed for a ferromagnetic rotor, the finite element mesh of the model (Fig. 3) was created in the software environment Comsol Multiphysics. Particular attention was paid to the air gap

at the interface between the stator and rotor of the electromechanical device. Statistics on the parameters of the mesh are given in Table. 1.
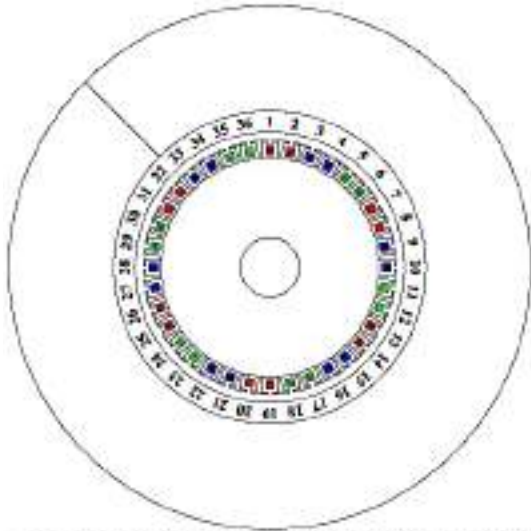
AAbbCCaaBBccAAbbCCaaBBccAAbbCCaaBBcc
Fig. 2. Stator winding circuit
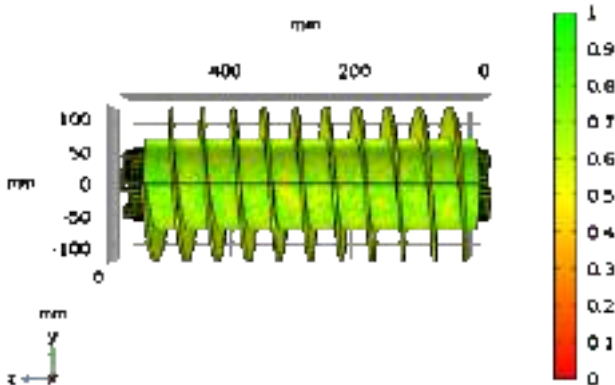
Fig. 3. Finite element mesh for ferromagnetic rotor model of double-screw electromagnetic hydrolyzer

Table 1
Parameters of the model finite element mesh

Mesh parameters	Values
Number of mesh vertices	241325
Tetrahedra	1444151
Triangles	277074
Edge elements	49887
Vertex elements	2759
Number of elements	1444151
Minimum element quality	0,0307
Average element quality	0,613
Element volume ratio	2,027E-6
Mesh volume	1,251E8 mm^3

MATLAB / Simulink model of indirect control with field orientation. In the case of low-speed orientation and for position control using an integration sensor-based flux sensor, a field-oriented indirect control model may not be acceptable for complex electromechanical systems. An alternative may be indirect control with field orientation without measuring the flux in the air gap [16]. Under such conditions, the torque can be regulated by the q-component of the stator current i_{qs}^e

and the difference in the angular frequencies of the magnetic field of the stator and rotor $\omega_e - \omega_e$. The rotor flux can be regulated by the d-component of the stator current i_{ds}^e. Setting some desired value of the magnetic flux of the rotor $\lambda_r^{'*}$, the desirable d- component of the stator current i_{ds}^{e*} can be obtained from the equation:

$$\lambda_{dr}^{'*} = \frac{r_r' L_m}{r_r' + L_r' p} i_{ds}^{e*}, \tag{3}$$

where $\lambda_{dr}^{'*}$ – desirable d-component of the rotor current, Wb; r_r' – induced active resistance of the rotor winding, Ω; L_m – mutual induction of stator windings, T; p – number of pole pairs.

For the desired torque value T_{em}^* at a certain value of the rotor flux, the desired value q-components of the stator current i_{qs}^e described by the equation:

$$T_{em}^* = \frac{3}{2} \cdot \frac{P}{2} \cdot \frac{L_m}{L_r'} \lambda_{dr}^{'e*} i_{qs}^{e*}, \tag{4}$$

where P – power, W; L_r' – transient inductance of the rotor, H.

Because at a certain orientation of the field $i_{dr}^{'e}$ equal to zero and $\lambda_{dr}^{'e} = L_m i_{ds}^e$, then the desired angular speed of the rotor ω_2^* (rad/s) described by the equation:

$$\omega_2^* = \omega_e - \omega_r = \frac{r_r' i_{qs}^{e*}}{L_r' i_{ds}^{e*}}, \tag{5}$$

where ω_e – angular rotation velocity of the magnetic field, rad/s; ω_r – angular rotation speed of the rotor, rad/s.

The measured flux in the air gap is the resultant or reciprocal flux. This is not the same as the current connecting the rotor winding, whose angle ρ is the desired angle for field orientation. But, as the following equations shows, in combination with the measured stator current, it is possible to determine the value of ρ and the magnitude of the rotor flux. The measured stator currents abc are first converted to a stationary current qd using the equations:

$$i_{qs}^s = \frac{2}{3} i_{as} - \frac{1}{3} i_{bs} - \frac{1}{3} i_{cs}, \tag{6}$$

$$i_{ds}^s = \frac{1}{\sqrt{3}} (i_{cs} - i_{bs}). \tag{7}$$

The flux coupling of the rotor on the q axis in a fixed coordinate system can be expressed as:

$$\lambda_{qr}^{'s} = \left(L_m + L_{lr}' - L_{lr}'\right) \cdot i_{qs}^s + \left(L_m + L_{lr}'\right) \cdot i_{qr}^{'s}. \tag{8}$$

Because λ_{mq}^s equal to $L_m \left(i_{qs}^s + i_{qr}^{'s}\right)$, it is possible to define $\lambda_{qr}^{'s}$ by measured values, i.e.

$$\lambda_{qr}^{'s} = \frac{L_r'}{L_m} \lambda_{mq}^s - L_{lr}' i_{qs}^s. \tag{9}$$

Similarly, $\lambda_{dr}^{'s}$ can be determined from

$$\lambda_{dr}^{'s} = \frac{L_r^{'}}{L_m}\lambda_{md}^s - L_{lr}^{'}i_{ds}^s . \qquad (10)$$

Using calculated $\lambda_{qr}^{'s}$ and $\lambda_{dr}^{'s}$, lets determine the cosine and sine ρ by geometric ratios:

$$\sin\left(\frac{\pi}{2}-\rho\right)=\cos\rho=\frac{\lambda_{dr}^{'s}}{\left|\lambda_r^{'s}\right|}, \qquad (11)$$

$$\cos\left(\frac{\pi}{2}-\rho\right)=\sin\rho=\frac{\lambda_{qr}^{'s}}{\left|\lambda_r^{'s}\right|}, \qquad (12)$$

where

$$\left|\lambda_r^{'e}\right|=\left|\lambda_r^{'s}\right|=\sqrt{\lambda_{dr}^{'s2}+\lambda_{qr}^{'s2}} . \qquad (13)$$

The above calculations (6) – (13) are performed inside the field orientation unit. Estimated value $\left|\lambda_r^{'e}\right|$ returns to the inlet of the flux regulator that control the flux in the air gap. Values are calculated inside the torque calculation unit $\lambda_r^{'e}$ and i_{qs}^e are used to estimate the value of the torque produced by the machine, then the calculated torque is returned to the input of the torque regulator.

The corresponding output data of the torque and flux regulators are the values of the commands, i_{qs}^{e*} and i_{ds}^{e*}, in the field-oriented rotor frame of reference. The transformations from *qde* to *qds* and *qds* to balanced *abc* take place in the whole unit of the *qd* to *abc* conversion unit:

$$\begin{cases} i_{qs}^{s*}=i_{qs}^{e*}\cos\rho+i_{ds}^{e*}\sin\rho; \\ i_{ds}^{s*}=-i_{qs}^{e*}\sin\rho+i_{ds}^{e*}\cos\rho; \\ i_{as}^{*}=i_{qs}^{s*}; \\ i_{bs}^{*}=-\frac{1}{2}i_{qs}^{s*}-\frac{\sqrt{3}}{2}i_{ds}^{s*}; \\ i_{cs}^{*}=-\frac{1}{2}i_{qs}^{s*}+\frac{\sqrt{3}}{2}i_{ds}^{s*}. \end{cases} \qquad (14)$$

The orientation of the stator current field can also be achieved by applying the appropriate stator voltages. Since the strategy in the field-oriented circuit is to avoid disrupting the rotor flux connection as much as possible in response to changes in load torque, we can use a transient model in combination with properly oriented stator currents *qd* to determine stator voltage. Field-oriented stator currents *qd* are determined by converting the measured *abc* currents to stationary *qd* and values ρ in the following transformation

$$i_{qs}^e = i_{qs}^s\cos\rho - i_{ds}^s\sin\rho ; \qquad (15)$$

$$i_{ds}^e = i_{qs}^s\sin\rho + i_{ds}^s\cos\rho . \qquad (16)$$

In the transient model for a situation where it can be assumed that the flux coupling of the rotor remains constant, the machine can be represented by a constant voltage on the transient inductance of the stator.

Stator flux coupling can only be expressed through stator currents and rotor flux coupling, i.e.

$$\lambda_{qs}^e = L_s^{'}i_{qs}^e + \frac{L_m}{L_r^{'}}\lambda_{qr}^{'e} ; \qquad (17)$$

$$\lambda_{ds}^e = L_s^{'}i_{ds}^e + \frac{L_m}{L_r^{'}}\lambda_{dr}^{'e} ; \qquad (18)$$

$$L_s^{'}\frac{di_{qs}^e}{dt}+\frac{L_m}{L_r^{'}}\frac{d\lambda_{qr}^{'e}}{dt}=v_{qs}^e-r_si_{qs}^e-E_{qs}^{'}-\omega_eL_s^{'}i_{ds}^e ; \qquad (19)$$

$$L_s^{'}\frac{di_{ds}^e}{dt}+\frac{L_m}{L_r^{'}}\frac{d\lambda_{dr}^{'e}}{dt}=v_{ds}^e-r_si_{ds}^e-E_{ds}^{'}+\omega_eL_s^{'}i_{qs}^e . \qquad (20)$$

Setting the derivatives of the time of flux coupling of the rotor to zero and rearranging so that the left side contains the sum of the voltage across the transient resistance and the voltage drop across the transient resistance of the stator, then we obtain

$$r_si_{qs}^e+L_s^{'}\frac{di_{qs}^e}{dt}+E_{qs}^{'}=v_{qs}^e-\omega_eL_s^{'}i_{ds}^e ; \qquad (21)$$

$$r_si_{ds}^e+L_s^{'}\frac{di_{ds}^e}{dt}+E_{ds}^{'}=v_{ds}^e+\omega_eL_s^{'}i_{qs}^e . \qquad (22)$$

By adjusting the outputs of the torque and flux controllers for the cross-current, we obtain the required command values for v_{qs}^e and v_{ds}^e. The command values for the stator voltages *abc* can be calculated as follows

$$\begin{cases} v_{qs}^{s*}=v_{qs}^e\cos\rho+v_{ds}^e\sin\rho; \\ v_{ds}^{s*}=-v_{qs}^e\sin\rho+v_{ds}^e\cos\rho; \\ v_{as}^{*}=v_{qs}^{s*}; \\ v_{bs}^{*}=-\frac{1}{2}v_{qs}^{s*}-\frac{\sqrt{3}}{2}v_{ds}^{s*}; \\ v_{cs}^{*}=-\frac{1}{2}v_{qs}^{S*}+\frac{\sqrt{3}}{2}v_{ds}^{s*}. \end{cases} \qquad (23)$$

The desired rotor speed less than the nominal with a certain nominal supply voltage is described by equations:

$$\left(v_{qs}^e-jv_{ds}^e\right)=\left(r_s+j\omega_eL_s^{'}\right)\cdot\left(i_{qs}^e-ji_{ds}^e\right)+\left(E_{qs}^e-jE_{ds}^{'}\right); \quad (24)$$

$$T_0^{'}=\frac{x_{lr}^{'}+x_m}{\omega_er_r^{'}}, \qquad (25)$$

where v_{qs}^e, v_{ds}^e – *q* and *d* voltage components, V; r_s – stator winding resistance, Ω; $L_s^{'}$ – stator inductance, H; $E_{qs}^{'}$, $E_{ds}^{'}$ – *q* and *d* component of the magnetizing voltage, V; $x_{lr}^{'}$ – inductive scattering resistance of the rotor winding, Ω; x_m – inductive resistance of the stator core magnetization, Ω.

Simulation results. Finite element modeling was performed for the model with the parameters given in Table. 2.

The materials of the model were chosen:
* *Soft Iron* (without losses) – as a material of stator core;
* *Iron* – as the shaft material;
* *Copper* – as the stator winding material.

Parameters of the stator double-screw electromechanical
hydrolyzer

Selected materials	
Current in stator winding	10,5 A
Simulation time	Range (0, 0.1, 1) s

Materials were selected from the library of materials of the Comsol software environment. As a material for the ferromagnetic rotor was chosen steel grade St3, the magnetization curve of which is shown in Fig. 4.
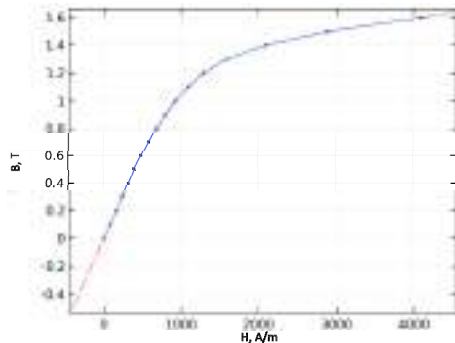
Fig. 4. B-H steel St3 magnetization curve

The picture of the distribution of magnetic induction for the nominal mode of operation of the ferromagnetic rotor of a double-screw electromechanical hydrolyzer is presented in Fig. 5.
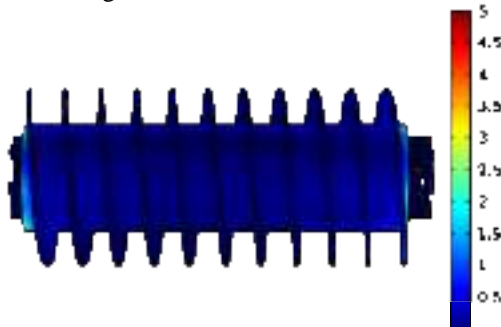
Fig. 5. Magnetic induction distribution pattern for the model ferromagnetic rotor of a double-screw electromechanical hydrolyzer, T

Graphical representation of the distribution of magnetic induction in the air gap of the ferromagnetic rotor of a double-screw electromechanical hydrolyzer, at the beginning and end of the simulation is presented in Fig. 6.
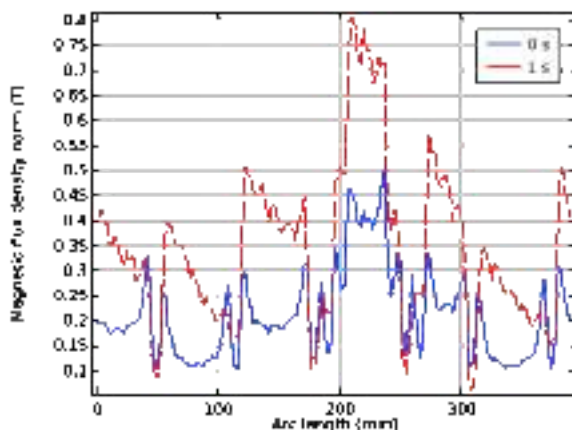
Fig. 6. Graphical representation of the distribution of magnetic induction in the air gap of a double-screw electromechanical hydrolyzer

For quantitative assessment in Table 3 shows the average and maximum values of magnetic flux density in the air gap of a double-screw electromechanical hydrolyzer.

Average and maximum values of magnetic flux density in the air gap of the double-screw electromechanical hydrolyzer

Time, s	Average value, T	Maximum value, T
0	0,216174	0,46575
0,1	0,347887	0,794864
0,2	0,348252	0,796307
0,3	0,348275	0,796473
0,4	0,348284	0,796515
0,5	0,348277	0,796508
0,6	0,348277	0,796515
0,7	0,348278	0,79652
0,8	0,348277	0,79652
0,9	0,348285	0,796534
1	0,348285	0,796536

According to the simulation results, it is noticeable that the discrete arrangement of the stators along the axial line of the ferromagnetic rotor of the double-screw electromechanical hydrolyzer forms stable zones with a cyclic level of magnetic field intensity. Around the air gap of the double-screw electromechanical hydrolyzer 6 narrow and wide zones, alternating with each other [14].

The main results of modulation were compared with the data obtained from the experimental study of the auger of the electromechanical hydrolyzer (Fig. 7).

Fig. 7. Experimental sample of an electromechanical hydrolyzer

During the research, magnetic induction was measured using MagneticFeldMeterTM-191 and PCE-MFM 4000 instruments (Fig. 8).

The average values of deviations between the results of mathematical and experimental research are 0.13 T, which is 2-3% in the measurement range of 0.4–0.8 T, so the mathematical model can be considered correct and used in further research.

Fig. 8. Measuring instruments MagneticFeldMeterTM-191 and PCE-MFM 4000

MATLAB / Simulink model of indirect control with field orientation is made for one stator of a double-screw electromechanical hydrolyzer with the parameters specified in Table 4. From studies of the electromechanical characteristics of the double-screw electromechanical hydrolyzer [14] it is known that the nominal speed of the working body (ferromagnetic rotor) is 200 rpm. Since it is known that the stator contains 6 poles, the slip calculated as following:

$$s = \frac{(n_1 - n_2)}{n_1} = \frac{(1000 - 200)}{1000} = 0.8$$

where n_1 – synchronous speed, rpm; n_2 – actual speed, rpm.

Table 4

Parameters of the replacement scheme for one stator and a ferromagnetic rotor of a double-screw electromechanical hydrolyzer

Parameter	Value
Power	1400 W
Rated voltage	118 V
Rated current	10,5 A
Power factor	0,65
Number of pole pairs	6
Rated frequency	50 Hz
Rated slip	0,8
Rated rotation speed	1000 rpm
Stator winding resistance	200 rpm
Reactive scattering resistance stator windings	0,1323 Ω
Reactive scattering resistance rotor windings	0,2033 Ω
Reactive magnetization resistance stator windings	0,2372 Ω
Rotor winding resistance	5,0475 Ω
The inertia of the rotor	0,174 Ω

The scheme of replacement of the double-screw electromechanical hydrolyzer is presented in Fig. 9-11.
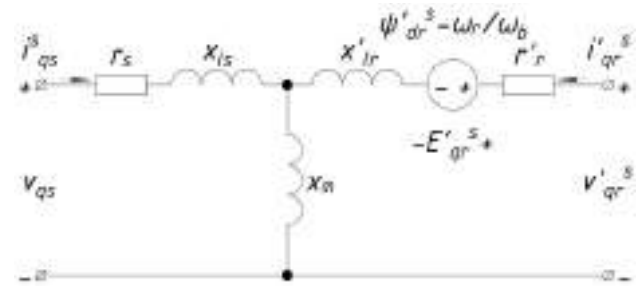
Fig. 9. Scheme of stator replacement of ferromagnetic rotor of double-screw electromechanical hydrolyzer in reference system *q*-axis
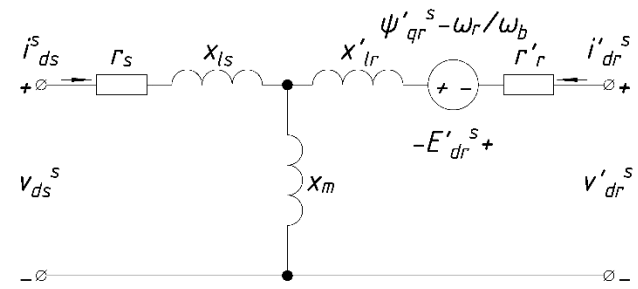
Fig. 10. Scheme of replacement of a stator of a ferromagnetic rotor of a double-screw electromechanical hydrolyzer in the frame of reference *d*-axis
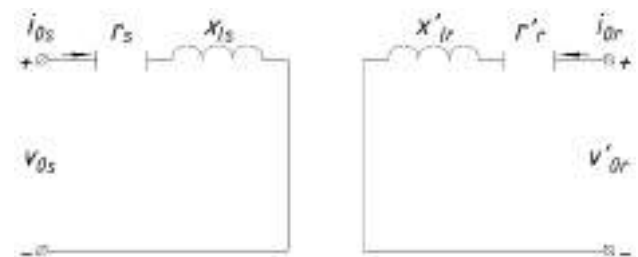
Fig. 11. Scheme of stator replacement of ferromagnetic rotor of double-screw electromechanical hydrolyzer in reference system zero-sequence

In Fig. 12 a general Simulink model of indirect control with field orientation is shown. To reduce the duration of the model calculation, the work does not consider the transients that occur in the PWM converter during control, only the main components of the output voltages are taken into account [18, 19].

Figure 13 presents the implementation of the non-direct control unit with field orientation. Values are calculated in the middle of the block i_{ds}^{e*}, i_{qs}^{e*}, ω_2^*, angle θ – the sum of the rotor rotation angle θ_2 and the angle of sliding integrated from the rotor rotation sensor θ_r. In the middle of the block *qde2abc* (Fig. 12) is the generation of reference *abc* currents.

During the simulation, two types of control were implemented. The first one is a step change of the torque according to the desired, fixed value of the angular velocity of rotation (Fig. 14 – Fig. 17).
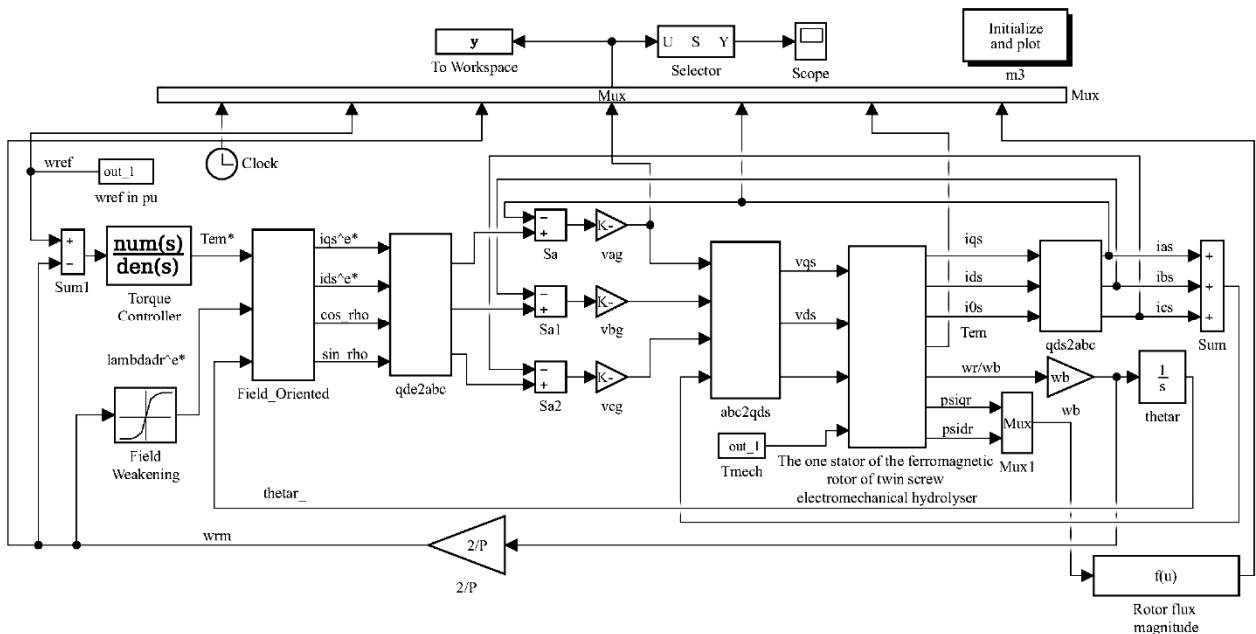
Fig. 12. MATLAB / Simulink model of double-screw electromechanical hydrolyzer with indirect control with field orientation
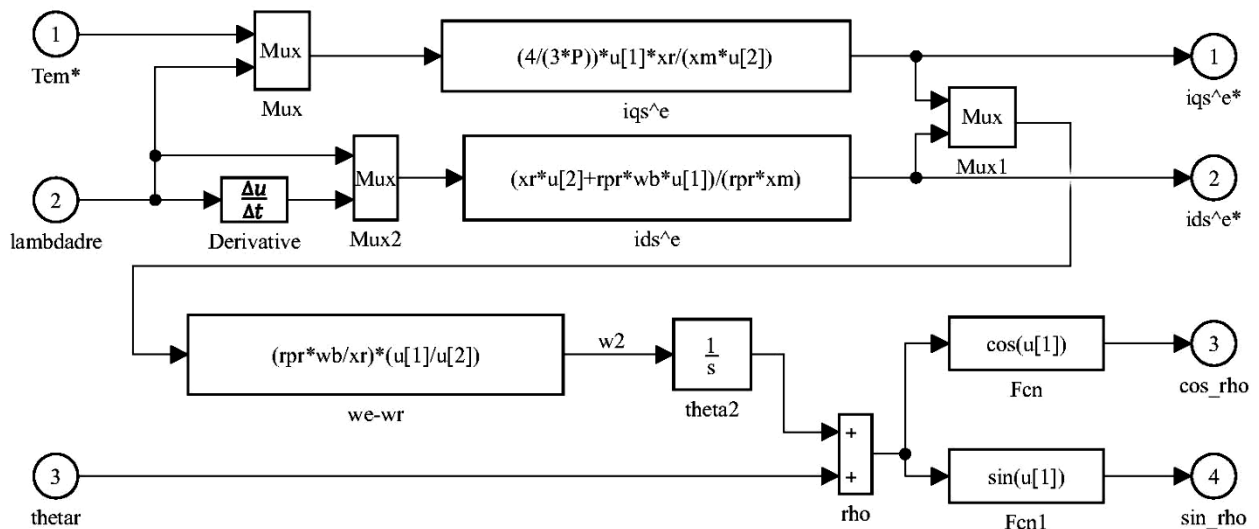
Fig. 13. Implementation of the model of indirect control of two-screw electromechanical hydrolyzer with field orientation
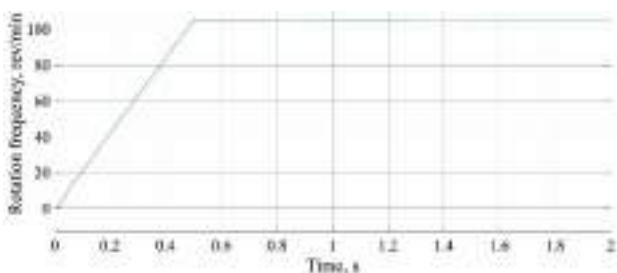
Fig. 14. Angular speed during start-up and loading, rad / s
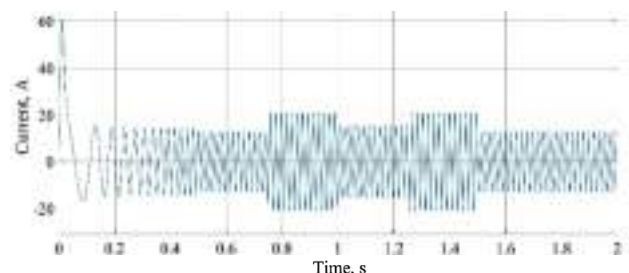
Fig. 16. Current during start-up and loading, A
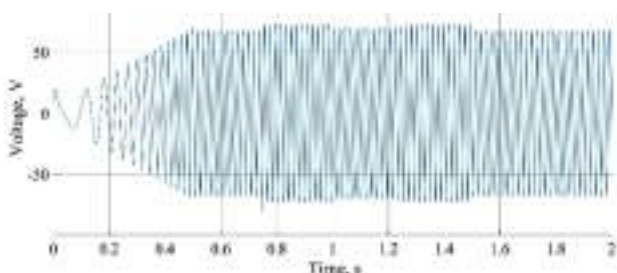
Fig. 15. Voltage during start-up and loading, V
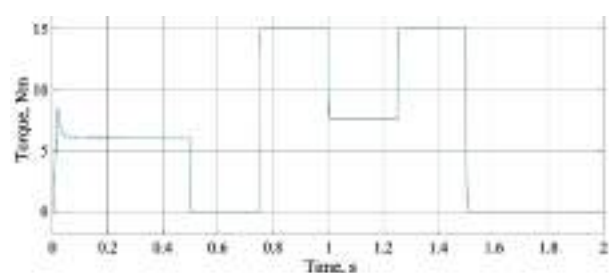
Fig. 17. Torque during start-up and loading, Nm

The second one is a cyclic change in the angular rotation velocity (Fig. 18 – Fig. 21).
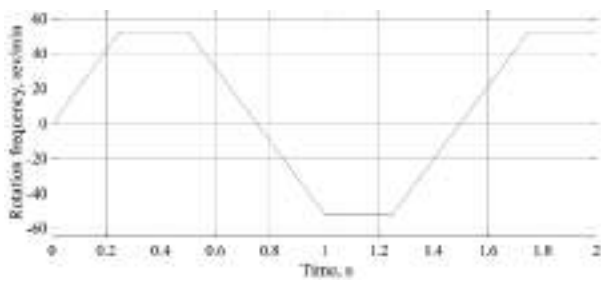
Fig. 18. Change of angular velocity during idle mode, rad / s
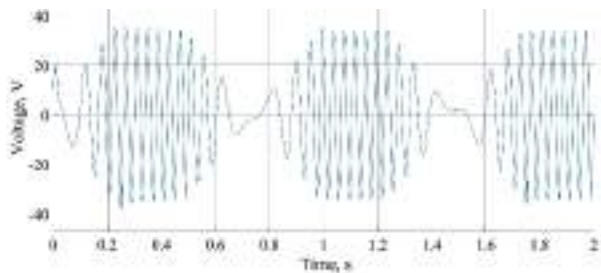
Fig. 19. Voltage dependents in idle mode, V
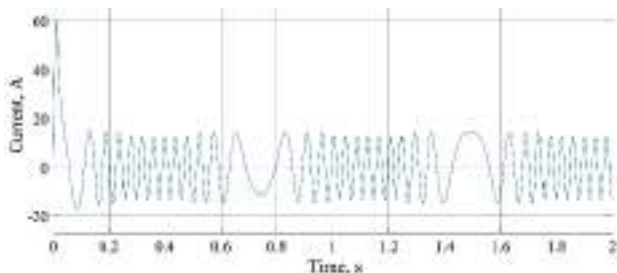
Fig. 20. Current dependents in idle mode, A
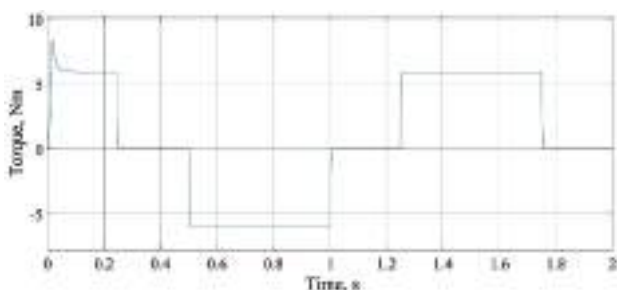
Fig. 21. Torque dependents in idle mode, Nm

Conclusions. Since the double-screw electromechanical hydrolyzer is a device that combines several technological processes, there is a need to maintain the exact parameters of the technological process. The simulation results were obtained under the following conditions: simulation time from 0 to 2 s with a step 0.5 s; the fixed value of the angular velocity at the torque step change is equal to the rated value; the time array of torque change is [0, 0.5, 0.75, 1, 1.25, 1.5] s; the time array of angular velocity cyclic change is [0, 0.25, 0.5, 1, 1.25, 1.7] s.

From the simulation results, the expediency of using the method of indirect control with field orientation in a double-screw electromechanical hydrolyzer is noticeable.

Compared to the considered control methods, indirect control with field orientation is simpler in design and implementation, allows to achieve the desired characteristics and opens further opportunities for the study of double-screw electromechanical hydrolyzer.

Conflict of interest. The authors of the paper state that there is no conflict of interest.

REFERENCES
1. Zablodskiy N., Kovalchuk S., Chuenko R., Romanenko O., Gritsyuk V. The nanofluids application in a twin-screw electromechanical hydrolyser. *2021 IEEE 21st International Conference on Nanotechnology (NANO)*, 2021, pp. 108-111. doi: https://doi.org/10.1109/NANO51122.2021.9514326.
2. Zablodskiy M., Kovalchuk S. The main aspects of the technology of processing keratin raw materials under the influence of a magnetic field. *2020 IEEE KhPI Week on Advanced Technology (KhPIWeek)*, 2020, pp. 278-282. doi: https://doi.org/10.1109/KhPIWeek51551.2020.9250153.
3. Yang S., Ding D., Li X., Xie Z., Zhang X., Chang L. A Novel Online Parameter Estimation Method for Indirect Field Oriented Induction Motor Drives. *IEEE Transactions on Energy Conversion*, 2017, vol. 32, no. 4, pp. 1562-1573. doi: https://doi.org/10.1109/TEC.2017.2699681.
4. Yan N., Cao X., Deng Z. Direct Torque Control for Switched Reluctance Motor to Obtain High Torque–Ampere Ratio. *IEEE Transactions on Industrial Electronics*, 2019, vol. 66, no. 7, pp. 5144-5152. doi: https://doi.org/10.1109/TIE.2018.2870355.
5. Kumar R.H., Iqbal A., Lenin N.C. Review of recent advancements of direct torque control in induction motor drives – a decade of progress. *IET Power Electronics*, 2018, vol. 11, no. 1, pp. 1-15. doi: https://doi.org/10.1049/iet-pel.2017.0252.
6. Wang F., Zhang Z., Mei X., Rodríguez J., Kennel R. Advanced Control Strategies of Induction Machine: Field Oriented Control, Direct Torque Control and Model Predictive Control. *Energies*, 2018, vol. 11, no. 1. doi: https://doi.org/10.3390/en11010120.
7. Amezquita-Brooks L., Liceaga-Castro J., Liceaga-Castro E. Speed and Position Controllers Using Indirect Field-Oriented Control: A Classical Control Approach. *IEEE Transactions on Industrial Electronics*, 2014, vol. 61, no. 4, pp. 1928-1943. doi: https://doi.org/10.1109/TIE.2013.2262750.
8. De Oliveira V M.R., Camargo R.S., Encarnação L.F. Field Oriented Predictive Current Control on NPC Driving an Induction Motor. *2020 IEEE International Conference on Industrial Technology (ICIT)*, 2020, pp. 169-174. doi: https://doi.org/10.1109/ICIT45562.2020.9067236.
9. Benbouhenni H. Seven-Level Direct Torque Control of Induction Motor Based on Artificial Neural Networks with Regulation Speed Using Fuzzy PI Controller. *Iranian Journal of Electrical and Electronic Engineering*, 2018, vol. 14, no. 1, pp. 85-94. doi: http://dx.doi.org/10.22068/IJEEE.14.1.85.
10. Nikzad M.R., Asaei B., Ahmadi S.O. Discrete Duty-Cycle-Control Method for Direct Torque Control of Induction Motor Drives With Model Predictive Solution. *IEEE Transactions on Power Electronics*, 2018, vol. 33, no. 3, pp. 2317-2329. doi: https://doi.org/10.1109/TPEL.2017.2690304.
11. Mousavi M.S., Davari S.A., Nekoukar V., Garcia C., Rodriguez J. A Robust Torque and Flux Prediction Model by a Modified Disturbance Rejection Method for Finite-Set Model-Predictive Control of Induction Motor. *IEEE Transactions on Power Electronics*, 2021, vol. 36, no. 8, pp. 9322-9333. doi: https://doi.org/10.1109/TPEL.2021.3054242.
12. Ekaputri C., Syaichu-Rohman A. Model predictive control (MPC) design and implementation using algorithm-3 on board SPARTAN 6 FPGA SP605 evaluation kit. *2013 3rd International Conference on Instrumentation Control and Automation (ICA)*, 2013, pp. 115-120. doi: https://doi.org/10.1109/ICA.2013.6734056.
13. Wang L. *Model Predictive Control System Design and Implementation Using MATLAB®*. Springer, London, 2009. doi: https://doi.org/10.1007/978-1-84882-331-0.

14. Zablodsky N., Chuenko R., Gritsyuk V., Kovalchuk S., Romanenko O. The Numerical Analysis of Electromechanical Characteristics of Twin-Screw Electromechanical Hydrolyzer. *2021 11th International Conference on Advanced Computer Information Technologies (ACIT)*, 2021, pp. 130-135. doi: https://doi.org/10.1109/ACIT52158.2021.9548392.

15. Zablodskiy M., Pliuhin V., Chuenko R. Simulation of induction machines with common solid rotor. *Technical Electrodynamics*, 2018, no. 6, pp. 42-45. doi: https://doi.org/10.15407/techned2018.06.042.

16. Hiware R.S., Chaudhari J.G. Indirect Field Oriented Control for Induction Motor. *2011 Fourth International Conference on Emerging Trends in Engineering & Technology*, 2011, pp. 191-194. doi: https://doi.org/10.1109/ICETET.2011.56.

17. Abu-Rub H., Iqbal A., Guziński J. *High Performance Control of AC Drives with MATLAB/Simulink Models*. John Wiley & Sons, 2012. doi: https://doi.org/10.1002/9781119969242.

18. Malyar V.S., Hamola O.Ye., Maday V.S., Vasylchyshyn I.I. Mathematical modelling of starting modes of induction motors with squirrel-cage rotor. *Electrical Engineering & Electromechanics*, 2021, no. 2, pp. 9-15. doi: https://doi.org/10.20998/2074-272X.2021.2.02.

19. Shurub Yu.V. Statistical optimization of frequency regulated induction electric drives with scalar control. *Electrical engineering & electromechanics*, 2017, no. 1, pp. 26-30. doi: https://doi.org/10.20998/2074-272X.2017.1.05.

M.M. Zablodskiy[1], Doctor of Technical Science, Professor,
V.E. Pliuhin[2], Doctor of Technical Science, Professor,
S.I. Kovalchuk[1], Postgraduate Student,
V.O. Tietieriev[2], Postgraduate Student,
[1] National University of Life and Environmental Sciences of Ukraine, 12, Heroyiv Oborony Str., Kyiv, 03041, Ukraine, e-mail: zablodskiynn@gmail.com, kovalchuk@it.nubip.edu.ua
[2] O.M. Beketov National University of Urban Economy on Kharkiv, 17, Marshal Bazhanov Str., Kharkiv, 61002, Ukraine, e-mail: vladyslav.pliuhin@kname.edu.ua (Corresponding author), vitaliy.teterev@kname.edu.ua

M. Zitouni

Improvement of power transformer differential protection through detection and exploitation of the negative sequence currents

*Introduction. Power transformers are the most important and the most expensive equipment used in transport and distribution of electrical energy. Their failure results in huge economic losses. Despite the great advances in the design of power equipment in recent years, the feeble link in the chain remains the insulation weakness of coil turns of the power transformer. **The novelty** of the proposed research consists in the development of a new procedure for diagnosing and localizing the occurrence of turn to turn short-circuits in the windings of three-phase power transformer. The main problems of the current differential relay are short circuits of one or more turns of a transformer winding. Hence a new approach using' the amplitude comparison between the negative sequence currents' is developed and a digital discriminator internal / external fault is applied to discriminate turn to turn faults among the other ones. The proposed procedure is based on the exploitation of the negative sequence currents. **The purpose** of using this new procedure is to identify small faults inside power transformer coils and to distinguish inner faults from the outer faults by using an ameliorate circuit. **The method** used in this paper is a novel algorithm which based on the comparison between the negative sequence current amplitudes and to calculate the corresponding phase angle shifts. The performance of the proposed procedure has been confirmed by MATLAB/Simulink environment. The **results** of simulation reveal the efficiency of the suggested procedure, and indicate that this procedure can provide fast and sensitive approach for detecting low level turn-to-turn faults.* References 22, figures 21.*
Key words: **power transformer, diagnosis, inter turn faults, symmetrical components, negative sequence currents**.

*Вступ. Силові трансформатори – найважливіше і найдорожче устаткування, яке використовується при передачі та розподілі електроенергії. Їх відмова призводить до величезних економічних втрат. Незважаючи на великі успіхи в проектуванні силового обладнання в останні роки, слабкою ланкою в ланцюзі залишається недостатня міцність ізоляції витків котушки силового трансформатора. **Новизна** запропонованого дослідження полягає в розробці нової методики діагностики та локалізації виникнення міжвиткових коротких замикань в обмотках трифазних силових трансформаторів. Основні проблеми диференціального реле струму – це коротке замикання одного або декількох витків обмотки трансформатора. Тому, розроблено новий підхід, який використовує порівняння амплітуд струмів зворотної послідовності, а також застосовується цифровий дискримінатор внутрішніх/зовнішніх несправностей для розрізнення міжвиткових короткого замкнень серед інших. Запропонована методика заснована на використанні струмів зворотній послідовності. **Мета** використання цієї нової методики – виявити невеликі несправності всередині котушок силового трансформатора і відрізнити внутрішні несправності від зовнішніх несправностей за допомогою поліпшеної схеми. **Метод**, який використовується в цій статті, це новий алгоритм, заснований на порівнянні амплітуд струму зворотної послідовності і обчисленні відповідних зміщень фазового кута. Еефективність запропонованої методики підтверджена у середовищі MATLAB/Simulink. **Результати** моделювання показують ефективність запропонованої методики і вказують на те, що цій метод може забезпечити швидкий і чутливий підхід для виявлення міжвиткових коротких замикань низького рівня.* Бібл. 22, рис. 21.
Ключові слова: **силовий трансформатор, діагностика, міжвиткові короткі замикання, симетричні складові, струми зворотної послідовності**.

1. Introduction. Protective relays constantly monitor the power system to assure maximum continuity of electrical service with minimum damage to life and property. Thus, they are on guard throughout – from the generation, through transmission into distribution and utilization. They are found in large and small systems, in the power companies and in the industrials. This wide usage, with high demands for reliable operation, has created a continuing desire for additional training. Such training is valuable not only to those directly implicated but also to the many others indirectly associated with relaying. For the latter group, a better understanding of the protective relaying can contribute considerably toward better system design and operation [1].

Power transformers are among the most important elements in electrical power systems. During their service they are exposed to various failures and abnormalities including dielectric, mechanical, or thermal failure. This means that the transformer cannot remain in service, and remedial actions are required before it can be returned to service [2].

Transformer abnormality means that the transformer operation is beyond the normal status, and this may adversely affect the performance or asset life of the transformer itself or other apparatus, or system reliability and operation. Power transformers can fail or be abnormal in a variety of factors and for a variety of reasons. The important factors and reasons are:

Electrical faults originated from internal faults, transient over voltages, over-currents, ageing, service loading, pre-existing faults, and timescales for fault development [3].

Winding faults are considered to be the most reason of transformer collapse. They involve a magnitude of fault current which is small relative to the power transformer nominal currents. This indicates that once a fault takes a place, a rapid, sensitive and reliable protection for its detection and location is necessary to prevent more retards in the network function.

Regarding to the IEEE recommendations [4], there is no unique standard way to protect all power transformers against small internal faults and at the same time to preserve basic protection recommendations such as sensitivity, selectivity, and rapidity. Turn to turn faults in transformer windings are considered to be among the difficult internal faults to detect because only a few turns is initially implicated. The IEEE Standard C37.91-2000 admits that about 10 % of the transformer coils may as well be short circuited to generate a noticeable

variation in the ultimate current [5]. Therefore, when small numbers of turns are short-circuited, the resulting differential current won't be detectable due to its initially small value.

The winding inter turn fault detection, particularly at low current is critical. It has a negative effect on the transformer duration life. The cause of the coil inter turn fault is the insulation breakdown and short circuit of conductors with different voltages [6].

According to [7], the frequency response analysis (FRA) technique is a powerful technique for diagnosing transformer winding distortion or for detection of small turn-to-turn short-circuits faults and several other types of troubles that are caused during fabrication, transportation, installation and/or exploitation. Article [7] studied and simulated many types of short-circuits under different fault severities in various winding points within the high voltage and low voltage. It introduces a novel approach for FRA signature by incorporating both magnitude and phase angle plots in one graph, which facilitates and standardized the FRA interpretation process. The suggested approach is simple, sensitive, and convenient to apply within current frequency response analyzers to normalize the FRA signature process.

Generally, transformers are subject to failing due to internally or externally conditions, so the protected area is delimited by the area that incorporates equipment such as current transformers (CT), relays and power transformer. When a fault is within this area is called internal fault, and when it is outside is called external fault. It is essential that differential protection operates for internal faults only.

From [1, 2], the examples of abnormal conditions are overvoltage, over excitation, and overload. For these cases a transformer is protected with a set of different relays (in case of electro-mechanical relays) or a multiple choice of different elements in one relay (in case of a numerical relay). Although this one is the most commonly used protection, still not yet powerful enough to detect small inter winding faults in power transformers. Since the resulted differential current is too small in comparison to input and output currents, so it will not be sensed by the percentage differential protection. This means that it is not sufficient and reliable in detecting minor internal faults in transformer windings. For instance, if the restraint characteristic of the percentage differential relay is set to 25 % and a minor internal fault gives a differential current of 10 %, thus the internal fault cannot be detected until this differential current fault exceeds a pre-determined value or the setting threshold value of 25 %. For this reason, the traditional percentage differential protection is not sensitive enough to determine small turn-to-turn faults. Alternatively, the literature review shows that detecting small inter turn faults in power transformer winding is not an easy problem to solve [5, 6, 8].

Techniques and schemes, which have been proposed to ameliorate the differential relay towards diagnosis and location of internal faults within the power transformer, were emphasized by many research and studies.

A digital relaying algorithm for detecting transformer winding faults in reference [9] introduces a protection algorithm based on verifying the validity of differential equations of voltages, currents and mutual flux linkages, at the primary and secondary windings during normal conditions, in the presence of external faults and magnetizing inrush. According to the results presented in this paper, the exposed algorithm was valid for 5 % of short circuited coil turns. Their algorithm is faster, supersensitive than the restraint differential current algorithm and is qualified in fault finding while energizing the transformer.

The algorithm in [10] presents differential algorithm which uses the negative sequence currents to find turn-to-turn fault in transformers. Studies presented in this paper were limited and dealt with one particular configuration and system conditions. It uses 1 % of shorted turns throughout ordinary function of the transformer.

Primary and secondary negative sequence current magnitudes and their phase shifts are used to recognize internal faults and decline external faults. The results were also not convincing because of limited studies and no detailed investigations.

The paper [11] proposes a transformer protection using Relay Increment of Flux Linkage (RIFL) for three phases Y-Y transformer, the increments of the flux linkages are calculated for a three phase Y-Δ transformer, the differences between the two phases of the increments of the flux linkages are calculated to use the line current because the delta winding current is unavailable. The RIFL is compared against the turn's ratio, if there is a difference between them that means an internal fault exists.

The performance of the proposed relay was compared with the conventional current differential relay with the harmonic blocking. Test results indicate that the proposed relay has perfectly distinguished the coil faults from inrush currents. It also, reduces the operating time of the relay for internal faults. The digital signal processor of prototype relay is implemented and it was concluded that the prototype algorithm is faster when compared to conventional relay with harmonic blocking.

The work [12], by using the advanced digital technology, it becomes possible to protect power transformers with new differential protection principle. This new principle possesses higher sensitivity than the traditional transformer differential protection for minor turn to turn faults. It investigates the negative sequence currents. The new protection principle yields a higher sensitive protection for very small internal faults in the order of 1 % short-circuited turns. The new negative-sequence current-based sensitive protection is an excellent backup to the traditional power transformer differential protection, which based on the famous differential characteristic. A case study of the new principle protection concludes some limitation of this algorithm, that it operates when power transformer is loaded and it does not indicate faulty phase(s).

The authors of [13] present an advanced model of the frequency response analysis (FRA) to analyze the integrity of power transformer parameters which depend on windings and their material properties. Among a wide range of transformer failure modes, the authors focused on using FRA for detecting changes in FRA signatures

caused by breakdown insulation and deformation of transformer winding. In practice, insulation breakdown occurs due to the circulation of high currents and voltages in the transformer. As they are too much superior at the nominal values, simultaneously to this, a flashover of winding turns begins and causes a winding short circuit which may lead to transformer failure.

In this work, the frequency of the input signal was varied over a certain range and resulting responses were profoundly studied and analyzed. This allows the detection of internal turn to turn faults and confirms the sensitivity of the FRA signature.

In the scheme of [14] the transient states are taken as models. These different models are recognized by neural network. Inputs to neural network are the harmonics of the positive sequence of differential current. These inputs are the 1st, 2nd, and 5th harmonic components of the positive sequence differential current. The application of neural networks has some limitations because it requires a lot of training models which are produced by simulation of many cases and applied just on some specific power transformers.

The work in [15] proposes to reduce the main losses of electricity which occur in distribution networks; transformers with power quantity up to 1000 kVA are used. The authors gave new technological proposals for improving the performance and effectiveness of transformers through structural-geometric transformations of active elements. Such transformers are mainly produced with rectangular section of rod and armored planar magnetic cores.

Methods of energy saving in transformer construction are based on new electrical materials high technologies able to produce composite conductors of windings with «high-temperature» superconductivity and amorphous electrical steel. This agrees with the previously known optimization and design data of transformers.

However, the cost increases significantly, and questions arise about the specifics of the design, operation and assembly of transformer and technological equipment. But a significant reduction in no-load losses is possible by performing all corner sections of the combined magnetic core from isotropic electrical steel and all rod and yoke sections from anisotropic electrical steel.

It is known that the presence of the negative sequence currents in the power transformer windings proves the existence of an internal turn-to-turn faults within this transformer [16]. Even though, sensing small power transformer coil faults is a difficult task to do, still the aim of our paper is to propose an algorithm based on the symmetrical components theory and the application of a procedure where comparison of the vector group amplitudes and phase angle shifts between negative sequence current components are realized.

The goal of the paper is to detect the internal faults for various operating conditions of the power transformer. And also, be sure that this proposed procedure is apt to accomplish its role significantly than any other classical relay.

2. The proposed procedure. Turn to turn winding fault are regarded as the main factor of the transformer deficiencies, and can lead to small changes on primary and secondary voltages and currents [17, 18].

This new algorithm is proposed to protect the power transformers against minor turn to turn faults through the exploitation of the negative sequence currents.

According to symmetrical components properties, the phase quantities are expressed in phasors notation using complex numbers, as shown in Fig. 1.
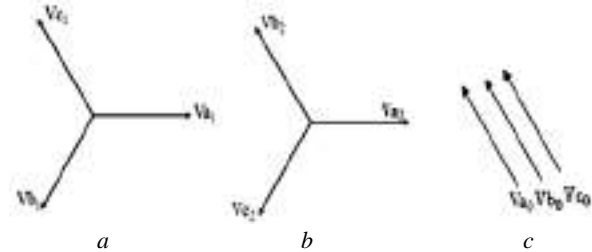
a   b   c
Fig. 1. Three phase voltage vector components:
(a) positive sequence; (b) negative sequence; (c) zero sequence

The three voltage phasors are expressed by the following formulas:
$$V_{abc} = \begin{bmatrix} V_a\ V_b\ V_c \end{bmatrix}. \quad (1)$$

This formula can be arranged as follows:
$$V_{012} = \begin{bmatrix} V_0\ V_1\ V_2 \end{bmatrix}, \quad (2)$$

where 0, 1, and 2 subscripts are respectively referring to zero, positive, and negative sequence components.

A phase rotation operator «a» is defined in (3) to rotate forward by 120 degrees. The [A] matrix is applied to convert phasors into symmetrical components:
$$[A] = \begin{bmatrix} 1 & 1 & 1 \\ 1 & a^2 & a \\ 1 & a & a^2 \end{bmatrix}. \quad (3)$$

The phase voltage sequences are represented by the sequence equation
$$V_{abc} = [A] \cdot V_{012}. \quad (4)$$

Conversely, the sequence components are represented as:
$$V_{012} = [A]^{-1} \cdot V_{abc}, \quad (5)$$

where
$$[A]^{-1} = 1/3 \begin{bmatrix} 1 & 1 & 1 \\ 1 & a & a^2 \\ 1 & a^2 & a \end{bmatrix}; \quad (6)$$

$$V_{012} = 1/3 \begin{bmatrix} 1 & 1 & 1 \\ 1 & a^2 & a \\ 1 & a & a^2 \end{bmatrix} \cdot [V_{abc}]; \quad (7)$$

$$I_{012} = 1/3 \begin{bmatrix} 1 & 1 & 1 \\ 1 & a^2 & a \\ 1 & a & a^2 \end{bmatrix} \cdot [I_{abc}]; \quad (8)$$

$$V_{abc} = \begin{bmatrix} 1 & 1 & 1 \\ 1 & a^2 & a \\ 1 & a & a^2 \end{bmatrix} \cdot [V_{012}]; \quad (9)$$

$$I_{abc} = \begin{bmatrix} 1 & 1 & 1 \\ 1 & a^2 & a \\ 1 & a & a^2 \end{bmatrix} \cdot [I_{012}]. \quad (10)$$

The symmetrical components must satisfy the constraint that their vector sum equals the original set of unbalanced phasors. The corresponding impedances are determined by using Ohm law as follows:

$$V_{abc} = [Z_{abc}] \cdot I_{abc}, \qquad (11)$$

or

$$I_{abc} = [Z_{abc}]^{-1} \cdot V_{abc} = [Y_{abc}] \cdot V_{abc}. \qquad (12)$$

It is known that, in faulty conditions the negative sequence currents in Fig. 1 are greater than the direct sequence currents [16–18]. The three symmetrical current components are described in this paper as:

• positive sequence current in the primary winding leads the positive sequence current in the secondary winding by an angle θ;

• negative sequence current in the primary winding lags the positive sequence current in the secondary winding by an angle θ;

• zero sequence current in the primary winding is in phase with the zero sequence current in the secondary winding.

It must be put in count that, when the turn to turn fault occurs inside the transformer, the negative-sequence current flows toward the fault point [19].

In this research, and in order to compare the negative sequence current amplitudes and the phase-angle shifts which separate them for both sides of the power transformer, three steps are to be followed.

First step. The measurement method of the negative sequence current amplitudes is applied to the previous electrical circuit of Fig. 2, 3, where the negative sequence currents in the primary and secondary sides are respectively written as: I_neg.seq_P and I_neg.seq_S, then compared with the preset value 2 % of the differential protection's base current. If the result is greater than the pre-set value a vector-group compensation for current amplitudes is done by the differential relay itself without changing the interposing CTs on both primary and secondary windings. The measured difference of the negative current amplitudes must be as small as possible to avoid unnecessary trip during normal operation. Ones, vector compensation is done, the second step will take place.

Second step. An evaluation of phase angles shift difference between the two phasors of the negative sequence currents on both sides of the power transformer and the threshold is done. Generally, during no internal fault operation of the transformer this difference is equal to zero degrees. When internal turn to turn fault occurs a small phase angle shift due to high current in the shorted turns will happen, therefore, a trip command is issued.

Third step. It consists on the use of powerful algorithm, which should discriminate between normal and abnormal operating conditions that occur in power system related to transformer such as external faults, internal faults and magnetizing inrush currents. If a fault occurs, within the protected area, the current balance will no longer maintained and the relay will close and release a trip signal to cause a certain circuit breakers to activate in order to disconnect the faulty transformer from the grid [15, 20].

3. Principle of operation. Fig. 2 shows a typical differential relay connection operating diagram

conditions, the fault is outside the protected transformer, the negative sequence currents will flow as illustrated in Fig. 2, where the I_neg.seq_P is flowing out of the protected area and the transformed I_neg.seq_P' will flow in the faulty side externally to the power transformer and will get out from the other side of the transformer. So I_neg.seq_P and I_neg.seq_P' will have the same direction This means that the phase shift between them is 0°, as it can be seen in the bellow electrical circuit of Fig.2. Meanwhile the current I_neg_P is getting from the external faulty secondary side towards the healthy primary side (it must be notice that I_neg.seq_P' is a *transformed* I_neg.seq_P).
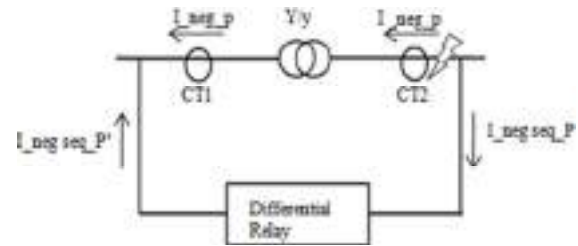
Fig. 2. Electrical circuit showing the negative sequence current directions during external fault

From Fig. 3 it can be seen that the fault is internal so, the negative currents I_neg.seq_P and I_neg.seq_S are flowing each from its own side towards the protected zone. But the negative sequence currents I_neg_P' and I_neg_S will flow out of the primary and secondary sides respectively and will have the opposite directions, so, the phase shift between them will be equal to 180°.
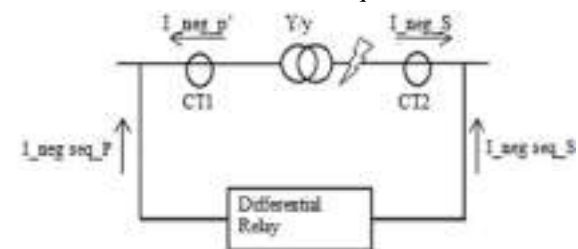
Fig. 3. Electrical circuit showing the negative sequence current directions during internal fault

In order to let the comparison of the negative sequence currents be relevant, the phase differences and turns ratio must be firstly compensated by the digital differential element which do this type of compensation automatically.

During external fault condition, the differential relay is well performing as long as the current transformers give primary currents correctly otherwise and in case of CTs saturation, a relay false operation is happened.

Modern logic differential relays are capable to accurately compute the negative sequence current quantities from actual measured current phases [21, 22]. So, internal/external fault discriminator algorithm can be developed on the basis of negative sequence current quantities and it can be reliable in detecting and locating external faults. It measures the amplitudes and their corresponding phase angle shifts of the negative sequence currents on both windings of the power transformer, and then detects the presence of the negative sequence currents which allows the fault location. It also uses the second

harmonic to prevent false tripping during magnetizing inrush conditions and the 5th harmonic to restrain the differential relay during over excitation conditions.

4. Simulation results. The performances and effectiveness of the proposed algorithm are simulated under normal and abnormal transformer operating conditions. When the power transformer is under the condition of small turn to turn faults, it is preferred to use the negative-sequence currents for the detection of such type of faults. Since, the investigated power transformer is connected in Y-y mode, and is 20 MVA, 31.5 kV / 400 V; the detection of internal fault can be done directly due to the availability of the winding currents.

Performance of the proposed scheme during external faults. Figures 4, 5 show that the differential relay is stable for external faults and didn't trip because the fault was outside the protected transformer. This means that the relay has detected the external fault and the output of the negative-sequence current differential element did not trip during external fault and the 3 phase primary and secondary current wave forms did not alter. Also, it can be seen that the maximum and minimum current values of the primary side are respectively:

- phase $A - I_{Amax} = 4$ kA, $I_{Amin} = -2.2$ kA;
- phase $B - I_{Bmax} = 2.3$ kA, $I_{Bmin} = -3.2$ kA;
- phase $C - I_{Cmax} = 2.3$ kA, $I_{Cmin} = -3.2$ kA.

The external fault was detected within one cycle (0.96 s).
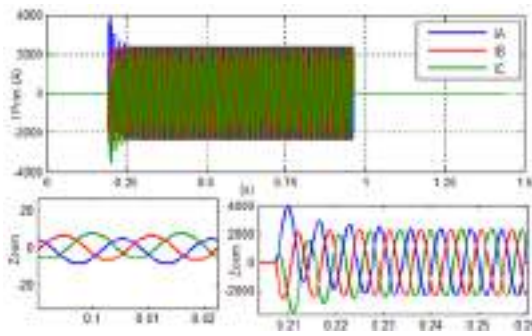
Fig. 4. Primary phase currents of the proposed scheme during external fault
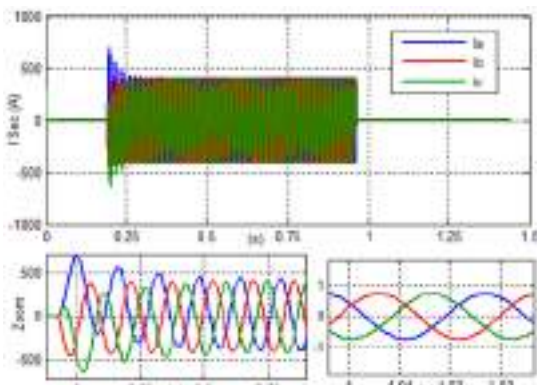
Fig. 5. Secondary phase currents of the proposed scheme during external fault

The maximum and minimum current phase values of the secondary side are respectively:

- phase $A - I_{amax} = 700$ A, $I_{amin} = -400$ A;
- phase $B - I_{bmax} = 400$ A, $I_{bmin} = -550$ A;
- phase $C - I_{cmax} = 700$ A, $I_{cmin} = -350$ A.

The differential relay did not issue the signal trip, because the fault was external.

In Fig. 5 the primary phase and secondary phase current wave forms did not alter, this means that, the relay signal trip didn't take place and no trip was executed, which confirms that the fault was external, as shown in Fig. 5.

Figure 6 shows the wave form of the three phase primary currents during internal turn to turn fault in the presence of inrush currents. It can be seen that the differential relay didn't send a trip signal because it considers the inrush currents as a transient phenomenon and will disappear quickly.

The primary phase currents values during turn to turn fault in the presence of inrush currents are:

- phase $A - I_{Amax} = 4$ kA, $I_{Amin} = -2.2$ kA;
- phase $B - I_{Bmax} = 2.3$ kA, $I_{Bmin} = -3.2$ kA;
- phase $C - I_{Cmax} = 2.3$ kA, $I_{Cmin} = -3.2$ kA.
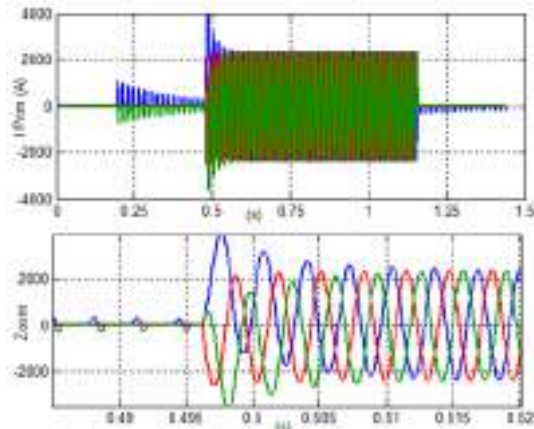
Fig. 6. Three phase primary currents during internal turn to turn fault in presence of inrush currents

In Fig. 7 it can be seen that the internal turn to turn fault has happened during an interval time of 0.645 s and the digital differential relay has ordered a signal trip, because the fault was internal and without the presence of inrush currents. The obtained data from the wave current forms is as bellow: The maximum and minimum values of the secondary phase currents from Fig. 7 are:

- phase $A - I_{amax} = 0.6$ A, $I_{amin} = -0.6$ A;
- phase $B - I_{bmax} = 0.6$ A, $I_{bmin} = -0.6$ A;
- phase $C - I_{cmax} = 0.6$ A, $I_{cmin} = -0.6$ A.

Fault duration interval was from 0.48 to 1.125 s.
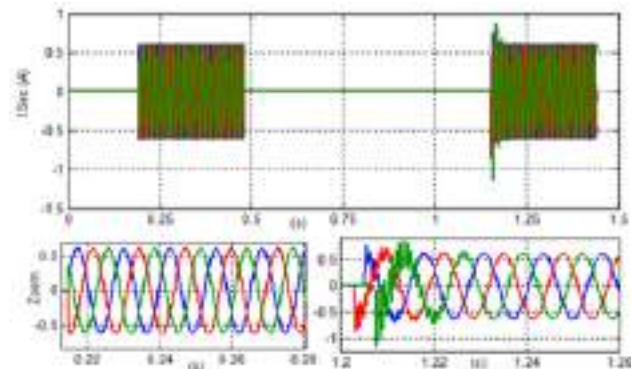
Fig. 7. Three phase secondary currents of the proposed scheme during internal turn to turn fault in the absence of the inrush currents

The inrush current phenomenon shown in Fig. 8 is obtained from simulation study using the MATLAB Simulink environment.

It can be noticed that the maximum value of the inrush current is higher many times than nominal current. The inrush currents may accidently push the protection relay to trip. In such conditions, the relay must be able to discriminate between the inrush currents and the internal turn to turn fault current and delay the trip signal until the inrush currents disappear, and then send a signal trip as illustrated in Fig. 9.
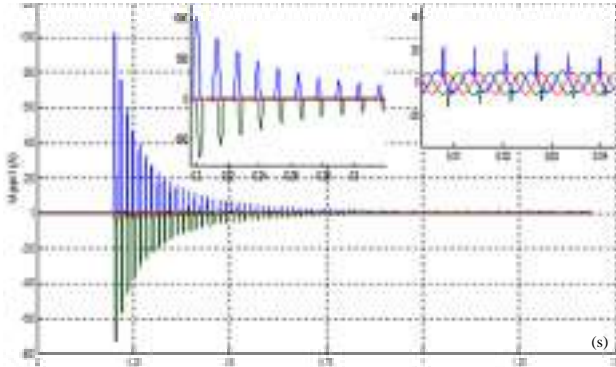
Fig. 8. Three phase inrush currents
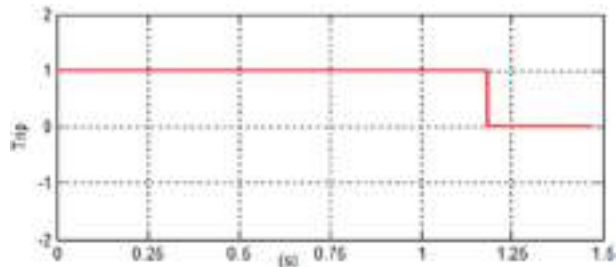
Fig. 9. Differential relay trip at 1.17 s

From Fig. 10–21 the primary, secondary and magnetization impedances are calculated in per unit (pu) system.

Performance of the proposed procedure during turn to turn faults. The performance of the proposed differential protection algorithm is profoundly studied and simulated by MATLAB/Simulink. Under turn to turn short-circuit conditions. Three sets of values for power transformer impedances are calculated in per unit system. Then, firstly, the negative sequence current amplitudes of primary and secondary sides are compared with the threshold 2 % of the winding. And secondly, the corresponding shift phase between these negative sequence currents are also compared to preset level which is from 0° to 3° to let the relay sensitivity higher for turn to turn faults recognition.

The simulation study is done for different per unit calculated values of primary impedance Z_1, secondary impedance Z_2 and magnetization impedance Z_M. These impedances values are equivalent to the percentage of short-circuited winding turns 10 %, 3 % and 0.5 %.

Case 1: Turn to turn fault on the secondary side. If the quantity of the negative current amplitudes is higher than the preset level, and the phase shift is zero, this means that an internal turn to turn fault has happened and a signal trip must be issued.

Figure 10 shows that a secondary internal turn to turn fault has happened in the calculated impedance values are: $Z_1 = Z_2 = 0.002$ pu, $Z_M = 0.5$ pu.

The corresponding negative sequence current amplitudes (I_neg.seq_P and I_neg.seq_P') are compared with each other and with the preset level of 2 %. They are found to be equal and superior to the preset level as it can be seen on Fig. 10.
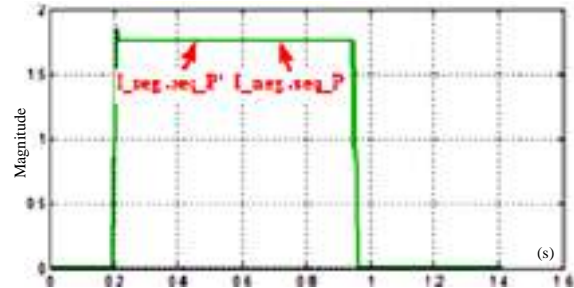
Fig. 10. Comparison of the negative sequence current amplitudes of I_neg.seq_P and I_neg.seq_P' where calculated impedances are: $Z_1 = Z_2 = 0.002$ pu, $Z_M = 0.5$ pu

Figure 11 shows the phase shift comparison between the negative sequence currents (I_neg.seq_P and I_neg.seq_P') during secondary turn to turn fault for calculated per unit impedances $Z_1 = Z_2 = 0.002$ pu, $Z_M = 0.5$ pu. It was found that the phase shift between them is 180°, which means that they are in opposite directions as it was expected.
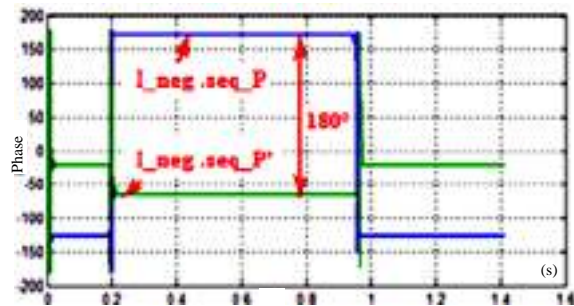
Fig. 11. Comparison of phase shift between I_neg.seq_P and I_neg.seq_P' where impedances are: $Z_1 = Z_2 = 0.002$ pu, $Z_M = 0.5$ pu

Figure 12 shows an amplitudes comparison between I_neg.seq_P and I_neg.seq_P' during turn to turn fault for calculated impedances $Z_1 = Z_2 = 0.008$ pu, $Z_M = 0.5$ pu. It can be seen from Fig. 12 that the negative sequence current amplitudes of the faulted side I_neg.seq_P' is equal to the magnitude of the negative sequence current I_neg.seq_P on the healthy side and both of them are higher than the preset level as expected.
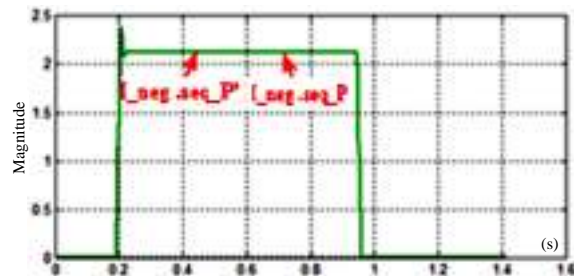
Fig. 12. Amplitude comparison between I_neg.seq_P, and I_neg.seq_P' where impedances are: $Z_1 = Z_2 = 0.008$ pu, $Z_M = 0.5$ pu

In Fig. 13 it can be seen that, the phase angle between the two negative sequence currents I_neg.seq_P, and I_neg.seq_P' during secondary turn to turn fault is 180°, this means that they are opposite in directions, which is already proven by the previous corresponding electrical circuit diagram (Fig. 2).
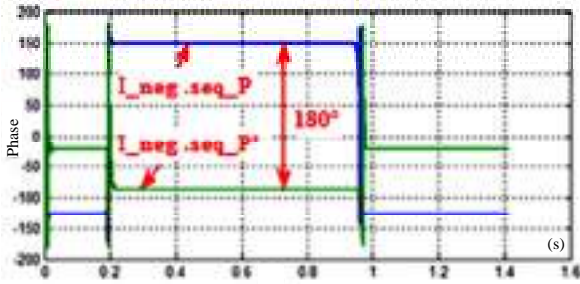
Fig. 13. Phase angle comparison between I_neg.seq_P and I_neg.seq_P' during secondary internal turn to turn fault for $Z_1 = Z_2 = 0.008$ pu, $Z_M = 0.5$ pu

Figure 14 shows equal amplitudes of the negative sequence currents on both sides of the power transformer. It can be seen in the previous electrical circuit (Fig. 2) which illustrating directions of the negative sequence currents during external fault. It can be noticed that I_neg.seq_P enters from the faulty side and leaves from the other side, after being transformed to become I_neg.seq_P' (Fig. 15).
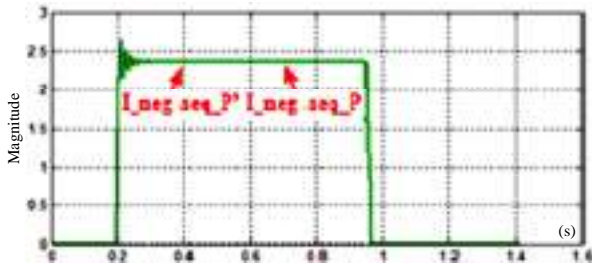
Fig. 14. Amplitudes comparison between I_neg.seq_P and I_neg.seq_P' during secondary external fault for calculated impedances: $Z_1 = Z_2 = 0.2$ pu, $Z_M = 0.5$ pu
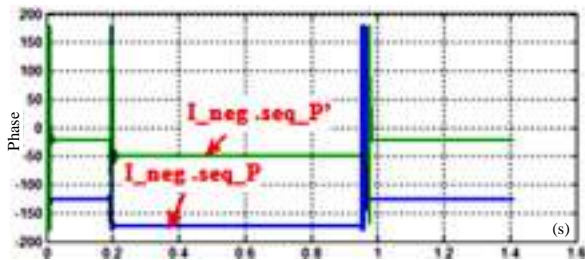
Fig. 15. Phase angle comparison between I_neg.seq_P and I_neg.seq_P' during secondary external fault side where calculated impedances are: $Z_1 = Z_2 = 0.2$ pu, $Z_M = 0.5$ pu

Case 2: Turn to turn fault at the primary side. Figures 16, 17 show that during internal turn to turn fault in the primary side, the negative current amplitudes of (I_neg.seq_S) are much higher than the amplitude of (I_neg.seq_P), due to the fault presence in the primary winding «very high resistance very low current Kirchhoff's second law» and the phase shift between them is moderate.
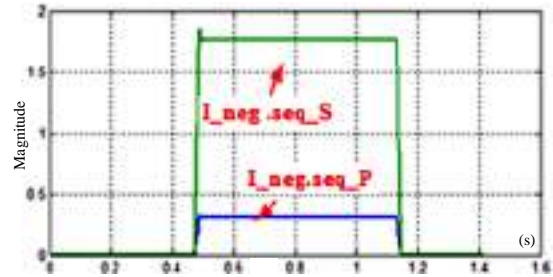
Fig. 16. Amplitudes comparison between I_neg.seq_P and I_neg.seq_S, during internal turn to turn fault, where calculated impedances are: $Z_1 = Z_2 = 0.002$ pu, $Z_M = 0.5$ pu
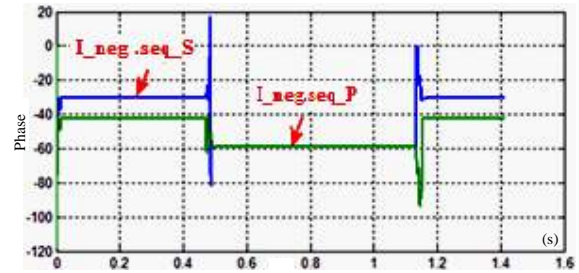
Fig. 17. Phase angle comparison between I_neg.seq_P and I_neg.seq_S during internal turn to turn fault, where calculated impedances are: $Z_1 = Z_2 = 0.002$ pu, $Z_M = 0.5$ pu

Figure 18 is illustrating the magnitudes of the negative sequence current in the primary and secondary sides respectively I_neg.seq_P and I_neg.seq_S during internal turn to turn fault for the corresponding impedances calculated in per unit system: $Z_1 = Z_2 = 0.008$ pu, $Z_M = 0.5$ pu. It can be seen on Fig. 18 that the amplitude of the secondary negative sequence current (I_neg.seq_S) is almost 3 times higher than the primary negative sequence current.
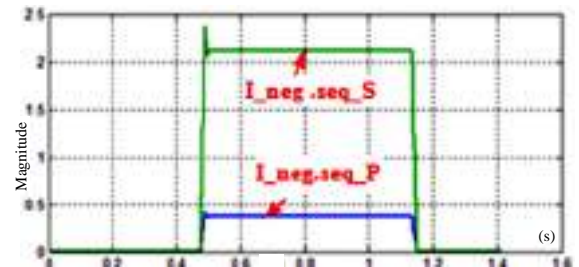
Fig. 18. Amplitude comparison between I_neg.seq_P and I_neg.seq_S during internal turn to turn fault, where impedances are: $Z_1 = Z_2 = 0.008$ pu, $Z_M = 0.5$ pu

Figure 19 shows the phase angle shift between the negative sequence currents (I_neg.Seq_P) and (I_neg.seq_S) where it can be remarked that its value is about 3° because the impedance values are very small.
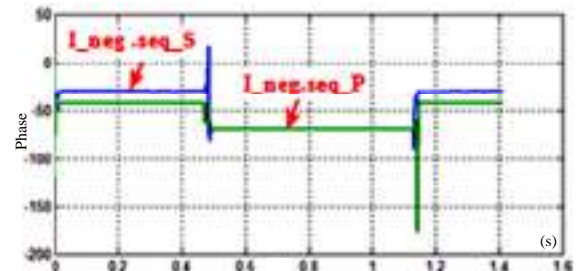
Fig. 19. Phase angle comparison between I_neg.Seq_P and I_neg.seq_S during internal turn to turn fault, where calculated impedances are: $Z_1 = Z_2 = 0.008$ pu, $Z_M = 0.5$ pu

In Fig. 20, 21 it can be seen that amplitude of I_neg.seq_S is higher than of I_neg.Seq_P, and the phase angle between the two corresponding negative sequence currents during internal turn to turn fault for primary winding, is almost 0°.
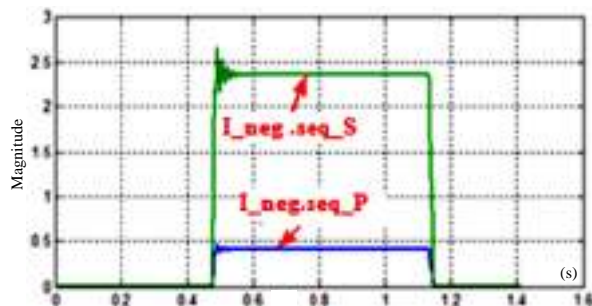
Fig. 20. Amplitude comparison between I_neg.seq_P and I_neg.seq_S during internal turn to turn fault, where impedances are: $Z_1 = Z_2 = 0.2$ pu, $Z_M = 0.5$ pu
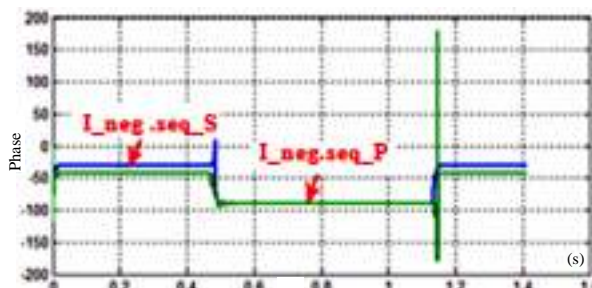
Fig. 21. Phase angle comparison between I_neg.Seq_P and I_neg.seq_S during internal turn to turn fault, where impedances are: $Z_1 = Z_2 = 0.2$ pu, $Z_M = 0.5$ pu

5. Conclusions.

This paper describes a new negative sequence current based protection method for detecting and locating the inter-turn faults in transformer windings that overcomes the limitation of the traditional transformer protection schemes in determining low level inter-turn faults. The negative current values are very exploited in the domain of protection in general and especially in the field of power transformers. In spite of that, the problem of detecting and locating the small internal turn to turn faults is a hard task to accomplish. Overall, when it consists to the power transformer itself. Because the variation in power transformer amplitudes and phase shifts is very difficult thing to be reestablished. The proposed procedure is built on the contributions to total negative sequence currents from both sides HV and LV of the power transformer, it has proved to be reliable, efficient, and fast. It takes only few milliseconds to detect faults up to 0.5 %, and to characterize it as internal or external.

The evaluation of the proposed scheme has been done for different faults and operating conditions. It was found to be more sensitive than the classical differential relay. Hence, the scheme is very robust in such disturbance conditions which involves only few turns among primary or secondary windings of the power transformer.

Conflict of interest. The author declares that he has no conflicts of interest.

REFERENCES
1. Blackburn J.L. *Applied protective relaying.* Westinghouse Electric Corporation. Relay Instrument Division. 2nd ed., 1979.
2. Summary of the «Guide for Protective Relay Applications to Power Transformers» ANSI C37.91. *IEEE Transactions on Power Apparatus and Systems*, 1985, vol. PAS-104, no. 12, pp. 3538-3543. doi: https://doi.org/10.1109/TPAS.1985.318907.
3. Lapworth J., McGrail T. Transformer failure modes and planned replacement. *IEE Colloquium on Transformer Life* Management (Ref. No. 1998/510), 1998, pp. 9/1-9/7. doi: https://doi.org/10.1049/ic:19981013.
4. *IEEE Guide for Protective Relay Applications to Power Transformers. IEEE Std C37.91-2000 (Revision of IEEE Std* C37.91-1985), 2000, pp. 1-85. doi: https://doi.org/10.1109/IEEESTD.2000.91943.
5. *IEEE Guide for the Protection of Network Transformers. IEEE Std C37.108-2002 (Revision of C37.108-1989)*, 2002, pp. 1-40. doi: https://doi.org/10.1109/IEEESTD.2002.94141.
6. Faiz J., Heydarabadi R. Diagnosing power transformers faults. *Russian Electrical Engineering*, 2014, vol. 85, no. 12, pp. 785-793. doi: https://doi.org/10.3103/s1068371214120207.
7. Aljohani O., Abu-Siada A. Application of Digital Image Processing to Detect Short-Circuit Turns in Power Transformers Using Frequency Response Analysis. *IEEE Transactions on Industrial Informatics*, 2016, vol. 12, no. 6, pp. 2062-2073. doi: https://doi.org/10.1109/TII.2016.2594773.
8. Torkaman A., Naeini V. Recognition and location of power transformer turn to turn fault by analysis of winding imposed forces. *Journal of Operation and Automation in Power Engineering*, 2019, vol. 7, no. 2, pp: 227-234. doi: https://dx.doi.org/10.22098/joape.2019.5735.1428.
9. Sachdev M.S., Sidhu T.S., Wood H.C. A digital relaying algorithm for detecting transformer winding faults. *IEEE Transactions on Power Delivery*, 1989, vol. 4, no. 3, pp. 1638-1648. doi: https://doi.org/10.1109/61.32654.
10. Chavhan R., Kulkarni V.A. Negative sequence component for detection of inter-turn fault of transformer. *International Journal of Innovative Research in Science, Engineering and Technology*, 2017, vol. 6, no. 7, pp. 13950-13958. Available at: https://www.ijirset.com/upload/2017/july/172_Negative.pdf (accessed 13 May 2021).
11. Zacharias D., Gokaraju R. Prototype of a Negative-Sequence Turn-to-Turn Fault Detection Scheme for Transformers. *IEEE Transactions on Power Delivery*, 2016, vol. 31, no. 1, pp. 122-129. doi: https://doi.org/10.1109/TPWRD.2015.2483524.
12. Ngaopitakkul A., Kunakorn A. Internal fault classification in transformer windings using combination of discrete wavelet transforms and back-propagation neural networks. *International Journal of Control, Automation and Systems*, 2006, vol. 4, no. 3, pp. 365-371. Available at: https://www.researchgate.net/publication/268338337_Internal_Fault_Classification_in_Transformer_Windings_using_Combination_of_Discrete_Wavelet_Transforms_and_365_Internal_Fault_Classification_in_Transformer_Windings_using_Combination_of_Discrete_Wavel/stats (accessed 13 May 2021).
13. Devadiga A.A., Harid N., Griffiths H., Al Sayari N., Barkat B., Jayaram S., Ikeda H., Koshizuka T., Taniguchi Y. Winding turn-to-turn short-circuit diagnosis using FRA method: sensitivity of measurement configuration. *IET Science, Measurement & Technology*, 2019, vol. 13, no. 1, pp. 17-24. doi: https://doi.org/10.1049/iet-smt.2018.5331.
14. Stavinskiy A.A., Tsyganov A.M. Design and technological proposals for improving a single-phase transformer with laminated magnetic core. *Electrical Engineering & Electromechanics*, 2020, no. 6, pp. 11-17. doi: https://doi.org/10.20998/2074-272x.2020.6.02.
15. Rizvi I.A., Reeser G. Using symmetrical components for internal external fault discrimination in differential protection

schemes. *2013 66th Annual Conference for Protective Relay Engineers*, 2013, pp. 68-79. doi: https://doi.org/10.1109/cpre.2013.6822028.

16. Subramanian M. Detection of winding inter-turn faults. Detection based on frequency response analysis - Part I. *Transformers Magazine*, 2020, vol. 7, iss. 1, pp. 112-118. Available at: https://transformers-magazine.com/magazine/7228-editorial-message-vol-7-issue-1/ (accessed 13 May 2021).

17. Panah M.S.P., Azarakhsh J., Raisi Z. A novel method in differential protection of power transformer using wavelet transform and correlation factor analysis. *Bulletin de la Societe Royale des Sciences de Liege*, 2016, vol. 85, p. 1119-1135. doi: https://doi.org/10.25518/0037-9565.5924.

18. Ivanchenko D., Smirnov A. Identification of interturn faults in power transformers by means of generalized symmetrical components analysis. *E3S Web of Conferences*, 2019, vol. 140, p. 04007. doi: https://doi.org/10.1051/e3sconf/201914004007.

19. Azizan N.S., Wooi C.L., Ismail B., Arshad S.N.M., Isa M., Mustafa W.A., Rohani M. Simulation of differential relay for transformer protection. *IOP Conference Series: Materials Science and Engineering*, 2020, vol. 767, p. 012004. doi: https://doi.org/10.1088/1757-899x/767/1/012004.

20. Syvokobylenko V.F., Lysenko V.A. Improving the efficiency of fault protection systems of electrical grids based on zero sequence voltages and currents wavelet transforms. *Electrical Engineering & Electromechanics*, 2020, no. 4, pp. 67-72. doi: https://doi.org/10.20998/2074-272X.2020.4.09.

21. Snitkov K.I., Shabatura Y.V. A method of reducing the error in determining the angular displacements when using inductive sensors. *Electrical Engineering & Electromechanics*, 2020, no. 6, pp. 3-10. doi: https://doi.org/10.20998/2074-272X.2020.6.01.

22. Liu C.-H., Muda W.H.P., Kuo C.-C. Turn-to-Turn Fault Diagnosis on Three-Phase Power Transformer Using Hybrid Detection Algorithm. *Applied Sciences*, 2021, vol. 11, no. 6, p. 2608. doi: https://doi.org/10.3390/app11062608.

Mokhtar Zitouni, PhD Student, Associate lecturer,
Electrical Engineering Department,
Automatic Laboratory,
University of Setif,
Route de Bejaia, 19000, Algeria,
e-mail: zitounimokhtar2005@yahoo.fr (Corresponding author)

B.I. Kuznetsov, T.B. Nikitina, I.V. Bovdui, O.V. Voloshko, V.V. Kolomiets, B.B. Kobilyanskiy

Method of adjustment of three circuit system of active shielding of magnetic field in multi-storey buildings from overhead power lines with wires triangular arrangement

Aim. *For the first time the method of adjustment of three circuit system of the active shielding of the magnetic field based on experimentally determined space-time characteristics to increase the shielding factor in a multi-storey building located near a single-circuit overhead transmission lines with a wires triangular arrangement was developed.* ***Methodology****. When synthesizing the laboratory model of system of active shielding the coordinates of spatial arrangement and of three shielding coils, the currents in shielding coils and resulting magnetic flux density value in the shielding space were calculated. The synthesis is based on the multi-criteria game decision, in which the payoff vector is calculated on the basis on quasi-stationary approximation solutions of the Maxwell equations. The game decision is calculated based on the stochastic particles multi swarm optimization algorithms.* ***Results****. Computer simulation and experimental research of the space-time characteristics of laboratory model of three circuit system of active shielding of magnetic field, generated by overhead power lines with phase conductors triangle arrangements in multi-storey building are given. The possibility of initial magnetic flux density level reducing to the sanitary standards level is shown.* ***Originality****. For the first time the synthesis and adjustment of laboratory model of three circuit system of active shielding of magnetic field based on experimentally determined space-time characteristics to increase the shielding factor in a multi-storey building located near a single-circuit overhead transmission lines with a wires triangular arrangement carried out.* ***Practical value****. Practical recommendations from the point of view of the implementation of developed method of adjustment of the three circuit system of the active shielding of the magnetic field based on experimentally determined space-time characteristics in a multi-storey building located near a single-circuit overhead transmission lines with a triangular arrangement of wires are given.* References 48, figures 11.*
Key words: **overhead power lines, magnetic field, space-time characteristics, system of active shielding, shielding factor, computer simulation, experimental research.**

Мета. *Вперше розроблено метод налаштовування триконтурної системи активного екранування магнітного поля на основі експериментально визначених просторово-часових характеристик для коефіцієнту екранування в багатоповерховому будинку, розташованому поблизу одноколових повітряних ліній електропередачі з трикутним розташуванням проводів.* ***Методологія****. При синтезі лабораторної моделі системи активного екранування були розраховані координати просторового розташування трьох екрануючих обмоток, струми в екрануючих обмотках та результуюче значення індукції магнітного поля в просторі екранування. Синтез системи базується на рішенні багатокритеріальної гри, в якій вектор виграшу розраховується на основі квазістаціонарних апроксимаційних розв'язків рівнянь Максвелла. Рішення гри розраховується на основі алгоритмів стохастичної оптимізації мультирою частинок.* ***Результати****. Наведено результати комп'ютерного моделювання та експериментальних досліджень просторово-часових характеристик лабораторної моделі триконтурної системи активного екранування магнітного поля, яке створюється повітряними лініями електропередачі з трикутним розташуванням фазних провідників у багатоповерховому будинку. Показано можливість зниження початкового рівня індукції магнітного поля до санітарних норм.* ***Оригінальність****. Вперше проведено синтез та налаштовування лабораторної моделі триконтурної системи активного екранування магнітного поля на основі експериментально визначених просторово-часових характеристик для підвищення фактору екранування провідників у багатоповерховому будинку, розташованому поблизу одноколових повітряних ліній електропередачі з трикутним розташуванням проводів.* ***Практична цінність****. Наведено практичні рекомендації з точки зору реалізації розробленого методу налаштовування триконтурної системи активного екранування магнітного поля на основі експериментально визначених просторово-часових характеристик в багатоповерховому будинку, який розташовано поблизу одноконтурних повітряних ліній електропередачі з трикутним розташуванням проводів.* Бібл. 48, рис. 11.*
Ключові слова: **повітряні лінії електропередачі, магнітне поле, просторово-часові характеристики, система активного екранування, коефіцієнт екранування, комп'ютерне моделювання, експериментальні дослідження.**

Introduction. Most of the existing 10-330 kV overhead transmission lines, which were built during the last 50 years, often pass near old residential buildings. These overhead transmission lines generate a magnetic field of power frequency inside residential buildings, the level of which exceeds the sanitary standards of Ukraine [1]. One of the most economically feasible approach to the further safe operation of these residential buildings is to reduce the level of magnetic field (MF) inside these buildings by means of active shielding [2–4]. In Ukraine, in the area of old residential buildings, 110 kV power transmission lines with a triangular suspension of wires are the most common.

Such overhead transmission lines generate magnetic field with a circular space-time characteristic. To compensate for such a magnetic field, at least two compensation windings are needed even when shielding magnetic field inside one-story residential buildings. When shielding such a magnetic field in multi-storey buildings, three or more compensation windings may be required [5–7]. The adjustment of such a three circuit system is a rather complex scientific problem. The problem of adjustment of three circuit system of the active shielding consists in experimentally adjustment of parameters of current regulators in compensation windings. For each compensation winding, it is necessary to determine the magnitude of the gain and phase shift for the regulator, which operates according to the open-loop control principle. And at the same time for each compensation winding, it is necessary to determine the magnitude of the gain for the regulator, which operates according to the closed-loop control principle with feedback on the induction of the resultant magnetic field.

A feature of the system of the active shielding under consideration is the highly elongated space-time

characteristic ellipses of the resulting MF during the operation of individual compensating windings [8–10]. Moreover, when the windings work together, the magnetic field generated by the individual windings is mutually compensated, which makes it possible to obtain a high compensation efficiency of the initial magnetic field [11, 12]. Therefore, when adjustment the system of the active shielding, it is necessary to use space-time characteristic and therefore the development of method of adjustment of three system of the active shielding of the magnetic field based on experimentally measured space-time characteristics is important and urgent scientific problem.

The aim of the work is to develop of method of adjustment of three circuit system of the active shielding of the magnetic field based on experimentally determined space-time characteristics to increase the shielding factor in a multi-storey building located near a single-circuit overhead transmission lines with wires triangular arrangement.

Statement of the research problem. The State Institution "Institute of Technical Problems of Magnetism of the NAS of Ukraine" developed the laboratory model of a single-circuit overhead power transmission line with a triangular arrangement of wires on a scale of 1 to 15. Figure 1 shows such a laboratory model.

Fig.1. The laboratory model of a single-circuit overhead power transmission line with a triangular arrangement of wires

Consider the synthesis and adjustment of the system of the active shielding of the space-time characteristic generated by this model of the power transmission line in the model of a multi-storey building, as it is shown in Fig. 2.
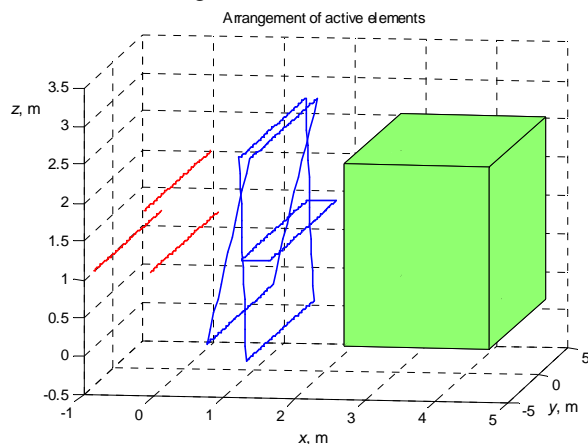
Let us introduce a vector of unknown parameters of the system of active shielding, the components of which are the coordinates of shielding coils and parameters of the regulator [13–18] and vector of uncertainty parameters of initial magnetic field model [19–23]. Then calculate of vector of unknown parameters of system of active shielding and of vector of uncertainty parameters in the form of a solution of multi-criteria game. The components vector payoff in this game are levels of magnetic flux density at points of the shielding space. These components are nonlinear functions of the vectors of unknown parameters and uncertainty parameters and are calculated on basis of Maxwell equations quasi-stationary approximation solutions [24–28]. First player is vector of unknown parameters and its strategy is minimization of vector payoff. Second player is vector of uncertainty parameters and this strategy is maximization of the same vector payoff [29–33].

And therefore the solution of multi-criteria game is calculated from the condition of minimum value of vector payoff for the vector of unknown parameters but the maximum value of vector payoff for the vector uncertainty parameters. This technique corresponds to the standard worst-case robust systems synthesis approach [34–38].

To find multi-criteria game solution from Pareto-optimal set solutions taking into account binary preference relations [39, 40] used particle multi swarm optimization algorithm [41–47], in which swarms number equal number of vector payoff components.

Computer simulation results. Consider the result of synthesis of model of system of the active shielding of magnetic field with circular space-time characteristic created by three-phase single-circuit overhead power line 110 kV with phase conductors triangular arrangements in a multi-storey building, as it is shown in Fig. 2. In order to reduce the level of magnetic flux density of the initial magnetic field throughout the entire multi-storey building to the level of sanitary standards of Ukraine, in this case, it is necessary to use three shielding windings, as it is shown in Fig. 2.

Figure 3 shows lines of equal level of module of the resultant magnetic flux density when the system of active shielding is on.

Fig. 2. The location of model of overhead power line, and shielding space in model of multi-storey building
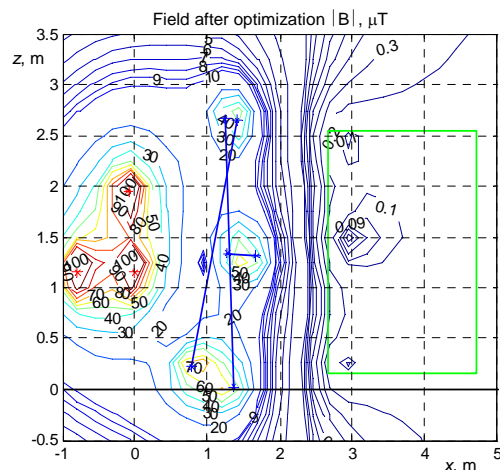
Fig. 3. Isolines of the resultant magnetic flux density when the system of active shielding is on

As follows from this figure, the level of magnetic flux density of the resulting magnetic field in the entire space of a multi-storey building does not exceed the level of 0.5 μT, which corresponds to the sanitary standards of Ukraine. Note that in the center of the multi-storey building under consideration, the level of magnetic flux density of the resulting magnetic field does not exceed 0.2 μT, and, therefore, in this part of the space, using an system of active shielding, the induction level of magnetic flux density of the initial magnetic field can be reduced by more than 20 times.

Figure 4 shows the space-time characteristics of the magnetic flux density vector of magnetic field generated by: 1) overhead power line; 2) all three shielding coils and 3) the resultant magnetic field when the all three shielding coils are on.
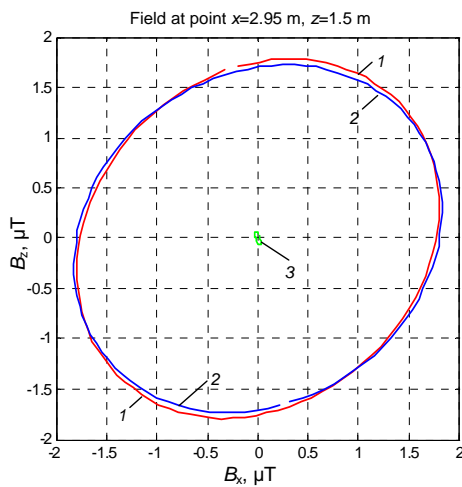
Fig. 4. Space-time characteristics of magnetic flux density without and with system of active shielding with all three shielding coils and only all three shielding coils

Now let us consider the shielding efficiency of the original magnetic field when only one single firs shielding coil is used at optimal values of the regulator of this coil. Figure 5 shows the space-time characteristics of the magnetic flux density vector of magnetic field generated by: 1) overhead power line; 2) the only one single first shielding coil and 3) the resultant magnetic field when the only one single first shielding coil is on.
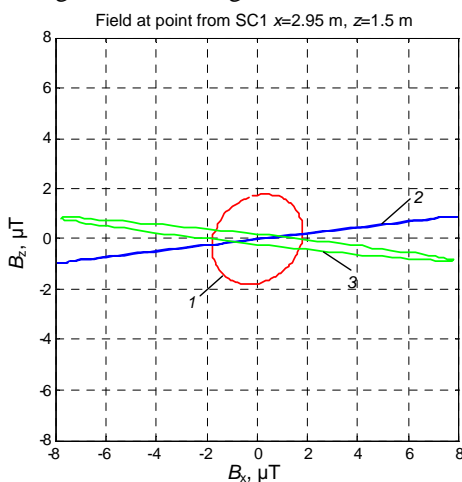
Fig. 5. Space-time characteristics of magnetic flux density without and with system of active shielding with only one single first shielding coil (SC1)

Now let us consider the shielding efficiency of the original magnetic field when only one single second shielding coil is used at optimal values of the regulator of this coil. Figure 6 shows the space-time characteristics of the magnetic flux density vector of magnetic field generated by: 1) overhead power line; 2) the only one single second shielding coil and 3) the resultant magnetic field when the only one single second shielding coil is on.
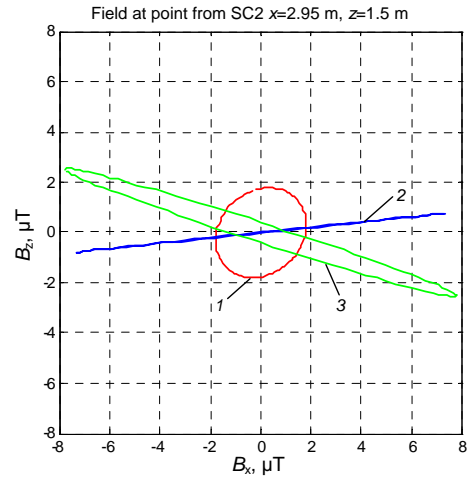
Fig. 6. Space-time characteristics of magnetic flux density without and with system of active shielding with only one single second shielding coil (SC2)

Now let us consider the shielding efficiency of the original magnetic field when only one single third shielding coil is used at optimal values of the regulator of this coil. Figure 7 shows the space-time characteristics of the magnetic flux density vector of magnetic field generated by: 1) overhead power line; 2) the only one single third shielding coil and 3) the resultant magnetic field when the only one single third shielding coil is on.
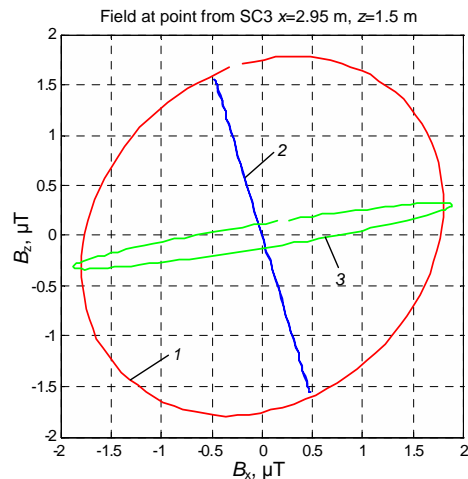
Fig. 7. Space-time characteristics of magnetic flux density without and with system of active shielding with only one single third shielding coil (SC3)

Now let us consider the shielding efficiency of the original magnetic field when only both first and second shielding coils are used at optimal values of the regulator of these coils. Figure 8 shows the space-time characteristics of the magnetic flux density vector of magnetic field generated by: 1) overhead power line; 2) only both first and second shielding coils and 3) the

resultant magnetic field when the only both first and second shielding coils are on.
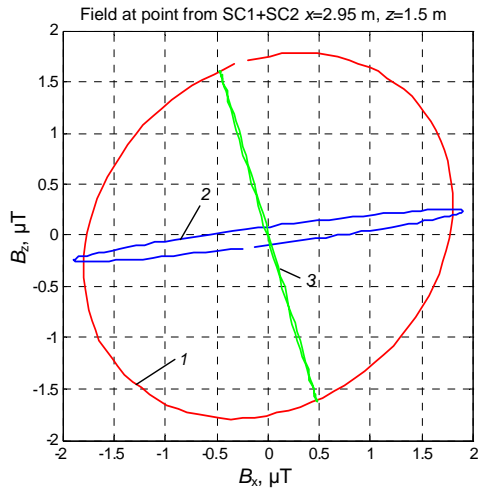
Fig. 8. Space-time characteristics of magnetic flux density without and with system of active shielding with only both first and second shielding coils and only both first and second shielding coils

Note that from a comparison of the space-time characteristics shown in Fig. 8 follows that the space-time characteristic of the resulting magnetic field remaining after the operation of the only first and second shielding coil is a highly elongated ellipse, the major axis of which practically coincides with the space-time characteristics of the magnetic field generated by only one third shielding coil, as it shown in Fig. 7.

As a result, with the help of the third shielding coil, the major axis of the space-time characteristic of the resulting magnetic field, which remains after the operation of the only first and second shielding coils, is compensated effectively. Due to such compensation, a sufficiently high shielding factor of 20 is provided in the system with the simultaneous operation of all three shielding coils.

Note that the calculated space-time characteristic for the laboratory model of a single-circuit overhead power transmission line with a triangular arrangement of wires shown in Fig. 3–7 differs from the corresponding space-time characteristic, calculated in [48] for a five-storey building.

Results of adjustment of system of the active shielding. Based on the system of the active shielding obtained as a result of the synthesis, the coordinates of the location of the compensation windings relative to the overhead transmission lines were calculated. According to the coordinates obtained, the installation of three compensation windings relative to the wires of the power transmission line was carried out.

A feature of the system under consideration is the fact that when compensating the initial magnetic field with the help of separate compensation windings, the space-time characteristic of the resulting space-time characteristic has the shape of a strongly elongated ellipse. In this case, there is a significant (2–3 times) overcompensation of the initial magnetic field. Such a magnetic field must be compensated for with another compensation winding.

To realize the high shielding efficiency of such a magnetic field, it is necessary that the space-time characteristic magnetic field generated by the compensation winding be strictly parallel to the space-time characteristic of the original magnetic field.

Therefore, to adjustment of such system of the active shielding, it is necessary to use space-time characteristic.

The simplest way is to calculate the magnetic induction of an infinitely long wire without taking into account its sagging. In this case, we can restrict ourselves to a two-dimensional model of the magnetic field, since the component of the magnetic induction vector, located parallel to this wire, is equal to zero. Taking into account the wire sag and the complex configuration of the wires, a three-dimensional model of the magnetic field is used with a significantly large number of elementary sections.

Naturally, to synthesize the initial exact model of the magnetic field, initial data are required for the spatial location of all conductors of the group of all power lines, relative to the space under consideration, as well as the values of the currents and phases of all conductors of all power lines. For this purpose, measurements were carried out, experimental studies of the geometric dimensions of all power lines and the values of the vectors of the magnetic field induction at various points in space.

Space-time characteristic of a three-dimensional space-time characteristic is a surface formed by the end of the magnetic field induction vector with time change. To measure the instantaneous value of the induction vector of such a space-time characteristic, it is necessary to have three measuring coils, the axes of which are orthogonal to each other. Figure 9,a shows such three coils for measuring system (Fig. 9,b) of three components of space-time characteristic.

a

b

Fig. 9. The measuring windings (*a*) of system for measuring space-time characteristic (*b*)

For sufficiently long transmission lines of the magnetic field component, the parallel line of wires is practically zero. Therefore, the mathematical model of a space-time characteristic power transmission line is often adopted in the form of a two-dimensional model. For such a model, the space-time characteristic is a flat figure.

A special measuring system has been developed for measuring space-time characteristic. This measuring system contains two measuring coils of magnetic field induction the axes of which are orthogonal to each other and directed along the axes of the original magnetic field. Figure 9,b shows such measuring system.

When setting up this space-time characteristic measurement system, it is important to ensure the identity of the channels for measuring the amplitude and phase of the induction of the original magnetic field.
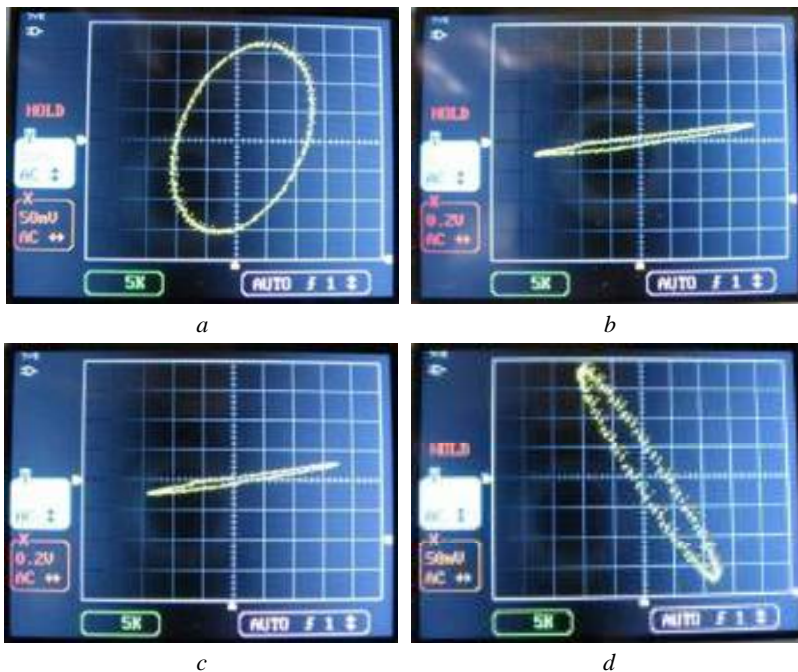
Figure 10,a shows space-time characteristic initial of magnetic flux density of laboratory model of overhead power line. Let us now consider the experimental space-time characteristic magnetic field generated by laboratory model of overhead power line and compensating windings during their autonomous operation.

Figures 10,b–d show space-time characteristic of three compensating windings during their autonomous operation. As you can see from this figure, the space-time characteristics of the first and second windings practically coincide.

Fig. 10. Experimentally measured space-time characteristics of initial magnetic flux density of laboratory model of overhead power line and shielding coils during their autonomous work

Let us consider the experimentally measured space-time characteristics of resultant magnetic flux density of laboratory model of overhead transmission lines and shielding coils during their simultaneous work.

Figure 11,a shows space-time characteristic of resultant magnetic flux density of laboratory model of overhead transmission lines and first shielding coils during their simultaneous work.

Figure 11,b shows space-time characteristic resultant magnetic flux density of laboratory model of overhead transmission lines and second shielding coils during their simultaneous work. As you can see from this figure, these space-time characteristic are practically coincide.

Let us now consider the space-time characteristic resulting magnetic field with the simultaneous operation overhead transmission lines, first and second windings. Figure 11,c shows the space-time characteristic of such an magnetic field. As can be seen from this figure, when the first and second windings work together, the horizontal components of the magnetic field generated by the first and second windings during their individual operation are practically compensated.
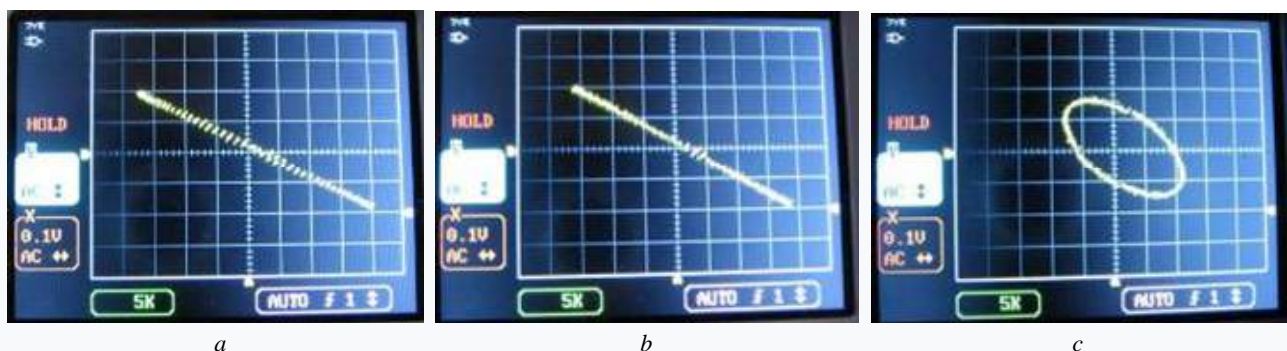
Fig. 11. Experimentally measured space-time characteristics of resultant magnetic flux density of laboratory model of overhead transmission lines and shielding coils during their simultaneous work

The space-time characteristic of the resulting magnetic field, which remained after the joint operation of the first and second compensating windings, is practically parallel to the space-time characteristic of the MF generated by the third winding during its separate operation, as shown in Fig. 10,d, 11,c.

With the simultaneous operation of the first and second windings, the third winding is adjusted in such a

way that, due to its operation, the magnetic flux density of the magnetic field remaining after the joint operation of the first and second windings is compensated. This allows makes it possible to effectively compensate the resulting magnetic field remaining from the simultaneous operation of the first and second compensating windings, and as a result – effectively compensate for the original magnetic field generated by the power transmission line.

The experimentally measured space-time characteristic of the resulting magnetic field, remaining after the simultaneous operation of all three compensating windings, is practically a point. The induction level of the resulting magnetic field measured by the magnetometer is 0.5 μT. Thus with the help of the developed method of adjustment of a three circuit system of the active shielding the level of magnetic flux density of the magnetic field generated in a multi-storey building by a overhead transmission lines with a triangular arrangement of wires based on experimentally measured space-time characteristics the shielding factor of initial magnetic field is increased by more than 8 times.

Note that the calculated value of the shielding factor in a small zone of the shielding space is more than 20 units, as follows from Fig. 3. However, the experimental value of the screening factor in the same small zone of the screening space does not exceed 8 units. This is due to the presence of noise in the magnetic field induction sensors.

Conclusions.

1. For the first time the method of adjustment of three circuit system of the active shielding of the magnetic field based on experimentally determined space-time characteristics allowing to significantly increase the shielding factor of the magnetic field in a multi-storey building located near a single-circuit overhead transmission lines with wires triangular arrangement was developed.

2. The possibility of increasing the shielding factor to 8 units of the magnetic field by the active shielding system in a multi-storey building located near an overhead power line with wires triangular arrangement by using the developed method of adjustment is theoretically substantiated and experimentally confirmed.

Conflict of interest. The authors declare that they have no conflicts of interest.

REFERENCES
1. Rozov V.Yu., Grinchenko V.S., Yerisov A.V., Dobrodeyev P.N. Efficient shielding of three-phase cable line magnetic field by passive loop under limited thermal effect on power cables. *Electrical Engineering & Electromechanics*, 2019, no. 6, pp. 50-54. doi: https://doi.org/10.20998/2074-272x.2019.6.07.
2. Rozov V., Grinchenko V. Simulation and analysis of power frequency electromagnetic field in buildings closed to overhead lines. *2017 IEEE First Ukraine Conference on Electrical and Computer Engineering (UKRCON)*, Kyiv, Ukraine, 2017, pp. 500-503. doi: https://doi.org/10.1109/ukrcon.2017.8100538.
3. Rozov V.Yu., Kundius K.D., Pelevin D.Ye. Active shielding of external magnetic field of built-in transformer substations. *Electrical Engineering & Electromechanics*, 2020, no. 3, pp. 24-30. doi: https://doi.org/10.20998/2074-272x.2020.3.04.
4. Rozov V.Y., Zavalnyi A.V., Zolotov S.M., Gretskikh S.V. The normalization methods of the static geomagnetic field inside houses. *Electrical Engineering & Electromechanics*,
2015, no. 2, pp. 35-40. doi: https://doi.org/10.20998/2074-272x.2015.2.07.
5. Salceanu A., Paulet M., Alistar B.D., Asiminicesei O. Upon the contribution of image currents on the magnetic fields generated by overhead power lines. *2019 International Conference on Electromechanical and Energy Systems (SIELMEN).* 2019. doi: https://doi.org/10.1109/sielmen.2019.8905880.
6. Del Pino Lopez J.C., Romero P.C. Influence of different types of magnetic shields on the thermal behavior and ampacity of underground power cables. *IEEE Transactions on Power Delivery*, Oct. 2011, vol. 26, no. 4, pp. 2659-2667. doi: https://doi.org/10.1109/tpwrd.2011.2158593.
7. Ippolito L., Siano P. Using multi-objective optimal power flow for reducing magnetic fields from power lines. *Electric Power Systems Research*, Feb. 2004, vol. 68, no. 2, pp. 93-101. doi: https://doi.org/10.1016/s0378-7796(03)00151-2.
8. Barsali S., Giglioli R., Poli D. Active shielding of overhead line magnetic field: Design and applications. *Electric Power Systems Research*, May 2014, vol. 110, pp. 55-63. doi: https://doi.org/10.1016/j.epsr.2014.01.005.
9. Bavastro D., Canova A., Freschi F., Giaccone L., Manca M. Magnetic field mitigation at power frequency: design principles and case studies. *IEEE Transactions on Industry Applications*, May 2015, vol. 51, no. 3, pp. 2009-2016. doi: https://doi.org/10.1109/tia.2014.2369813.
10. Beltran H., Fuster V., García M. Magnetic field reduction screening system for a magnetic field source used in industrial applications. *9 Congreso Hispano Luso de Ingeniería Eléctrica (9 CHLIE)*, Marbella (Málaga, Spain), 2005, pp. 84-99. Available at: https://www.researchgate.net/publication/229020921_Magnetic_field_reduction_screening_system_for_a_magnetic_field_source_used_in_industrial_applications (Accessed 22.06.2021).
11. Bravo-Rodríguez J., Del-Pino-López J., Cruz-Romero P. A Survey on Optimization Techniques Applied to Magnetic Field Mitigation in Power Systems. *Energies*, 2019, vol. 12, no. 7, p. 1332. doi: https://doi.org/10.3390/en12071332.
12. Canova A., del-Pino-López J.C., Giaccone L., Manca M. Active Shielding System for ELF Magnetic Fields. *IEEE Transactions on Magnetics*, March 2015, vol. 51, no. 3, pp. 1-4. doi: https://doi.org/10.1109/tmag.2014.2354515.
13. Canova A., Giaccone L. Real-time optimization of active loops for the magnetic field minimization. *International Journal of Applied Electromagnetics and Mechanics*, Feb. 2018, vol. 56, pp. 97-106. doi: https://doi.org/10.3233/jae-172286.
14. Canova A., Giaccone L., Cirimele V. Active and passive shield for aerial power lines. *Proc. of the 25th International Conference on Electricity Distribution (CIRED 2019)*, 3-6 June 2019, Madrid, Spain. Paper no. 1096. Available at: https://www.cired-repository.org/handle/20.500.12455/290 (Accessed 28.10.2020).
15. Canova A., Giaccone L. High-performance magnetic shielding solution for extremely low frequency (ELF) sources. *CIRED - Open Access Proceedings Journal*, Oct. 2017, vol. 2017, no. 1, pp. 686-690. doi: https://doi.org/10.1049/oap-cired.2017.1029.
16. Celozzi S. Active compensation and partial shields for the power-frequency magnetic field reduction. *2002 IEEE International Symposium on Electromagnetic Compatibility*, Minneapolis, MN, USA, 2002, vol. 1, pp. 222-226. doi: https://doi.org/10.1109/isemc.2002.1032478.
17. Celozzi S., Garzia F. Active shielding for power-frequency magnetic field reduction using genetic algorithms optimization. *IEE Proceedings - Science, Measurement and Technology*, 2004, vol. 151, no. 1, pp. 2-7. doi: https://doi.org/10.1049/ip-smt:20040002.
18. Celozzi S., Garzia F. Magnetic field reduction by means of active shielding techniques. *WIT Transactions on Biomedicine*

and Health, 2003, vol. 7, pp. 79-89. doi: https://doi.org/10.2495/ehr030091.

19. Martynenko G. Practical application of the analytical method of electromagnetic circuit analysis for determining magnetic forces in active magnetic bearings. *2020 IEEE Problems of Automated Electrodrive. Theory and Practice (PAEP)*, 2020, pp. 1-4, doi: https://doi.org/10.1109/paep49887.2020.9240774.

20. Martynenko G., Martynenko V. Modeling of the dynamics of rotors of an energy gas turbine installation using an analytical method for analyzing active magnetic bearing circuits. *2020 IEEE KhPI Week on Advanced Technology (KhPIWeek)*, 2020, pp. 92-97 .doi: https://doi.org/10.1109/KhPIWeek51551.2020.9250156.

21. Buriakovskyi S.G., Maslii A.S., Pasko O.V., Smirnov V.V. Mathematical modelling of transients in the electric drive of the switch – the main executive element of railway automation. *Electrical Engineering & Electromechanics*, 2020, no. 4, pp. 17-23. doi: https://doi.org/10.20998/2074-272X.2020.4.03.

22. Ostroverkhov M., Chumack V., Monakhov E., Ponomarev A. Hybrid Excited Synchronous Generator for Microhydropower Unit. *2019 IEEE 6th International Conference on Energy Smart Systems (ESS)*, Kyiv, Ukraine, 2019, pp. 219-222. doi: https://doi.org/10.1109/ess.2019.8764202.

23. Ostroverkhov M., Chumack V., Monakhov E. Ouput Voltage Stabilization Process Simulation in Generator with Hybrid Excitation at Variable Drive Speed. *2019 IEEE 2nd Ukraine Conference on Electrical and Computer Engineering (UKRCON)*, Lviv, Ukraine, 2019, pp. 310-313. doi: https://doi.org/10.1109/ukrcon.2019.8879781.

24. Tytiuk V., Chornyi O., Baranovskaya M., Serhiienko S., Zachepa I., Tsvirkun L., Kuznetsov V., Tryputen N. Synthesis of a fractional-order $PI^\lambda D^\mu$-controller for a closed system of switched reluctance motor control. *Eastern-European Journal of Enterprise Technologies*, 2019, no. 2 (98), pp. 35-42. doi: https://doi.org/10.15587/1729-4061.2019.160946.

25. Zagirnyak M., Chornyi O., Zachepa I. The autonomous sources of energy supply for the liquidation of technogenic accidents. *Przeglad Elektrotechniczny*, 2019, no. 5, pp. 47-50. doi: https://doi.org/10.15199/48.2019.05.12.

26. Chornyi O., Serhiienko S. A virtual complex with the parametric adjustment to electromechanical system parameters. *Technical Electrodynamics*, 2019, pp. 38-41. doi: https://doi.org/10.15407/techned2019.01.038.

27. Shchur I., Kasha L., Bukavyn M. Efficiency Evaluation of Single and Modular Cascade Machines Operation in Electric Vehicle. *2020 IEEE 15th International Conference on Advanced Trends in Radioelectronics, Telecommunications and Computer Engineering (TCSET)*, Lviv-Slavske, Ukraine, 2020, pp. 156-161. doi: https://doi.org/10.1109/tcset49122.2020.235413.

28. Shchur I., Turkovskyi V. Comparative Study of Brushless DC Motor Drives with Different Configurations of Modular Multilevel Cascaded Converters. *2020 IEEE 15th International Conference on Advanced Trends in Radioelectronics, Telecommunications and Computer Engineering (TCSET)*, Lviv-Slavske, Ukraine, 2020, pp. 447-451. doi: https://doi.org/10.1109/tcset49122.2020.235473.

29. Ostroumov I., Kuzmenko N., Sushchenko O., Pavlikov V., Zhyla S., Solomentsev O., Zaliskyi M., Averyanova Y., Tserne E., Popov A., Volosyuk V., Ruzhentsev N., Dergachov K., Havrylenko O., Kuznetsov B., Nikitina T., Shmatko O. Modelling and simulation of DME navigation global service volume. *Advances in Space Research*, 2021, vol. 68, no. 8, pp. 3495-3507. doi: https://doi.org/10.1016/j.asr.2021.06.027.

30. Averyanova Y., Sushchenko O., Ostroumov I., Kuzmenko N., Zaliskyi M., Solomentsev O., Kuznetsov B., Nikitina T., Havrylenko O., Popov A., Volosyuk V., Shmatko O., Ruzhentsev N., Zhyla S., Pavlikov V., Dergachov K., Tserne E. UAS cyber security hazards analysis and approach to qualitative assessment. In: Shukla S., Unal A., Varghese Kureethara J., Mishra D.K., Han D.S. (eds) *Data Science and Security. Lecture*

Notes in Networks and Systems, 2021, vol. 290, pp. 258-265. Springer, Singapore. doi: https://doi.org/10.1007/978-981-16-4486-3_28.

31. Zaliskyi M., Solomentsev O., Shcherbyna O., Ostroumov I., Sushchenko O., Averyanova Y., Kuzmenko N., Shmatko O., Ruzhentsev N., Popov A., Zhyla S., Volosyuk V., Havrylenko O., Pavlikov V., Dergachov K., Tserne E., Nikitina T., Kuznetsov B. Heteroskedasticity analysis during operational data processing of radio electronic systems. In: Shukla S., Unal A., Varghese Kureethara J., Mishra D.K., Han D.S. (eds) *Data Science and Security. Lecture Notes in Networks and Systems*, 2021, vol. 290, pp. 168-175. Springer, Singapore. doi: https://doi.org/10.1007/978-981-16-4486-3_18.

32. Sushchenko O.A. Robust control of angular motion of platform with payload based on H_∞-synthesis. *Journal of Automation and Information Sciences*, 2016, vol. 48, no. 12, pp. 13-26. doi: https://doi.org/10.1615/jautomatinfscien.v48.i12.20.

33. Chikovani V., Sushchenko O. Self-compensation for disturbances in differential vibratory gyroscope for space navigation. *International Journal of Aerospace Engineering*, 2019, vol. 2019, Article ID 5234061, 9 p. doi: https://doi.org/10.1155/2019/5234061.

34. Gal'chenko V.Y., Vorob'ev M.A. Structural synthesis of attachable eddy-current probes with a given distribution of the probing field in the test zone. *Russian Journal of Nondestructive Testing*, Jan. 2005, vol. 41, no. 1, pp. 29-33. doi: https://doi.org/10.1007/s11181-005-0124-7.

35. Halchenko V.Y., Ostapushchenko D.L., Vorobyov M.A. Mathematical simulation of magnetization processes of arbitrarily shaped ferromagnetic test objects in fields of given spatial configurations. *Russian Journal of Nondestructive Testing*, Sep. 2008, vol. 44, no. 9, pp. 589-600. doi: https://doi.org/10.1134/S1061830908090015.

36. Ostroumov I., Kuzmenko N., Sushchenko O., Zaliskyi M., Solomentsev O., Averyanova Y., Zhyla S., Pavlikov V., Tserne E., Volosyuk V., Dergachov K., Havrylenko O., Shmatko O., Popov A., Ruzhentsev N., Kuznetsov B., Nikitina T. A probability estimation of aircraft departures and arrivals delays. In: Gervasi O. et al. (eds) *Computational Science and Its Applications – ICCSA 2021. ICCSA 2021. Lecture Notes in Computer Science*, vol. 12950, pp. 363-377. Springer, Cham. doi: https://doi.org/10.1007/978-3-030-86960-1_26.

37. Chystiakov P., Chornyi O., Zhautikov B., Sivyakova G. Remote control of electromechanical systems based on computer simulators. *2017 International Conference on Modern Electrical and Energy Systems (MEES)*, Kremenchuk, Ukraine, 2017, pp. 364-367. doi: https://doi.org/10.1109/mees.2017.8248934.

38. Zagirnyak M., Bisikalo O., Chorna O., Chornyi O. A Model of the Assessment of an Induction Motor Condition and Operation Life, Based on the Measurement of the External Magnetic Field. *2018 IEEE 3rd International Conference on Intelligent Energy and Power Systems (IEPS)*, Kharkiv, 2018, pp. 316-321. doi: https://doi.org/10.1109/ieps.2018.8559564.

39. Ummels M. *Stochastic Multiplayer Games Theory and Algorithms*. Amsterdam University Press, 2010. 174 p.

40. Shoham Y., Leyton-Brown K. *Multiagent Systems: Algorithmic, Game-Theoretic, and Logical Foundations.* Cambridge University Press, 2009. 504 p.

41. Ray T., Liew K.M. A Swarm Metaphor for Multiobjective Design Optimization. *Engineering Optimization*, 2002, vol. 34, no. 2, pp. 141-153. doi: https://doi.org/10.1080/03052150210915.

42. Zilzter Eckart. *Evolutionary algorithms for multiobjective optimizations: methods and applications*. PhD Thesis Swiss Federal Institute of Technology, Zurich, 1999. 114 p.

43. Xiaohui Hu, Eberhart R.C., Yuhui Shi. Particle swarm with extended memory for multiobjective optimization. *Proceedings of the 2003 IEEE Swarm Intelligence Symposium*. SIS'03 (Cat. No.03EX706), Indianapolis, IN, USA, 2003, pp. 193-197. doi: https://doi.org/10.1109/sis.2003.1202267.

44. Michalewicz Z., Schoenauer M. Evolutionary Algorithms for Constrained Parameter Optimization Problems. *Evolutionary Computation*, 1996, vol. 4, no. 1, pp. 1-32. doi: https://doi.org/10.1162/evco.1996.4.1.1.

45. Parsopoulos K.E., Vrahatis M.N. Particle swarm optimization method for constrained optimization problems. *Proceedings of the Euro-International Symposium on Computational Intelligence*, 2002, pp. 174-181.

46. Xin-She Yang, Zhihua Cui, Renbin Xiao, Amir Hossein Gandomi, Mehmet Karamanoglu. *Swarm Intelligence and Bio-Inspired Computation: Theory and Applications*, Elsevier Inc., 2013. 450 p.

47. Pulido G.T., Coello C.A.C. A constraint-handling mechanism for particle swarm optimization. *Proceedings of the 2004 Congress on Evolutionary Computation* (IEEE Cat. No.04TH8753), Portland, OR, USA, 2004, vol. 2, pp. 1396-1403. doi: https://doi.org/10.1109/cec.2004.1331060.

48. Kuznetsov B.I., Nikitina T.B., Bovdui I.V., Kolomiets V.V., Kobylianskiy B.B. Overhead power lines magnetic field reducing in multi-story building by active shielding means. *Electrical Engineering & Electromechanics*, 2021, no. 2, pp. 23-29. doi: https://doi.org/10.20998/2074-272X.2021.2.04.

B.I. Kuznetsov[1], *Doctor of Technical Science, Professor,*
T.B. Nikitina[2], *Doctor of Technical Science, Professor,*
I.V. Bovdui[1], *PhD, Senior Research Scientist,*
O.V. Voloshko[1], *PhD, Research Scientist,*
V.V. Kolomiets[2], *PhD, Associate Professor,*
B.B. Kobylianskiy[2], *PhD, Associate Professor,*
[1] State Institution «Institute of Technical Problems of Magnetism of the National Academy of Sciences of Ukraine», 19, Industrialna Str., Kharkiv, 61106, Ukraine.
e-mail: kuznetsov.boris.i@gmail.com (Corresponding author)
[2] Educational scientific professional pedagogical Institute of Ukrainian Engineering Pedagogical Academy, 9a, Nosakov Str., Bakhmut, Donetsk Region, 84511, Ukraine,
e-mail: tatjana55555@gmail.com;   nnppiuipa@ukr.net

L. Moussaoui

Performance enhancement of direct torque control induction motor drive using space vector modulation strategy

*Purpose. The main objective of this work is to demonstrate the advantages brought by the use of space vector modulation technique in the direct torque control of the induction motor. To achieve this purpose, two different direct torque control approaches (with space vector modulation) are proposed and studied from a comparative aspect with each other and with the conventional direct torque control. **The novelty** of this work consists in the employment of an Integral-Proportional (IP) speed controller in the two proposed direct torque control approaches and a more in-depth evaluation for their performance mainly the switching frequency of inverter semiconductor components and motor torque ripples. **Methods.** Two different direct torque control approaches that use the space vector modulation strategy and/or fuzzy-logic control, are described in detail and simulated with IP speed controller. The simulation experiments are carried out using Matlab/Simulink software and/or fuzzy-logic tools. **Results. Practical value.** Comparison results show that the two proposed direct torque control structures (with space vector modulation) exhibit a large reduction in torque ripples and can also avoid random variation problem of switching frequency (over a wide range of speed or torque control). On the other hand, the use of IP speed regulator ensured good dynamic performance for the drive system as well as considerably minimized peak overshoot in the speed response. Practically all of these benefits are achieved while retaining the simplicity and the best dynamic characteristics of the classical direct torque control, especially with the modified direct torque control approach in which the design or implementation requires minimal computational effort. References 23, tables 4, figures 17.*
Key words: **induction motor drive, direct torque control, voltage source inverter, space vector modulation, IP controller, fuzzy control.**

*Мета. Основна мета даної роботи – продемонструвати переваги використання методу модуляції просторового вектора при прямому регулюванні крутного моменту асинхронного двигуна. Для досягнення цієї мети запропоновано два різних підходи до прямого управління крутним моментом (з модуляцією просторового вектора), які досліджуються з порівняльної точки зору одного з іншим, а також зі звичайним прямим керуванням крутним моментом. **Новизна** роботи полягає у використанні інтегрально-пропорційного (ІП) регулятора швидкості в двох запропонованих підходах до прямого регулювання крутного моменту та більш поглибленій оцінці їх ефективності, головним чином, частоти перемикань напівпровідникових компонентів інвертора та пульсації крутного моменту двигуна. **Методи.** Два різних підходи до прямого керування крутним моментом, які використовують стратегію модуляції просторового вектора та/або керування нечіткою логікою, детально описані та змодельовані за допомогою ІП-регулятора швидкості. Обчислювальні експерименти проводяться з використанням програмного забезпечення Matlab/Simulink та/або інструментів нечіткої логіки. **Результати. Практична цінність.** Результати порівняння показують, що дві запропоновані структури прямого керування крутним моментом (з модуляцією просторового вектора) демонструють значне зниження пульсації крутного моменту, а також можуть уникнути проблеми випадкових змін частоти перемикання (у широкому діапазоні регулювання швидкості або крутного моменту). З іншого боку, використання ІП-регулятора швидкості забезпечило хороші динамічні характеристики для приводної системи, а також значно знизило пікове перевищення швидкості. Практично всі ці переваги досягаються при збереженні простоти та найкращих динамічних характеристик класичного прямого керування крутним моментом, особливо з модифікованим підходом прямого керування крутним моментом, при якому проектування або впровадження вимагає мінімальних обчислювальних витрат. Бібл. 23, табл. 4, рис. 17.*
Ключові слова: **електропривод з асинхронним двигуном, пряме керування крутним моментом, інвертор джерела напруги, модуляція просторового вектора, ІП-регулятор, нечітке керування.**

Introduction. Three-phase induction motors have been widely used in industrial applications due to their low maintenance, high robustness, simple structure and high efficiency. In fact, in high performance applications such as motion control of an induction motor (IM), it is generally desirable that motor can provide a good dynamic torque response as it's in DC motor drive. In order to achieve this objective, many researchers have focused on developing several control algorithms. Recently, an innovative control method, called Direct Torque Control (DTC) is introduced because of its capability to produce a fast torque control for the IM without to use much on-line computation as it's in field oriented control [1-13].

Indeed, the main advantages offered by DTC are:

• Excellent torque dynamic with minimal response time;

• robustness against rotor parameters variation;

• decoupled control between the torque and stator flux;

• no need of voltage modulator;

• control method without inherent speed sensor.

These merits are counterbalanced by some drawbacks like:

• Possible problems either when starting the machine, or running at low speed or changing the load torque;

• requirement for torque and flux estimation which includes machine parameters identification;

• inherent ripples in the torque and stator flux;

• greater harmonic distortion in stator voltages and waveforms of currents;

• inverter switching states remain unchanged in a number of sample cycles. Thus, the switching frequency is not constant and inverter power components capacity will not be wholly utilized;

• acoustical noise produced because of random inverter switching frequency variation [1-4], [14-18].

To overcome these problems, a variety of techniques with different concepts are described in the literature. Some of diverse proposed solutions include DTC with; space vector modulation, various power converter topologies such as: multi-level inverter and matrix converter, sensorless

control methods, optimal stator flux estimation for high speed operation and artificial intelligence techniques (fuzzy or neuro controllers) [1, 2, 4-8, 14-21]. These methods achieve certain improvements such as reduction of torque ripples and fixed switching frequency operation. However, control system complexity is greatly increased.

The goal of the paper. In order to solve problems, of ripples in both electromagnetic torque and stator flux and of random variation of inverter switching frequency, we have proposed and study in this work two different Direct Torque Control approaches making use of Space Vector Modulation technique (DTC-SVM) and/or fuzzy logic control.

Practically, fuzzy logic is considered as an interesting alternative approach for its advantages such as: analysis close to exigencies of users, ability of nonlinear systems control, best dynamic performances and inherent quality of robustness. On the other hand, SVM strategy uses a digital algorithm to obtain an appropriate switching states sequence for Voltage Source Inverter (VSI) control. Thus, inverter can generate an output voltage vector which is closest to its reference voltage vector, with a previously imposed switching frequency. Also, in conventional DTC a single voltage vector is applied throughout the sample time. Therefore, for small torque errors, motor torque may exceed its upper or lower limit. Instead, with SVM strategy, which uses more than one vector during sample period, torque ripples can be reduced.

Subject of investigations. First proposed DTC-SVM approach, called Direct Fuzzy Torque Control (DFTC), is introduced with the aim of reducing ripples of electromagnetic torque and stator flux and improving stator currents waveform. The so-called DFTC uses both SVM technique and hysteresis comparators. In this approach, a look-up table decides angle choice of voltage vector applied to the motor, while an estimator based on fuzzy logic calculates the amplitude of this vector. Thus, reference voltage vector will be synthesized using the space vector modulation.

The second DTC-SVM approach, named Modified Direct Torque Control (MDTC), uses an efficient algorithm, based on direct stator flux control, to independently control amplitude and position of reference stator flux vector of the IM. In fact, the proposed algorithm of MDTC structure is designed to calculate reference voltage vector amplitude leading to an optimal torque and stator flux control.

Performances of these two DTC-SVM approaches are demonstrated by simulation using Matlab/Simulink software and/or fuzzy logic tools. Simulation results are compared to those of classical DTC with the use of an IP controller in all studied DTC structures. Systems performances evaluation is carried out mainly based on; inverter switching frequency, dynamic responses of torque/speed and flux, ripples content in torque and stator flux and distortion of stator currents or stator voltages. The comparison results illustrate clearly the effectiveness and superiority of the proposed DTC-SVM approaches over conventional DTC.

Modeling of the induction motor and voltage source inverter. In order to properly design or simulate a control structure, mathematical model of the latter must

be considered [4, 11, 12, 16]. So, under the usual assumption of no hysteresis, no eddy currents and no space harmonics, electrical model of IM can be expressed (in a stationary reference frame) by the following nonlinear equations:

$$
\begin{cases}
\overrightarrow{V_S} = R_S \cdot \overrightarrow{i_S} + \dfrac{d\overrightarrow{\phi_S}}{dt}; \\[2mm]
\overrightarrow{V_r} = R_r \cdot \overrightarrow{i_r} + \dfrac{d\overrightarrow{\phi_r}}{dt} - j \cdot \omega \cdot \overrightarrow{\phi_r};
\end{cases}
\tag{1}
$$

$$
\begin{cases}
\overrightarrow{\phi_S} = L_S \cdot \overrightarrow{i_S} + L_m \cdot \overrightarrow{i_r}; \\[2mm]
\overrightarrow{\phi_r} = L_r \cdot \overrightarrow{i_r} + L_m \cdot \overrightarrow{i_S},
\end{cases}
\tag{2}
$$

where R_S, L_S, R_r, L_r are the resistances and cyclic inductances of stator and rotor respectively; $\overrightarrow{V_S}$, $\overrightarrow{i_S}$, $\overrightarrow{\phi_S}$, $\overrightarrow{V_r}$, $\overrightarrow{i_r}$, $\overrightarrow{\phi_r}$ are the voltage, current and flux vectors of stator and rotor respectively; L_m, ω are the mutual inductance and electric motor speed (or rotor frequency).

The electromagnetic torque is expressed as a function of the stator and rotor fluxes

$$
\Gamma_e = \frac{3}{2} \cdot p \cdot \frac{L_m}{\sigma \cdot L_S \cdot L_r} \cdot \left(\overrightarrow{\phi_S} \times \overrightarrow{\phi_r} \right),
\tag{3}
$$

where p is the number of pairs of poles and σ ($\sigma = 1 - L_m^2 / L_S \cdot L_r$) is the motor dispersion coefficient.

Elimination of $\overrightarrow{i_S}$ and $\overrightarrow{i_r}$ from (1) and (2), gives the state form model of the induction machine with the stator and rotor fluxes as state variables and τ_S ($\tau_S = L_S/R_S$), τ_r ($\tau_r = L_r/R_r$) are the stator and rotor time constants respectively

$$
\begin{bmatrix} \dfrac{d\overrightarrow{\phi_S}}{dt} \\[3mm] \dfrac{d\overrightarrow{\phi_r}}{dt} \end{bmatrix} =
\begin{bmatrix} -\dfrac{1}{\sigma \cdot \tau_S} & \dfrac{L_m}{\sigma \cdot \tau_S \cdot L_r} \\[3mm] \dfrac{L_m}{\sigma \cdot \tau_r \cdot L_S} & j \cdot \omega - \dfrac{1}{\sigma \cdot \tau_r} \end{bmatrix} \cdot
\begin{bmatrix} \overrightarrow{\phi_S} \\[3mm] \overrightarrow{\phi_r} \end{bmatrix} +
\begin{bmatrix} 1 \\[3mm] 0 \end{bmatrix} \cdot \overrightarrow{V_S} \; , \tag{4}
$$

The mechanical mode, associated with the rotor motion, is described by:

$$
J \cdot \frac{d\Omega}{dt} + f \cdot \Omega = \Gamma_e - \Gamma_r(\Omega),
\tag{5}
$$

where Γ_r and Γ_e are respectively the load torque and electromagnetic torque developed by the machine; J, f and Ω are the respectively inertia, friction motor coefficient and mechanical rotation speed ($\Omega = \omega / p$).

Figure 1 reveals the diagram of a typical three-phase VSI [4, 9, 10, 13, 22]. Here semiconductors are considered as ideal switches and S_a, S_b, S_c are switching states of each leg of this inverter. Relationships between switching states and phase output voltages (v_{an}, v_{an}, v_{cn}) can be expressed as below:

$$
\begin{bmatrix} v_{an} \\ v_{bn} \\ v_{cn} \end{bmatrix} = \frac{V_{dc}}{3}
\begin{bmatrix} 2 & -1 & -1 \\ -1 & 2 & -1 \\ -1 & -1 & 2 \end{bmatrix} \cdot
\begin{bmatrix} S_a \\ S_b \\ S_c \end{bmatrix},
\tag{6}
$$

where n is the neutral point of inverter load.

As it is well known, two-level voltage inverter has in principle eight possible combinations for its switching states. Where two of these combinations are termed as zero vectors and they are designated homogeneously as state 0 ($\overrightarrow{V_0} = \overrightarrow{V_7} = \vec{0}$), as their effects are equal.

The remaining six states represent stationary vectors in the complex α–β plane (Fig. 2).
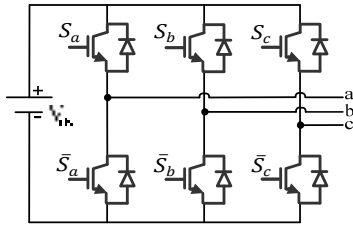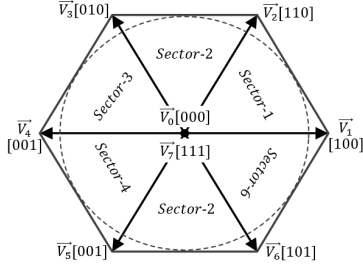

Fig. 1. Schematic diagram of a two-level VSI

Fig. 2. Illustration of VSI state vectors in the α–β plane

These six active state vectors can be expressed as follows:

$$\overrightarrow{V_k} = \frac{2}{3} \cdot V_{dc} \cdot e^{j \cdot (k-1)\frac{\pi}{3}}, \quad k = 1, 2, \dots 6, \quad (7)$$

where V_{dc} is the DC-link voltage.

This equation shows that the amplitude of each active vector is $(2/3) \cdot V_{dc}$ with a deviation angle of $\pi/3$ between the different active vectors, thus building a regular hexagon with two zero vectors which are located at its origin (Fig. 2).

Basic concepts of DTC. The basic configuration of conventional DTC, proposed by Takahashi, is shown in Fig. 3.
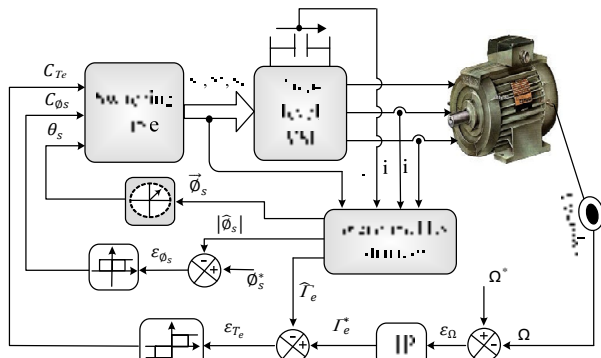

Fig. 3. Block diagram of the classical DTC

It consists of a pair of hysteresis comparators, torque and flux estimators, voltage vector selector and a two-level VSI. The fundamental idea of DTC is to choose the most appropriate voltage vector which allows simultaneous and independent control of stator flux and electromagnetic torque, thus ensuring decoupled control for these two machine quantities. In fact, the performance of this control technique depends directly on the estimation of torque and stator flux so that an incorrect estimation will result in a wrong selection of inverter state vectors [1-8, 14, 16-18, 20, 21, 23].

Mainly in DTC technique, torque and stator flux estimation can be done by means of measurement; of two or three different phase currents (i_{Sa}, i_{Sb}, i_{Sc}) and of DC-link voltage. In fact, estimation procedure is carried out using the following equations:

$$\begin{cases} i_{S\alpha} = i_{Sa}; \\ i_{S\beta} = \frac{1}{\sqrt{3}} \cdot (i_{Sb} - i_{Sc}); \end{cases} \quad (8)$$

$$\begin{cases} v_{S\alpha} = \frac{2}{3} \cdot V_{dc} \cdot \left(S_a - \frac{S_b + S_c}{2} \right); \\ v_{S\beta} = \frac{1}{\sqrt{3}} \cdot V_{dc} \cdot (S_b - S_c). \end{cases} \quad (9)$$

Estimated stator flux is then given by:

$$\begin{cases} \hat{\phi}_{S\alpha} = \int_0^t (v_{S\alpha} - R_S \cdot i_{S\alpha}) \mathrm{d}t; \\ \hat{\phi}_{S\beta} = \int_0^t (v_{S\beta} - R_S \cdot i_{S\beta}) \mathrm{d}t, \end{cases} \quad (10)$$

where $v_{s\alpha,\beta}$, $i_{s\alpha,\beta}$ and $\hat{\phi}_{S\alpha,\beta}$ are the two α–β components of stator voltage, current and estimated flux respectively.

The electromagnetic torque is estimated on-line by knowledge of instantaneous values of direct and quadratic components of the stator flux and stator current:

$$\hat{\Gamma}_e = \frac{3}{2} \cdot p \cdot \left(\hat{\phi}_{S\alpha} \cdot i_{S\beta} - \hat{\phi}_{S\beta} \cdot i_{S\alpha} \right). \quad (11)$$

As it can be seen in Fig. 3, there are two different loops corresponding to magnitude control of stator flux and electromagnetic torque. Thus reference values of torque and stator flux are compared with their estimated values and resulting errors are then used as inputs into two hysteresis blocks with three-level and two-level respectively. Outputs of these latter blocks, giving torque and stator flux correction states, as well as stator flux position, are used as inputs in the look-up table of Takahashi, as it's depicted in Table 1.

Table 1
Switching table of the classical DTC

Flux sector		1	2	3	4	5	6
$C_{\phi s} = 1$	$C_{Te}=1$	$V2_{(110)}$	$V3_{(010)}$	$V4_{(011)}$	$V5_{(001)}$	$V6_{(101)}$	$V1_{(100)}$
	$C_{Te}=0$	$V7_{(111)}$	$V0_{(000)}$	$V7_{(111)}$	$V0_{(000)}$	$V7_{(111)}$	$V0_{(000)}$
	$C_{Te}=-1$	$V6_{(101)}$	$V1_{(100)}$	$V2_{(110)}$	$V3_{(010)}$	$V4_{(011)}$	$V5_{(001)}$
$C_{\phi s} = 0$	$C_{Te}=1$	$V3_{(010)}$	$V4_{(011)}$	$V5_{(001)}$	$V6_{(101)}$	$V1_{(100)}$	$V2_{(110)}$
	$C_{Te}=0$	$V0_{(000)}$	$V7_{(111)}$	$V0_{(000)}$	$V7_{(111)}$	$V0_{(000)}$	$V7_{(111)}$
	$C_{Te}=-1$	$V5_{(001)}$	$V6_{(101)}$	$V1_{(100)}$	$V2_{(110)}$	$V3_{(010)}$	$V4_{(011)}$

This switching table gives the inverter state vectors which will be applied, to the IM, during a sample period. Such that torque and stator flux errors tend to be restricted in their respective hysteresis bands [1, 4, 8, 15, 16, 19, 20, 23].

In order to reduce motor speed response time and cancel its static error while maintaining system stability, a Proportional-Integral (PI) corrector is generally used. In this work, an Integral-Proportional (IP) controller is applied for IM speed control, because of its various advantages such as good rejection of perturbations (zero static error) and overshoot restriction are obtained by a judicious tuning of its parameters.

The speed control block diagram, including the IP regulator, is illustrated in the Fig. 4, where the integral

part is in the feedforward path and the proportional part is in the feedback path.
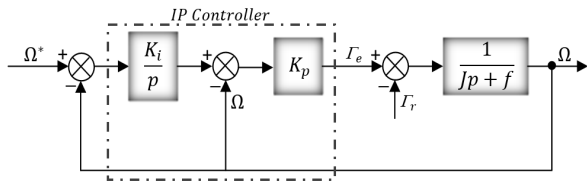

Fig. 4. Speed control loop with IP regulator

Direct Fuzzy Torque Control (DFTC). The corresponding structure of DFTC employs space vector modulation strategy as shown in Fig. 5. In this case, flux and torque errors are used as two inputs either to fuzzy logic estimator of reference voltage vector amplitude $|\vec{V}_S^*|$ or to hysteresis comparators that deliver errors levels ($C_{\Gamma e}$, $C_{\phi S}$) which are used for determining $\vec{V}_S^*$ position (via a lookup table).

Unlike the conventional DTC technique, where the applied voltage vector has constant amplitude even if the motor torque is outside its hysteresis band, DFTC structure allows the calculation of an optimum voltage, which will be used in the control of IM, according to the states of torque and stator flux in relation to their desired values. Thus providing a fast and accurate control of the electromagnetic torque. In fact, this optimal voltage vector is synthesized using SVM block which generates the most appropriate switching states to the inverter [3, 14, 16, 23].
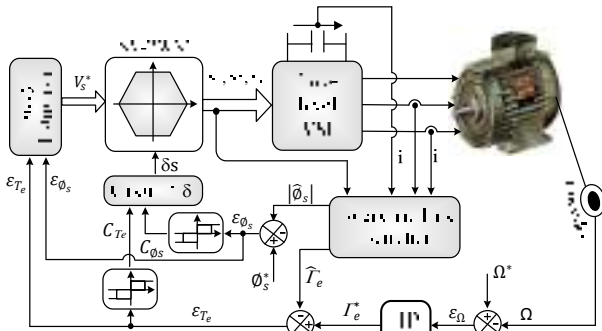

Fig. 5. Block diagram of the proposed DFTC approach

In this DTC approach, the reference voltage vector position relative to the stator flux vector must be chosen so as to maintain the stator flux and electromagnetic torque in an optimal error band around their respective reference values. Indeed, the position of this voltage vector (δ_S) is obtained by adding an angle (δ) to the position of stator flux (θ_S) such as:

$$\delta_S = \delta + \theta_S . \qquad (12)$$

The angle δ is selected based on hysteresis comparators output values as depicted in Table 2. It should be noted here, that both hysteresis regulators of torque and stator flux are three levels comparators.

Table 2

Selection of the stator voltage vector position

$C_{\Gamma e}$		−1			0			1	
$C_{\phi S}$	−1	0	1	−1	0	1	−1	0	1
δ	$-\frac{2\pi}{3}$	$+\pi$	$+\frac{2\pi}{3}$	$-\frac{\pi}{2}$	$+\frac{\pi}{2}$	$+\frac{\pi}{2}$	$-\frac{\pi}{3}$	0	$+\frac{\pi}{3}$

Also, reference voltage vector amplitude must be chosen so as to reduce flux and torque errors. Thus, a fuzzy logic estimator (FLE) is designed to generate the most appropriate amplitude of the reference voltage vector. Proposed estimator block diagram, that combines «fuzzification – rules base – defuzzification» modules, is given in the Fig. 6.
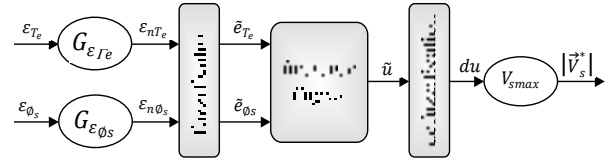

Fig. 6. Proposed fuzzy estimator for voltage vector amplitude estimation

In fuzzification module, inputs are crisp physical signals ($\varepsilon_{n\Gamma e}$, $\varepsilon_{n\phi s}$) of real process and outputs are fuzzy subsets consisting of intervals and membership functions ($\tilde{e}_{\Gamma e}$, $\tilde{e}_{\phi s}$). These outputs will be inputs for the next module, fuzzy logic IF-THEN rules base of control, which requires fuzzy-subset inputs in order to be compatible with fuzzy logic rules [15, 18, 19, 22].

The general procedure in designing a fuzzy logic rules base includes the following:
- defining process states and control variables;
- determining input variables to inference engine block;
- forming a fuzzy logic IF-THEN rules base (determined input variables in previous step will be used in rules base design);
- establishing a fuzzy logic inference engine.

In fact, this latter phase explains how FLE decides on an optimal reference voltage vector amplitude ($|\vec{V}_S^*|$) based on the control rules and linguistic terms. In general, inference systems have two types, namely Mandani and Takagi-sugeno [18, 21, 22]. Mandani method is used in this study because of its simple structure and design. Fuzzy rules consist of IF-THEN linguistic terms, and output membership functions are operated by fuzzy rules that are related to both inputs ($\varepsilon_{\Gamma e}$, $\varepsilon_{\phi s}$) and output ($|\vec{V}_S^*|$). Inference engine block, based on input fuzzy variables uses forty-nine IF-THEN rules, where AND method corresponds to minimum fuzzy inputs, in order to obtain final output fuzzy sets as shown in Table 3. These rules are setting in turn to take maximal amplitude for voltage vector, when torque is outside its error band. Otherwise, zero amplitude is assigned to this voltage vector.

Table 3

Complete rules base for the proposed FLE

$\tilde{e}_{\phi s}$	$\tilde{e}_{\Gamma e}$						
	NH	NM	NS	ZE	PS	PM	PH
NH	PH	PM	PS	PS	PS	PM	PH
NM	PH	PM	PS	PS	PS	PM	PH
NS	PH	PM	PS	ZE	PS	PM	PH
ZE	PH	PM	PS	ZE	PS	PM	PH
PS	PH	PM	PS	ZE	PS	PM	PH
PM	PH	PM	PS	PS	PS	PM	PH
PH	PH	PM	PS	PS	PS	PM	PH
NH – negative high, NM – negative medium, NS – negative small, ZE – zero, PS – positive small, PM – positive medium, PH – positive high							

In this work the fuzzification and defuzzification processes are carried out using asymmetrical triangular membership functions (so that computation complexity can be reduced) as shown in Fig. 7, where each of input variables ($\varepsilon_{n\Gamma e}$, $\varepsilon_{n\phi s}$) is mapped into seven different linguistic values. Mapping relationship between the inputs and output variables of FLE is also given in Fig. 8.
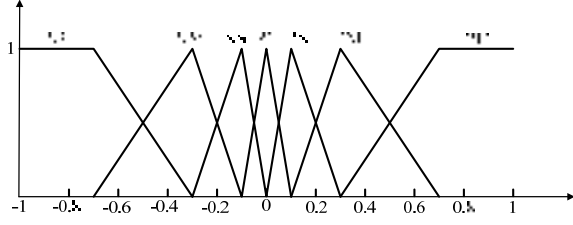

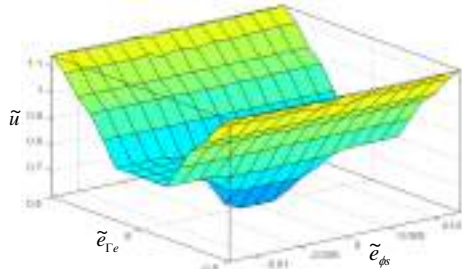Fig. 7. Fuzzy membership functions of the proposed FLE

Fig. 8. Control surface of the fuzzy logic estimator

Just like the first step of fuzzification, the defuzzification module transforms the overall control output ($\tilde{u}$) obtained in the previous phase, to corresponding physical values (voltage) that system can accept. The voltage vector amplitude is then obtained by multiplying the crisp output value (du), by an appropriate gain. This latter is chosen so that the maximum amplitude of the reference voltage vector should not exceed the voltage vector maximum amplitude generated by a two level PWM inverter.

Principle of Space Vector Modulation strategy. SVM technique is an advanced computation intensive PWM method and possibly the best PWM strategy for three-phase VSI used in industrial applications such as control of induction motors. Practically this modulation technique has several advantages either for inverter or motor such as; better utilization of DC-link voltage, less of torque ripples, motor current with lower Total Harmonic Distortion (THD), minimum of switching losses, and simplicity of implementation in digital systems [9, 10, 14, 23].

SVM principle is based on the concept of approximating a rotating reference voltage vector ($\overrightarrow{V_S^*}$) by using a combination of two out of the eight possible state vectors that can be generated from a three-phase VSI. This strategy differs from the sinusoidal PWM in such way that, there is no separate modulator used for each of three phases. Instead, the reference voltage vector is processed as a whole. In fact, the SVM is produced by a regular sampling of circular locus reference voltage created on the α–β plane. These voltage samples are then represented by two actives vectors, chosen from $\overrightarrow{V_1}$ to $\overrightarrow{V_6}$, that are adjacent to the reference voltage vector together with either two null vectors; $\overrightarrow{V_0}$ and $\overrightarrow{V_7}$. The

respective times corresponding to these state vectors are adjusted within a sample period [9, 10, 14].

Figure 9 shows the SVM principle, where reference vector ($\overrightarrow{V_S^*}$) is sampled at time intervals fixed and equal (T_s), called «sub-cycles». The sampled value $\overrightarrow{V_S^*}(T_S)$ is then used to solve the following equations:

$$\begin{cases} T_k \cdot \overrightarrow{V_k} + T_{k+1} \cdot \overrightarrow{V_{k+1}} = T_S \cdot \overrightarrow{V_S^*}(T_S); \\ T_0 = T_7 = T_S - T_k - T_{k+1}, \end{cases} \quad (13)$$

where $\overrightarrow{V_k}$ and $\overrightarrow{V_{k+1}}$ are two switching state vectors adjacent in space, to the reference voltage vector ($\overrightarrow{V_S^*}$).

Solution of (13) gives application times of switching state vectors

$$\begin{cases} T_k = \sqrt{3}\left(\sin\left[k \cdot \dfrac{\pi}{3}\right] \cdot V_{s\alpha}^* - \cos\left[k \cdot \dfrac{\pi}{3}\right] \cdot V_{s\beta}^*\right) \cdot \dfrac{T_S}{V_{dc}}; \\ T_{k+1} = \sqrt{3}\left(-\sin\left[(k-1) \cdot \dfrac{\pi}{3}\right] \cdot V_{s\alpha}^* + \cos\left[(k-1) \cdot \dfrac{\pi}{3}\right] \cdot V_{s\beta}^*\right) \cdot \dfrac{T_S}{V_{dc}}. \end{cases} \quad (14)$$

If the over-modulation mode ($T_k+T_{k+1}>T_S$) occurs, state vectors application time should be scaled as (15) to generate the best approximation of the reference voltage vector. This may be detected by examining the sign of calculated T_0 and limit is then applied by maintaining the same angle for the reference voltage vector

$$\begin{cases} T_{k,k+1}' = T_{k,k+1} \cdot \dfrac{T_S}{T_k + T_{k+1}}; \\ T_0' = T_7' = 0. \end{cases} \quad (15)$$
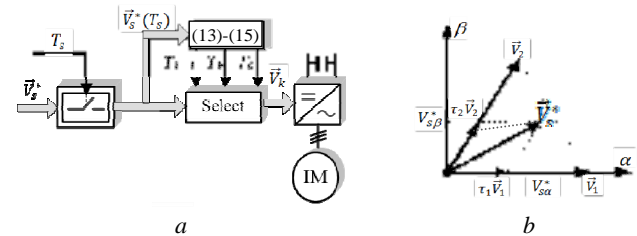
Fig. 9. Principle of the SVM: *a* – functional diagram; *b* – switching state vectors in the first 60°–sector

Having computed these modulation times, an adequate sequence of the state vectors must be well determined. The modulation scheme, used in this work, is based on a symmetrical sequence within each sample period (Fig. 10). Thus, switching sequence applied for a given sector can be described as:

$$\overrightarrow{V_{0,7}} \Rightarrow \overrightarrow{V_k} \Rightarrow \overrightarrow{V_{k+1}} \Rightarrow \overrightarrow{V_{0,7}} \Rightarrow \overrightarrow{V_{k+1}} \Rightarrow \overrightarrow{V_k} \Rightarrow \overrightarrow{V_{0,7}}.$$

This sequence is characterized by the weakest switching losses and also the lowest harmonic distortion due to the resulted symmetry in switching pulses waveform of the inverter power components.
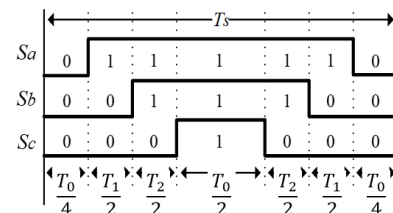
Fig. 10. Switching pulses waveform for the first 60°–sector

Modified Direct Torque Control (MDTC). The proposed MDTC structure for IM is shown in Fig. 11, where the hysteresis comparators and switching table of conventional DTC are eliminated and replaced by

- prediction of the reference stator flux;
- determination of the reference voltage space vector;
- application of the SVM technique.
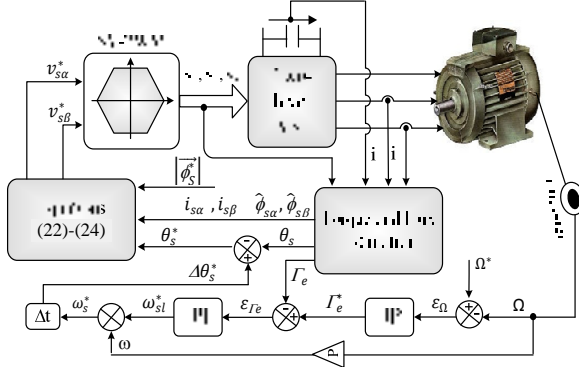
Fig. 11. Block diagram of the proposed MDTC approach

In fact, in MDTC structure, the torque control is achieved by maintaining constant amplitude for the reference stator flux. From (16) torque control is directly performed by controlling the torque angle changes (Fig. 12). This latter represents the angle between the two flux vectors (of stator and rotor). Thus, the instantaneous electromagnetic torque can be described as follows:

$$\Gamma_e = \frac{3}{2} \cdot p \cdot \frac{L_m^2}{R_r \cdot L_S^2} \cdot \left|\overrightarrow{\phi_S^*}\right|^2 \cdot \left[1 - e^{-t/\tau}\right] \cdot (\omega_S - \omega), \quad (16)$$

where $\tau = \sigma \cdot L_r / R_r$ is the time constant.
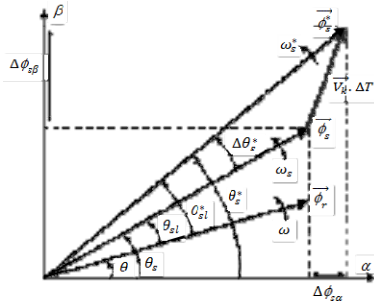

Fig. 12. Direct control of the stator flux vector

The slip angular frequency depended on the stator angular frequency (ω_S) and rotor angular frequency (ω), can be written as:

$$\omega_{Sl} = \omega_S - \omega , \quad (17)$$

or

$$\omega_{Sl} = \frac{d\theta_{Sl}}{dt} \approx \frac{\Delta\theta_{Sl}}{\Delta t} , \quad (18)$$

where θ_{Sl} is the angle between the two flux vectors and Δt is the sampling time.

By substituting (18) in (16), the instantaneous electromagnetic torque is given by:

$$\Gamma_e = \frac{3}{2} \cdot p \cdot \frac{L_m^2}{R_r \cdot L_S^2} \cdot \left|\overrightarrow{\phi_S^*}\right|^2 \cdot \left[1 - e^{-t/\tau}\right] \cdot \left(\frac{\Delta\theta_{Sl}}{\Delta t}\right). \quad (19)$$

According to (19), the control of the instantaneous electromagnetic torque is achieved by changing the value of slip angle that is controlled by using a direct control method for the stator flux vector. On the other hand, the reference torque is generated from the speed IP controller. Therefore, quantity $\varepsilon_{\Gamma e}$ is the obtained error between the reference torque and estimated or real torque (Fig. 11). In order to compensate this error, the angle of stator flux (θ_S) must be increased using the following expression (where ω_{Sl}^* is the slip angle that is generated from the torque PI controller)

$$\theta_S^* = \theta_S + \Delta\theta_S^* = \theta_S + \left(\omega_{Sl}^* + \omega\right) \cdot \Delta t . \quad (20)$$

Therefore, the required reference stator flux vector will be given in a polar form by:

$$\overrightarrow{\phi_S^*} = \left|\overrightarrow{\phi_S^*}\right| \angle \theta_s^* , \quad (21)$$

where $\left|\overrightarrow{\phi_S^*}\right|$ is maintained constant at its rated value.

The reference stator flux components and corresponding flux errors are given respectively by:

$$\begin{cases} \phi_{S\alpha}^* = \left|\overrightarrow{\phi_S^*}\right| \cdot \cos\theta_s^* \\ \phi_{S\beta}^* = \left|\overrightarrow{\phi_S^*}\right| \cdot \sin\theta_s^* \end{cases}, \quad (22)$$

$$\begin{cases} \Delta\phi_{S\alpha} = \phi_{S\alpha}^* - \hat{\phi}_{S\alpha} \\ \Delta\phi_{S\beta} = \phi_{S\beta}^* - \hat{\phi}_{S\beta} \end{cases}, \quad (23)$$

Then the reference stator voltage vector components are given by the following expressions:

$$\begin{cases} v_{S\alpha}^* = R_S \cdot i_{S\alpha} + \dfrac{\Delta\phi_{S\alpha}}{\Delta t} \\ v_{S\beta}^* = R_S \cdot i_{S\beta} + \dfrac{\Delta\phi_{S\beta}}{\Delta t} \end{cases}, \quad (24)$$

Subsequently, by using these reference voltage components, the inverter control signals will be designed in such way that the average space vector generated within sample period is equal to the sampled value of the reference stator voltage vector.

Simulation results and discussion. To show the effectiveness of the two proposed DTC-SVM structures, the simulation work is carried out, on an IM, using the Matlab/Simulink software and/or fuzzy logic tools. The parameters of used motor are listed in Table 4.

Table 4
Induction motor parameters

Parameters	Values
Rated power, kW	4
Stator voltage, V	220
Stator resistance, Ω	1.2
Rotor resistance, Ω	1.8
Stator cyclic inductance, H	0.1554
Rotor cyclic inductance, H	0.1568
Mutual inductance, H	0.15
Number of pairs of poles	2
Inertia, N·m/rad·s	0.07
Friction coefficient, kg·m²	0.0001

In order to validate these two approaches of DTC-SVM, their performances are compared, under the same conditions, with those of classical DTC. In turn, the

dynamic behaviour of these three DTC structures (with speed IP controller) is tested under high and low speed and with various load torque commands. Simulation results, included in Fig. 13, show that a good tracking performances can still be achieved in the responses of speed, torque, flux and current with no distinct difference among the three DTC approaches (for all tested cases in terms of the damping capability and transient response under different reference speeds and mechanical loads).

For a close inspection of the steady-state performances, we give in Fig. 14, 15 the static responses of the three DTC structures. Where for all, the machine is operating at high speed (100 rad/s) and with full load (20 N·m). From these results, it is possible to see that the two DTC-SVM approaches illustrate some better performances by reducing the ripples in the torque and stator flux and attenuating the speed vibrations.

Fig. 13. System responses for various operating conditions:
a – classical DTC; *b* – DFTC; *c* –MDTC
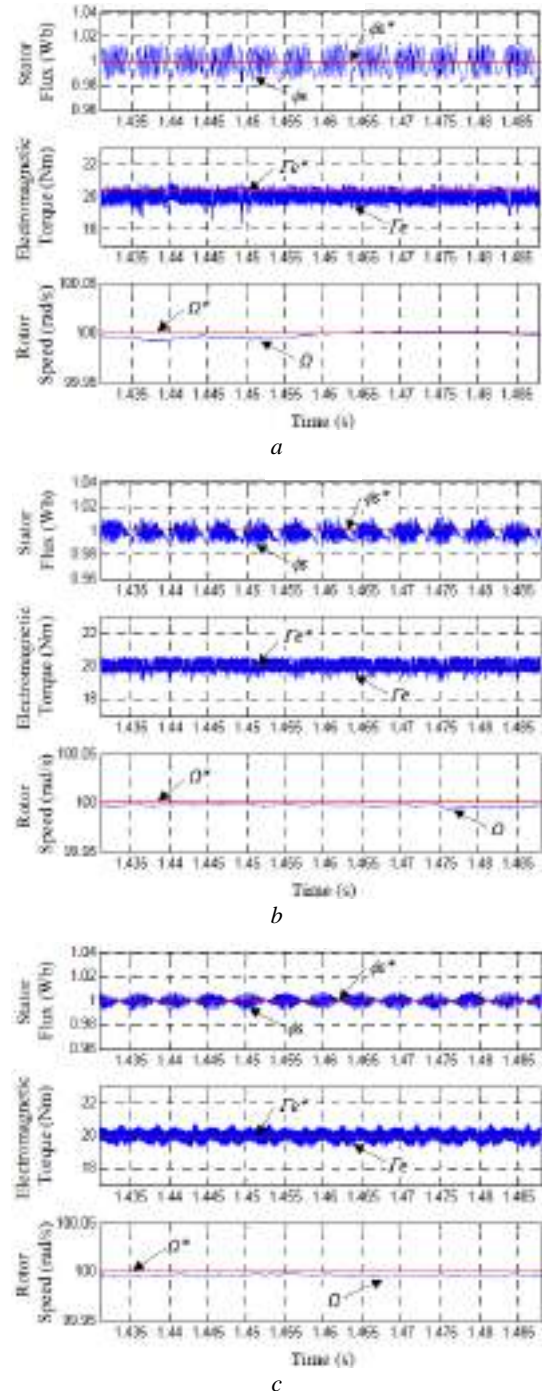
Fig. 14. Steady-state responses of stator flux, torque and speed:
a – classical DTC; *b* – DFTC; *c* – MDTC

For the same steady-state operating conditions, we see significantly in Fig. 15 that the harmonic content of the stator current is quite attenuated by employing mainly the MDTC structure, wherein the stator line voltage is found closer to the desired staircase form.
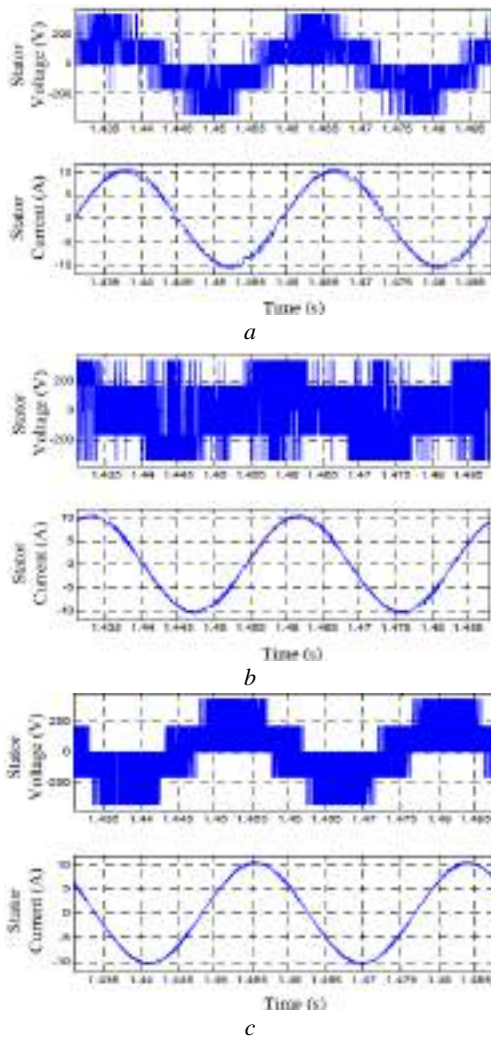
Fig. 15. Static responses of stator voltages and currents:
a – Classical DTC; *b* – DFTC; *c* – MDTC

Moreover, from the trajectories of the stator flux given in Fig. 16, we can notice an appreciable reduction in stator flux ripples, which is obtained with the two DTC-SVM structures. Particularly using the MDTC approach, the stator flux path represents the fastest dynamic response with the lowest ripples.

Fig. 16. Locus of stator flux in the three DTC approaches:
a – classical DTC;
b – DFTC; *c* – MDTC

By representing the inverter switching frequency in Fig. 17, we have demonstrated that the use of SVM strategy in MDTC structure gives in reality a fixed switching frequency and equalling the sample frequency (5 kHz) used in the modulation sequence of stator voltage space vector. On the 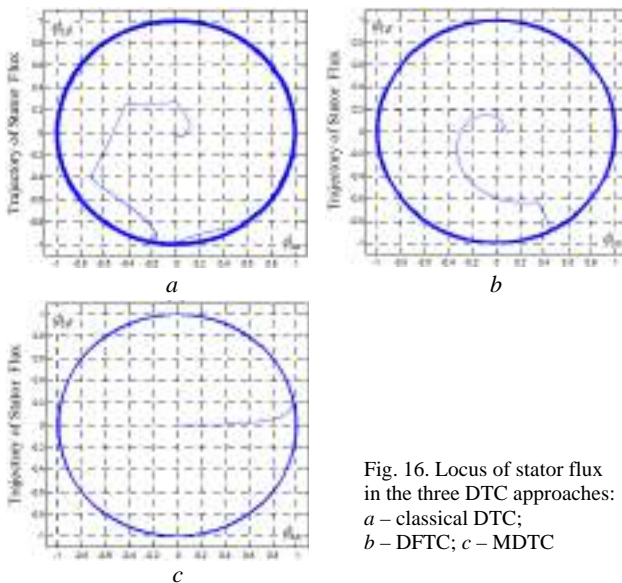other hand, we have verified that with DFTC structure the switching frequency has a fixed average value for various speed or torque references.

Therefore, from this analysis we have shown that the two proposed structures of DTC-SVM exhibit good static and dynamic performances with low torque ripples and a fixed switching frequency (over a wide range of torque or speed control). All of these benefits are obtained through the use of the SVM strategy and the speed IP controller.
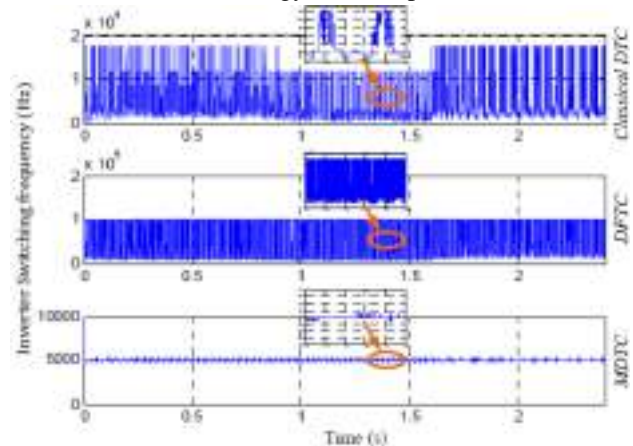
Fig. 17. Inverter switching frequency in each DTC approach

Conclusions.

The study of the two proposed direct torque control approaches (with space vector modulation), applied to the induction motor drive, is carried out here by means of physical considerations, analytical developments and simulation tests. Thus demonstrating how the electromagnetic torque and the stator flux can be kept under control through the application of the space vector modulation strategy.

A comparison between the classical direct torque control and the two direct torque control structures (with space vector modulation) is presented where the modification aim was some drawbacks attenuation of conventional direct torque control such as; the torque ripples, current distortion and random switching frequency variation. Indeed, the two proposed direct torque control approaches (with speed IP controller) have shown, through the different simulation tests, their effectiveness and superiority over the classical direct torque control without deteriorating the dynamic control capability of this technique.

The foremost revealed improvements of these two approaches are:

• ripples reduction in the torque and stator flux for either static or dynamic responses (under high and low speed operation);

• more attenuated distortion in the stator voltage and current waveforms by using the modified direct torque control structure;

• a switching frequency with fixed average value is achieved under various operating conditions (thanks to use of the space vector modulation strategy);

• fast dynamic response for the stator flux and a constant switching frequency in the inverter by using particularly the modified direct torque control structure.

In fact, the lowest switching frequency is obtained with the modified direct torque control approach. That will reduce the switching losses as well as stress on the inverter semiconductor components. Also, the modified direct torque control structure is more suitable for real time implementation due to its efficiency and simplicity.

Conflict of interest. The author declares that he has no conflicts of interest.

REFERENCES
1. Naganathan P., Srinivas S. Direct Torque Control Techniques of Three-Level H-Bridge Inverter Fed Induction Motor for Torque Ripple Reduction at Low Speed Operations. *IEEE Transactions on Industrial Electronics*, 2020, vol. 67, no. 10, pp. 8262-8270. doi: https://doi.org/10.1109/TIE.2019.2950840.
2. Djagarov N., Milushev H., Kononov Y., Djagarova J. Adaptive Controller for Induction Machine Direct Torque Control. *2021 17th Conference on Electrical Machines, Drives and Power Systems (ELMA)*, 2021, pp. 1-4. doi: https://doi.org/10.1109/ELMA52514.2021.9503085.
3. Ravi H.K., Chokkalingam L.N. Three Dimensional Switching Table for Reducing Torque Ripple and Switching Frequency in Direct Torque Controlled Induction Motor Drives. *2021 IEEE 12th Energy Conversion Congress & Exposition - Asia (ECCE-Asia)*, 2021, pp. 1515-1519. doi: https://doi.org/10.1109/ECCE-Asia49820.2021.9479266.
4. Moussaoui L. Direct torque control for a three-level NPC voltage source inverter fed induction motor drive. *International Conference on Electrical Engineering and Automatic Control.* Setif, Algeria, 2013.
5. Viet N.H., Paraschiv N. An Investigation on Twelve Sectors Direct Torque Control for Induction Motors fed by Matrix Converter. *2020 12th International Conference on Electronics, Computers and Artificial Intelligence (ECAI)*, 2020, pp. 1-5. doi: https://doi.org/10.1109/ECAI50035.2020.9223148.
6. Singh P., Gaur P., Mittal A.P. Improved Direct Torque Control Scheme based on Modified Torque Hysteresis Band. *2020 IEEE 5th International Conference on Computing Communication and Automation (ICCCA)*, 2020, pp. 725-729. doi: https://doi.org/10.1109/ICCCA49541.2020.9250910.
7. Koratkar P.J., Sabnis A. Comparative analysis of different control approaches of direct torque control induction motor drive. *2017 International Conference on Intelligent Computing, Instrumentation and Control Technologies (ICICICT)*, 2017, pp. 831-835. doi: https://doi.org/10.1109/ICICICT1.2017.8342672.
8. Pal A., Srivastava G.D., Kulkarni R.D. Simulation of Sensorless Speed Control of Induction Motor Using Direct Torque Control Technique Employing Five Level Torque Comparator and Twelve Sector Method. *2019 International Conference on Nascent Technologies in Engineering (ICNTE)*, 2019, pp. 1-6. doi: https://doi.org/10.1109/ICNTE44896.2019.8945936.
9. Moussaoui L., Moussi A. An open loop space vector PWM control for CSI-fed field-oriented induction motor drive with improved performances and reduced pulsating torque. *WSEAS Transactions on Circuits and Systems*, 2005, vol. 4, no. 2, pp. 71-77.
10. Moussaoui L., Moussi A. Performances improvement and torque ripple mitigation for CSI-fed vector controlled induction motor based on space vector PWM control. *Journal of Electrical Engineering*, 2005, vol. 5, no. 1, pp. 5-12.
11. Malyar V.S., Hamola O.Y., Maday V.S. Modelling of dynamic modes of an induction electric drive at periodic load. *Electrical Engineering & Electromechanics*, 2020, no. 3, pp. 9-14. doi: https://doi.org/10.20998/2074-272X.2020.3.02.
12. Petrushin V.S., Bielikova L.Y., Plotkin Y.R., Yenoktaiev R.N. Comparison of adjustable high-phase order induction motors' merits. *Electrical Engineering & Electromechanics*, 2016, no. 1, pp. 38-41. doi: https://doi.org/10.20998/2074-272X.2016.1.07.
13. Lobov V.I., Lobova K.V. The thyristor converter influence on the pulsations of the electromagnetic torque of the induction motor at parametrical control. *Electrical Engineering & Electromechanics*, 2017, no. 4, pp. 34-41. doi: https://doi.org/10.20998/2074-272X.2017.4.06.
14. Setiana H., Husnayain F., Yusivar F. Speed Sensorless Control of Dual Induction Motor using Direct Torque Control - Space Vector Modulation. *2019 IEEE 2nd International Conference on Power and Energy Applications (ICPEA)*, 2019, pp. 110-114. doi: https://doi.org/10.1109/ICPEA.2019.8818504.
15. Dehigolle Gedara A., Ekneligoda N.C. Direct torque control of induction motor using sliding-mode and fuzzy-logic methods. *2018 IEEE Power & Energy Society Innovative Smart Grid Technologies Conference (ISGT)*, 2018, pp. 1-5. doi: https://doi.org/10.1109/ISGT.2018.8403326.
16. Rosic M.M., Bebic M.Z. Analysis of torque ripple reduction in induction motor DTC drive with multiple voltage vectors. *Advances in Electrical and Computer Engineering*, 2015, vol. 15, no. 1, pp. 105-114. doi: https://doi.org/10.4316/AECE.2015.01015.
17. Lunardi A.S., Sguarezi A.J., Filho. Experimental results for predictive direct torque control for a squirrel cage induction motor. *2017 Brazilian Power Electronics Conference (COBEP)*, 2017, pp. 1-5. doi: https://doi.org/10.1109/COBEP.2017.8257222.
18. Manuprasad P., Mohanty K.B. Implementation of 12 Sector Fuzzy Controller for Direct Torque Control of Induction Motor. *2019 Innovations in Power and Advanced Computing Technologies (i-PACT)*, 2019, pp. 1-6. doi: https://doi.org/10.1109/i-PACT44901.2019.8960096.
19. Yu C., Wang H., Sung G., Huang H. Modified Direct Torque Control Application-Specific Integrated Circuit with Five-Stage Fuzzy Hysteresis and a Proportional–Integral–Derivative Controller for a Three-Phase Induction Motor. *2018 IEEE International Conference on Systems, Man, and Cybernetics (SMC)*, 2018, pp. 2413-2417. doi: https://doi.org/10.1109/SMC.2018.00414.
20. Wu X., Huang W., Lin X. A Novel Direct Torque Control with or without Duty Ratio Optimization for Induction Motors. *2019 22nd International Conference on Electrical Machines and Systems (ICEMS)*, 2019, pp. 1-4. doi: https://doi.org/10.1109/ICEMS.2019.8922455.
21. Venkataramana Naik N., Singh S.P. A Novel Interval Type-2 Fuzzy-Based Direct Torque Control of Induction Motor Drive Using Five-Level Diode-Clamped Inverter. *IEEE Transactions on Industrial Electronics*, 2021, vol. 68, no. 1, pp. 149-159. doi: https://doi.org/10.1109/TIE.2019.2960738.
22. Moussaoui L. Study and simulation of a fuzzy-controlled shunt active power filter using two different control algorithms. *1st International Conference on Electrical Engineering*, Biskra, Algeria, 2014.
23. Wu X., Huang W., Lin X., Zhu S. An Initial Trial to Drive Induction Motors by Synchronized SVPWM-Based Direct Torque Control. *2020 IEEE 9th International Power Electronics and Motion Control Conference (IPEMC2020-ECCE Asia)*, 2020, pp. 342-345. doi: https://doi.org/10.1109/IPEMC-ECCEAsia48364.2020.9368145.

Leila Moussaoui, Doctor of Electrical Engineering,
Department of Electrical Engineering, Faculty of Technology,
Ferhat Abbas Setif 1 University,
Cité Maabouda, Route de Bejaia, Setif, 19000, Algeria,
e-mail: ufas.lmoussaoui@gmail.com (Corresponding author)

G. Rosu, V. Velicu, A. Boitan, G. Mihai, L. Tuta, O. Baltag

On the electromagnetic shielding properties of carbon fiber materials

*Introduction. Due to the good electrical and thermal properties of carbon, carbon-based materials represent a major trend is various applications, including electromagnetic compatibility. Among carbon-based materials, graphite-impregnated woven fabrics represent a new trend in the field of electromagnetic shielding, with the perspective of being used for protective clothing. **The novelty** of the proposed work consists in the exhaustive comparative analysis of various carbon-based sample shields by employing both simulation and experimental methods. The selected configurations included a simple graphite plate, a graphite powder strip network, and a graphite-impregnated fabric with 2×2 twill weave. **Purpose.** The main scope of the analysis is to prove the efficiency of the graphite-impregnated twill woven fabric in the field of electromagnetic shielding. **Methods.** Two main research methods were employed: simulation and experiment, both following the same protocol: the shield placed in the middle, with the excitation (transmitting antenna) on one side and the measurement / receiving antenna on the other. The experimental stage was thorough, being performed in two different laboratories and by applying the double transverse electromagnetic (TEM) cell method and the shielded box method. **Results.** A significant difference yielded from the comparison of the simulation and experimental results for the shielding effectiveness, probably due to the fact that the virtual model is an idealized version of the physical one, not taking into account its imperfections. The virtual analysis yielded the graphite plate shield as the most efficient, followed closely by the twill fabric. The graphite strip network had significantly poorer performance compared to the other two shields, probably due to the electrical contact imperfections between the graphite strips and the optical transparency of the shield. The main focus of the analysis was the twill woven graphite-impregnated fabric; therefore, its shielding effectiveness was determined through simulation and experiment. The experimental analysis was performed in two stages in two different electromagnetic compatibility laboratories, by employing the double TEM cell method and the shielded box method, respectively, both methods providing similar results and classifying the shielding performance as good. **Practical value.** The paper provides an accurate analysis of the graphite-impregnated 2×2 twill woven fabric in terms of electromagnetic shielding effectiveness, by employing both simulation and experimental methods, and comparing its performance to the one other graphite-based shields. References 14, tables 2, figures 14.*
Key words: **carbon fiber, double TEM cell, electromagnetic shielding, graphite, shielded box method, shielding effectiveness.**

*Вступ. Завдяки хорошим електричним і тепловим властивостям вуглецю, вуглецевмісні матеріали являють собою основні напрямки у різних застосуваннях, у тому числі в області електромагнітної сумісності, завдяки хорошим екрануючим властивостям. Серед матеріалів на основі вуглецю просочені графітом тканини є новою тенденцією в області електромагнітного екранування з перспективою використання для захисного одягу. **Новизна** запропонованої роботи полягає у вичерпному порівняльному аналізі різних зразків екранів на основі вуглецю з використанням як моделювання, так і експериментального методів. Вибрані конфігурації включали просту графітову пластину, сітку зі смуг з графітового порошку і просочену графітом тканину з переплетенням саржею 2×2. **Ціль.** Основною метою аналізу є доказ ефективності саржевого полотна, просоченого графітом, у галузі електромагнітного екранування. **Методи.** Використовувалися два основних методи дослідження: моделювання та експеримент, обидва слідували одному й тому ж протоколу: екран розташовувався посередині, з збуджуванням (передаючою антеною) з одного боку і вимірювальною/приймальною антеною з іншого. Експериментальний етап був ретельним і проводився у двох різних лабораторіях із застосуванням методу подвійної поперечної електромагнітної (ПЕМ) комірки та методу екранованої скриньки. **Результати.** Порівняння результатів моделювання та експериментів стосовно ефективності екранування демонструє суттєву відмінність, ймовірно, через те, що віртуальна модель є ідеалізованою версією фізичної, не враховуючи її недосконалості. Віртуальний аналіз показав, що екран із графітових пластин є найбільш ефективним, за ним близько слідує саржева тканина. Мережа з графітових смуг мала значно гірші характеристики порівняно з двома іншими екранами, ймовірно, через недосконалість електричного контакту між графітовими смужками та оптичною прозорістю екрана. Основним предметом аналізу була тканина саржевого переплетення, просочена графітом; тому її ефективність екранування визначалася шляхом моделювання та експерименту. Експериментальний аналіз був виконаний у два етапи у двох різних лабораторіях електромагнітної сумісності з використанням методу подвійної ПЕМ комірки та методу екранованої скриньки, відповідно, обидва методи дали аналогічні результати та визначили характеристики екранування як хороші. **Практична цінність.** У статті наведено точний аналіз просоченої графітом саржевої тканини 2×2 з точки зору ефективності електромагнітного екранування з використанням як моделювання, так і експериментальних методів, а також порівняння її характеристик з іншими екранами на основі графіту. Бібл. 14, табл. 2, рис. 14.*
Ключові слова: **вуглецеве волокно, подвійна ПЕМ комірка, електромагнітне екранування, графіт, метод екранованої скриньки, ефективність екранування.**

Introduction. Carbon exists in nature in different forms with different physical properties: as diamond, as graphite (also called amorphous carbon), as fullerene – geodesic dome-type structures and in cylindrical structures – as carbon nanotubes. Graphite is one of the two allotropic states of carbon, in which the atomic lattice – also known as stratified lattice – occupies a volume of space formed by parallel planes of carbon atoms arranged in a regular planar hexagonal structure. The planar two-dimensional structure of graphite, actually having a monoatomic thickness, is called graphene and has superior properties in terms of electrical and thermal

conductivity. It was obtained in 2004 by Andrei Geim through an exfoliation technique. The research undertaken by Andrei Geim and Konstantin Novoselov on this type of material brought them in 2010 the Nobel Prize [1].

The low mass density and high tensile strength of carbon fiber recommend it for the use in aerospace industry, in automotive industry (the sports competition sector), or sports articles, while the high electrical conductivity of carbon turns it into a solid option for electromagnetic shielding materials. Although metals are traditionally used in electromagnetic shielding, their high

mass density prevents using them in applications where the shield portability is required. Another limitation of the metal shield is given by the fact that the shielding mechanism relies mostly on reflection, which renders such shields inadequate for stealth applications, for instance. Conductive polymers come as an alternative for electromagnetic shielding, but with the inconveniences of low thermal stability and high processing cost. Carbon-based polymer nanocomposites offer the advantages of both conductive polymers and carbon, having low mass density, high electrical conductivity, and a shielding efficiency based on absorption and multiple internal reflections mechanisms [2].

Depending on the application, several types of carbon-based shielding materials such as polymer composites, cellulose composites, woven fabrics, or fabric/epoxy composites are investigated in [2-9]. Carbon-based technical textiles have also proved their economic efficiency in the aerospace industry, yielding a 20 % fuel saving for aircrafts with wing movables made of carbon fiber epoxy composites instead of aluminum [7].

Referring to carbon woven fabrics, several papers report the results of their analyzes on the impact of weave type, the number of carbon fiber layers, as well as their direction. In [9], Rea et al. investigate the shielding effectiveness (SE) of two woven carbon fiber composites used in aerospace industry, and placed in satin weave. Both samples are made of three plies, the difference between samples consisting in the direction of the middle ply.

The twill weave was analyzed in terms of shielding effectiveness in the frequency band up to 3 GHz, when compared to the plain weave and the uniform direction weave [6, 8, 10, 11]. In [10], Pamuk et al indicate the 2×1 twill structure has higher shielding effectiveness compared to a plain 1×1 weave and a satin 6 weave.

The goal of the paper is to perform a comparative analysis in terms of electromagnetic shielding effectiveness, of various carbon-based materials through both numerical and experimental methods.

Subject of investigations. Due to its high absorption properties, carbon is extremely efficient in electromagnetic shielding [12]. In this paper, the properties of various carbon fiber materials are studied, including graphite powder and graphite impregnated woven fabric [12-14]. Since the textile carbon fiber materials represent a new tendency in electromagnetic shielding, a sample of twill woven fabric is analyzed with reference to other carbon-based screen types. The shielding effectiveness of three selected samples, for the 1 GHz frequency, is initially investigated through simulation in a commercial Finite Element Method (FEM) software, by following an approach similar to the standard experimental procedure. The carbon-based fabric is built in great detail in the virtual environment. The second research method described in this paper was experimental and it investigated the efficiency of two sample shields. The experimental stage was carried out in two different electromagnetic compatibility (EMC) laboratories employing different methods – the double transverse electromagnetic (TEM) cell method and the shielded box method, respectively. The results obtained

for the same frequency as in the simulation stage are presented and discussed.

Presentation of the selected samples. The following types of screens are investigated:
- a shielding material consisting of graphite impregnated fabric with twill weave (Fig. 1);
- a graphite plate;
- an orthogonal grid graphite powder screen (Fig. 2).

From the materials listed above, the fabric and the graphite strip mesh have been practically made and studied both theoretically and experimentally. The graphite plate was investigated only in the simulation.

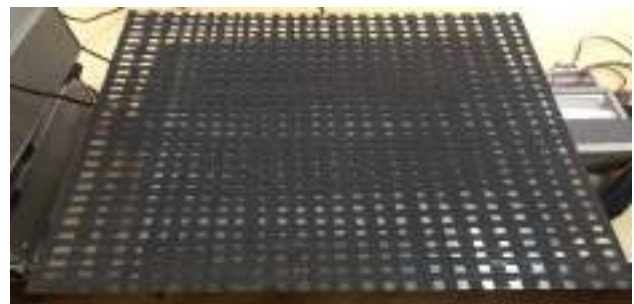Fig. 1. The 2×2 twill carbon-based weave

Fig. 2. Orthogonal grid with graphite powder strips

Description of the twill weave. Twill weave is a diagonally woven fabric and is characterized by the interweaving of warp and weft yarns at a specific angle. In this case, the two categories are perpendicular. This characteristic binding gives the fabric a particular appearance. Diagonal weaves can be: diagonal weft (when the weft yarns are visible on the face of the fabric and outnumber the warp yarns), diagonal warp (when the visible warp yarns are predominant on the face of the fabric) and diagonal balanced. The cross stitches are fewer than in the woven pile bond and therefore the fabric will be smoother, looser, softer and less durable than woven pile bond fabrics. Diagonal-bonded fabrics are softer, suppler, with more friction-resistant stitches. Diagonal bonded fabrics do not have high bond strength like woven bonded fabrics and therefore these fabrics will have mechanical properties inferior to the ones of woven bonded fabrics. The 2×2 twill weave is widely used in the decoration field and in the automotive industry and is made according to the following pattern: the warp yarns are arranged in the Ox direction, at a fixed distance, and the warp yarns are arranged perpendicularly, in the Oy direction, so that the warp yarn passes over two warp yarns, then under two other warp yarns. The 2×2 twill fabric model was built in the Ansys HFSS simulation

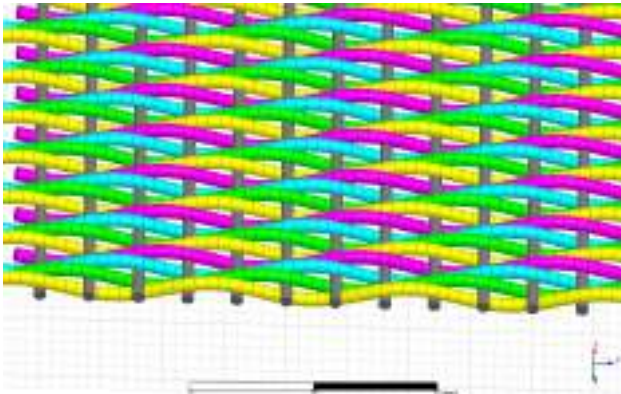environment (Fig. 3), following textile industry standards. The model characteristics are given in Table 1.

Fig. 3. Geometric pattern of 2×2 twill fabric

Table 1
Virtual twill fabric model parameters

Parameter specification	Value
Threads diameter	1 mm
Distance between warp threads	3 mm
Distance between batting yarns	0.1 mm
Shield width	20 mm
Shield length	1000 mm

Calculation of shielding effectiveness by means of simulation. To obtain the shielding effectiveness (SE), the procedure is similar to the experimental method: place the shield in the middle of a field, with excitation at one end, and determine the field or power level at the other end, with respect to the no-shield situation.

The model used is illustrated in Fig. 4 and is represented by a parallelepiped-shaped air box, with a square cross-section with a side equal to one screen side and a length of 1 m. The following boundary conditions were applied: on the top-bottom surfaces the «Perfect E» boundary condition was imposed, and on the front-back surfaces, the «Perfect H» condition, and thus waveguide propagation medium was obtained.
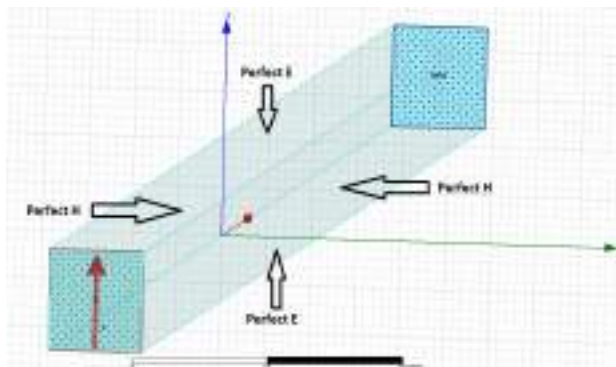

Fig. 4. Simulation domain, boundaries and excitation

«Wave Port» excitation is applied to one end of the domain, corresponding to the cross section of the domain and having the electric field distribution mode such that the curvilinear integral of the electric field along a vertical line is positive. At the opposite end of the excitation, a «Radiation» boundary condition was applied, which is actually an Absorbing Boundary Condition (ABC). This minimizes reflections of waves incoming from the perpendicular direction or nearly perpendicular to the boundary. Figure 4 shows the excitation applied to the near-plane base, the «Radiation» condition on the far-plane base, and the side surfaces with the «Perfect E» (top and bottom) and «Perfect H» (left and right) condition, respectively. The working frequency of the simulation is 1 GHz.

In the absence of the shield, the simulation domain behaves like a waveguide with the excitation on the left side, as shown in Fig. 5, which illustrates the electric field distribution in the longitudinal plane.
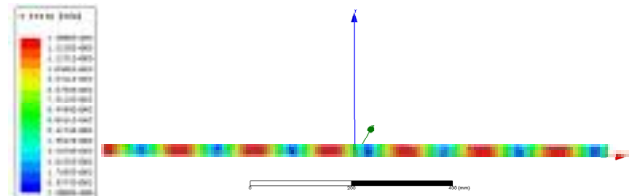

Fig. 5. Propagation of the electromagnetic field within the domain in the absence of the shield

Simulation of the shielding effectiveness of the graphite twill fabric. In the analysis of the shielding effectiveness of the carbon material, the 2×2 twill geometric model is extended to a 20 mm wide square-shaped screen, arranged in the air box at mid-length, and the excitation on the left side. The electric field distribution, illustrated in Fig. 6, highlights the mechanisms of electromagnetic field reflection and absorption. Thus, in the left half of the longitudinal plane, an increase of the electric field is observed – highlighted by the increase of the peak values compared to the previous case, due to the reflection process of the electromagnetic (EM) waves by the screen located in the middle. The right-hand side shows the electric field transmitted through the screen after the internal reflection, absorption and refraction mechanisms have occurred; it is approximately half compared to the situation without the shield.
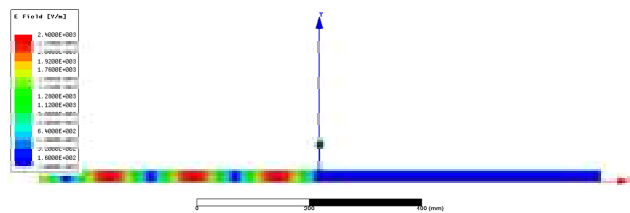
Fig. 6. Propagation of the EM field, with the shield placed in the middle of the domain

In both cases the same distance is observed between the maximum and minimum points, which means that the wavelength does not change, due to the fact that the propagation medium is the same (air) and the impedance of the medium is constant. For a more precise determination of the shielding effectiveness of the carbon fabric, the electric field strength E and the electromagnetic wave power density S are plotted on the central longitudinal axis. The variation of the two physical quantities on the central longitudinal axis in the two cases is given in Fig. 7, 8, respectively.

For the first case – in the absence of the shield, the maximum value of the electric field strength

$E_{max} = 1315.34$ V/m and $S_{max} = 2423.35$ W/m². As noted in Fig. 7, there is a natural fluctuation of the power density S, generated by the discontinuous structure of the discretization mesh. Depending on how the mesh was applied, only a portion of the mesh vertices are located on the longitudinal axis on which the E and S quantities were calculated. For points on the longitudinal axis that do not coincide with the mesh vertices, the E and S quantities are calculated by interpolating the values of adjacent vertices. The S graph in Fig. 7 shows an average value of the transmitted power and a peak deviation of 250 W/m² which, compared to the average value, indicates a relative deviation of approximately 10 %.
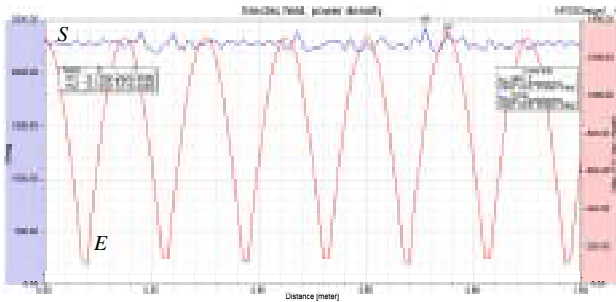

Fig. 7. The power density S (blue line) and the electric field strength E (red line) on the central longitudinal axis – in the absence of any shield
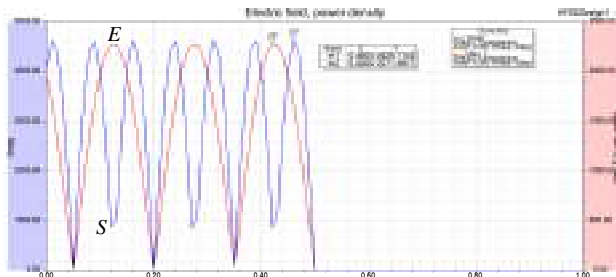

Fig. 8. The power density S (blue line) and the electric field strength E (red line) on the central longitudinal axis – in the presence of the fabric material shield

In the second case – in the presence of the shield, a significant reduction of the values of the two magnitudes in the second half of the axis and an increase of the values on the left side (compared to the first case) is evident, as shown in Fig. 8. On the right side, the value of S is zero and that of $E = 0.06$ V/m. Applying the formula for calculating SE based on the electric field strength, we obtained:

$$SE = 20 \cdot \lg\left(\frac{E_1}{E_2}\right) = 20 \cdot \lg\left(\frac{1315.34}{0.06}\right) = 86.8 \text{ dB}.$$

In this case, the value of SE indicates a very high degree of shielding.

Simulating the shielding efficiency of a graphite plate. To complete the analysis of the carbon powder fabric, we evaluate the results obtained from the simulation by comparing it with a shield consisting of a continuous graphite plate with the same dimensions as the first shield. The results for the two sizes considered are given in Fig. 9. Using the same formula and the same value for E_1, but modifying $E_2 = 0.03$ V/m, we obtain $SE = 92.8$ dB.

Fig. 9. The power density S (blue line) and the electric field strength E (red line) on the central longitudinal axis – in the presence of the graphite plate shield

Simulation of shielding effectiveness of an orthogonal network made of graphite powder strips. The shielding material is an orthogonal network of graphite powder strips of 1 mm thickness and 10 mm width. These are arranged in parallel at 10 mm intervals. The physical screen has been illustrated in Fig. 3. A mesh has been represented in the simulation (Fig. 10) which falls within the same simulation domain used in the previous cases.
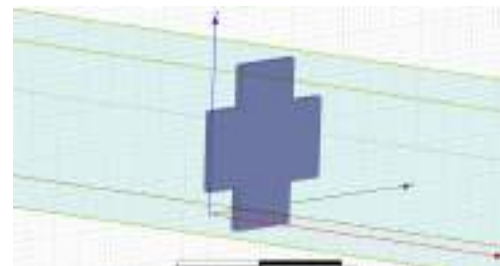
Fig. 10. The geometric pattern of the graphite mesh

The simulation results, shown in Fig. 11, indicate a maximum electric field level after the screen of $E_2 = 10.3$ V/m and also a good degree of shielding effectiveness of about 42.1 dB.

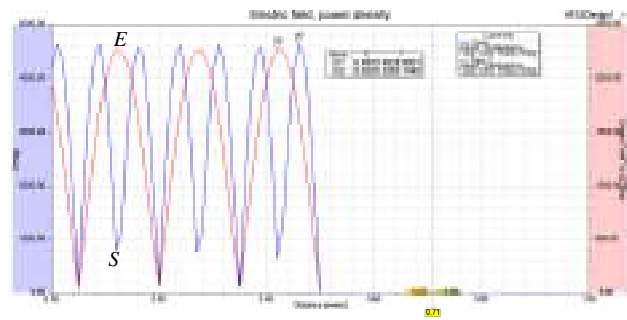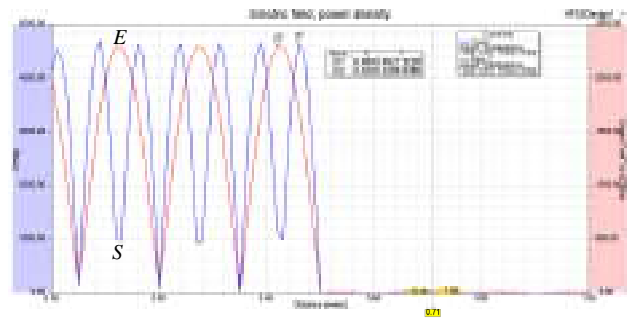

Fig. 11. Power density S (blue line) and electric field strength E (red line) on the central longitudinal axis – in the presence of a graphite strip grid shield

Experimental determination of shielding effectiveness. The experimental determination was carried out in two steps performed in two different EMC laboratories. Although the experimental investigation covered a wide band of frequencies, for the purpose of comparison with the numerical method only the SE values for the 1 GHz frequency will be presented.

In the first experimental stage, a double TEM (DTEM) cell from TESEO was used. A DTEM cell consists of two cells that provide a good approximation of

the far field propagation and which are coupled through a rectangular aperture. The DTEM cell has two of its ports connected to a Rohde & Schwarz FSH3 spectrum analyzer with tracking generator. The textile shield was placed inside the DTEM cell, covering the common aperture between the two parts. The other two ports of the DTEM cell there were connected 50 Ω impedances. The input port was fed from the spectrum analyzer with signals in the 500 MHz – 1 GHz frequency range, and the transmitted signal was received at the output port of the cell into the spectrum analyzer. The measurement setup described above is illustrated in Fig. 12. This experimental stage was focused on the textile shield.

Fig. 12. The experimental setup used in stage 1

Second stage of the experimental investigation of the shielding effectiveness was based on the use of a steel box in a cubic shape with the side of 60 cm. The shield partly replaced one box side – as it can be noticed in Fig. 13. The measurements were performed in a different EMC laboratory and investigated both the textile material and graphite strips screen. The measurement setup drawn in Fig. 14 consisted in placing the transmitting (Tx) antenna outside the steel box and the receiving (Rx) antenna inside it, along with a Signal Hound BB60C SDR receiver, a personal computer (PC), and a media converter (MC). The MC was connected through optical fiber to another PC, and the Tx antenna was fed by a Rohde & Schwarz SMP04 signal generator. Both Tx and Rx antenna were Rohde & Schwarz HF906 horn type and were placed so as to have horizontal polarization.

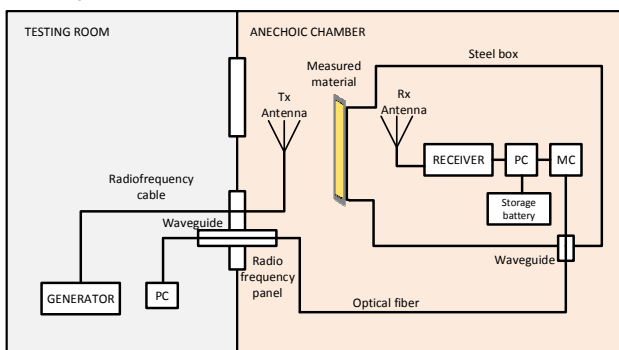Fig. 13. Shield installation on one side of the steel box

Fig. 14. The experimental setup used in stage 2

Shielding effectiveness results. In order to compare the simulation and experimental results, the SE values for the test frequency of 1 GHz are presented in Table 2.

Table 2
Values obtained for the shielding effectiveness of the three sample screens, at a test frequency of 1 GHz

Shield pattern	Simulation results	Experimental results	
		Stage 1	Stage 2
Twill weave	86.8 dB	57 dB	54.8 dB
Graphite plate	92.8 dB	–	–
Graphite strip network	42.1 dB	–	6.5 dB

Results discussion. Significant differences are observed between the simulation results and the experimental results. Among the three sample shields, the graphite plate was investigated only through simulation, but its shielding performance proved to be superior to the other ones, although closely followed by the carbon-based fabric. The superiority of the graphite plate is obvious due to the fact that there are no holes or apertures in the shield structure. Since the twill sample was the focus of the investigation, it was analyzed through both simulation and experiment – in both EMC laboratories. As it can be seen in Table 2, there is a slight difference between the SE results obtained through different methods. Although a 30 dB difference is noted when compared to the simulation results. A similar 35 dB difference between simulation and experiment is also obtained for the graphite strips shield. This difference could be explained by the virtual model construction, which does not include imperfections in electrical contact between strips and has a constant thickness on the entire surface of the screen.

Conclusions.

1. There is analyzed the shielding performance at 1 GHz of three types of carbon-based screens: a graphite plate, a network of orthogonal graphite powder strips, and a twill woven graphite-impregnated fabric. All screens were investigated by simulation means, following an approach similar to the experimental procedure. The second and third screens were investigated experimentally.

2. From the virtual analysis, the graphite plate shield was the most efficient, followed closely by the twill fabric. The graphite strip network had the poorest performance, 45-50 dB lower than the other shields, probably due to electrical contact imperfections between graphite strips and the shield optical transparency.

3. The main focus of the analysis was the twill woven graphite-impregnated fabric; therefore, its shielding effectiveness (SE) was determined through simulation and experiment – by employing the DTEM cell and the shielded box method. The experimental results of the two stages were similar: SE = 57 dB from the former and SE = 54.8 dB from the latter, respectively.

4. A significant difference yielded from the comparison of the simulation and experimental results for the SE. This is probably due to the fact that the virtual model is an idealized version of the physical one, not taking into account its imperfections.

5. Both from the simulation and experimental stages, the efficiency of the graphite-based twill fabric proved to be at least at a good level, with SE ≈ 55 dB.

6. Graphite has considerable advantages over other materials currently used due to its properties: high electrical conductivity, lower mass density than metals, corrosion resistance in hostile environments, mechanical flexibility, easy processing. Compact graphite structures have higher attenuation than other structures due to their low transparency to the electromagnetic field.

7. Properties related to the electromagnetic field absorption and the mechanical properties recommend the use of graphite fabric for protective clothing and electromagnetic security. The protective clothing has variable and dynamic geometric structure, and such qualities are provided by the carbon fiber fabric.

8. A further research direction consists in manufacturing a twill woven protective suit and investigating its shielding properties in terms of specific absorption rate reduction.

Conflict of interest. The authors declare that they have no conflicts of interest.

REFERENCES

1. Gerstner E. Nobel Prize 2010: Andre Geim & Konstantin Novoselov. *Nature Physics*, 2010, vol. 6, no. 11, pp. 836-836. doi: https://doi.org/10.1038/nphys1836.
2. Abbasi H., Antunes M., Velasco J.I. Recent advances in carbon-based polymer nanocomposites for electromagnetic interference shielding, *Progress in Materials Science*, 2019, no. 103, pp. 319-373. doi: https://doi.org/10.1016/j.pmatsci.2019.02.003.
3. Jia H., Kong Q.-Q., Liu Z., Wei X.-X., Li X.-M., Chen J.-P., Li F., Yang X., Sun G.-H., Chen C.-M. 3D graphene/ carbon nanotubes/ polydimethylsiloxane composites as high-performance electromagnetic shielding material in X-band. *Composites Part A: Applied Science and Manufacturing*, 2020, vol. 129, pp. 105712. doi: https://doi.org/10.1016/j.compositesa.2019.105712.
4. Anju V.P., Manoj M., Mohanan P., Narayanankutty S.K. A comparative study on electromagnetic interference shielding effectiveness of carbon nanofiber and nanofibrillated cellulose composites. *Synthetic Metals*, 2019, vol. 247, pp. 285-297. doi: https://doi.org/10.1016/j.synthmet.2018.12.021.
5. Gupta S., Tai N.-H. Carbon materials and their composites for electromagnetic interference shielding effectiveness in X-band. *Carbon*, 2019, vol. 152, pp. 159-187. doi: https://doi.org/10.1016/j.carbon.2019.06.002.
6. Jou W.S. A Novel Structure of Woven Continuous-Carbon Fiber Composites with High Electromagnetic Shielding. *Journal of Electronic Materials*, 2004, vol. 33, no. 3, pp. 162-170. doi: https://doi.org/10.1007/s11664-004-0175-x.
7. Ucar N., Kayaoğlu B.K., Bilge A., Gurel G., Sencandan P., Paker S. Electromagnetic shielding effectiveness of carbon fabric/epoxy composite with continuous graphene oxide fiber and multiwalled carbon nanotube. *Journal of Composite Materials*, 2018, vol. 52, no. 24, pp. 3341-3350. doi: https://doi.org/10.1177/0021998318765273.
8. Jou W.S. The high electromagnetic shielding of woven carbon fiber composites applied to optoelectronic devices. *CLEO/Pacific Rim 2003. The 5th Pacific Rim Conference on Lasers and Electro-Optics*, 2003, vol. 2, pp. 755. doi: https://doi.org/10.1109/CLEOPR.2003.1277291.
9. Rea S.P., Wylie D., Linton D., Orr E., McConnell J. EMI shielding of woven carbon fibre composites. *High Frequency Postgraduate Student Colloquium*, 2004, pp. 205-210. doi: https://doi.org/10.1109/HFPSC.2004.1360389.
10. Pamuk G., Kayacan Ö., Kayacan O., Seçkin Uğurlu Ş. Electromagnetic shielding effectiveness of carbon yarn-based woven fabrics. *Journal of Industrial Textiles*, 2022, vol. 51, no. 7, pp. 1143-1160. doi: https://doi.org/10.1177/1528083719896769.
11. Keskin H.I., Ozen S., Ates K., Polat L.N. Analysis and Measurement of the Electromagnetic Shielding Efficiency of the Multi-Layered Carbon Fiber Composite Fabrics. *2019 PhotonIcs & Electromagnetics Research Symposium - Spring (PIERS-Spring)*, 2019, pp. 4354-4360. doi: https://doi.org/10.1109/PIERS-Spring46901.2019.9017787.
12. Baltag O., Rosu G. Applications of Graphite Materials in the Field of Electromagnetic Compatibility. *Carbon-Related Materials*, 2020, pp. 19-44. doi: https://doi.org/10.1007/978-3-030-44230-9_2.
13. Miclăuş S., Bechet P., Paljanos A., Aron A.M., Mihai G., Pătru I., Baltag O. Shielding Effectiveness of Some Conductive Textiles and Their Capability to Reduce the Mobile Phones Radiation. *International Conference KNOWLEDGE-BASED ORGANIZATION*, 2016, vol. 22, no. 3, pp. 524-530. doi: https://doi.org/10.1515/kbo-2016-0091.
14. Patel S.M., Patel K., Negi P.S., Ojha V.N. Shielding effectiveness measurements and uncertainty estimation for textiles by a VNA-based free space transmission method. *International Journal of Metrology and Quality Engineering*, 2013, vol. 4, no. 2, pp. 109-115. doi: https://doi.org/10.1051/ijmqe/2013042.

Georgiana Rosu[1], *PhD, Assistant Professor,*
Valentin Velicu[2], *PhD Student,*
Alexandru Boitan[2], *PhD Student,*
George Mihai[3], *Head of Laboratory,*
Leontin Tuta[4], *Master, Teaching Assistant,*
Octavian Baltag[5], *Professor,*
[1] Department of Military Electronic Systems and Equipment,
«Ferdinand I» Military Technical Academy,
39-49 George Cosbuc Blv, Bucharest, PO 050141, Romania,
e-mail: georgianamarin01@gmail.com (Corresponding Author)
[2] Special Telecommunications Service,
323A Splaiul Independentei, 6th District, Bucharest,
060044, Romania,
e-mail: valentin.velicu@stsnet.ro;   alexandru.boitan@stsnet.ro
[3] Laboratory for Electromagnetic Compatibility and Equipment Testing,
National Authority for Management and Regulation in Communications of Romania (ANCOM),
Str. Mitropolit Andrei Şaguna, 1033D, Prejmer, Braşov, Romania,
e-mail: george.mihai@ancom.ro
[4] Department of Communications and Information Technology,
«Ferdinand I» Military Technical Academy,
39-49 George Cosbuc Blv, Bucharest, PO 050141, Romania,
e-mail: leontin.tuta@mta.ro
[5] Grigore T. Popa University Medicine and Pharmacy of Iasi,
Medical Bioengineering Department,
65, Tatarasi Street, Iasi, 700395, Romania,
e-mail: octavian.baltag@bioinginerie.ro

S. Gopal Reddy, S. Ganapathy, M. Manikandan

Power quality improvement in distribution system based on dynamic voltage restorer using PI tuned fuzzy logic controller

Purpose. This article proposes a new control strategy for Dynamic Voltage Restorer (DVR) in utility grid for distribution system. The proposed DVR using PI tuned fuzzy logic scheme is based on replacement of conventional DVR and voltage sag compensation in distribution system network. ***The novelty*** *of the proposed work consists in presenting an enhanced PI tuned fuzzy logic algorithm to control efficiently the dynamic voltage restorer when voltage sag is suddenly occurred.* ***Methods.*** *The proposed algorithm which provides sophisticated and cost-effective solution for power quality problems. Our strategy is based on tuned fuzzy control of reactive powers and also closed loop for harmonic reduction in distribution system. The proposed control technique strategy is validated using MATLAB / Simulink software to analysis the working performances.* ***Results.*** *The results obtained clearly show that DVR using PI tuned fuzzy logic have good performances (sag compensation, harmonic reduction) compared to conventional DVR.* ***Originality.*** *Compensation of voltage sag/ swell in distribution for reactive power and current harmonic reduction by using DVR based PI tuned fuzzy logic controller.* ***Practical value****. The work concerns the comparative study and the application of DVR based on PI tuned fuzzy techniques to achieve a good performance control system of the distribution system. This article presents a comparative study between the conventional DVR control and PI tuned fuzzy DVR control. The strategy based on the use of a PI tuned fuzzy controller algorithm for the control of the continuous voltage sag and harmonic for the distribution network-linear as well as non-linear loads in efficient manner. The study is validated by the simulation results based on MATLAB / Simulink software.* References 27, tables 3, figures 20.
Key words: **dynamic voltage restorer, proportional integral controller, proportional integral tuned fuzzy logic controller, voltage source inverter, pulse-width modulation generator, total harmonic distortion.**

Мета. *У статті пропонується нова стратегія управління пристроєм динамічного відновлення напруги (ДВН) в мережі розподільної системи. Запропонований ДВН, що використовує схему нечіткої логіки з ПІ-налаштуванням, заснований на заміні звичайного ДВН та компенсації провалів напруги в мережі розподільної системи.* ***Новизна*** *запропонованої роботи полягає у поданні удосконаленого алгоритму нечіткої логіки з ПІ-налаштуванням для ефективного управління динамічним відновником напруги при раптовому виникненні провалу напруги.* ***Методи.*** *Запропоновано алгоритм, який забезпечує складне та економічне вирішення проблем якості електроенергії. Наша стратегія заснована на нечіткому керуванні реактивною потужністю, що налаштовується, а також на замкненому контурі для зниження гармонік в розподільній системі. Запропонована методика управління перевіряється за допомогою програмного забезпечення MATLAB/Simulink для аналізу робочих характеристик.* ***Результати***. *Отримані результати чітко показують, що ДВН, який використовує нечітку логіку з ПІ-налаштуванням, має хороші характеристики (компенсація провалів, зниження гармонік) порівняно із звичайним ДВН.* ***Оригінальність***. *Компенсація провалів/стрибків напруги у розподільній мережі для зниження реактивної потужності та гармонік струму за допомогою нечіткої логіки з використанням ДВН на основі контролера нечіткої логіки з ПІ-налаштуванням.* ***Практична цінність***. *Робота стосується порівняльного дослідження та застосування ДВН на основі нечіткої логіки з ПІ-налаштуванням для досягнення хороших параметрів системи керування розподільною системою. У статті представлено порівняльне дослідження звичайного керуванням ДВН та нечіткого керування ДВН з ПІ-налаштуванням. Стратегія, заснована на використанні алгоритму нечіткої логіки з ПІ-налаштуванням для ефективного керування безперервним провалом напруги та гармоніками для лінійних та нелінійних навантажень розподільчої мережі. Дослідження підтверджено результатами моделювання на основі програмного забезпечення MATLAB/Simulink.* Бібл. 27, табл. 3, рис. 20.
Ключові слова: **динамічний відновник напруги, пропорційно-інтегральний контролер, контролер нечіткої логіки з пропорційно-інтегральним налаштуванням, інвертор джерела напруги, генератор широтно-імпульсної модуляції, повне гармонічне спотворення.**

Introduction. Power quality management has become a crucial challenge in today's electrical power system. Load with increased sensitivity and complexity leads to voltage fluctuation, non-standard current and frequency, thereby lowering the power quality. Even a short term voltage fluctuation results in malfunctioning of the entire distribution system. As a result, it is highly crucial to enhance the power quality, which is considered to be a difficult task for industrial customers as it leads to the failure of variety of sensitive electronic equipment.

The demand for electricity is increasing day by day and the issues associated with transmitting the power through the distribution system are growing as well. Voltage fluctuation is regarded to be the most serious PQ issue that must be addressed. Voltage fluctuation often leads to power distribution system failure or malfunction of a continuous process [1, 2]. The voltage fluctuation issues that cause the system to malfunction are voltage sag, swell,

transient disruptions, harmonic distortions, spikes and surges [3]. However, voltage sag and swell are regarded to be the most serious power PQ among them. On the other hand, the magnitude of the voltage is one of the most important elements that determine the quality of electrical power, and it is essential to increase the quality of the power before it is utilized further [4]. A reliable power supply is essential in today's economy, and both power distributors and consumers have realized the value of power quality throughout time. Furthermore, authorities are now very interested in ensuring that power distributors have met their PQ responsibilities or not [5, 6].

The power produced by the power generation system has to be upgraded in order to offer clean and pure power to the power consumers. Previously, generation and transmission systems are responsible for power quality maintenance, but now the primary focus is on the

distribution system, which is highly susceptible to electrical breakdowns [7-9]. So that, power distributors have to ensure that the quality of power supplied to the customer have met the operational norms and national standards or not [10].

Therefore, FACTS (Flexible AC Transmission System) controllers are utilized to improve the behavior of the power distribution system [11, 12]. These devices are employed to solve various PQ issues like harmonic distortion and transient stability [13, 14]. FACTS devices such as Static synchronous compensator (STATCOM), Static synchronous series compensator, unified power flow controller (UPFC), interline power flow controller (IPFC) are utilized to deliver high quality electricity. Custom power devices are FACTS devices that have been customized to be employed in electrical distribution systems. Therefore, unified power quality conditioner, active filter, DVR and distribution static synchronous compensator (DSTATCOM) are the commonly employed custom power devices. Such devices are utilized to solve power quality issues in power distribution network [15-18]. Among all custom power devices, DVR has attracted the researchers as it possesses quick response, smaller size and provides cost effective solutions. Therefore, in this work, DVR is utilized to compensate the voltage fluctuations by injecting the voltage in series with the supply from another feeder.

In steady state condition, the DVR has been operated in such a way that it does not receive or supply any real power. However, for any system, the DVR have to maintain minimum VA rating without reducing the compensation capability. To enhance the behavior of the DVR, a control scheme has been utilized [19]. The output generated by the DVR is controlled by the control signal generated by the proportional integral (PI) controller and the switching pulse generated by a Pulse-Width Modulated (PWM) generator. PI follows feedback control strategy and it produces the required control signal for the PWM generator using a weighted sum of error signal [20-23]. The non-linearity of semiconductor components present in the inverter leads to distortions in the output waveform. To solve this problem, a highly qualified power supply with an excellent LC filter unit is utilized [24]. However, the PI controller doesn't respond to the abrupt change in error signal, which is considered to be a serious drawback [25-27]. Therefore, a PI tuned Fuzzy Logic Controller (FLC) is utilized in this work. Here, an inference engine with a rule base of if-then rules is used to determine an output control signal.

In this proposed control scheme, a DVR is employed in this work in order to enhance the PQ in distribution systems. A PI tuned FLC is utilized to control the DVR's inverter. The rest of the work are explained such as modeling of DVR, PI controller and PI tuned FLC.

Proposed control scheme. The proposed block diagram comprises 3 phases AC supply, source inductance, PI tuned FLC, PWM generator, 3 phases Voltage Source Inverter (VSI) and non-linear load. The schematic representation of control scheme is shown in Fig. 1.

Recurrent Neural Network based reference current generation is utilized for effective harmonic elimination. 3 phases VSI for inverting the input DC voltage along

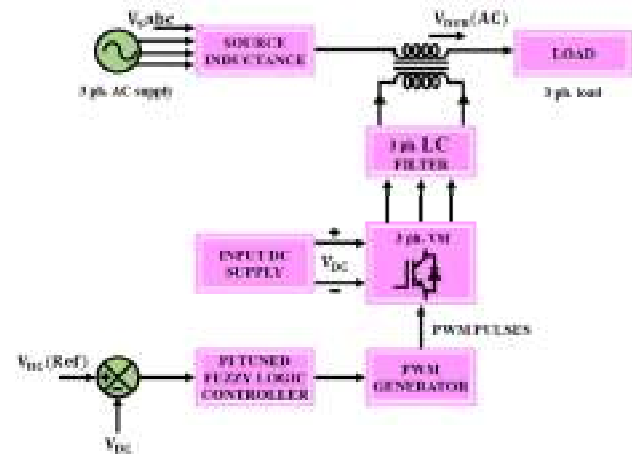with LC filter and AC grid is also employed in STATCOM applications.

Fig. 1. Schematic representation of control scheme

3 phases AC supply, which is given to the non-linear load, creates voltage oscillations in the distribution system. For reducing the voltage oscillations in the distribution system, the DVR is utilized in this proposed work, which provides sophisticated and cost-effective solution for PQ problems. DVR is a variable or controllable voltage source, which is linked in series with the point of common coupling and the load. DVR controls the active and reactive power, which helps to regulate the load voltage by injecting the suitable voltage during the voltage quality events. The capacitor will be discharged, in order to retain the DC-link voltage as constant. Here an external energy source is needed to deliver reactive power injection. To control the DVR's inverter, the gating pulses for VSI are generated with the aid of PI tuned FLC through which the VSI is controlled and so the reactive power compensation takes place.

Modeling of proposed system.

Dynamic Voltage Restorer (DVR). For sag voltage compensation a DVR is widely utilized equipment. The sensitive loads are linked in series to the DVR, which adds the required voltage when needed. It is a cost effective technique, which is used to compensate the voltage sag in small and big loads up to 45 MVA or even more. VSI, a voltage injection device, a filter, an energy storage device and a controlling device are the essential components of DVR. The structure of DVR is illustrated in Figure 2.
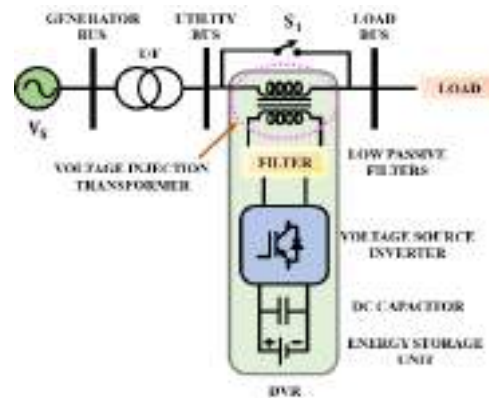

Fig. 2. Structure of DVR

Construction of DVR. The power and control circuits are the two components of DVR. The DVR system injects the control signal, which is made up of complex variables like magnitude, phase shift and the frequency. The switches are utilized in the power circuit in order to produce voltage-dependent control signals.

Energy Storage Unit. Superconducting magnetic energy storage, flywheels, super-capacitors and lead-acid batteries are the equipments, which are used to store energy. The storage unit's major duty is to deliver the required real power when the occurrence of voltage sags. The real power, which is generated by the energy storage device determines the DVR's compensating capability. Instead of employing other storage devices, lead batteries are chosen because they have a fast charging and discharging response time. The rate of discharge which is based on a chemical reaction that controls the amount of internal space available for energy storage.

Voltage Source Inverter. PWM VSI technique is commonly utilized. A DC voltage has been generated using an energy storage instrument. A VSI is utilized, to convert the voltage from DC-AC voltage. To boost the magnitude of voltage at the time of sag, DVR power circuit's step-up voltage injection transformer has been utilized. As a result, a minimal voltage with VSI is sufficient.

Passive Filters. In this technique, the inverted pulse waveform of PWM, which is transformed into a sinusoidal with the utilization of low passive filters. In order to accomplish this conversion in VSI, the higher harmonics are eliminated during the conversion of DC-AC, which also alters the compensated output voltage. Circuit layout of different filters in DVR are indicated in Fig. 3.
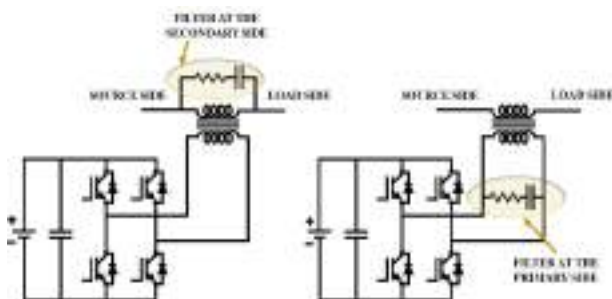
Fig. 3. Different filters in DVR

If the filters are placed on the inverter side, the harmonics are eliminated. The phase shift and voltage drop problems are occurs, when it is placed on the side of inverter. This issue can be resolved by placing the filter on the load side. Because a high valued transformer is required, the transformer's secondary side allows high harmonics currents.

By-Pass Switch. A DVR is equipment which linked in series. If a fault occurs in the downstream, the current flows through the inverter, which creates a fault current. A By-pass switch is utilized for inverter protection. A crowbar switch is commonly utilized to bypass the circuit of inverter. The crowbar identifies current scale, if the current is within the range of parts of inverter. If the current is too large, however, it will be possible to bypass the inverter's components.

Voltage Injection Transformers. The voltage injection transformer consists of two parts, such as primary and secondary side. The primary, which is linked in series with a distribution line and the secondary, which is linked to the DVR's power circuit. One 3 phases (3 ph.) or 1 phase (1 ph.) transformers are utilized for 3 ph. DVRs. However, only one 1 ph. transformer is utilized for 1 ph. DVRs. At the point of contact between three 1 ph. transformers and a 3 ph. DVR, a «Δ–Δ» type connection is employed.

The voltage level, which is delivered by the filtered output of VSI to a required level usually simulates the circuit of DVR from the setup transformer's transformation system. The pre-examined as well as significant values are winding ratios, which are determined by the needed voltage at the secondary side of voltage. The current on primary side with ratio of higher frequency affects the inverter circuit parts and the winding ratio's higher cost with higher frequency currents also affect the inverter circuit parts. When calculating the DVR's operating efficiency, the transformer value is a crucial factor. The upward distribution transformer, which is influenced by the transformer's winding ratio. As a result, the DVR rewards the arrangement of positive and negative segments.

PI controller. The effectiveness of the PI controller in controlling the steady state error as well as its simple instigation are the reasons for its widespread use. However, this controller has the drawback of not being able to increase the system's transient response. As indicated in Fig. 4, the PI controller's equation (1) has the control output which is given to the PWM generator is denoted as U, the proportional and integral gains, which are denoted as K_P and K_I, these gains are dependent on the system variables and the error signal is denoted as ε.

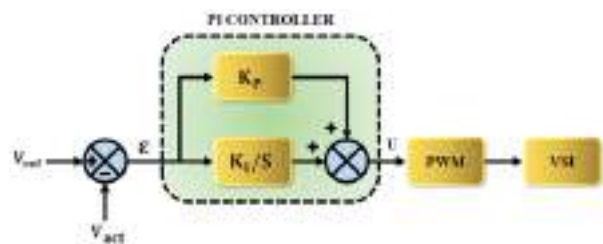$$U(t) = K_P \cdot \varepsilon(t) + K_I \cdot \int_0^t \varepsilon(t) dt . \qquad (1)$$

Fig. 4. Block diagram of PI controller

The PI controller creates a pole in the whole feedback loop, which causes the root locus to change. In terms of analysis, the pole causes a change in the response of control scheme. The end result is a decrease in steady state error. The constants K_P and K_I, on the other hand, control the system's stability and transient response in (2).

$$K_P \in [K_{P\min}, K_{P\max}] \quad \text{and} \quad K_I \in [K_{I\min}, K_{I\max}] . \qquad (2)$$

The minimum as well as maximum constants of PI are estimated in practice using experimentation and iterative methods. As a result, the expert's knowledge is required for the design of a PI controller. The control system becomes unstable if the constants of compensator exceed the permitted values. The tuning of instantaneous

parameter constants occurs after the domain of the PI constants has been determined. Depending on the error signal ε, the parameter constants has been adjusted. The constants K_P and K_I are varies to ensure that the system's steady state error is kept to a minimal, if not zero.

PI tuned fuzzy controller. The drawback of PI controller is that it is incapable of reacting to abrupt changes in the error signal ε since it determines only error signal's instantaneous value without taking into account the change in the error signal's the rise and fall, which is the error signal's derivative $\Delta\varepsilon$. To overcome this issue, a fuzzy based PI is utilized as it is indicated in Fig. 5. The control signal's output, which is determined by an inference engine with a rule base of if then rules, which is shown in equation (3):

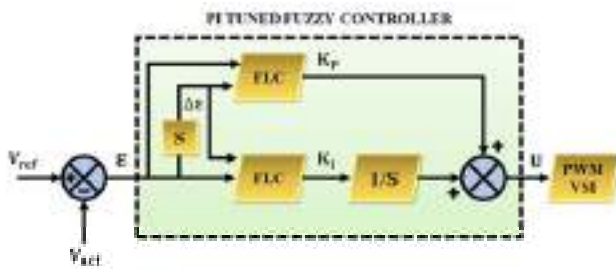$$\text{if } \varepsilon \text{ and } \Delta\varepsilon, \text{ then } K_P \text{ and } K_I. \qquad (3)$$

Fig. 5. Block diagram of PI tuned FLC

The constants K_P and K_I are changed by the rule base, which is based on the error signal ε and the change in error $\Delta\varepsilon$. Trial-and-error procedures are utilized to structure and determine the rule basis.

The fuzzy subsets of all the parameters for the inputs ε and $\Delta\varepsilon$ are specified as (*NB*, *NM*, *NS*, *Z*, *PS*, *PM*, *PB*). The fuzzy subsets employs a membership function of «Z»-shaped on the left, triangular shaped on the middle, as well as the «S»-shaped on the right are taken into consideration. The input membership function curves, which are represented in Fig. 6.
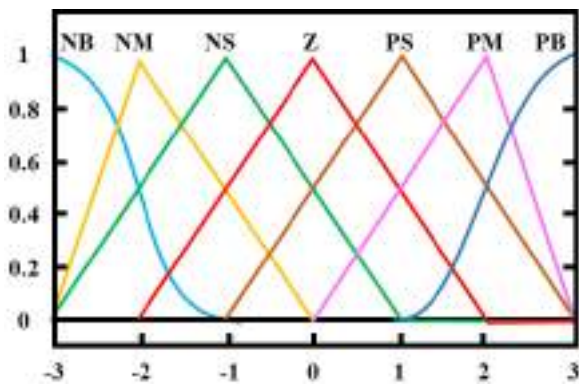

Fig. 6. Input membership function curve

The fuzzy subsets of output parameters K_P and K_I only have a membership function of triangular form, which is represented in Fig. 7. The fuzzy control rule, which is based on the modelling of long-term practical experience of operators, however, the rules were established by the repetitive simulation by means of a PI controller. The fuzzy control rules for the output parameters K_P and K_I are represented in Tables 1, 2.
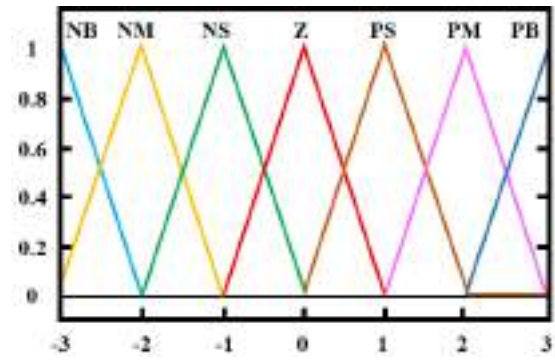

Fig. 7. Output membership function curve

Table 1

Fuzzy control rules for K_P

$\varepsilon/\Delta\varepsilon$	NB	NM	NS	Z	PS	PM	PB
NB	PB	PB	PM	PM	PS	PS	Z
NM	PB	PB	PM	PM	PS	Z	NS
NS	PM	PM	PM	PS	Z	NS	NM
Z	PM	PS	PS	Z	NS	NM	NM
PS	PS	PS	Z	NS	NS	NM	NM
PM	PS	Z	NS	NM	NM	NM	NB
PB	Z	NS	NS	NM	NM	NB	NB

Table 2

Fuzzy control rules for K_I

$\varepsilon/\Delta\varepsilon$	NB	NM	NS	Z	PS	PM	PB
NB	NB	NB	NB	NM	NM	NS	Z
NM	NB	NB	NM	NM	NS	Z	PS
NS	NM	NM	NS	NS	Z	PS	PS
Z	NM	NS	NS	Z	PS	PS	PM
PS	NS	NS	Z	PS	PS	PM	PM
PM	NS	Z	PS	PM	PM	PB	PB
PB	Z	NS	PS	NM	PB	PB	PB

Results and discussions. The behavior of proposed control scheme is simulated through MATLAB software. To rectify the PQ issues, a DVR is utilized in this work, which provides sophisticated and cost-effective solution for PQ issues. To control the DVR's inverter, a PI based FLC is utilized in order to generate the required injected voltage, through which the reactive power compensation takes place. The specifications, which are used for DVR is represented in Table 3.

Table 3

Specifications of DVR

Specifications	Values
Source voltage	415
Line resistance	0.1 Ω
Line inductance	0.5 mH
Turns ratio of series transformer	1:1
DC bus voltage	120 V
DC capacitor	220 μF
Filter	L_F = 3 mH, C_F = 1 μF
Line frequency	50 Hz
Switching frequency	10 kHz

The waveforms of AC source voltage and current are illustrated in Fig. 8, 9 respectively. From the voltage waveform, it is noticed that the input source voltage of 415 V is retained as constant. When this input voltage of 415 V is fed to the non-linear load, the harmonics are occurred in the current waveform.
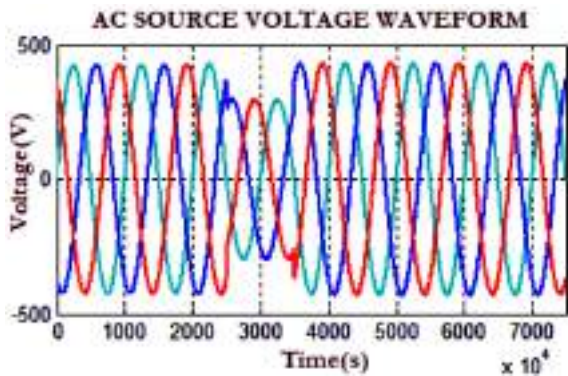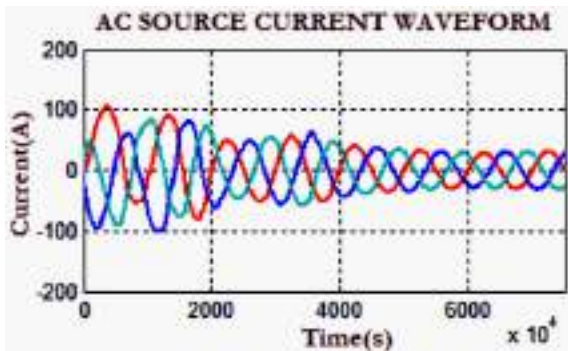
Fig. 8. AC source voltage waveform

Fig. 9. Waveform of AC source voltage

The waveforms of input AC source voltage and current using DVR are illustrated in Fig. 10. When the input voltage of 415 V is fed to the non-linear load, the harmonics are removed with the utilization of DVR. Thus, it is observed that the waveform becomes sinusoidal by using DVR.
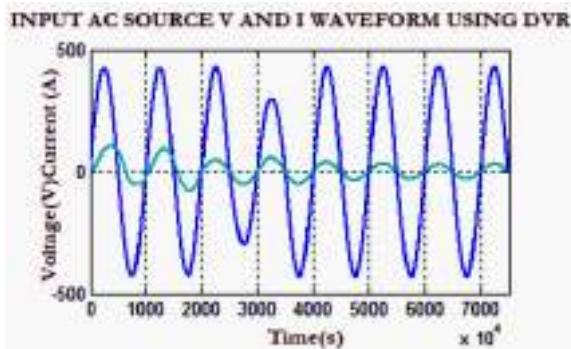

Fig. 10. Input AC source V and I waveform using DVR

The waveforms of reference and actual voltages of DVR are illustrated in Fig. 11, 12 respectively. The actual and reference voltages are analogized with the aid of PI tuned FLC, through which the gating pulses are generated to control the inverter of DVR.
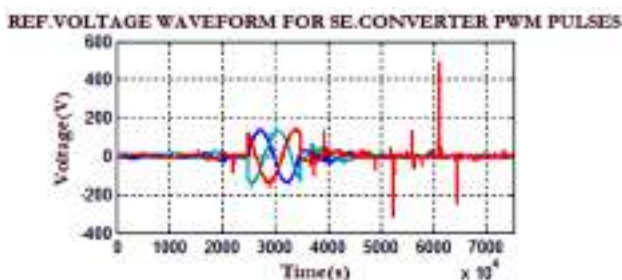

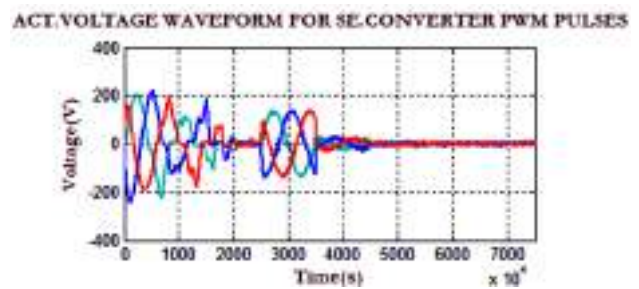Fig.11. Reference voltage waveform of DVR

Fig. 12. Actual voltage waveform of DVR

The DC-link voltage waveform is represented in Fig. 13. When the DVR is controlled, the DC-link voltage of 900 V is attained. The occurrence of voltage fluctuations in the initial stage is eliminated and retained as constant after the time of 0.7 s.
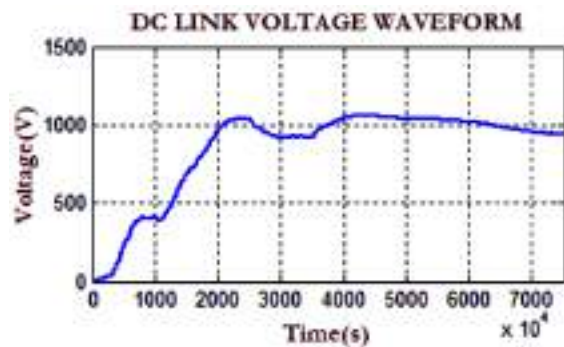

Fig. 13. DC-link voltage waveform

The waveforms of load voltage and current using DVR are illustrated in Fig. 14, 15 respectively. The occurrence of fluctuations in the load voltage and current are minimized after the time 0.2 s with the utilization of DVR. With the assistance of PI tuned FLC, the inverter in the DVR is controlled. Thus the voltage and current become sinusoidal in nature.
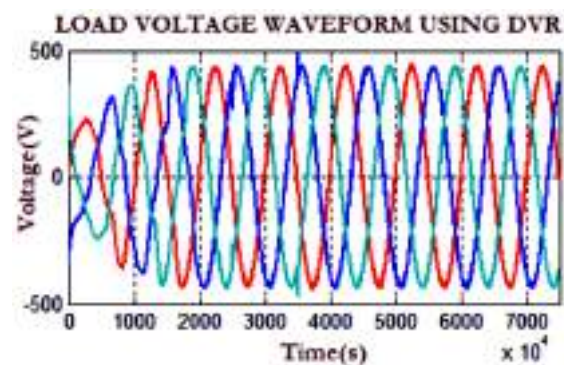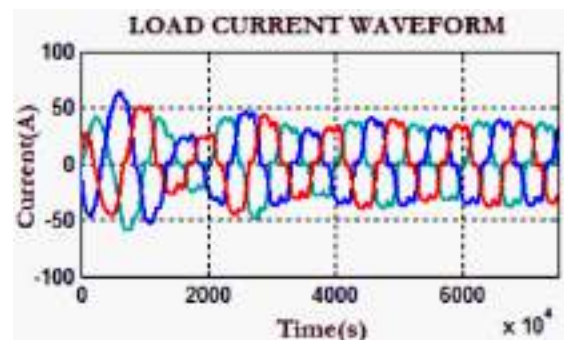

Fig. 14. Waveform of load voltage using DVR

Fig. 15. Waveform of load current using DVR

The waveforms of real and reactive power are illustrated in Fig. 16, 17 respectively. The waveforms have shown that the reactive power compensation is achieved after the time of 0.5 s with the aid of DVR by minimizing the power quality issues.
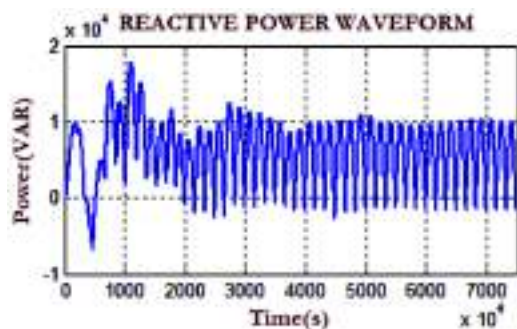

Fig. 16. Waveform of real power

Fig. 17. Waveform of reactive power

The waveform of power factor is illustrated in Fig. 18. When supplying the input voltage to the non-linear loads, certain power quality issues are occur, which are overcome by implementing the DVR. Thus it assists in attaining the UPF through the reactive power compensation. From this waveform, it is noted that the UPF is attained after the time 0.3 s.
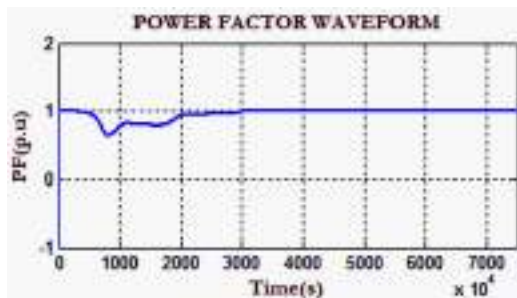

Fig. 18. Waveform of power factor

The waveform of total harmonic distortion (THD) with the utilization of PI tuned FLC is illustrated in Fig. 19. From the above graph, it is noted that the THD of 4.1 % is attained for the PI tuned FLC.
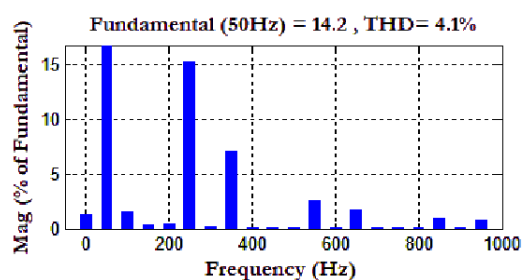

Fig. 19. Waveform of THD

The comparative analysis of THD is illustrated in Fig. 20. The THD of PI tuned FLC is which is comparatively better than the THD values 4.1 %, of FLC and PI. Thus, it is observed that the PI tuned FLC gives better performance than the FLC and PI controllers in the minimization of THD.
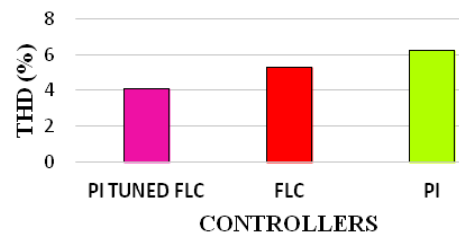

Fig. 20. Comparative analysis of THD

Conclusions.

This paper describes the control strategy of DVR which offers a self-sufficient solution for tackling several issues of power quality. It provides solution for different PQ issues like voltage sag/swell compensation and harmonics. The proposed DVR maintains the significant features and eliminates the complexity by using PI tuned FLC. It generates compensating voltages for the control of DVR and handles the error signal resulted due to system disturbances. The entire work is validated through MATLAB simulation. Thus, the proposed method has delivered improved performance in reducing the PQ issues with the minimum THD of 4.1 %.

Conflict of interest. The authors declare that they have no conflicts of interest.

REFERENCES
1. Tu C., Guo Q., Jiang F., Wang H., Shuai Z. A Comprehensive Study to Mitigate Voltage Sags and Phase Jumps Using a Dynamic Voltage Restorer. *IEEE Journal of Emerging and Selected Topics in Power Electronics*, 2020, vol. 8, no. 2, pp. 1490-1502. doi: https://doi.org/10.1109/JESTPE.2019.2914308.
2. Khergade A.V., Satputaley R.J., Borghate V.B., Raghava B. Harmonics Reduction of Adjustable Speed Drive Using Transistor Clamped H-Bridge Inverter Based DVR With Enhanced Capacitor Voltage Balancing. *IEEE Transactions on Industry Applications*, 2020, vol. 56, no. 6, pp. 6744-6755. doi: https://doi.org/10.1109/TIA.2020.3013823.
3. Alkahtani A.A., Alfalahi S.T.Y., Athamneh A.A., Al-Shetwi A.Q., Mansor M. Bin, Hannan M.A., Agelidis V.G. Power Quality in Microgrids Including Supraharmonics: Issues, Standards, and Mitigations. *IEEE Access*, 2020, vol. 8, pp. 127104-127122. doi: https://doi.org/10.1109/ACCESS.2020.3008042.
4. Li P., Xie L., Han J., Pang S., Li P. New Decentralized Control Scheme for a Dynamic Voltage Restorer Based on the Elliptical Trajectory Compensation. *IEEE Transactions on Industrial Electronics*, 2017, vol. 64, no. 8, pp. 6484-6495. doi: https://doi.org/10.1109/TIE.2017.2682785.
5. Elphick S., Ciufo P., Drury G., Smith V., Perera S., Gosbell V. Large Scale Proactive Power-Quality Monitoring: An Example From Australia. *IEEE Transactions on Power Delivery*, 2017, vol. 32, no. 2, pp. 881-889. doi: https://doi.org/10.1109/TPWRD.2016.2562680.
6. Yaghoobi J., Abdullah A., Kumar D., Zare F., Soltani H. Power Quality Issues of Distorted and Weak Distribution Networks in Mining Industry: A Review. *IEEE Access*, 2019, vol. 7, pp. 162500-162518. doi: https://doi.org/10.1109/ACCESS.2019.2950911.
7. Islam F.R., Prakash K., Mamun K.A., Lallu A., Pota H.R. Aromatic Network: A Novel Structure for Power Distribution

System. *IEEE Access*, 2017, vol. 5, pp. 25236-25257. doi: https://doi.org/10.1109/ACCESS.2017.2767037.

8. Roy N.K., Pota H.R. Current Status and Issues of Concern for the Integration of Distributed Generation Into Electricity Networks. *IEEE Systems Journal*, 2015, vol. 9, no. 3, pp. 933-944. doi: https://doi.org/10.1109/JSYST.2014.2305282.

9. Antoniadou-Plytaria K.E., Kouveliotis-Lysikatos I.N., Georgilakis P.S., Hatziargyriou N.D. Distributed and Decentralized Voltage Control of Smart Distribution Networks: Models, Methods, and Future Research. *IEEE Transactions on Smart Grid*, 2017, vol. 8, no. 6, pp. 2999-3008. doi: https://doi.org/10.1109/TSG.2017.2679238.

10. Elphick S., Gosbell V., Smith V., Perera S., Ciufo P., Drury G. Methods for Harmonic Analysis and Reporting in Future Grid Applications. *IEEE Transactions on Power Delivery*, 2017, vol. 32, no. 2, pp. 989-995. doi: https://doi.org/10.1109/TPWRD.2016.2586963.

11. Bone G., Pantos M., Mihalic R. Newtonian Steady State Modeling of FACTS Devices Using Unaltered Power-Flow Routines. *IEEE Transactions on Power Systems*, 2019, vol. 34, no. 2, pp. 1216-1226. doi: https://doi.org/10.1109/TPWRS.2018.2876407.

12. El-Azab M., Omran W.A., Mekhamer S.F., Talaat H.E.A. Allocation of FACTS Devices Using a Probabilistic Multi-Objective Approach Incorporating Various Sources of Uncertainty and Dynamic Line Rating. *IEEE Access*, 2020, vol. 8, pp. 167647-167664. doi: https://doi.org/10.1109/ACCESS.2020.3023744.

13. Eladany M.M., Eldesouky A.A., Sallam A.A. Power System Transient Stability: An Algorithm for Assessment and Enhancement Based on Catastrophe Theory and FACTS Devices. *IEEE Access*, 2018, vol. 6, pp. 26424-26437. doi: https://doi.org/10.1109/ACCESS.2018.2834906.

14. Frolov V., Thakurta P.G., Backhaus S., Bialek J., Chertkov M. Operations- and Uncertainty-Aware Installation of FACTS Devices in a Large Transmission System. *IEEE Transactions on Control of Network Systems*, 2019, vol. 6, no. 3, pp. 961-970. doi: https://doi.org/10.1109/TCNS.2019.2899104.

15. Gandoman F.H., Ahmadi A., Sharaf A.M., Siano P., Pou J., Hredzak B., Agelidis V.G. Review of FACTS technologies and applications for power quality in smart grids with renewable energy systems. *Renewable and Sustainable Energy Reviews*, 2018, vol. 82, pp. 502-514. doi: https://doi.org/10.1016/j.rser.2017.09.062.

16. Chawda G.S., Shaik A.G., Mahela O.P., Padmanaban S., Holm-Nielsen J.B. Comprehensive Review of Distributed FACTS Control Algorithms for Power Quality Enhancement in Utility Grid With Renewable Energy Penetration. *IEEE Access*, 2020, vol. 8, pp. 107614-107634. doi: https://doi.org/10.1109/ACCESS.2020.3000931.

17. Molla E.M., Kuo C.-C. Voltage Sag Enhancement of Grid Connected Hybrid PV-Wind Power System Using Battery and SMES Based Dynamic Voltage Restorer. *IEEE Access*, 2020, vol. 8, pp. 130003-130013. doi: https://doi.org/10.1109/ACCESS.2020.3009420.

18. Ashok Kumar L., Indragandhi V. Power quality improvement of grid-connected wind energy system using facts devices. *International Journal of Ambient Energy*, 2020, vol. 41, no. 6, pp. 631-640. doi: https://doi.org/10.1080/01430750.2018.1484801.

19. Elmetwaly A.H., Eldesouky A.A., Sallam A.A. An Adaptive D-FACTS for Power Quality Enhancement in an Isolated Microgrid. *IEEE Access*, 2020, vol. 8, pp. 57923-57942. doi: https://doi.org/10.1109/ACCESS.2020.2981444.

20. Mosaad M.I., Abed El-Raouf M.O., Al-Ahmar M.A., Bendary F.M. (). Optimal PI controller of DVR to enhance the performance of hybrid power system feeding a remote area in Egypt. *Sustainable Cities and Society*, 2019, vol. 47, p. 101469. doi: https://doi.org/10.1016/j.scs.2019.101469.

21. Ganthia B.P., Mohanty S., Rana P.K., Sahu P.K. Compensation of voltage sag using DVR with PI controller. *2016 International Conference on Electrical, Electronics, and Optimization Techniques (ICEEOT)*, 2016, pp. 2138-2142. doi: https://doi.org/10.1109/ICEEOT.2016.7755068.

22. Thaha H.S., Ruban Deva Prakash T. Reduction of power quality issues in micro-grid using GA tuned PI controller based DVR. *International Journal of Innovative Technology and Exploring Engineering*, 2019, vol. 8, no. 10, pp. 4166-4172. doi: https://doi.org/10.35940/ijitee.J1050.0881019.

23. Babu V., Ahmed K.S., Shuaib Y.M., Mani M. A novel intrinsic space vector transformation based solar fed dynamic voltage restorer for power quality improvement in distribution system. *Journal of Ambient Intelligence and Humanized Computing*. 2021. doi: https://doi.org/10.1007/s12652-020-02831-0.

24. Babu V., Ahmed K.S., Shuaib Y.M., Manikandan M., Basha S.S. Voltage sag/swell compensation using solar photovoltaic inverter based dynamic voltage restorer (SPVI-DVR). *Journal of Green Engineering*, 2020, vol. 10, no. 9, pp. 7102-7114.

25. Babu V., Basha S.S., Shuaib Y.M., Manikandan M., Enayathali S.S. A Novel Integration of Solar Fed Dynamic Voltage Restorer for Compensating Sag and Swell Voltage in Distribution System Using Enhanced Space Vector Pulse Width Modulation (ESVPWM). *Universal Journal of Electrical and Electronic Engineering*, 2019, vol. 6, no. 5, pp. 329-350. doi: https://doi.org/10.13189/ujeee.2019.060504.

26. Manikandan M., Basha A.M. ODFF: Optimized Dual Fuzzy Flow Controller Based Voltage Sag Compensation for SMES-Based DVR in Power Quality Applications. *Circuits and Systems*, 2016, vol. 7, no. 10, pp. 2959-2974. doi: https://doi.org/10.4236/cs.2016.710254.

27. Manikandan M., Basha A.M. Voltage Sag Compensation using DVR based Superconducting Magnetic Energy Storage Coil with Pi Controller. *Asian Journal of Research in Social Sciences and Humanities*, 2016, vol. 6, no. 10, pp. 152-161. doi: https://doi.org/10.5958/2249-7315.2016.01004.2.

Sanepalle Gopal Reddy[1], *PhD, Research Scholar,*
Somaskandan Ganapathy[1], *Dr.,*
Mani Manikandan[2], *Professor,*
[1] Annamalai University,
Chidambaram, Tamil Nadu, 608002, India,
e-mail: sanepalle.gopal1980@gmail.com,
ganapathy1967@gmail.com
[2] Jyothishmathi Institute of Technology and Science,
Karimnagar, Telangana, 505481, India,
e-mail: cm.manikandan@gmail.com (Corresponding author)

O. Oualah, D. Kerdoun, A. Boumassata

Comparative study between sliding mode control and the vector control of a brushless doubly fed reluctance generator based on wind energy conversion systems

Introduction. *Nowadays, global investment in renewable energy sources has been growing intensely. In particular, we mention here that wind source of energy has grown recently.* ***Purpose.*** *Comparative study between sliding mode control and vector control of a brushless doubly fed reluctance generator based on wind energy conversion systems.* ***Methods.*** *This paper deals with conceptual analysis and comparative study of two control techniques of a promising low-cost brushless doubly-fed reluctance generator for variable-speed wind turbine considering maximum power point tracking. This machine's growing interest because of the partially rated power electronics and the high reliability of the brushless design while offering performance competitive to its famous spring counterpart, the doubly-fed induction generator. We are particularly interested in comparing two kinds of control methods. We indicate here the direct vector control based on Proportional-Integral controller and sliding mode controller.* ***Results.*** *Simulation results show the optimized performances of the vector control strategy based on a sliding mode controller. We observe high performances in terms of response time and reference tracking without overshoots through the response characteristics. The decoupling, the stability, and the convergence towards the equilibrium are assured.* References 29, figures 10.*
Key words: **wind energy, brushless doubly fed reluctance generator, vector control, sliding mode controller, maximum power point tracking.**

Вступ. Нині глобальні інвестиції у відновлювані джерела енергії стрімко зростають. Зокрема, звернемо увагу, що останнім часом має місце зростання вітряних джерел енергії. Мета. Порівняльне дослідження між управлінням ковзним режимом та векторним управлінням безщіткового реактивного генератора з подвійним живленням на основі систем перетворення енергії вітру. Методи. Стаття присвячена концептуальному аналізу та порівняльному дослідженню двох методів управління перспективним недорогим безщітковим реактивним генератором з подвійним живленням для вітряної турбіни зі змінною швидкістю з урахуванням відстеження точки максимальної потужності. Інтерес до цієї машини зростає частково завдяки силовій електроніці, а також високій надійності безщіткової конструкції, яка при цьому пропонує характеристики, порівняні з його загальновідомим пружинним аналогом, індукційним генератором з подвійним живленням. Автори особливо зацікавлені у порівнянні двох видів методів управління. Автори вказують тут на пряме векторне управління на основі пропорційно-інтегрального регулятора та регулятора ковзного режиму. Результати. Результати моделювання показують оптимізовані характеристики векторної стратегії управління на основі контролера ковзного режиму. Спостерігаються високі показники з точки зору часу відгуку та відстеження еталонних значень без перевищення показників відгуку. Розв'язка, стабільність та прагнення до рівноваги гарантуються. Бібл. 29, рис. 10.
Ключові слова: **енергія вітру, безщітковий реактивний генератор з подвійним живленням, векторне управління, регулятор ковзного режиму, відстеження точки максимальної потужності.**

1. Introduction. The earth climate can be seriously influenced by increasing green house gas emissions from conventional energy sources (such as oil and coal) as well as the growing concern of depletion of these resources in the near future [1].Wind turbine is one way to generate electricity from renewable sources, mainly because it is clean and economically viable [2]. At the same time, there has been a rapid development of related wind turbine [3].

The wind turbine is a very effective component in wind energy conversion systems (WECS) that converts the wind kinetic energy into mechanical energy that can be used to derive an electrical generator. The wind turbine generator converts the output mechanical energy of the wind turbine into electric power [4]. It can be connected either to stand-alone loads or connected to the utility grid [5].

Wind turbine generators used in wind energy conversion systems can be classified into two types: fixed speed wind turbine (FSWT) and variable speed wind turbine (VSWT). For the first one, the generator is connected directly to the grid without any intermediate of power electronic converters (PECs), and for the other one, the generator is connected through PECs [6–8]. Their findings show that the VSWT provides better energy capture over the FSWT because it can quickly adapt to a wide range of wind speed variations [9]. For this reason, the model considered in this research is the VSWT coupled to a Brushless Doubly Fed Reluctance Generator (BDFRG).

The brushless doubly-fed generator (BDFG) is a prominent economical solution to reliability and maintenance problems of brushes and slip-rings with the traditional doubly-fed induction generator (DFIG) in WECS [10, 11]. The BDFRG merits have inspired the research on its design, control, and grid integration aspects targeting WECS as one of the leading applications [12]. The strengths of this design include simple infrastructure, economical, reliable high efficiency, and robust power factor control capability [13]. Due to its high reliability these machines are also adaptable in air craft industry but some of design challenges include harsh aerodynamic and complex rotor design [14]. The background and fundamental structure of the Brushless Doubly Fed Reluctance Motor (BDFRM) was described in [15].

Control research [16], similar in context to that conducted on the BDFIG [17], and DFIG [18], has been carried out on the BDFRM(G) involving: scalar control, voltage vector-oriented control (VC) [19], direct torque and flux control (DTC) [20], torque, and reactive power control (TQC) [21, 22], direct power control (DPC) [23], sliding-mode power control [24], and even nonlinear multiple-input-multiple-output control [3]. Recently, sliding mode control (SMC) was integrated largely in the command of nonlinear systems [25].

The variable structure control possesses this robustness using the sliding mode controller. It offers

excellent performances compared to unmodelled dynamics [26], insensitivity to parameter variation, external disturbance rejection, and fast dynamic [27].

The proposed system comprises a wind turbine, a BDFRG, an inverter, and a vector control based on PI controller and sliding mode controller.

This paper is organized as follows. A description of the studied WECS is presented in section 2. In section 3 the modeling of the wind turbine and the control of the maximum power point tracking (MPPT) are provided. Then, the BDFRG is modeled in Section 4. The vector control of BDFRG is given in Section 5. The sliding mode control is described in Section 6. The sliding mode control of the BDFRG is given in Section 7. Finally, simulation results and interpretations are presented in Section 8.

2. Description of the studied WECS. The WECS adopted here is shown in Fig. 1. The proposed system is constituted of a wind turbine, BDFRG, inverter, and power control. The BDFRG has two stator windings of different pole numbers. Generally, different applied frequencies (Fig. 1): the primary (power) winding is grid-connected, and the secondary (control) winding is converter fed. The performance of the proposed system has been tested to prove the MPPT control. The independent control of grid active and reactive powers using stator flux oriented control technique is used to test the ability to operate in two quadrant modes (sub-synchronous and super-synchronous modes).
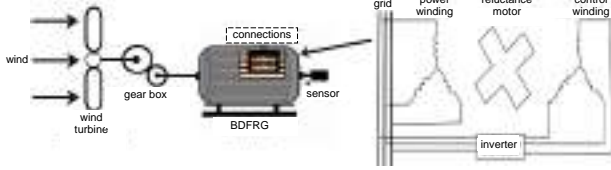

Fig. 1. Conceptual diagram of the BDFRG-based WECS

3. Modeling of the wind turbine. The mechanical power extracted by the turbine from the wind is defined as:

$$P_t = \frac{1}{2} \cdot \rho \cdot A \cdot C_p \cdot V^3, \tag{1}$$

where ρ is the air density; $A = \pi \cdot R^2$ is the rotor swept area; R is the turbine radius; C_p is the power coefficient; V is the wind speed.

The power coefficient C_p represents the aerodynamic efficiency of the wind turbine. It depends on the tip speed ratio λ and the pitch angle β (Fig. 2, 3). The tip speed ratio is given as:

$$\lambda = \frac{\Omega_t \cdot R}{V}, \tag{2}$$

where Ω_t is the turbine speed.

For our example, the power coefficient C_p is given by the following equations

$$C_p(\lambda, \beta) = 0.5176 \cdot \left(\frac{116}{\lambda_x} - 0.4 \cdot \beta - 5 \right) \cdot e^{-\frac{21}{\lambda_x}} + 0.0068 \cdot \lambda, \tag{3}$$

where

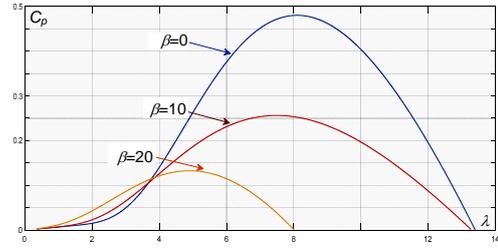$$\frac{1}{\lambda_x} = \frac{1}{\lambda + 0.08 \cdot \beta} - \frac{0.035}{\beta^3 + 1}. \tag{4}$$

Fig. 2. Characteristics of the wind turbine power coefficient C_p with the tip speed ratio λ at different values of the blade pitch angle β
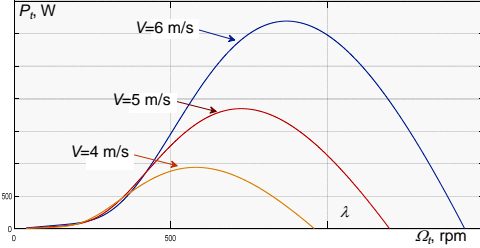

Fig. 3. Power speed characteristics for different wind speeds

The maximum value of C_p ($C_{p\ max} = 0.48$) is for $\beta = 0$ degree and for $\lambda = 8.1$. The turbine torque T_t can be written as:

$$T_t = P_t / \Omega_t. \tag{5}$$

The mechanical speed of the generator Ω_m and the torque of the turbine referred to the generator T_m are given by:

$$\begin{cases} \Omega_m = \Omega_t \cdot G; \\ T_m = T_t / G, \end{cases} \tag{6}$$

where G is the gearbox ratio.

The mechanical equation of the system can be characterized by:

$$J \cdot \frac{d\Omega_m}{dt} = T_m - T_e - f \cdot \Omega_m, \tag{7}$$

where J is the equivalent total inertia of the generator shaft; f is the equivalent total friction coefficient; T_e is the electromagnetic torque.

To extract the maximum power from the wind turbine the electromagnetic torque command of the BDFRG $T_{e\text{-}ref}$ should be determined at the optimal value of the tip speed ratio and the corresponding maximum value of wind turbine power coefficient.

4. Mathematical model of BDFRG. The electrical equations of the BDFRG in the (d–q) Park reference frame are given by:

$$\begin{cases} U_{pd} = R_p \cdot I_{pd} + \dfrac{d\Phi_{pd}}{dt} - \omega_p \cdot \psi_{pq}; \\[2mm] U_{pq} = R_p \cdot I_{pq} + \dfrac{d\Phi_{pq}}{dt} + \omega \cdot \psi_{pd}; \\[2mm] U_{sd} = R_s \cdot I_{sd} + \dfrac{d\Phi_{sd}}{dt} - (\omega_r - \omega) \cdot \psi_{sq}; \\[2mm] U_{sq} = R_s \cdot I_{sq} + \dfrac{d\Phi_{sq}}{dt} + (\omega_r - \omega) \cdot \psi_{sd}, \end{cases} \tag{8}$$

$$\begin{cases} \psi_{pd} = L_p \cdot I_{pd} + L_m \cdot I_{sd}; \\ \psi_{pq} = L_p \cdot I_{pq} - L_m \cdot I_{sq}; \\ \psi_{sd} = L_s \cdot I_{sd} + L_m \cdot I_{pd}; \\ \psi_{sq} = L_s \cdot I_{sq} - L_m \cdot I_{pq}. \end{cases} \tag{9}$$

The electromagnetic torque is expressed as:

$$T_e = \frac{3 \cdot P_r \cdot L_m}{2 \cdot L_p} \cdot \left(\psi_{pd} \cdot I_{sq} + \psi_{pq} \cdot I_{sd} \right). \quad (10)$$

The active and reactive powers equations at the primary stator, the secondary stator, and the grid are written as, respectively:

$$\begin{cases} P_p = \frac{3}{2} \cdot \left(U_{pd} \cdot I_{pd} + U_{pq} \cdot I_{pq} \right); \\ Q_p = \frac{3}{2} \cdot \left(U_{pq} \cdot I_{pd} - U_{pd} \cdot I_{pq} \right); \end{cases} \quad (11)$$

$$\begin{cases} P_s = \frac{3}{2} \cdot \left(U_{sd} \cdot I_{sd} + U_{sq} \cdot I_{sq} \right); \\ Q_s = \frac{3}{2} \cdot \left(U_{sq} \cdot I_{sd} - U_{sd} \cdot I_{sq} \right); \end{cases} \quad (12)$$

$$\begin{cases} P_g = P_p + P_s; \\ Q_g = Q_p + Q_s; \end{cases} \quad (13)$$

where U_p and U_s are power and control windings voltages in the dq axis, respectively; I_p and I_s are power and control windings currents in the dq axis, respectively; R_p and R_s are power and control windings resistances, respectively; L_p and L_s are leakage inductances of power and control windings, respectively; L_m is the mutual inductance between power and control windings; ω_p and ω_s are angular frequencies of the power and control windings, respectively; ω_r is the BDFRG mechanical rotor angular speed; ψ_p and ψ_s are power and control windings flux linkages in the dq axis, respectively.

5. Vector control of the BDFRG. In order to decouple the stator active and reactive powers, the primary stator flux vector will be aligned with d-axis φ_{pd} ($\varphi_{pd} = \varphi_p$ and $\varphi_{pq} = 0$), and the stator voltages will be expressed by:

$$\begin{cases} U_{pd} = 0; \\ U_{pq} = U_p = \omega_p \cdot \psi_p. \end{cases} \quad (14)$$

The expressions of the primary stator currents are written as:

$$\begin{cases} I_{pd} = \frac{\psi_{pd} - L_m \cdot I_{sd}}{L_p}; \\ I_{pq} = \frac{L_m \cdot I_{sq}}{L_p}. \end{cases} \quad (15)$$

By replacing these currents in the secondary stator fluxes equations, we obtain:

$$\begin{cases} \psi_{sd} = \sigma \cdot L_s \cdot I_{sd} + \frac{L_m}{L_p} \cdot \psi_{pd}; \\ \psi_{sq} = \sigma \cdot L_s \cdot I_{sq}. \end{cases} \quad (16)$$

where σ is the leakage coefficient defined by:

$$\sigma = 1 - \frac{L_m^2}{L_p \cdot L_s} \quad (17)$$

The secondary stator voltages can be written according to the secondary stator currents as:

$$\begin{cases} U_{sd} = R_s \cdot I_{sd} + L_s \cdot \sigma \cdot \dfrac{\mathrm{d}I_{sd}}{\mathrm{d}t} + e_q; \\ U_{sq} = R_s \cdot I_{sq} + L_s \cdot \sigma \cdot \dfrac{\mathrm{d}I_{sq}}{\mathrm{d}t} + e_d + e_\varphi, \end{cases} \quad (18)$$

where

$$\begin{cases} e_q = -\omega_s \cdot \sigma \cdot L_s \cdot I_{sq}; \\ e_d = \omega_s \cdot \sigma \cdot L_s \cdot I_{sd}; \\ e_\varphi = \omega_s \cdot \dfrac{L_m}{L_p} \cdot \psi_p. \end{cases} \quad (19)$$

The active and reactive stator powers of the BDFRG are expressed by:

$$\begin{cases} P_p = \dfrac{3}{2} \cdot \dfrac{U_{pq} \cdot L_m}{L_p} \cdot I_{sq}; \\ Q_p = \dfrac{3}{2} \cdot \dfrac{U_{pq}^2}{\omega_p \cdot L_p} - \dfrac{3}{2} \cdot U_{pq} \cdot \dfrac{L_m}{L_p} \cdot I_{sd}, \end{cases} \quad (20)$$

where s is the slip of the BDFRG.

The electromagnetic torque can be written as:

$$T_e = \frac{3 \cdot P_r \cdot L_m}{2 \cdot L_p} \cdot \psi_{pd} \cdot I_{sq}. \quad (21)$$
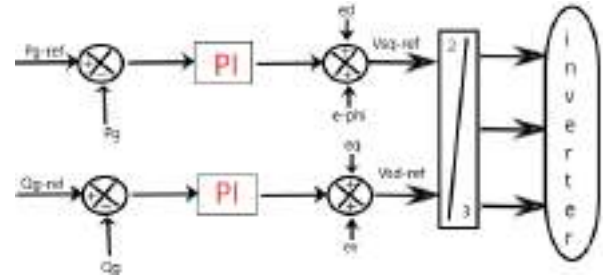

Fig. 4. Block diagram of power control

For relatively weak sleep values and by neglecting the voltage drops, the grid active and reactive powers are simplified into:

$$\begin{cases} P_g = \dfrac{3 \cdot (1-s) \cdot U_{pq} \cdot L_m}{2 \cdot L_p} \cdot I_{sq}; \\ Q_g = \dfrac{3}{2} \cdot \dfrac{U_{pq}^2}{\omega_p \cdot L_p} - \dfrac{3 \cdot (1-s)}{2} \cdot U_{pq} \cdot \dfrac{L_m}{L_p} \cdot I_{sd}. \end{cases} \quad (22)$$

From (22) we have:

$$\begin{cases} I_{sq} = \dfrac{2 \cdot L_p}{3 \cdot (1-s) \cdot U_{pq} \cdot L_m} \cdot P_g; \\ I_{sd} = \dfrac{\left(\dfrac{3 \cdot U_{pq}^2}{2 \cdot \omega_p \cdot L_p} - Q_g \right) \cdot 2 \cdot L_p}{3 \cdot (1-s) \cdot U_{pq} \cdot L_m}. \end{cases} \quad (23)$$

Substitute (23) in (18), we obtain:

$$\begin{cases} \dot{P}_g = \dfrac{U_{sq}}{A \cdot L_s \cdot \sigma} - \dfrac{R_s}{L_s \cdot \sigma} \cdot P_g - \dfrac{e_d}{A \cdot L_s \cdot \sigma} - \dfrac{e_\varphi}{A \cdot L_s \cdot \sigma}; \\ \dot{Q}_g = \dfrac{-U_{sd}}{A \cdot L_s \cdot \sigma} - \dfrac{R_s}{L_s \cdot \sigma} \cdot Q_g + \dfrac{e_q}{A \cdot L_s \cdot \sigma} + \dfrac{e_\upsilon}{A \cdot L_s \cdot \sigma}, \end{cases} \quad (24)$$

where

$$
\begin{cases}
A = \dfrac{2 \cdot L_p}{3 \cdot (1-s) \cdot U_{pq} \cdot L_m}; \\[4mm]
e_\upsilon = A \cdot R_s \cdot \dfrac{3 \cdot U_{pq}^2}{2 \cdot \omega_p \cdot L_p}.
\end{cases} \qquad (25)
$$

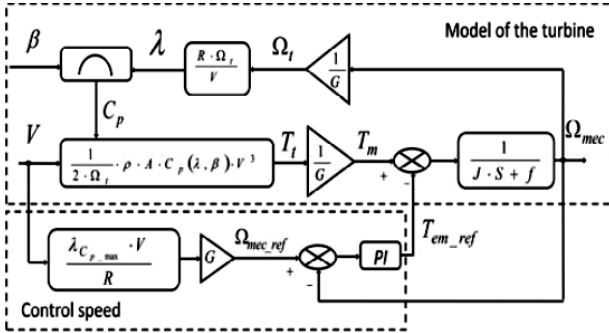In order to capture the optimal mechanical power, the control of the mechanical speed is applied (Fig. 5).

Fig. 5. MPPT with the control of the speed

The reference value of the active power exchanged between the wind generator and the grid is generated by MPPT control, and it's given by:

$$P_{g-ref} = T_{em-ref} \cdot \Omega_{mech}. \qquad (26)$$

The reference grid reactive power Q_{g-ref} is fixed to zero value to maintain the power factor at unity. The detailed scheme of the studied system is illustrated in Fig. 6.
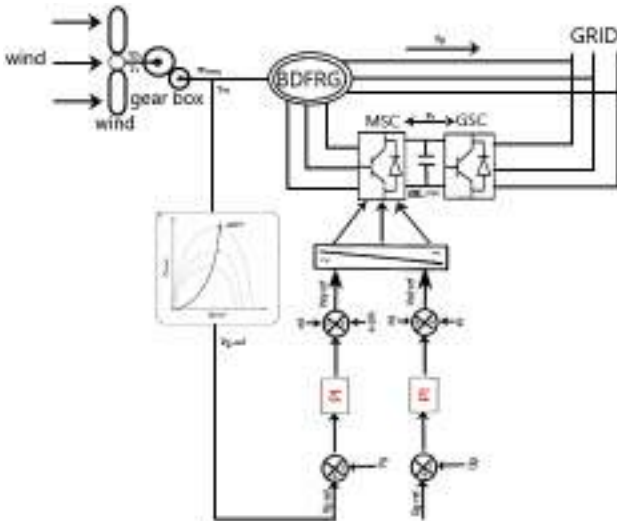

Fig. 6. The scheme of BDFRG using vector control

6. Sliding mode control. A Sliding Mode Controller (SMC) is a Variable Structure Controller (VSC) [28], which VSC includes several different continuous functions that can map plant state to a control surface, whereas switching among different functions is determined by plant state represented by a switching function [29]. The design of the control system will be demonstrated for the following nonlinear system:

$$\dot{X} = f(x,t) + B(x,t) \cdot u(x,t), \qquad (27)$$

where $X \in R^n$ is the state vector; $u \in R^m$ is the control vector; $f(x, t) \in R^n$; $B(x, t) \in R^{n \cdot m}$.

From the system (16), it possible to define a set S of the state trajectories X such as:

$$S = \{x(t) | \sigma(x,t) = 0\}, \qquad (28)$$

where

$$\sigma(x,t) = [\sigma_1(x,t), \sigma_2(x,t), ..., \sigma_m(x,t)]^T, \qquad (29)$$

where T denotes the transposed vector; S is called the sliding surface.

To bring the state variable to the sliding surfaces, the following two conditions have to be satisfied:

$$\sigma(x,t) = 0; \quad \dot{\sigma}(x,t) = 0. \qquad (30)$$

The control law satisfies the precedent conditions is presented in the following form:

$$
\begin{cases}
U = U_{eq} + U_n; \\
U_n = -K_f \cdot \text{sgn}(\sigma(x,t)),
\end{cases} \qquad (31)
$$

where U is the control vector; U_{eq} is the equivalent control vector; U_n is the switching part of the control (the correction factor); K_f is the controller gain.

U_{eq} can be obtained by considering the condition for the sliding regimen, $\sigma(x, t) = 0$. The equivalent control keeps the state variable on the sliding surface, once they reach it. For a defined function φ:

$$
\text{sgn}(\varphi) = \begin{cases}
1, & \text{if } \varphi > 0; \\
0, & \text{if } \varphi = 0; \\
-1, & \text{if } \varphi < 0.
\end{cases} \qquad (32)
$$

The controller described by (29) presents high robustness, insensitive to parameter fluctuations and disturbances. However, it will have high-frequency switching (chattering phenomena) near the sliding surface due to the (sgn) function involved. These drastic input changes can be avoided by introducing a boundary layer with width ξ. Thus replacing $\text{sgn}(\sigma(t))$ by saturation function $\text{sat}(\sigma(t)/\xi)$ in (29) we have

$$U = U_{eq} - K_f \cdot \text{sat}(\sigma(x,t)), \qquad (33)$$

where $\xi > 0$

$$
\text{sat}(\varphi) = \begin{cases}
\text{sgn}(\varphi), & \text{if } |\varphi| \geq 1; \\
\varphi, & \text{if } |\varphi| < 1.
\end{cases} \qquad (34)
$$

Consider a Lyapunov function:

$$V = \frac{1}{2} \cdot \sigma^2. \qquad (35)$$

From the Lyapunov theorem we know that if $\dot{V}$ is negative definite, the system trajectory will be driven and attracted toward the sliding surface and remain sliding on it until the origin is reached asymptotically:

$$\dot{V} = \frac{1}{2} \cdot \frac{d\sigma}{dt} = \dot{\sigma} \cdot \sigma \leq -\eta \cdot |\sigma|, \qquad (36)$$

where η is the constant positive value.

In this work we use the sliding surface proposed by J.J. Slotine

$$\sigma(x,t) = \left(\frac{d}{dt} + \gamma\right)^{n-1} \cdot e, \qquad (37)$$

where
$x = [x, x, x, ..., x^{n-1}]$ is the state vector;
$x^d = [x^d, x^d, x^d, ..., x^{d-1}]$ is the desired state vector;
$e = x^d - x = [e, e, e, ..., e^{n-1}]$ is the error vector;
γ is a positive coefficient; n is the system order [28].

In BDFRG control using sliding mode theory the surface is chosen as a function of the error between the reference input signal and the measured signals.

7. Sliding mode control of the BDFRG. The mathematical model of the grid active and reactive powers in (24) has two vector controls, so we define two switching surfaces, and we set $n = 1$. According to (37) the switching surfaces of the stator powers are given by:

$$\begin{cases} S(P_g) = e(P_g) = P_{g-ref} - P_g; \\ S(Q_g) = e(Q_g) = Q_{g-ref} - Q_g. \end{cases} \quad (38)$$

The second step consists of giving the structure of the vector control. One of the possible solutions is given by:

$$U_c = U_{eq} + U_n; \quad (39)$$

$$\begin{cases} U_{sq} = U_{sqeq} + U_{sqn}; \\ U_{sd} = U_{sdeq} + U_{sdn}, \end{cases} \quad (40)$$

where U_{eq} (U_{sqeq}, U_{sdeq}) and U_n (U_{sqn}, U_{sdn}) indicate the equivalent and discontinuous components of the control input vector U_c (U_{sq} and U_{sd}), respectively.

U_{eq} is calculated from $\dot{S}(x) = 0$

$$\dot{S}(x) = 0 \Rightarrow \begin{cases} \dot{S}(P_g) = \dot{P}_{g-ref} - \dot{P}_g = 0; \\ \dot{S}(Q_g) = \dot{Q}_{g-ref} - \dot{Q}_g = 0. \end{cases} \quad (41)$$

Substituting (24) in (41) we will have:

$$\begin{cases} \dot{P}_{g-ref} - \left(\dfrac{U_{sq}}{A \cdot L_s \cdot \sigma} - \dfrac{R_s}{L_s \cdot \sigma} \cdot P_g - \dfrac{e_d}{A \cdot L_s \cdot \sigma} - \dfrac{e_\varphi}{A \cdot L_s \cdot \sigma} \right) = 0; \\ \dot{Q}_{g-ref} - \left(\dfrac{-U_{sd}}{A \cdot L_s \cdot \sigma} - \dfrac{R_s}{L_s \cdot \sigma} \cdot Q_g + \dfrac{e_q}{A \cdot L_s \cdot \sigma} + \dfrac{e_\upsilon}{A \cdot L_s \cdot \sigma} \right) = 0. \end{cases} \quad (42)$$

Replaced U_{sq} and U_{sd} from (40) in (42) we obtain:

$$\begin{cases} \dot{P}_{g-ref} - \left(\dfrac{(U_{sqeq} + U_{sqn})}{A \cdot L_s \cdot \sigma} - \dfrac{R_s}{L_s \cdot \sigma} \cdot P_g - \dfrac{e_d}{A \cdot L_s \cdot \sigma} - \dfrac{e_\varphi}{A \cdot L_s \cdot \sigma} \right) = 0; \\ \dot{Q}_{g-ref} - \left(\dfrac{-(U_{sdeq} + U_{sdn})}{A \cdot L_s \cdot \sigma} - \dfrac{R_s}{L_s \cdot \sigma} \cdot Q_g + \dfrac{e_q}{A \cdot L_s \cdot \sigma} + \dfrac{e_\upsilon}{A \cdot L_s \cdot \sigma} \right) = 0. \end{cases} \quad (43)$$

In the permanent regime $U_n = 0$ ($U_{sqn} = 0$ and $U_{sdn} = 0$). Replaced them in (43) and we extract U_{sqeq} and U_{sdeq}:

$$\begin{cases} U_{sqeq} = A \cdot L_s \cdot \sigma \cdot \dot{P}_{g-ref} + A \cdot R_s \cdot P_g - (e_d - e_\varphi); \\ U_{sdeq} = -A \cdot L_s \cdot \sigma \cdot \dot{Q}_{g-ref} - A \cdot R_s \cdot Q_g + (e_q + e_\upsilon). \end{cases} \quad (44)$$

U_{sqn} and U_{sdn} are achieved by the condition:

$$S(x) \cdot \dot{S}(x) < 0 \Rightarrow S(P_g) \cdot \dot{S}(P_g) < 0 \text{ and } S(Q_g) \cdot \dot{S}(Q_g) < 0 \quad (45)$$

$$\begin{cases} \dfrac{-1}{A \cdot \sigma \cdot L_s} \cdot U_{sqn} \cdot S(P_g) < 0; \\ \dfrac{1}{A \cdot \sigma \cdot L_s} \cdot U_{sdn} \cdot S(Q_g) < 0. \end{cases} \quad (46)$$

A simple used form of U_n is a relay function:

$$U_n = -k \cdot \text{sgn}(S(x)); \quad (47)$$

$$\begin{cases} U_{sqn} = -k_1 \cdot \text{sgn}(S(P_g)); \\ U_{sdn} = -k_2 \cdot \text{sgn}(S(Q_g)), \end{cases} \quad (48)$$

where k (k_1, k_2) must be positive to satisfy the previous condition.

Substituting (44) and (48) into (40) we obtain the expressions of the reference rotor voltages such as:

$$\begin{cases} U_{rq} = A \cdot L_s \cdot \sigma \cdot \dot{P}_{g-ref} + A \cdot R_s \cdot P_g - (e_d - e_\varphi) - \\ - k_1 \cdot \text{sgn}(S(P_g)); \\ U_{rd} = -A \cdot L_s \cdot \sigma \cdot \dot{Q}_{g-ref} - A \cdot R_s \cdot Q_g + (e_q + e_\upsilon) - \\ - k_2 \cdot \text{sgn}(S(Q_g)). \end{cases} \quad (49)$$

The reference value of the active power exchanged between the wind generator and the grid is generated by MPPT control and it has given by (26). The reference grid reactive power Q_{g-ref} is fixed to zero value to maintain the power factor at unity. The detailed scheme of the studied system is illustrated in Fig. 7.
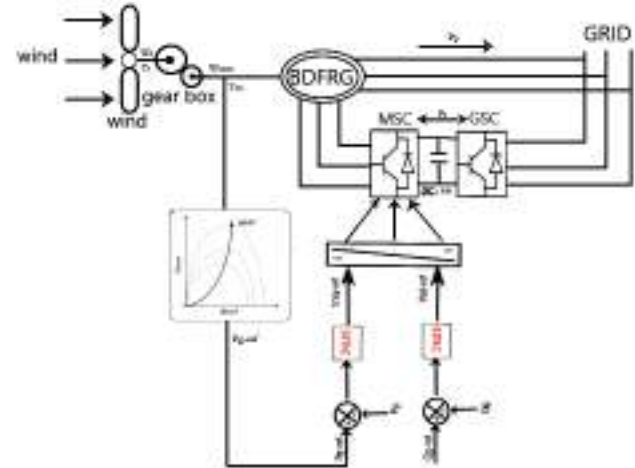

Fig. 7. The scheme of BDFRG using the sliding mode controller

8. Results and interpretations. The control technique suggested in this paper has been approved by the Matlab/Simulink software. The generator used in this simulation is 4.5 kW. This generator is connected directly to the grid through its primary stator and controlled through its secondary stator. Rated parameters are next [5]: $R_p = 3.781$ Ω, $R_s = 2.441$ Ω, $L_p = 0.41$ H, $L_s = 0.316$ H, $L_m = 0.3$ H, $J = 0.2$ kg·m^2, $P_r = 4$. Wind turbine parameters are next: blade radius $R = 4$ m, gearbox ratio $G = 7.5$, turbine inertia 1.5 kg·m^2, air density $\rho = 1.225$ kg/m^3 and number of blades is 3.

Figure 8 indicates the speed of the wind. The mechanical speed generated by the turbine is similar to the wind profile applied to the turbine. The reference value P_{g-ref} of the grid active power is determined by (26), and the reference of the reactive power is maintained at zero to guarantee unity power factor.
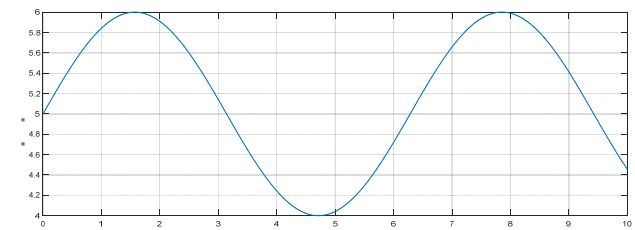

Fig. 8. Wind speed

Figures 9 demonstrate the performances of the vector control and SMC of the grid active and reactive powers used to a wind turbine mechanism structured from a BDFRG.
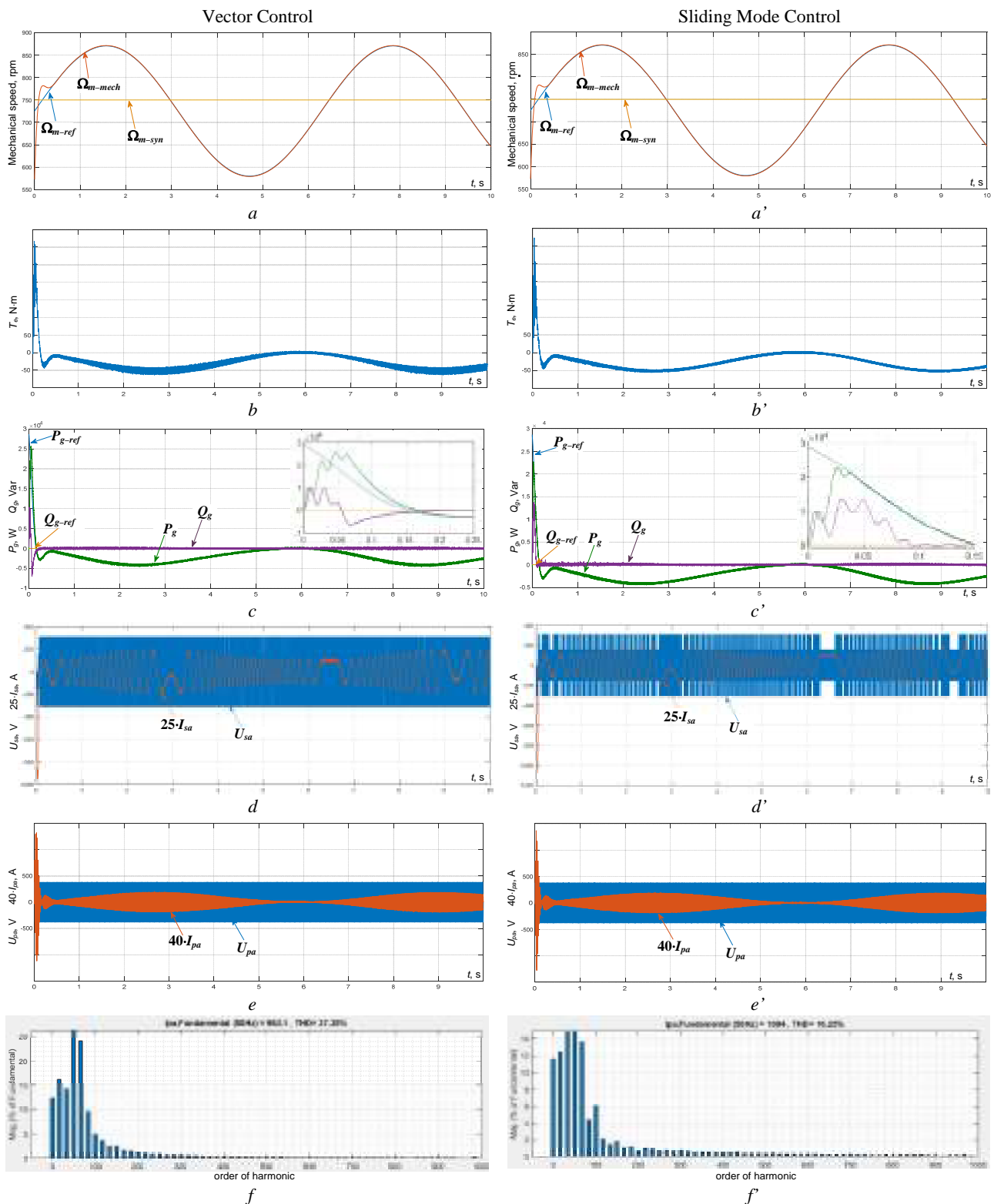
Fig. 9. Vector control and sliding mode control of the BDFRG:
a and *a'* – mechanical speed; *b* and *b'* – electromagnetic torque; *c* and *c'* – grid active and reactive power;
d and *d'* – secondary stator phase voltage and current; *e* and *e'* – primary stator phase voltage and current;
f and *f'* – total harmonic distortion of line current

Both control strategies approve an idealist decoupling between both elements of the BDFRG power (active and reactive). The outcomes found, without any doubt, demonstrate that the usage of the two commands can maintain the active and reactive powers to their aimed values. Figure 9 is the simulation results for active and reactive power response in using MPPT when the traditional PI controller (Fig. 9,*a–e*) and sliding mode control (Fig. 9,*a'–e'*) are applied. In this study, simulation results show clearly the improvement of active and reactive power demand obtained by applying sliding mode control in terms of time response and good reference tracking accuracy than those obtained using the traditional PI regulator. In the case of star-up, we notice

that the sliding mode controller transient responses of both active and reactive powers present no overshoot, whereas the steady-state error is close to zero.

Figures 9,*d*,*e* and Fig. 9,*d'*,*e'* present the winding currents in which we observe that both the frequency and the amplitude of these control currents (secondary currents I_s) change during the period of variation of active and reactive powers. On the other hand, the frequency of

the current of the supply winding (primary currents I_p) remains constant to be adapted to the supply frequency of the grid, so when the reference of the active power is changed, the amplitude of the current also is changed.

Robustness tests. Figure 10 represents a comparison between the two controllers robustness: PI and SMC with parametric variations L_p, L_s, R_s and L_m of –20 % and +20 % of their nominal values.
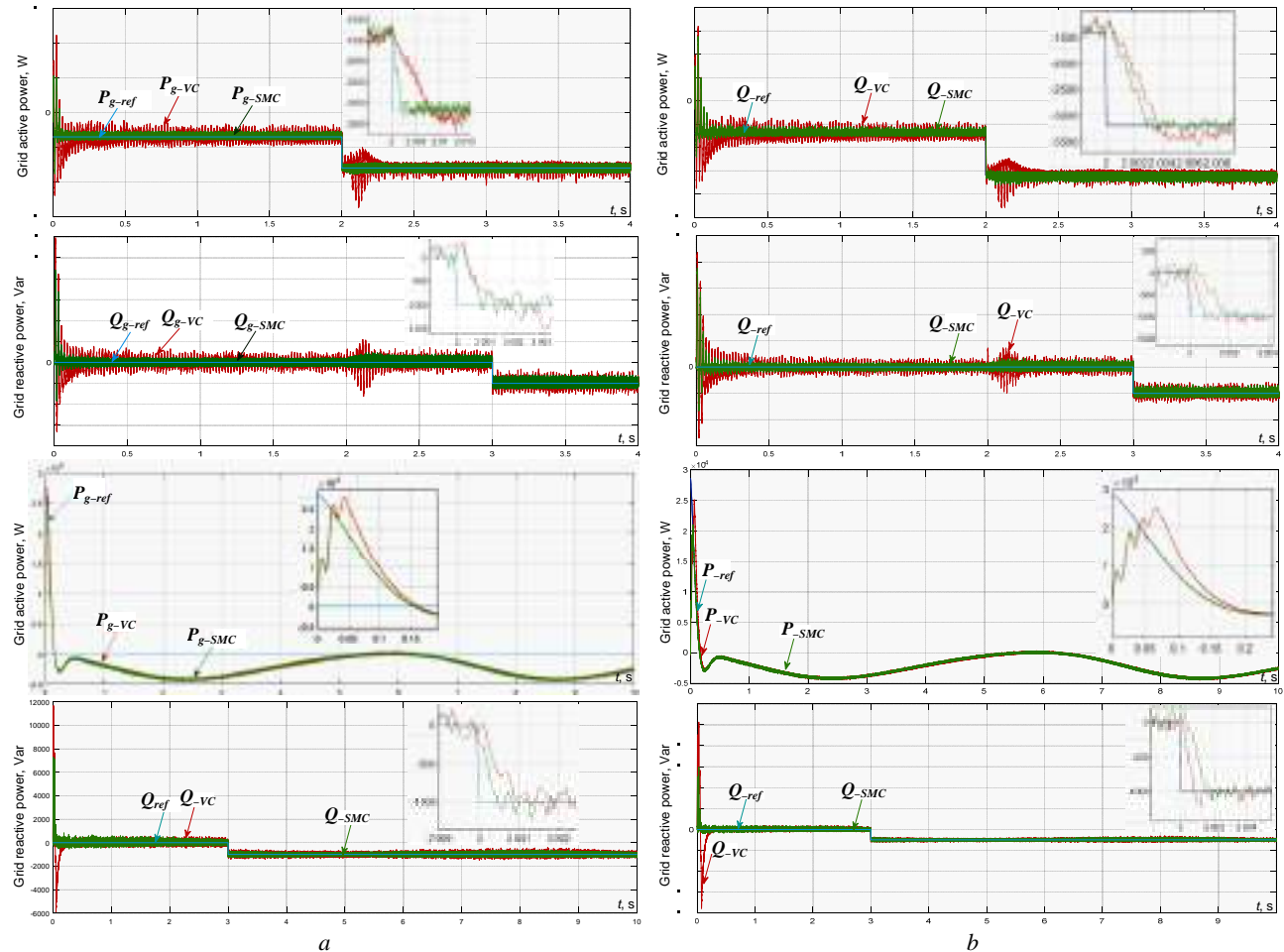

Fig. 10. Comparison of robustness between power control with PI and SMC of BDFRG
with parametric variations L_p, L_s, R_s and L_m of –20 % (*a*) and +20 % (*b*) of their nominal values

From the obtained results (Fig. 10,*a* and Fig. 10,*b*) the SMC strategy is better than the vector control with PI in terms of response time and reference tracking.

Conclusions. This paper has presented a comparative study between two controllers of active and reactive powers for the wind energy system equipped with a brushless doubly fed reluctance generator. The first one is a proportional-integral controller, and the second is a sliding mode controller-based field oriented control strategy.

Simulation results show the optimized performances of the vector control strategy based on a sliding mode controller. We observe high performances in terms of response time for vector control is 0.2 s and for sliding mode is 0.04 s. Spectral analysis of line current shows that total harmonic distortion of vector control is 27.25 % unlike sliding mode able to reduce the total harmonic distortion to a low value of around 16.25 % (without filter) and reference tracking without overshoots through the response characteristics. The decoupling, the stability, and the convergence towards the equilibrium are assured. Furthermore, this regulation presents a high dynamic

response, and it is more robust against parameter variation of the brushless doubly fed reluctance generator versus the conventional proportional-integral controller.

Conflict of interest. The authors declare that they have no conflicts of interest.

REFERENCES
1. Hasan M.S. *Control of Brushless Doubly-Fed Reluctance Machines under Normal and Faulty Operating Conditions. Doctoral thesis.* University of Northumbria at Newcastle, United Kingdom, 2014. Available at: https://nrl.northumbria.ac.uk/id/eprint/21433/ (Accessed 23.06.2021).
2. Boumassata A., Kerdoun D. Direct powers control of DFIG through direct converter and sliding mode control for WECS. *2015 3rd International Conference on Control, Engineering & Information Technology (CEIT)*, 2015, pp. 1-5. doi: https://doi.org/10.1109/CEIT.2015.7233058.
3. Tapia A., Tapia G., Ostolaza J.X., Saenz J.R. Modeling and control of a wind turbine driven doubly fed induction generator. *IEEE Transactions on Energy Conversion*, 2003, vol. 18, no. 2, pp. 194-204. doi: https://doi.org/10.1109/TEC.2003.811727.

4. Wu B., Lang Y., Zargari N., Kouro S. *Power Conversion and Control of Wind Energy Systems*. The Institute of Electrical and Electronics Engineers, 2011. doi: https://doi.org/10.1002/9781118029008.

5. Mousa M.G., Allam S.M., Rashad E.M. Vector control strategy for maximum wind-power extraction of a grid-connected wind-driven Brushless Doubly-Fed Reluctance Generator. *2015 4th International Conference on Electric Power and Energy Conversion Systems (EPECS)*, 2015, pp. 1-6. doi: https://doi.org/10.1109/EPECS.2015.7368515.

6. Tazil M., Kumar V., Bansal R.C., Kong S., Dong Z.Y., Freitas W. Three-phase doubly fed induction generators: an overview. *IET Electric Power Applications*, 2010, vol. 4, no. 2, p. 75. doi: https://doi.org/10.1049/iet-epa.2009.0071.

7. Kim H.S., Lu D.D.-C. Review on wind turbine generators and power electronic converters with the grid-connection issues. *AUPEC 2010 – 20th Australasian Universities Power Engineering Conference: «Power Quality for the 21st Century»*, 2010, art. no. 5710761. Available at: https://ieeexplore.ieee.org/document/5710761/ (Accessed 23.06.2021).

8. Iov F., Ciobotaru M., Blaabjerg F. Power electronics control of wind energy in distributed power systems. *2008 11th International Conference on Optimization of Electrical and Electronic Equipment*, 2008, pp. XXIX-XLIV. doi: https://doi.org/10.1109/OPTIM.2008.4602332.

9. Arifi E. *Modelling & Simulation of a Wind Turbine with Doubly-Fed Induction Generator (DFIG)*. Thesis, November 2020.

10. Cheng M., Han P., Buja G., Jovanović M.G. Emerging Multiport Electrical Machines and Systems: Past Developments, Current Challenges, and Future Prospects. *IEEE Transactions on Industrial Electronics*, 2018, vol. 65, no. 7, pp. 5422-5435. doi: https://doi.org/10.1109/TIE.2017.2777388.

11. Jovanović M., Ademi S., Llano D.X. Control of Doubly-Fed Reluctance Machines without a Shaft Position or Speed Sensor. *2018 International Symposium on Power Electronics, Electrical Drives, Automation and Motion (SPEEDAM)*, 2018, pp. 1245-1250. doi: https://doi.org/10.1109/SPEEDAM.2018.8445405.

12. Agha Kashkooli M.R., Jovanović M.G. A MRAS Observer for Sensorless Operation of Grid-Connected BDFRG Wind Turbines. *2020 IEEE 29th International Symposium on Industrial Electronics (ISIE)*, 2020, pp. 1517-1522. doi: https://doi.org/10.1109/ISIE45063.2020.9152461.

13. Abdel-Khalik A., Elserougi A., Massoud A., Ahmed S. A power control strategy for flywheel doubly-fed induction machine storage system using artificial neural network. *Electric Power Systems Research*, 2013, vol. 96, pp. 267-276. doi: https://doi.org/10.1016/j.epsr.2012.11.012.

14. Bhutto D.K., Ahmed Ansari J., Hussain Bukhari S.S., Akhtar Chachar F. Wind energy conversion systems (WECS) generators: A review. *2019 2nd International Conference on Computing, Mathematics and Engineering Technologies (iCoMET)*, 2019, pp. 1-6. doi: https://doi.org/10.1109/ICOMET.2019.8673429.

15. Betz R.E., Jovanovic M. *Introduction to Brushless Doubly Fed Reluctance Machines – The Basic Equations*. Technical Report EE0023. 19 March 1998. doi: http://dx.doi.org/10.13140/RG.2.1.2646.4483.

16. Ademi S., Jovanović M.G., Hasan M. Control of Brushless Doubly-Fed Reluctance Generators for Wind Energy Conversion Systems. *IEEE Transactions on Energy Conversion*, 2015, vol. 30, no. 2, pp. 596-604. doi: https://doi.org/10.1109/TEC.2014.2385472.

17. Zhang A., Wang X., Jia W., Ma Y. Indirect Stator-Quantities Control for the Brushless Doubly Fed Induction Machine. *IEEE Transactions on Power Electronics*, 2014, vol. 29, no. 3, pp. 1392-1401. doi: https://doi.org/10.1109/TPEL.2013.2260870.

18. Cardenas R., Pena R., Alepuz S., Asher G. Overview of Control Systems for the Operation of DFIGs in Wind Energy Applications. *IEEE Transactions on Industrial Electronics*, 2013, vol. 60, no. 7, pp. 2776-2798. doi: https://doi.org/10.1109/TIE.2013.2243372.

19. Jovanovic M. Sensored and sensorless speed control methods for brushless doubly fed reluctance motors. *IET Electric Power Applications*, 2009, vol. 3, no. 6, p. 503-513. doi: https://doi.org/10.1049/iet-epa.2008.0227.

20. Jovanovic M.G., Jian Yu, Levi E. Encoderless direct torque controller for limited speed range applications of brushless doubly fed reluctance motors. *IEEE Transactions on Industry Applications*, 2006, vol. 42, no. 3, pp. 712-722. doi: https://doi.org/10.1109/TIA.2006.872955.

21. Chaal H., Jovanovic M. Toward a Generic Torque and Reactive Power Controller for Doubly Fed Machines. *IEEE Transactions on Power Electronics*, 2012, vol. 27, no. 1, pp. 113-121. doi: https://doi.org/10.1109/TPEL.2011.2160731.

22. Chaal H., Jovanovic M. Practical Implementation of Sensorless Torque and Reactive Power Control of Doubly Fed Machines. *IEEE Transactions on Industrial Electronics*, 2012, vol. 59, no. 6, pp. 2645-2653. doi: https://doi.org/10.1109/TIE.2011.2161065.

23. Chaal H., Jovanovic M. Power control of brushless doubly-fed reluctance drive and generator systems. *Renewable Energy*, 2012, vol. 37, no. 1, pp. 419-425. doi: https://doi.org/10.1016/j.renene.2011.06.011.

24. Valenciaga F. Second order sliding power control for a variable speed-constant frequency energy conversion system. *Energy Conversion and Management*, 2010, vol. 51, no. 12, pp. 3000-3008. doi: https://doi.org/10.1016/j.enconman.2010.06.047.

25. Farid B., Tarek B., Sebti B. Fuzzy super twisting algorithm dual direct torque control of doubly fed induction machine. *International Journal of Electrical and Computer Engineering (IJECE)*, 2021, vol. 11, no. 5, p. 3782-3790. doi: https://doi.org/10.11591/ijece.v11i5.pp3782-3790.

26. Bekakra Y., Ben Attous D. A sliding mode speed and flux control of a doubly fed induction machine. *2009 International Conference on Electrical and Electronics Engineering - ELECO 2009*, 2009, pp. I-174-I-178. doi: https://doi.org/10.1109/ELECO.2009.5355328.

27. Abid M., Aissaoui A.G., Bounoua H. Sliding mode application in speed and flux control of an induction machine. *Istanbul University - Journal of Electrical and Electronics Engineering*, 2006, vol. 6, no. 2, pp. 197-204.

28. Abderazak S., Farid N. Comparative study between Sliding mode controller and Fuzzy Sliding mode controller in a speed control for doubly fed induction motor. *2016 4th International Conference on Control Engineering & Information Technology (CEIT)*, 2016, pp. 1-6. doi: https://doi.org/10.1109/CEIT.2016.7929044.

29. Routray S.K., Nayak N., Rout P.K. A Robust Fuzzy Sliding Mode Control Design for Current Source Inverter based STATCOM Application. *Procedia Technology*, 2012, vol. 4, pp. 342-349. doi: https://doi.org/10.1016/j.protcy.2012.05.052.

Oualah Oussama[1], *PhD Student,*
Djallel Kerdoun[1], *Professor,*
Abderraouf Boumassata[2], *Dr.,*
[1] Electrical Engineering Laboratory of Constantine (LGEC),
Department of Electrical Engineering,
Mentouri Brothers University, Constantine 1,
Campus Ahmed Hamani Zerzara,
Constantine, 25000, Algeria
e-mail: oussama.oulha@umc.edu.dz (Corresponding author);
Kerdjallel@yahoo.fr
[2] Department of Electronics, Electrical Engineering and Automation,
Laboratory of Electrical Engineering of Polytechnic School of Constantine (LGEPC),
National Polytechnic School of Constantine, Algeria
e-mail: a_boumassata@umc.edu.dz

M.S. Shah, T. Mahmood, M.F. Ullah

Power quality improvement using ultra capacitor based dynamic voltage restorer with real twisting sliding mode control

Introduction. Power quality is a major problem in today's power system, since it may have an impact on customers and utilities. Problem. Power quality is important issue of financial consequences for utilities, their consumers and load apparatus vendors. Voltage sag/swell are the most significant and usually occurring power quality issues in a secondary distribution system for sensitive loads. Goal. Dynamic voltage restorer is a fast, flexible, effective and dynamic custom power device can be used to compensate voltage sag/swell with integration of energy storage. Ultra capacitors have ideal properties of great power density and low energy density for elimination of voltage sag/swell. Their performance is mostly determined by the control strategy established for switching of voltage source converters. Originality. In this research, a strategy for the voltage source converter of dynamic voltage restorer based on the real twisting sliding mode control and ultra capacitor is developed to correct the fault that successfully eliminates the impacts of voltage sag/swell. Methodology. Ultra capacitor along with real twisting sliding mode control gives the more robustness and faster response, with also increasing the compensation time of the dynamic voltage restorer. Testing environment. To evaluate the performance of the proposed control approach, the MATLAB / Simulink SimPower System tool box is employed. Practical values. According to Simulation results clearly shows that the ultra capacitor along with real twisting sliding mode control effectively eliminate the voltage sag/swell in a very short time of 2 ms as compared to IEEE standards that is 20 ms, with less than 5 % total harmonic distortion for sensitive loads as per Information Technology Industry Council Curve and SEMI-F-47 Standards. References 18, tables 1, figures 8.
Key words: **dynamic voltage restorer, power quality issues, sliding mode control, real twisting algorithm, voltage sag/swell.**

Вступ. Якість електроенергії являє собою серйозну проблему в сучасній енергосистемі, оскільки вона може впливати на споживачів та комунальні служби. Проблема. Якість електроенергії є важливим питанням з точки хору фінансових наслідків для комунальних підприємств, їх споживачів та постачальників апаратури-навантажень. Провали/стрибки напруги є найбільш серйозними проблемами з огляду на якість електроенергії, які зазвичай виникають у вторинній системі розподілу для чутливих навантажень. Мета. Динамічний відновник напруги — це швидкий, гнучкий, ефективний і динамічний пристрій живлення, який можна використовувати для компенсації провалів/стрибків напруги за допомогою інтеграції накопичувача енергії. Суперконденсатори мають ідеальні властивості високої щільності потужності та низької щільності енергії для усунення провалів/стрибків напруги. Їх ефективність переважно визначається стратегією управління, встановленої для комутації перетворювачів джерел напруги. Оригінальність. У цьому дослідженні розроблено стратегію для перетворювача джерела напруги динамічного відновника напруги на основі керування реальним ковзним режимом скручування та суперконденсатора для виправлення несправності, яка успішно усуває наслідки провалу/стрибка напруги. Методологія. Суперконденсатор разом із керуванням реальним ковзним режимом скручування забезпечує більшу надійність та швидшу реакцію, а також збільшує час компенсації динамічного відновника напруги. Середовище для тестування. Для оцінки ефективності запропонованого підходу до управління використовується комплекс програмного забезпечення MATLAB/Simulink SimPower System. Практична цінність. Згідно з результатами моделювання ясно видно, що суперконденсатор разом з керуванням реальним ковзним режимом скручування ефективно усувають провали/стрибки напруги за дуже короткий час 2 мс у порівнянні зі стандартами IEEE, у відповідності до яких він становить 20 мс, із загальним спотворенням гармонік менше 5 % для чутливого навантаження відповідно зі стандартами Information Technology Industry Council Curve та SEMI-F-47. Бібл. 18, табл. 1, рис. 8.
Ключові слова: **динамічний відновник напруги, проблеми з якістю електроенергії, керування ковзним режимом, реальний алгоритм скручування, провали/скачки напруги.**

1. Introduction. Power quality is a key problem in today's power system, since it may have an impact on customers and utilities [1, 2]. The development in the new technology lead to improve the sensitive load that presents in the distribution system, these sensitive loads have badly effected on the quality of power supply. Power quality frequently occurred due to the problems like voltage sag/swell and harmonic distortion [3]. According to IEEE standards, voltage sag is defined by IEEE 1152-1995 as a sudden reduction in RMS value of the AC voltage from the 0.1 to 0.9 p.u. during a half-cycle to 1 min. While the voltage swell is defined as an increase in rated voltage caused by an abrupt disengagement of the load or by a highly capacitive load from 1.1 p.u. to 1.8 p.u. for duration of 0.5 cycles to 1 min [4]. These issues voltage sag/swell are small period voltage change that do not present for more than 1 min as available in Fig. 1 [5].

To eliminate these power quality problems, Dynamic Voltage Restorer (DVR) is the most efficient and best solution over other custom power devices like unified power quality conditioner (UPQC), distribution static synchronous compensator (DSTATCOM), static var compensator (SVCs) and uninterrupted power supply (UPS), due to its smaller size, fast response, effective and dynamically behavior [6-8].
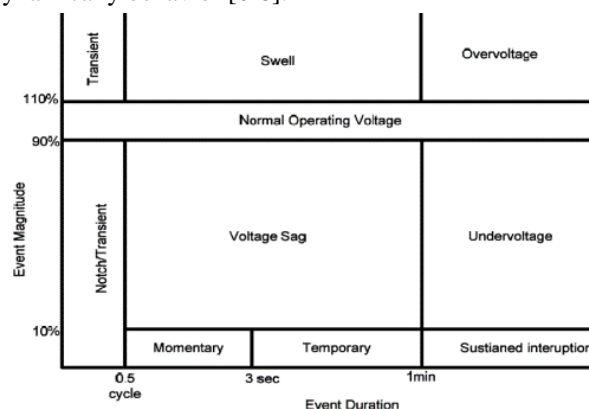

Fig. 1. IEEE Standard 1159-1995 for voltage decrease

The DVR contains Voltage Source Converter (VSC) with ultra capacitor (UC) as battery storage, LC filter, injection transformer and control circuit, which are

connected with source voltage and load voltage at point of common coupling (PCC) as shown in Fig. 2 [9], where R_s, L_s are the source resistance and inductance, respectively; V_d is DVR injected voltage; V_L is load voltage; L_f, C_f are the filter inductance and capacitance, respectively.
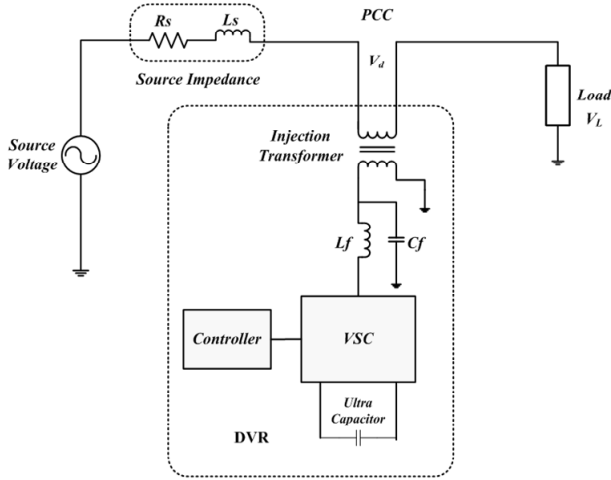

Fig. 2. DVR component

Various forms of rechargeable energy storage technologies are contrasted, including flywheels, ultra capacitors, superconducting magnets energy storage, and batteries in [10]. The method of ultra capacitors rises the DVR compensation time as compared to the previous techniques because of its properties of great power density and low energy density [11]. It connects to the system to improve the sag/swell compensation. In [12-14] many control schemes are discussed for the VSC of DVR to remove voltage sag/swell, but this has some disadvantage of depending on mathematical modeling of system and some stability problem. Therefore, a non-linear sliding mode controller is introduced as it has advantage of independent on mathematical modelling of the system, but it has important disadvantage named chattering effect [15]. To avoid this chattering effect, some algorithms such as real twisting, super-twisting, optimal, sub-optimal, global, integral and state-observer algorithms are used in literature [16-18]. Among these algorithms, real twisting algorithm has upper hand due to its stability, robustness and more tracking accuracy with less chattering effect.

The goal of the article. In this research, a control scheme of real twisting sliding mode controller (RTSMC) with integration of ultra capacitor is presented for the voltage source converter of dynamic voltage restorer using MATLAB/Simulink software package which can successfully mitigate voltage sag/swell and total harmonic distortion according to IEEE Standard [5].

2. Mathematical modeling of DVR in distribution system. Figure 3 depicts the equivalent circuit diagram of a DVR. In the figure, the distribution system is linked in series with a DVR, as well as source and load. The voltage injected by DVR stated as

$$V_L + = V_{source} + V_{dvr}, \tag{1}$$

where V_L, V_{source}, V_{dvr} are the load, source and DVR voltages, respectively.

Filter parameters L_f and C_f are depicted in Fig. 3. These filter settings are used to remove the high-frequency component present in the VSC's AC output. The filter capacitor is defined as follows:
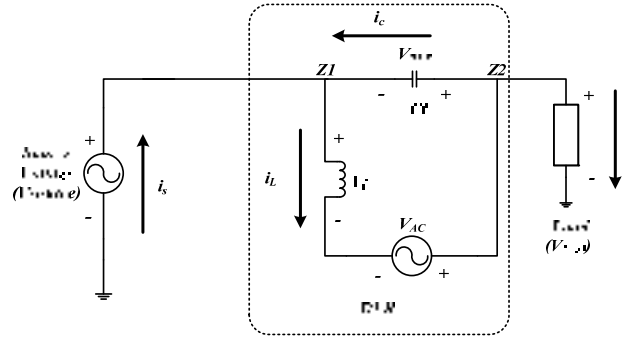
$$i_c = C_f \cdot \frac{dV_{dvr}}{dt}. \tag{2}$$

Fig. 3. DVR equivalent circuit

By applying Kirchhoff's circuit law at node Z_1 in Fig. 3 we have

$$i_s - i_L + i_C = 0. \tag{3}$$

where i_s is the source current; i_L is the inductor current of filter.

By putting i_c from (2) in (3), we have

$$i_s - i_L + C_f \cdot \frac{dV_{dvr}}{dt} = 0. \tag{4}$$

Equation (4) after the simplification gets the form

$$\frac{dV_{dvr}}{dt} = \frac{(i_L - i_s)}{C_f}. \tag{5}$$

The above equation (5) is the 1st DVR state equation. For the second DVR state equation, apply Kirchhoff's voltage law at closed loop (Fig. 3)

$$V_{dvr} + V_L - V_{in} = 0, \tag{6}$$

where V_{in} is the VSC AC voltage; V_l is the load voltage

$$V_L = L_f \cdot \frac{di_L}{dt}. \tag{7}$$

So, substituting (7) in (6) we have

$$V_{dvr} + L_f \cdot \frac{di_L}{dt} - V_{in} = 0. \tag{8}$$

After the simplification, we get

$$\frac{di_L}{dt} = \frac{(V_{in} - V_{dvr})}{L_f}. \tag{9}$$

Finally, the state space model DVR is

$$\frac{d}{dt}\begin{bmatrix} i_L \\ V_{dvr} \end{bmatrix} = \begin{bmatrix} 0 & -\dfrac{1}{L_f} \\ \dfrac{1}{C_f} & 0 \end{bmatrix} \cdot \begin{bmatrix} i_L \\ V_{dvr} \end{bmatrix} + \begin{bmatrix} 0 & \dfrac{1}{L_f} \\ -\dfrac{1}{C_f} & 0 \end{bmatrix} \cdot \begin{bmatrix} i_s \\ V_{in} \end{bmatrix}, \tag{10}$$

where i_L and V_{dvr} are the state variables, while the i_s and V_{in} are the input variables.

3. Mathematical modelling of ultra capacitor (UC). The ultra capacitor model consists of equivalent series resistance (ESR), capacitance and equivalent parallel resistance (EPR) as shown in Fig. 4. The charging and discharging resistances of system are represented by the ESR, while EPR represents the self-discharging losses of the system.

The UC voltage with the capacitance and resistance can be described as follows

$$V(t) = V_i \cdot \exp(-t/\tau), \tag{11}$$

where $\tau = R \cdot C$ is the time constant to determine the charging and discharging process for some capacitor initial voltages.
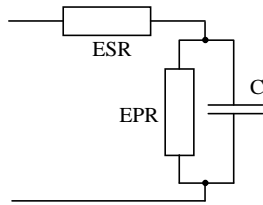
Fig. 4. UC equivalent model

The change in voltage terminal and the capacitance are directly proportional to the energy drawn from the UC expressed as

$$E = \frac{1}{2} \cdot C \cdot \left(V_i^2 - V_f^2 \right), \qquad (12)$$

where V_i is the initial voltage before discharging start; V_f is the final voltage after discharging start.

The total UC system resistance (R_{total}) and capacitance (C_{total}) of the UC bank are calculated as

$$R_{total} = n_s \cdot \frac{ESR}{n_p}; \qquad (13)$$

$$C_{total} = n_p \cdot \frac{C}{n_s}, \qquad (14)$$

where n_s is the number of capacitor cells in series; n_p is the number of capacitor cells in parallel.

4. Designing of second order real twisting sliding mode control. There are two steps, which are necessary for the implementation of sliding mode control. The first stage is to select the sliding surface. The DVR displays the desired performance when the state trajectory is pushed on the specified sliding line. The second stage is to drive the system's state to reach and remain on the chosen sliding surface in finite period.

4.1: Sliding surface selection. Create a control strategy for DVR that is free of system parameters and load. This approach will be used to eliminate voltage sag/swell, hence the state vector will be defined as

$$V = \begin{bmatrix} v \\ \dot{v} \end{bmatrix}, \qquad (15)$$

where V is the state vector; v is the state variable and $\dot{v}$ is the first derivative state variable V.

Select which sliding surface that is utilized to adjust the DVR's VSC AC output voltage for these state variables. For the chosen method, the change between reference and load voltage is a sliding surface (S). The sliding surface is indicated by signal (S) in Fig. 5. As indicated in Eq. (16), this signal (S) is based on the computed error voltage (V_{error})

$$V_{error} = V_{reference} - V_{load}. \qquad (16)$$

In (16) the sliding surface which comprises the difference of $V_{reference}$ and V_{Load} and after this takes derivative of this error voltage and finally add it

$$S = V_{error} + k \cdot \frac{dV_{error}}{dt}, \qquad (17)$$
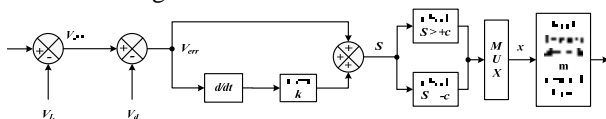
where k is the gain of feedback.

Fig. 5. RTSMC block diagram

When detect the error in actual voltage compare the sliding surface (S) with $\pm c$ constant quantity. When comparison is done, then outcomes go through the

multiplexer. Multiplexer is used for applying the switching law on the desired signal.

4.2 Reachability condition. The following condition must be satisfied in order to obtain the state trajectory onto the sliding surface and confirm the operation's existence

$$S = 0; \qquad (18)$$

$$\dot{S} = 0. \qquad (19)$$

In a short period of time, the control approach used here will turn all of the state vectors into a sliding surface. The switching law that we employ will reveal the system's stability status while it is in the sliding mode. The following is the criterion for the presence of sliding mode

$$S \cdot \dot{S} = 0. \qquad (20)$$

The above equation is basically the Lyapunov function, used to check the stability condition for the system stability. Some key points are listed below.

- if $S > 0$ and $\dot{S} < 0$, then S will be reduce to 0;
- if $S < 0$ and $\dot{S} > 0$, then S will be increase to 0.

4.3 Determination of control law. The switching law may be expressed as follows

$$x(t) = \begin{cases} +1, \text{if } S > +c; \\ -1, \text{if } S < -c, \end{cases} \qquad (21)$$

where $x(t)$ is represented as the variable for switching control; c is the constant for the comparison with faulty signal.

If we receive $x(t) = +1$, inverter switch S1 and switch S4 are turned on as shown in Fig. 6. If we receive $x(t) = -1$, inverter S2 and S3 will be turned on as shown in Fig. 6.
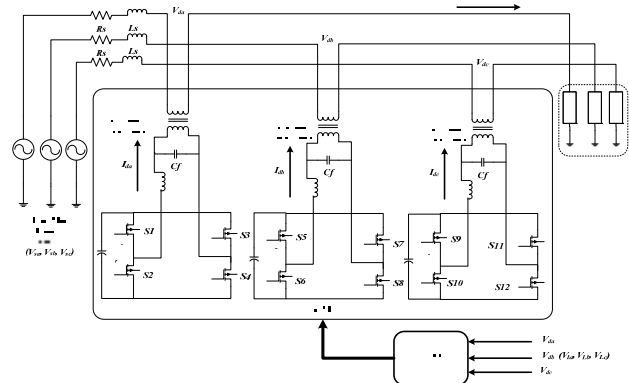

Fig. 6. Three phase system with connected DVR

Basically an ideal SMC is working on the infinite frequency, when the state vector is aimed directly towards the sliding surface. However, power converters do not have an infinite switching frequency, that is why the converter does not operate properly and state vector will not move towards origin, but keep travelling with the some discontinuous surface with unwanted oscillation, which is known as chattering. Therefore real twisting algorithm (RTA) is utilized in SMC to remove the chattering effect.

The block diagram of SMC along RTA is show in Fig. 5. When the RTA is apply on sliding surface, switching law gives the modified input of control Z as given below

$$Z = -n_1 \cdot sign(S) - n_2 \cdot sign(\dot{S}), \qquad (22)$$

To remove the undesirable switching components, two tuning constants n_1 and n_2 are used in the control law of RTA. The sliding manifold term $sign(S)$, removes the

switching frequency of components to increase the life of switches. When the designed sliding surface s is greater or less than zero, the signum function *sign(S)* of the sliding manifold gives the +1 and –1 output respectively. The total effect of RTA on SMC results in less chattering effect, faster response and robustness to variation in external parameter.

5. Simulation result and discussion. To test the efficiency of a real twisting sliding mode control (RTSMC) for DVR in MATLAB/Simulink, a test system is develop (Fig. 6). All the parameter detail is given in Table 1.

Figure 6 depicts the suggested distribution system that used to model and simulate the UC based DVR using the RTSMC. Three-phase programming source produces voltage sag/swell in distribution test system, which is then corrected by DVR. The following analysis is carried out to evaluate the effectiveness of the suggested control approach.

- voltage sag/swell mitigation;
- Total harmonic distortion.

Table 1

Parameter of distribution test system

No.	Description of parameters	Values
1	Grid voltage(phase-phase)	400 V
2	Frequency of system(*f*)	50 Hz
3	Impedance of line (R_s, L_s)	0.8929 Ω, 16.58 mH
4	Loads rating	Linear load: $P = 10$ kW, $Q = 1$ kVar
5	Switching constant ±*c*	0.1
6	Ultra capacitor	40 V
7	*LC* filter (L_f, C_f)	1.8 mH, 5.5 μF
8	Power rating for coupling transformer	100 kVA
9	Control action	RTSMC
10	SMC gain *γ*	$0.142 \cdot 10^{-6}$
11	Switching frequency (f_s)	10 kHz
12	Solver for simulation	Ode23tb (stiff/TR-BDF2)
13	Time of sampling	5 μs
14	Filter cutoff frequency	405 Hz
15	RTSMC tuning gains, n_1 and n_2	0.5 and 0.5

The RTSMC does not provide any switching signal to run the DVR when the system voltage does not change (normal state). When the voltage (voltage sag/swell) of the system deviates from its tolerated range, the controller begins to operate. RTSMC operates in the following manner:

- detect voltage sag/swell;
- compute the voltage sag/swell (in percentage);
- determine the signal of switching control;
- generate switching signal of pulse width modulation (PWM) for VSC to activate source and load voltage;
- generations of necessary switching signal uninterruptedly to ensure that voltage sag and swell is compensated;
- Terminate the switching PWM signal, when voltage sag/swell is resolved.

5.1. Voltage sag mitigation. A three-phase balanced voltage sag of 30 % arises as a result of the rapid switching ON of sensitive load on the supply side. As shown in Fig 7,*a*, the occurrence time of this sag begins at 0.1 s and ends at 0.2 s. To correct the disturbance, the controller is utilized. If there is no sag during normal operation, no voltage is introduced. When a fault occurs, the controller detects the sag and evaluate the sag magnitude.

The problem (voltage sag) is resolved in a relatively short period (2 ms) compared to the IEEE Standard acceptable limit of 20 ms. Figure 7,*b* illustrates that DVR just injects the missing value. To reduce unwanted high frequency elements, a low pass filter is used. Figure 7,*c* shows the pure and sag-free corrected system voltage. The voltage corrected Total Harmonic Distortion (THD) value for phase A, B and C is 1.13 %, 4.62 % and 4.05 % respectively, indicating that the harmonic content in the load voltage is less than the 5 % suggested by IEEE Standard 1159-1995.
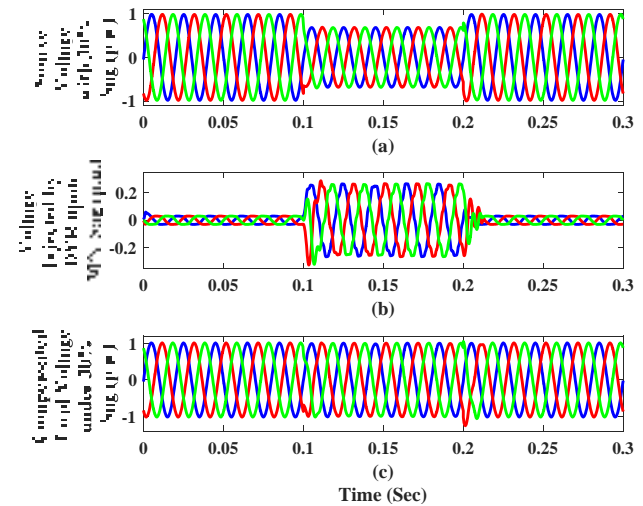

Fig. 7. Voltage sag waveform before and after mitigation:
(*a*) source voltage with 30 % sag;
(*b*) voltage injected by DVR to mitigate sag;
(*c*) compensated load voltage

5.2. Voltage swell compensation. A three-phase balanced voltage swell of 30 % arises as a result of the rapid switching ON of sensitive load on the supply side. As shown in Fig 8,*a*, the occurrence time of this swell begins at 0.1 s and ends at 0.2 s.
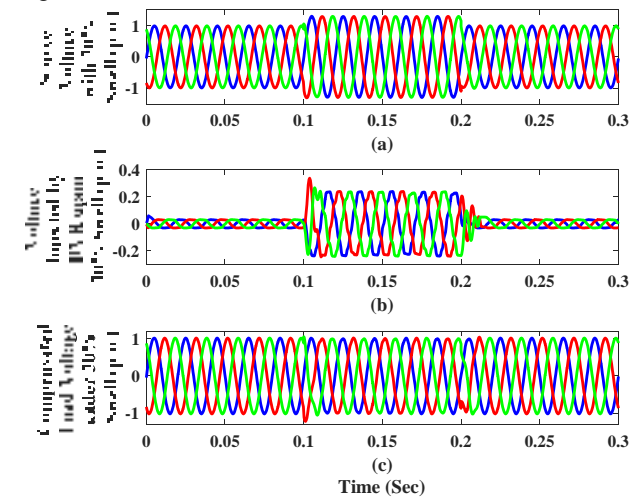

Fig. 8. Voltage swell waveform before and after mitigation:
(*a*) source voltage with 30 % swell;
(*b*) voltage injected by DVR to mitigate swell;
(*c*) compensated load voltage

The problem (voltage swell) is resolved in a relatively short period (2 ms) compared to the IEEE Standard acceptable limit of 20 ms. Figure 8,*b* illustrates that DVR just injects the missing value. To reduce unwanted high frequency elements, a low pass filter is used. Figure 8,*c* shows the pure and swell-free corrected system voltage.

The corrected voltage THD value is for phase A, B, and C is 1.83 %, 4.91 % and 4.51 % respectively, indicating that the harmonic content in the load voltage is less than the 5 % suggested by IEEE Standard 1159-1995.

Conclusion. A control scheme of real twisting sliding mode control with integration of ultra capacitor is presented for the voltage source converter of dynamic voltage restorer using MATLAB/Simulink software package which can successfully mitigate voltage sag/swell and total harmonic distortion according to IEEE Standard. The ultra capacitors rise the dynamic voltage restorer compensation time due to its ideal properties of great power density and low energy density for elimination of voltage sag/swell and control mechanism eliminates chattering, while attains a constant switching frequency. As a result of using real twisting algorithm in dynamic voltage restorer control, a continuous control input is generated, which can be contrasted to the triangular carrier signal to generate pulse width modulation signals. To evaluate the performance of the suggested approach, the MATLAB/Simulink SimPower System tool box is employed. According to simulation results this clearly shows that the ultra capacitor along with real twisting sliding mode control effectively eliminates the voltage sag/swell in a very short time of 2 ms as compared to IEEE Standards that is 20 ms, with less than 5 % total harmonic distortion for sensitive loads as per Information Technology Industry Council Curve and SEMI-F-47 standards.

Conflict of interest. The authors declare that they have no conflicts of interest.

REFERENCES

1. Sahoo B., Routray S.K., Rout P.K. Robust control and inverter approach for power quality improvement. In *Green technology for smart city and society*, 2021, pp. 143-156. Springer, Singapore, 2021. doi: https://doi.org/10.1007/978-981-15-8218-9_12.
2. Akbar F., Mehmood T., Sadiq K., Ullah M.F. Optimization of accurate estimation of single diode solar photovoltaic parameters and extraction of maximum power point under different conditions. *Electrical Engineering & Electromechanics*, 2021, no. 6, pp. 46-53. doi: https://doi.org/10.20998/2074-272X.2021.6.07.
3. Bangarraju J., Jayalaxmi A., Rajagopal V. Mitigation of Voltage Sag and Swell Using Battery Based Dynamic Voltage Restorer: A Detailed Study. *Innovations in Science and Technology*, 2021, vol. 1, pp. 90-98. doi: https://doi.org/10.9734/bpi/ist/v1/5222F.
4. Chen Y., Wang Y., Xiao X., Zheng Z., Zhang H., Wu X. Improved Premium Model of Voltage Sag Insurance Based on Voltage Sag Risk. *IEEE Transactions on Power Delivery*, 2021, pp. 1–1. doi: https://doi.org/10.1109/TPWRD.2021.3128176.
5. *IEEE Recommended Practice for Monitoring Electric Power Quality. IEEE Std 1159-2019*, pp. 1-98, 13 Aug. 2019. doi: https://doi.org/10.1109/IEEESTD.2019.8796486.
6. Zellagui M., Lasmari A., Settoul S., El-Sehiemy R.A., El-Bayeh C.Z., Chenni R. Simultaneous allocation of photovoltaic DG and DSTATCOM for techno-economic and environmental benefits in electrical distribution systems at different loading conditions using novel hybrid optimization algorithms. *International Transactions on Electrical Energy Systems*, 2021, vol. 31, no. 8, art. no. e12992. doi: https://doi.org/10.1002/2050-7038.12992.
7. Zaineb Nisar Jan. Power Quality Issues and Improvement Using Custom Power Device. *International Research Journal of Engineering and Technology*, 2021, vol. 8, no. 6, pp. 1322-1324. Available at: https://www.irjet.net/archives/V8/i6/IRJET-V8I6241.pdf (accessed 16 October 2021).
8. Kumar M., Uqaili M.A., Memon Z.A., Das B. Mathematical Modeling of THD Mitigation Using HAPF for UPS System with Experimental Analysis via Hybrid Interface of Optical USB and Power Quality Meter. *Mathematical Problems in Engineering*, 2021, pp. 1-15. doi: https://doi.org/10.1155/2021/3981287.
9. Mohammed A.B., Mohd Ariff M.A., Najwa Ramli S. Power quality improvement using dynamic voltage restorer in electrical distribution system: an overview. *Indonesian Journal of Electrical Engineering and Computer Science*, 2020, vol. 17, no. 1, pp. 86-93. doi: https://doi.org/10.11591/ijeecs.v17.i1.pp86-93.
10. Olabi A.G., Onumaegbu C., Wilberforce T., Ramadan M., Abdelkareem M.A., Al-Alami A.H. Critical review of energy storage systems. *Energy*, 2021, vol. 214, art. no. 118987. doi: https://doi.org/10.1016/j.energy.2020.118987.
11. Ahmed W., Sheikh J.A., Nouman M., Ullah M.F., Mahmud M.A.P. Techno-economic analysis for the role of single end energy user in mitigating GHG emission. *Energy, Sustainability and Society*, 2021, vol. 11, no. 1, art. no. 32. doi: https://doi.org/10.1186/s13705-021-00307-3.
12. Nambiar R.E., Darshan M, Lavanya B., Pavan Kumar A.J., Priyadarshini V. Comparative study between different controllers of DVR for power quality improvement. *2021 International Conference on Design Innovations for 3Cs Compute Communicate Control (ICDI3C)*, 2021, pp. 84-87. doi: https://doi.org/10.1109/ICDI3C53598.2021.00025.
13. Moghassemi A., Padmanaban S. Dynamic Voltage Restorer (DVR): A Comprehensive Review of Topologies, Power Converters, Control Methods, and Modified Configurations. *Energies*, 2020, vol. 13, no. 16, art. no. 4152. doi: https://doi.org/10.3390/en13164152.
14. Choudhury S., Bajaj M., Dash T., Kamel S., Jurado F. Multilevel Inverter: A Survey on Classical and Advanced Topologies, Control Schemes, Applications to Power System and Future Prospects. *Energies*, 2021, vol. 14, no. 18, art. no. 5773. doi: https://doi.org/10.3390/en14185773.
15. Ullah M.F., Hanif A. Power quality improvement in distribution system using distribution static compensator with super twisting sliding mode control. *International Transactions on Electrical Energy Systems*, 2021, vol. 31, no. 9, art. no. e12997. doi: https://doi.org/10.1002/2050-7038.12997.
16. Navabi M., Davoodi N. Design of a Robust Controller Using Real Twisting Algorithm for a Fixed Wing Airplane. *2019 5th Conference on Knowledge Based Engineering and Innovation (KBEI)*, 2019, pp. 605-610. doi: https://doi.org/10.1109/KBEI.2019.8734903.
17. Anwar N., Hanif A.H., Khan H.F., Ullah M.F. Transient Stability Analysis of the IEEE-9 Bus System under Multiple Contingencies. *Engineering, Technology & Applied Science Research*, 2020, vol. 10, no. 4, pp. 5925-5932. doi: https://doi.org/10.48084/etasr.3273.
18. Mehdi M.F., Ahmad A., Ul Haq S.S., Saqib M., Ullah M.F. Dynamic economic emission dispatch using whale optimization algorithm for multi-objective function. *Electrical Engineering & Electromechanics*, 2021, no. 2, pp. 64-69. doi: https://doi.org/10.20998/2074-272X.2021.2.09.

Muhammad Shahzaib Shah[1], *MS Scholar,*
Tahir Mahmood[1], *Professor,*
Mian Farhan Ullah[2], *Lecturer,*
[1] Department of Electrical Engineering,
University of Engineering and Technology, Taxila, Pakistan,
e-mail: mshahzaib.Shah@students.uettaxila.edu.pk,
tahir.mehmood@uettaxila.edu.pk,
[2] Department of Electrical Engineering,
Wah Engineering College, University of Wah,
47040, Wah Cantt, Quaid Avenue, Pakistan,
e-mail: farhan.ullah@wecuw.edu.pk (Corresponding Author)

S.T. Zahra, R.U. Khan, M.F. Ullah, B. Begum, N. Anwar

Simulation-based analysis of dynamic voltage restorer with sliding mode controller at optimal voltage for power quality enhancement in distribution system

Introduction. Nowadays, power quality issues are of considerable interest to both utilities and end users as they cause significant financial losses to the industrial customers. Due to this, power quality assurance in power distribution systems is very important, when considering commercial and industrial applications. Problem Statement. Unfortunately, sudden faults such as sag, transients, harmonics distortion and notching in the power system create disturbances and affect the load voltages. Out of these, voltage sag and harmonics seriously affect sensitive devices. Harmonics in the power system cause increased heating of equipment and conductors, misfires in variable speed drives, and torque pulsations in motors. Harmonics reduction is considered desirable. Methodology. This paper presents an efficient and robust solution to this problem by using dynamic voltage restorer in series with distribution system. Dynamic voltage restorer is economical and effective solution for protecting sensitive loads from harmonics and sag. Control strategy is adopted with dynamic voltage restorer topology and the performance with the proposed controller is analyzed. Novelty. In this research work modelling, analysis and simulation of dynamic voltage restorer with proportional integral controller and dynamic voltage restorer with sliding-mode controller at optimal voltage is used to improve the dynamic voltage restorer performance by reducing total harmonic distortion. Results. The simulation is performed in MATLAB / Simulink software package and comparative analysis of dynamic voltage restorer with different controllers for distribution system is presented. The proposed scheme successfully reduced percentage total harmonics distortion and voltage sag using dynamic voltage restorer with sliding mode controller at optimal voltage which is found to be 0.38 %. References 22, tables 1, figures 19.
Key words: **dynamic voltage restorer, sliding-mode controller, total harmonics distortion, voltage sag, power quality improvement**.

Вступ. Сьогодні питання якості електроенергії викликають значний інтерес як для комунальних підприємств, так і для кінцевих споживачів, оскільки вони завдають значних фінансових втрат промисловим споживачам. У зв'язку з цим забезпечення якості електроенергії в розподільних системах є дуже важливим при розгляді комерційних та промислових застосувань. Постановка задачі. На жаль, раптові несправності, такі як прогини, перехідні процеси, спотворення гармонік і виїмки в енергосистемі створюють збурення та впливають на напругу навантаження. З них провали напруги та гармоніки серйозно впливають на чутливі пристрої. Гармоніки в енергосистемі викликають посилений нагрів обладнання та провідників, пропуски запалювання в приводах із змінною частотою обертання, пульсації крутного моменту в двигунах. Зниження гармонік вважається бажаним. Методологія. У цій статті представлено ефективне та надійне рішення цієї проблеми за допомогою динамічного відновника напруги послідовно з розподільною системою. Динамічний відновник напруги – це економне та ефективне рішення для захисту чутливих навантажень від гармоній та провисань. Прийнято стратегію керування з топологією динамічного відновника напруги та проаналізовано ефективність при використанні запропонованого контролера. Новизна. У цій дослідницькій роботі використовується моделювання, аналіз та чисельне дослідження динамічного відновника напруги з пропорційним інтегральним контролером та динамічного відновника напруги з регулятором ковзного режиму при оптимальній напрузі для підвищення ефективності динамічного відновника напруги за рахунок зменшення сумарних гармонійних спотворень. Результати. Моделювання виконано в програмному комплексі MATLAB / Simulink та представлено порівняльний аналіз динамічного відновника напруги з різними контролерами для розподільчої системи. Запропонована схема успішно зменшила відсоток спотворення сумарних гармонік і провалів напруги за допомогою динамічного відновника напруги з регулятором ковзного режиму при оптимальній напрузі, який становить 0,38 %. Бібл. 22, табл. 1, рис. 19.
Ключові слова: **динамічний відновник напруги, регулятор ковзного режиму, загальні гармонічні спотворення, провал напруги, покращення якості електроенергії**.

1. Introduction. Nowadays, power quality issues are of considerable interest to both utilities and end users as they cause significant financial losses to the industrial customers. Due to this, power quality assurance in power distribution systems is very important when considering commercial and industrial applications. Unfortunately, sudden faults such as sag, transients, harmonics distortion and notching in the power system create disturbances and affect the load voltages. Out of these, voltage sag and harmonics seriously affect sensitive devices. Harmonics in the power system cause increased heating of equipment and conductors, misfires in variable speed drives, and torque pulsations in motors. Harmonics reduction is considered desirable. Voltage total harmonics distortion (THD) also plays very important role in a power system and power quality. According to standard of IEEE 519-1992, the value of THD should be equal or less than 5 % of the fundamental frequency. Standard of IEEE 1152-1995 define the voltage sags root mean square i.e. RMS voltage variation having a magnitude in between (0.1-0.9) p.u. of value of nominal voltage and its duration typically varies from 0.5 cycle to 60 s. Installation of custom power device, voltage mitigation

or compensation can be achieved to remove/cancel out the disturbances at the load side [1, 2]. Number of customized power devices are obtainable each having its own Pros and Cons for voltage reduction compensation such as DSTATCOM, Superconducting Magnetic Energy Storage (SMES), Dynamic Voltage Restorer (DVR) and Static VAR Compensation (SVC).

DVR refers a controllable voltage source usually inserted between the sensitive load voltage and network, which accurately generates a disturbance that perturbs the sensitive load voltage by inserting the voltage into the distribution line through a transformer. Lead-acid battery-powered DVRs are the best and most attractive technology, providing superior dynamic voltage restoration compared to shunt-connected devices. The main function of a voltage source inverter power system equipped with a DVR is to inject the desired three-phase voltage into the load [3, 4]. In this paper modelling, analysis and simulation of DVR with PI controller and DVR with Sliding-Mode Controller (SMC) at optimal voltage is used to reduce THD to

improve DVR performance. DVR with SMC at optimal V_{dc} has successfully reduced THD and voltage sag to 0.38 %.

2. Dynamic Voltage Restorer. DVR is a series connected power electronics switching device and is connected in series with the distribution line to inject the desirable controlled voltage. The DVR includes injection transformer, harmonic filter, voltage source inverter, control unit and DC storage unit [3-7].

The heart of DVR is the control unit, which is mainly used to monitor the presence of drop in voltage in the network and if necessary to compensate/insert the missing voltage after determining its phase and magnitude. Control unit has a reference voltage (V_{ref}) structure for the purpose of comparison. A three-phase reference voltage scheme is used as a reference in a dynamic voltage restorer. However, the V_{ref} three-phase voltage must be needs to synchronize with the load voltage (V_L) to correctly inject the missing voltage based on magnitude and phase. Simulink diagram for obtaining the reference waveform of voltage is shown in Fig. 1.
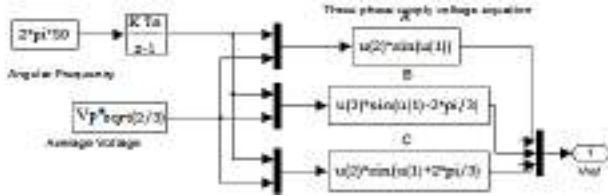
Fig. 1. Simulink reference voltage diagram

In the control unit, a Park transformation also known as direct-quadrature-zero ($dq0$) transformation has been used to control the DVR. The 3-phase system is more of a simplified system, and it can easily be controlled after transformation from 3-phase abc voltage to two voltage components i.e. V_d and V_q. The V_0 which is zero sequence components are ignored for simplicity

$$\begin{vmatrix} V_d \\ V_q \\ V_0 \end{vmatrix} = \frac{1}{3} \cdot |M| \cdot \begin{vmatrix} V_a \\ V_b \\ V_c \end{vmatrix}, \qquad (1)$$

where M is as follow

$$\begin{vmatrix} V_d \\ V_q \\ V_0 \end{vmatrix} = \frac{1}{3} \cdot \begin{vmatrix} 2\sin\omega t & 2\sin\left(\omega t - \frac{2\pi}{3}\right) & 2\sin\left(\omega t + \frac{2\pi}{3}\right) \\ 2\cos\omega t & 2\cos\left(\omega t - \frac{2\pi}{3}\right) & 2\cos\left(\omega t + \frac{2\pi}{3}\right) \\ 1 & 1 & 1 \end{vmatrix} \cdot \begin{vmatrix} V_a \\ V_b \\ V_c \end{vmatrix}, (2)$$

where ω is the angular frequency.

There are two modes of DVR which are given below.

In first injection mode, voltage inject operation has been done using DVR to correct the sag. While in the second mode, monitoring operation is usually done in standby mode [8-10]. So, there is no type of other voltage is being injected. Injected transformer low voltage side is shorted using the voltage source inverter. The sag voltage, DVR voltages and load current are written as

$$I_L = (P_L + jQ_L)/V_L; \qquad (3)$$

$$V_{DVR} = V_L + (Z_S \times I_S) - V_S; \qquad (4)$$

$$V_{SAG} = V_S - (I_L \times Z_S), \qquad (5)$$

where I_L is the load current; P_L, Q_L are load active and reactive powers respectively; V_L, V_S are the load and supply voltages respectively; Z_S, I_S are source impedance and current respectively; V_{DVR} is the injection voltage by DVR and V_{SAG} is sag voltage.

The equivalent circuit of the power system under study is shown in Fig. 2 and phasor diagram of distribution system with DVR is shown in Fig. 3 [11, 12].
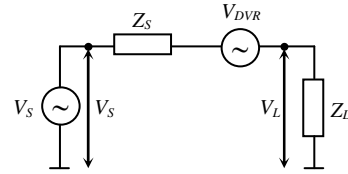

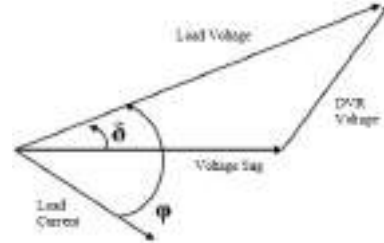Fig. 2. Equivalent circuit of the power system under study

Fig. 3. Phasor diagram of distribution network using DVR

3. DVR with PI controller. The DVR plays a key role in detecting voltage sag events, correcting voltage sag problems, and generating Pulse Width Modulation (PWM) trigger pulses. The control unit generates a three-phase V_{ref} and compares the V_L to the V_{ref} value [13]. An error signal is generated when voltage is missing from the power system due to voltage sag. If the difference between V_{ref} missing V_L is equal to the error signal, the DVR starts to work and injects the missing voltage into the power distribution network. That is, an error signal is transmitted to the PI controller and then PI controller output is converted back to a Park transformation. The signal is transmitted in a discrete pulse width modulation block. Discrete PWM compares the input three-phase converted signal to a saw tooth wave and the PWM generates a pulse to trigger the PWM V_S (voltage source) inverter with the desired firing arrangement. The DVR collects the required direct current voltage from the storage device (e.g. 500 V). A voltage source inverter is used to invert the DC storage unit voltage to an AC voltage, and eventually the missing voltage is injected through a three-phase injection transformer, which is then connected in series with the distribution line. The phase-locked loop for a DVR with PI controller is shown in Fig. 4 and the Simulink model is shown in Fig. 5.
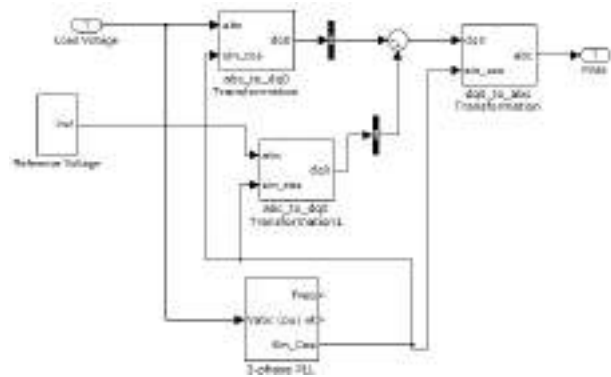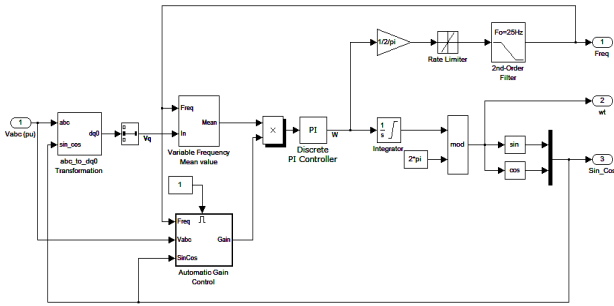

Fig. 4. Phase Locked Loop for DVR with PI controller

Fig. 5. Simulink Model of DVR with PI controller

4. Control circuit for DVR with SMC. SMC is a robust and nonlinear control scheme at which the arrangement of the controller is being modified in reaction to the varying state of the system to obtain a desire result. The control procedure for fast switching is used and the trajectory of the system is forced to move along the selected switching area in the state space [14].

There are three major advantages of SMC i.e. model reduction, performance design and robustness parameters. The *sliding phase* (S.P.) at which a system slides and properly to approach to zero to make the system stable i.e. $S = 0$ (S is the sliding surface variable). While a system approaches to sliding phase is known as *reaching phase* (R.P.) i.e. $S \neq 0$. Equation (6) gives the main equation of SMC

$$u = -sign(S);\tag{6}$$

$$S = \dot{x} + a \cdot x,\tag{7}$$

where $S = 0$ and a is the variable

$$\dot{x} = -a \cdot x,\tag{8}$$

Reachability phase is very simple and it says that any controller which obeys $S\dot{S} < 0$ will reach to sliding surface/phase. The system has an inertia due to which the reaching phase will little bit move forward as shown in Fig. 6.
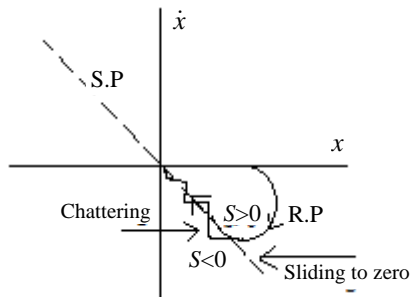
Fig. 6. Phase plot for actual SMC control

The control law determination of reaching phase is given below in (9) to maintain the system in the sliding surface and due to system inertia, the sliding mode trajectories often chatter back and forth motion along the sliding surface to reach the system at origin which is a chattering also known as oscillation [14]. The S and $\dot{S}$ signs are always opposite to each other and $\delta|t|$ is the switching function of the voltage source inverter i.e. 1 or –1

$$\delta|t| = \begin{cases} 1\,(\text{on time})\,\text{for } S < 0; \\ -1\,(\text{off time})\,\text{for } \dot{S} < 0. \end{cases},\tag{9}$$

The equivalent circuit of the DVR has been checked and it is investigated that the DVR can work on the sliding surface and is following the rule of reaching phase $S\cdot\dot{S} < 0$ to reach at the sliding surface. The tracking error

of injection voltage dynamics, when the system is on sliding mode, is stable and is given in (10) [4-6]

$$u_f = -V_d \cdot sign(S),\tag{10}$$

where u_f is control input to voltage source inverter; V_d is DVR voltage.

So, the voltage source inverter switches DC storage unit voltage according to sliding function. SMC was traditionally defined using the state space formulation and this practice continuous in sliding mode studies but in recent studies, sliding mode can also be attained by relay control system because this approach is very simple [15, 16]. The relay sliding mode controller does not compulsory any knowledge of system states and a complete system model is not required in relay sliding mode controller [17, 18]. SMC has been added at the end of Park transformation or $dq0$ to abc transformation. The error signal coming from $dq0\_to\_abc$ transformation will become input of SMC which is being used to switch the inverter. We have tuned the SMC to reduce the THD to make our DVR valuable and effective [19-22]. Phase locked loop for DVR with SMC is shown in Fig. 7 and its Simulink model is shown in Fig. 8.
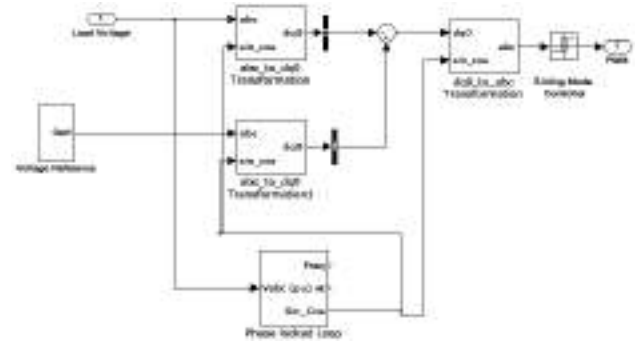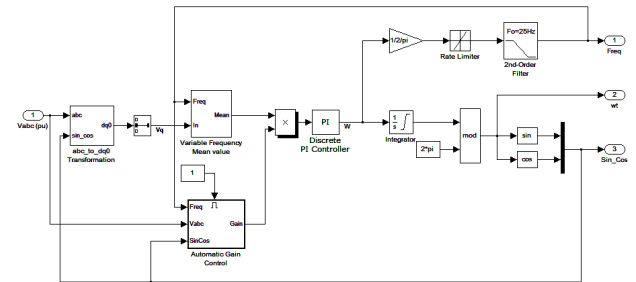

Fig. 7. Phase locked loop for DVR with SMC

Fig. 8. Simulink model of DVR with SMC

5. Simulation and results. The power system parameters selected for the simulation are given in the Table 1.

Table 1. Power system and DVR parameters

Parameter	Value
Line resistance, Ω	1
Line inductance, mH	5
Line frequency, Hz	50
Filter series capacitance, F	100
Filer series resistance, Ω	1
Load phase voltage, V	220
Load power per phase, W	100
Load inductive reactive power per phase, kVar	0.2
DC supply voltage, V	500
Injection transformer turns ratio	1:1
Load capacitive reactive power per phase, kVar	0.5
Saw-tooth carrier wave frequency, Hz	5500

5.1. Test system with DVR for distribution system. Three phase power test system with DVR coupled with injection transformer is shown in Fig. 9.

The DVR coupling boost transformer is connected in delta in a voltage source inverter side. The 13 kV, 50 Hz three phase supply is step up using three phase transformer star/delta/delta, 13/66/66 kV feeding two transmission lines. Both transmission lines are step down to 380 V to drive the sensitive load and non-sensitive load. The performance of the system with DVR has been simulated and investigated under three phase short circuit fault.
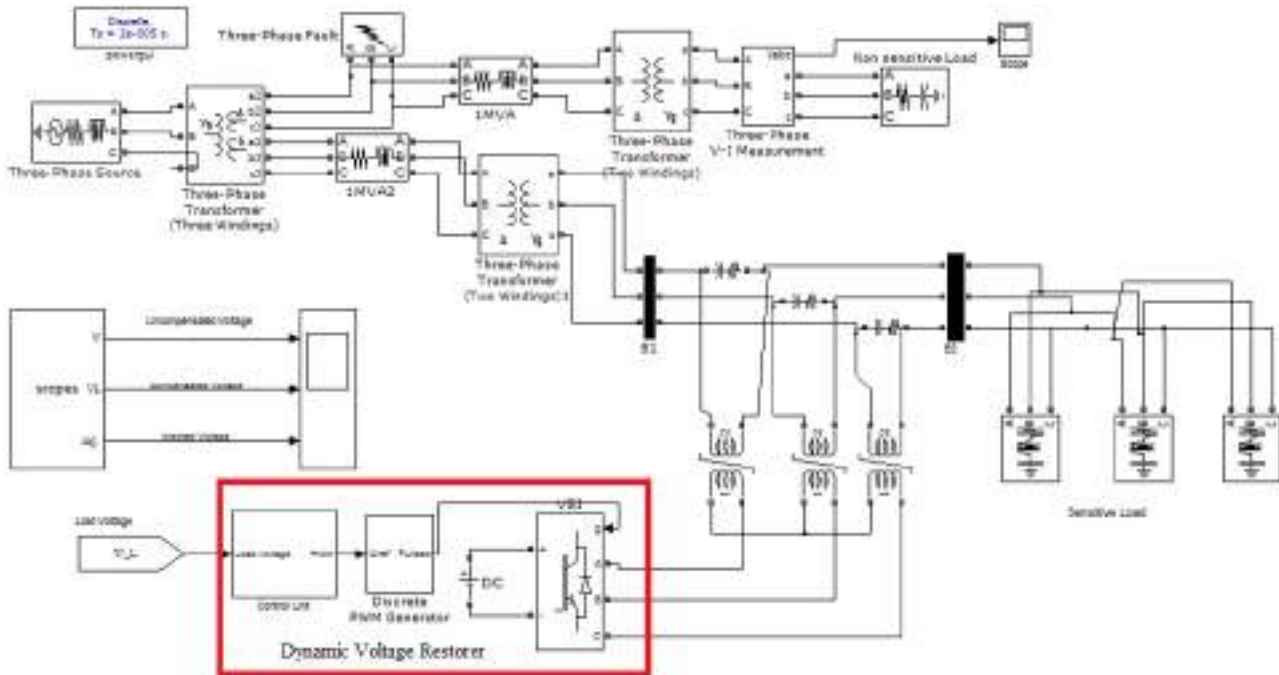
Fig. 9. Test System with DVR

5.2. Distribution system without DVR. The first simulation did not include a DVR and a three-phase fault was applied to one of the transmission lines, creating a voltage sag before the injection transformer through a fault resistor of 2 kΩ. A voltage drop event occurred on the transmission line for 0.05 to 0.185 s and the fault reduced the three-phase load voltage, which could disturb sensitive loads and cause system failure. Also, without a DVR, the voltage drop increased THD to 5.16 %. The load voltage obtained in this case is shown in Fig. 10 and the THD without DVR is shown in Fig. 11.
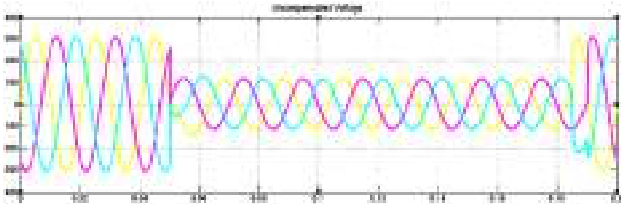
Fig. 10. Load voltage during fault without DVR
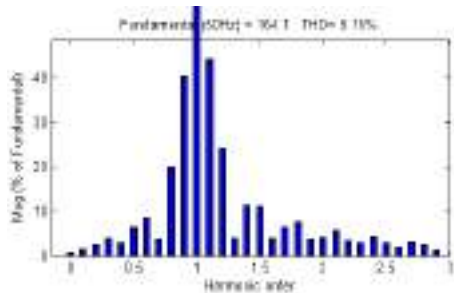
Fig. 11. THD during fault without DVR

5.3. Distribution system using DVR with PI controller. The second simulation is carried out using DVR based on PI controller which is connected to distribution system through an injection transformer. We have investigated that the missing voltage in the distribution line has been mitigated completely. Furthermore, THD has also been reduced as per power quality standard to 1.03 % with DVR with PI controller is shown in Fig. 12. Load voltage obtained in this case is shown in Fig. 13.
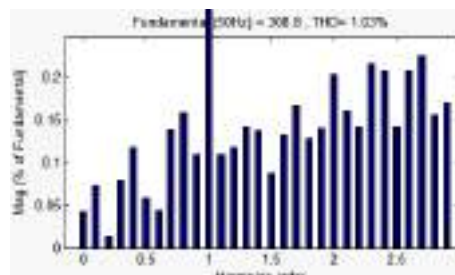
Fig. 12. THD during fault using DVR with PI controller
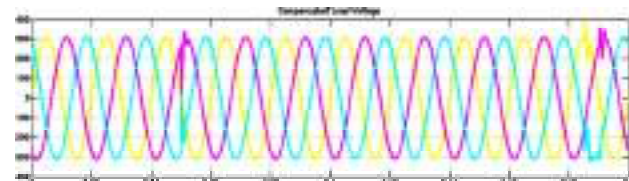
Fig. 13. Load voltage during fault with DVR using PI controller

5.4. Distribution system using DVR with SMC. The third simulation is being carried out using DVR with SMC which is connected to mitigate more voltage sag

margin with reduction in THD. The load voltage obtained using DVR with SMC is shown in Fig. 14 and THD obtained in this case is shown in Fig. 15.
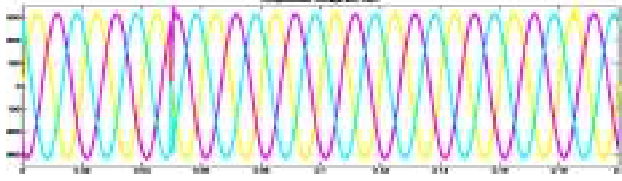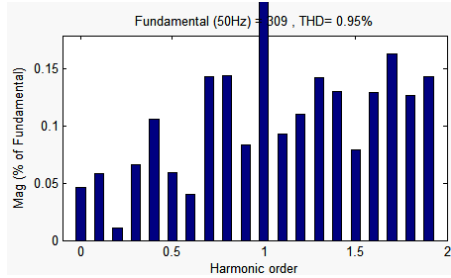

Fig. 14. Load voltage during fault using DVR with SMC

Fig. 15. THD during fault with DVR with SMC

5.5. Selection of optimal V_{dc} for THD reduction. The fourth simulation of DVR with SMC is based on the different values of V_{dc} to get optimal V_{dc} for THD reduction. The DC storage unit has a main impact on THD, we have simulated the DVR on different V_{dc} values and analyzed that at 1500 V storage unit, THD has been reduced to 0.44 %. Furthermore, we have changed the reference voltage i.e. 385 V and tuned on/off time of SMC i.e. 0.00001 s and –0.070 s then THD has been reduced from 0.44 % to 0.38 % as shown in Fig. 16. Load voltage obtained in this case is shown in Fig. 17 and THD is shown in Fig. 18.
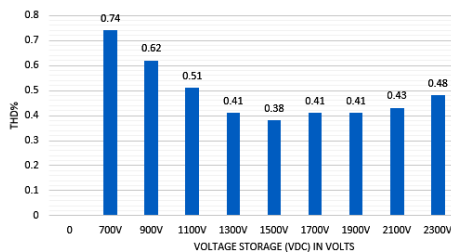
Fig. 16. Selection of optimal V_{dc} for THD reduction
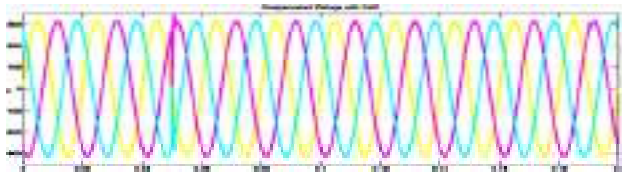
Fig. 17. Load voltage using DVR with SMC at optimal V_{dc}
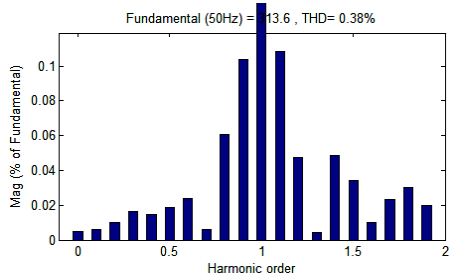
Fig. 18. THD for selected signal during fault using DVR with SMC at optimal V_{dc}

6. Comparative analysis of DVR with different controllers for distribution system. MATLAB / Simulink software package is employed to get a comparison of all the results offered by DVR with different controllers for distribution system. Initially, three phase fault has been applied in transmission line to create voltage sag. This fault has reduced the three-phase load voltage with increase of THD up to 5.16 %. The second simulation is carried out using DVR with PI controller which is connected to distribution system through an injection transformer. We have investigated that the missing voltage in the distribution line has been mitigated completely and THD has also been reduced to 1.03 % using DVR with PI controller. The third simulation is being carried out using DVR with SMC which is connected to mitigate more voltage sag margin with reduction in THD up to 0.95 %. Finally, DVR with SMC at optimal V_{dc} gives reduction of THD up to 0.38 %. The performance comparison of DVR with different controllers is shown in Fig. 19.
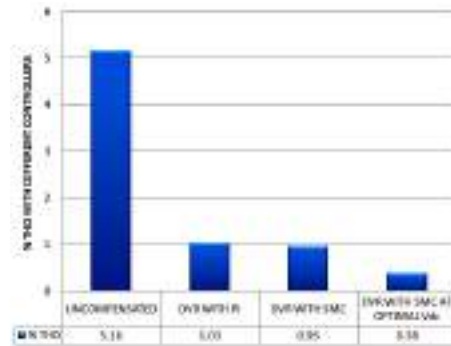

Fig. 19. Comparative analysis of DVR with different controllers for distribution system

Conclusions.

In this research paper, dynamic voltage restorer with PI controller and dynamic voltage restorer with sliding mode controller at optimal voltage V_{dc} is used to enhance the performance of dynamic voltage restorer by reducing THD. The effectiveness and performance of the proposed control scheme under voltage sag condition are examined. Simulation results shows that percentage total harmonic distortion and voltage sag are successfully reduced by using dynamic voltage restorer with sliding mode controller in distribution system under random fault condition. Percentage total harmonic distortion during fault using dynamic voltage restorer with PI controller, dynamic voltage restorer with sliding mode controller and dynamic voltage restorer with sliding mode controller at optimal voltage is 1.03 %, 0.95 % and 0.38 % respectively. It is obvious that dynamic voltage restorer with sliding mode controller at optimal value of voltage V_{dc} can mitigate the voltage sag very quickly with minimum percentage total harmonic distortion as compared to dynamic voltage restorer with PI controller to keep the voltage balance under fault events circumstances.

Conflict of interest. The authors declare that they have no conflicts of interest.

REFERENCES
1. Ullah M.F., Hanif A. Power quality improvement in distribution system using distribution static compensator with super twisting sliding mode control. *International Transactions*

on Electrical Energy Systems, 2021, vol. 31, no. 9, art. no. e12997. doi: https://doi.org/10.1002/2050-7038.12997.

2. Sathish Babu P., Sundarabalan C.K., Balasundar C. SOFC-Supported Hybrid PSOGSA-Optimized Dynamic Voltage Restorer for Power Quality Enhancement. *Journal of Circuits, Systems and Computers*, 2021, p. 2250006. doi: https://doi.org/10.1142/S0218126622500062.

3. Duy T.T., Trung T.B., Tien D.V. Voltage Sag Reduction using a Dynamic Voltage Restorer under Different Types of Faults in The Power System. *2021 International Conference on System Science and Engineering (ICSSE)*, 2021, pp. 246-251. doi: https://doi.org/10.1109/ICSSE52999.2021.9538493.

4. Akbar F., Mehmood T., Sadiq K., Ullah M.F. Optimization of accurate estimation of single diode solar photovoltaic parameters and extraction of maximum power point under different conditions. *Electrical Engineering & Electromechanics*, 2021, no. 6, pp. 46-53. doi: https://doi.org/10.20998/2074-272X.2021.6.07.

5. DaneshvarDehnavi S., Negri C., Bayne S., Giesselmann M. Dynamic Voltage Restorer (DVR) with a novel robust control strategy. *ISA Transactions*, 2021. In Press. doi: https://doi.org/10.1016/j.isatra.2021.04.010.

6. Darvish Falehi A., Torkaman H. Promoted supercapacitor control scheme based on robust fractional-order super-twisting sliding mode control for dynamic voltage restorer to enhance FRT and PQ capabilities of DFIG-based wind turbine. *Journal of Energy Storage*, 2021, vol. 42, p. 102983. doi: https://doi.org/10.1016/j.est.2021.102983.

7. Nasrollahi R., Farahani H.F., Asadi M., Farhadi-Kangarlu M. Sliding mode control of a dynamic voltage restorer based on PWM AC chopper in three-phase three-wire systems. *International Journal of Electrical Power & Energy Systems*, 2022, vol. 134, p. 107480. doi: https://doi.org/10.1016/j.ijepes.2021.107480.

8. Papineni P. Modeling and Simulation of Battery and SMES-based DVR for Grid-Connected Hybrid PV-Wind Power System with Improved Power Quality Features. *Turkish Journal of Computer and Mathematics Education (TURCOMAT)*, 2021, vol. 12, no. 12, pp. 1883-1890. Available at: https://turcomat.org/index.php/turkbilmat/article/view/7708 (Accessed 15 May 2021).

9. Guo Q., Tu C., Jiang F., Zhu R., Xiao F., Chen C. Improved dynamic voltage restorer with reduced capacity of power inverter and energy storage for voltage sag mitigation. *IET Power Electronics*, 2021, vol. 14, no. 5, pp. 958-968. doi: https://doi.org/10.1049/pel2.12078.

10. Paramasivam S.K., Ramu S.K., Mani S., Muthusamy S., Sundararajan S.C.M., Panchal H., Sadasivuni K.K. Solar photovoltaic based dynamic voltage restorer with DC-DC boost converter for mitigating power quality issues in single phase grid. *Energy Sources, Part A: Recovery, Utilization, and Environmental Effects*, 2021, pp. 1-25. doi: https://doi.org/10.1080/15567036.2021.1984614.

11. Kumar A.V., Praveen J., Kalyani S.T. An improvised control methodology for voltage sag mitigation, harmonics reduction with a dynamic voltage restorer to improve power quality: Considering fast-operating DSP. *Intelligent and Reliable Engineering Systems*, 2021, pp. 26-30. doi: https://doi.org/10.1201/9781003208365-5.

12. Kim S.-H. Power Quality Improvement using DVR. *Journal of IKEEE*, 2021, vol. 25, no. 3, pp. 462-466. doi: https://doi.org/10.7471/ikeee.2021.25.3.462.

13. Dongre A.A., Mishra Y.P., Kumar Dubey A. Carrier PWM Based Capacitor Supported Dynamic Voltage Restorer for Voltage Sag and Swell Mitigation in Distribution System.

Michael Faraday IET International Summit 2020 (MFIIS 2020), 2020, pp. 273-278. doi: https://doi.org/10.1049/icp.2021.1066.

14. Orman K., Design of a memristor-based chattering free sliding mode controller and speed control of the BLDC motor. Tehnicki Vjesnik, 2021, vol. 28, no. 3, pp. 754-762. doi: https://doi.org/10.17559/TV-20200105141443.

15. Chen Y.-K., Qiu X.-Z., Wu Y.-C., Song C.-C. Compensation of Voltage Sags and Swells Using Dynamic Voltage Restorer Based on Bi-Directional H-Bridge AC/AC Converter. *Processes*, 2021, vol. 9, no. 9, p. 1541. doi: https://doi.org/10.3390/pr9091541.

16. Nagarajan L., Senthilkumar M. Power Quality Improvement in Distribution System Based on Dynamic Voltage Restorer Using Rational Energy Transformative Optimization Algorithm. *Journal of Electrical Engineering & Technology*, 2022, vol. 17, no. 1, pp. 121-137. doi: https://doi.org/10.1007/s42835-021-00869-4.

17. Nhu Ngoc Thanh H.L., Vu M.T., Nguyen N.P., Mung N.X., Hong S.K. Finite-Time Stability of MIMO Nonlinear Systems Based on Robust Adaptive Sliding Control: Methodology and Application to Stabilize Chaotic Motions. *IEEE Access*, 2021, vol. 9, pp. 21759-21768. doi: https://doi.org/10.1109/ACCESS.2021.3054901.

18. Kelkoul B., Boumediene A. Stability analysis and study between classical sliding mode control (SMC) and super twisting algorithm (STA) for doubly fed induction generator (DFIG) under wind turbine. *Energy*, 2021, vol. 214, p. 118871. doi: https://doi.org/10.1016/j.energy.2020.118871.

19. Gupta A. Power quality evaluation of photovoltaic grid interfaced cascaded H-bridge nine-level multilevel inverter systems using D-STATCOM and UPQC. *Energy*, 2022, vol. 238, p. 121707. doi: https://doi.org/10.1016/j.energy.2021.121707.

20. Anwar N., Hanif A.H., Khan H.F., Ullah M.F. Transient Stability Analysis of the IEEE-9 Bus System under Multiple Contingencies. *Engineering, Technology & Applied Science Research*, 2020, vol. 10, no. 4, pp. 5925-5932. doi: https://doi.org/10.48084/etasr.3273.

21. Mehdi M.F., Ahmad A., Ul Haq S.S., Saqib M., Ullah M.F. Dynamic economic emission dispatch using whale optimization algorithm for multi-objective function. *Electrical Engineering & Electromechanics*, 2021, no. 2, pp. 64-69. doi: https://doi.org/10.20998/2074-272X.2021.2.09.

22. Anwar N., Hanif A., Ali M.U., Zafar A. Chaotic-based particle swarm optimization algorithm for optimal PID tuning in automatic voltage regulator systems. *Electrical Engineering & Electromechanics*, 2021, no. 1, pp. 50-59. doi: https://doi.org/10.20998/2074-272X.2021.1.08.

Syeda Tahreem Zahra[1]*, Lecturer, PhD Scholar,*
Rizwan Ullah Khan[2]*, Laboratory Engineer,*
Mian Farhan Ullah[2]*, Lecturer,*
Balqees Begum[2]*, Graduate Assistant,*
Naveed Anwar[2]*, Junior Lecturer,*
[1] Faculty of Electrical Engineering,
Riphah International University, Islamabad, Pakistan,
e-mail: tahreem.zahra@riphah.edu.pk
[2] Faculty of Electrical Engineering,
Wah Engineering College, University of Wah, Pakistan,
e-mail: rizwan.ullah@wecuw.edu.pk,
farhan.ullah@wecuw.edu.pk,
balquees.begum@wecuw.edu.pk ,
naveed.anwar@wecuw.edu.pk (Corresponding Author)

J. Lasocki, P. Krawczyk, A. Kopczyński, P. Roszczyk, A. Hajduga

Analysis of the strategies for managing extended-range electric vehicle powertrain in the urban driving cycle

Introduction. An Extended-Range Electric Vehicle (EREV) is a type of electric vehicle that uses an additional internal combustion engine (ICE) to charge the battery in order to provide the vehicle with a greater range than in electric only mode. **Purpose.** *Analysis and comparison of the performance of EREV powertrain managed according to three control strategies: pure electric mode, hybrid mode with ICE constantly working, and hybrid mode with ICE working only at high power demand.* **Methods.** *The tests were carried out using a laboratory test stand that represented the structure of EREV powertrain. Liquefied petroleum gas was used as a fuel to supply the ICE. The test conditions were defined by a special driving cycle simulating urban driving.* **Results.** *Time series plots of selected parameters of electric motor, electrochemical battery pack, range extender generator and active load system.* **Practical value.** *Among the considered control strategies of EREV powertrain, the energy balance of the electrochemical battery is negative for a purely electric mode, significantly positive for continuous range extenders (REXs) operation mode and moderately positive for the mode with REX activation only in dynamic states.* References 16, figures 22.
Key words: **extended-range electric vehicle, alternative fuel, liquefied petroleum gas, driving cycle.**

Вступ. Електромобіль зі збільшеним запасом ходу (ЕЗЗХ) – це тип електромобіля, який використовує додатковий двигун внутрішнього згоряння (ДВЗ) для заряджання акумулятора, щоб забезпечити транспортний засіб більшим запасом ходу, ніж у режимі лише на електричному ходу. **Мета.** *Аналіз та порівняння ефективності силової передачі ЕЗЗХ, керованої відповідно до трьох стратегій управління: чисто електричний режим, гібридний режим з постійно працюючим ДВЗ та гібридний режим з ДВЗ, що працює тільки при високому споживанні потужності.* **Методи.** *Випробування проводилися на лабораторному стенді, що представляє собою конструкцію силової передачі ЕЗЗХ. Скраплений газ використовувався як паливо для живлення ДВЗ. Умови випробувань визначалися спеціальним циклом водіння, що імітує водіння в умовах міста.* **Результати.** *Графіки часових рядів вибраних параметрів електродвигуна, електрохімічної акумуляторної батареї, генератора-розширювача діапазону та системи активного навантаження.* **Практична цінність.** *Серед розглянутих стратегій керування силовою установкою ЕЗЗХ, баланс енергії електрохімічної батареї негативний для чисто електричного режиму, суттєво позитивний для режиму роботи розширювачів діапазону (РД) та помірно позитивний для режиму з активацією РД лише у динамічних станах.* Бібл. 13, рис. 22.
Ключові слова: **електромобіль зі збільшеним запасом ходу, альтернативне паливо, скраплений газ, цикл водіння.**

Introduction. After over a century of domination of internal combustion engine (ICE) as the basic energy converter in vehicles, there is currently a dynamic development of electric propulsion systems in the automotive field [1, 2]. The latest powertrain solutions improve the performance, efficiency, safety and sustainability of electric passenger cars, commercial vehicles, buses, off-road utility vehicles, motorcycles etc.

Vehicle electrification takes different forms, depending on the purpose and conditions of use of vehicles, users' needs as well as availability of charging infrastructure. Common solutions include: Hybrid Electric Vehicles (HEVs), Plug-in Hybrid Electric Vehicles (PHEVs), Battery Electric Vehicles (BEVs), and recently also Extended-Range Electric Vehicles (EREVs) [1, 3, 4]. This paper focuses on the last of the above approaches. In essence, EREV is an all-electric vehicle with wheels driven solely by an electric motor, but equipped with a small ICE that provides energy for charging a battery and/or supplying the electric motor [1, 5]. In the literature, this arrangement is often classified as a PHEV [1, 5, 6]. Regardless of the definition, the main purpose of introducing EREV to the market was to beat the range limitation that is inherent in EVs.

A reliable control of power flow and energy management is of great significance towards the performance enhancement of EREVs. The main goal is to find the optimal control strategy for different powertrain operating conditions which would yield the minimum fuel consumption. There are many methods used for designing optimal EREV control strategies, among which several are based on estimating the battery State Of Charge (SOC) and vehicle speed.

Dynamic Programming (DP) has been particularly successful in this scope and can be considered as a benchmark method for control of hybrid powertrains [7]. Pontryagin's Minimum Principle (PMP) has also been widely applied and has been proven to provide near-optimal solutions [8]. A traditional PMP-based control strategy becomes a practicable and effective solution when combined with an adaptive concept for balancing SOC of a battery [9]. Other EREV control strategies are usually an extension of the DP- and PMP-based methods.

For example, the charge-deplete-charge-sustain strategy [10] has been developed via Power Split Ratio (PSR) from simulation of Extended-Range Electric Bus (EREB) using DP algorithm. Obtained results show that the overall energy efficiency can be improved and operating costs can be reduced to a great extent. Other research works [11] utilize even more factors affecting the system costs and performance, ranging from fuel consumption to noise emissions up to battery aging and engine start-up costs.

However, most EREV control strategies may not be as highly effective in practice as they are in theory, unless the future driving conditions are known. In order to solve this problem, paper [12] introduces an energy management strategy based on driving cycle identification. The results of simulation show that this strategy is effective in terms of reducing fuel consumption and pollutant emission from EREV. Finally, an energy

management strategy that can adapt to the driving characteristics of the driver and adjust the control parameters on-line is proposed [13]. It has been verified in simulation, achieving good fuel-saving and emission-reduction results.

Extensive research on electric vehicles has been carried out at the Faculty of Automotive and Construction Machinery Engineering of the Warsaw University of Technology. Recently, much attention has been paid to EREVs, which results in publications [14–16]. Current paper presents the results of testing extended-range electric powertrain in laboratory conditions. An important aspect is the use of alternative fuel – Liquefied Petroleum Gas (LPG) to supply the ICE, which is very rare in commonly used range extenders (REXs).

The goal of the paper is to analyze and compare the performance of EREV powertrain managed according to three control strategies: pure electric mode, hybrid mode with ICE constantly working, and hybrid mode with ICE working only at high power demand.

Materials and methods. The tests were carried out on a laboratory test stand shown in Fig. 1 and Fig. 2. It consisted of a traction electric motor powered by an electrochemical battery pack. The battery pack was controlled by a master control unit that managed its energy flow – discharge to provide power to the electric motor and recharge using REX. The range extender was based on a spark-ignition ICE supplied with LPG. The traction electric motor was connected by the gear transmission to the shaft that drives the inertia disc, simulating the inertia of the vehicle. The electric motor was loaded by an active load system, allowing for better representation of rolling and aerodynamic resistance, depending on the vehicle speed. This system consisted of a DC generator, which excitation circuit was connected to a controllable power supply while the main circuit – to an electric load, i.e. resistors cooled with external forced air circulation. The DC generator was connected to the shaft with inertia disc through a belt transmission. An external measuring system connected to a computer recorded the operating parameters of the components of laboratory test stand.
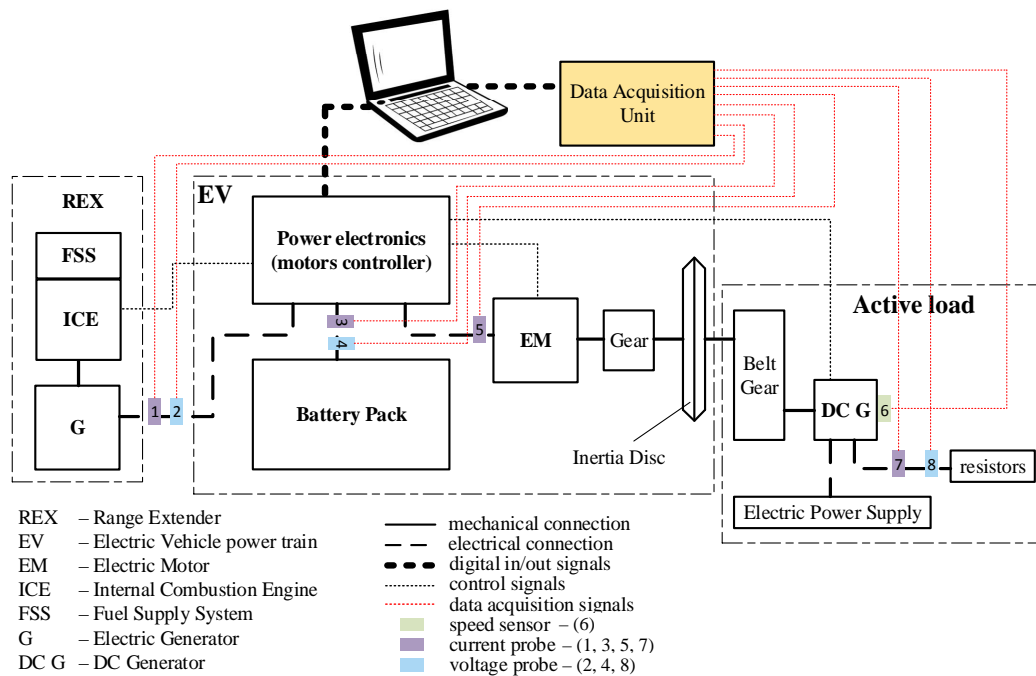

REX – Range Extender
EV – Electric Vehicle power train
EM – Electric Motor
ICE – Internal Combustion Engine
FSS – Fuel Supply System
G – Electric Generator
DC G – DC Generator

—— mechanical connection
– – – electrical connection
●—● digital in/out signals
·········· control signals
·········· data acquisition signals
speed sensor – (6)
current probe – (1, 3, 5, 7)
voltage probe – (2, 4, 8)

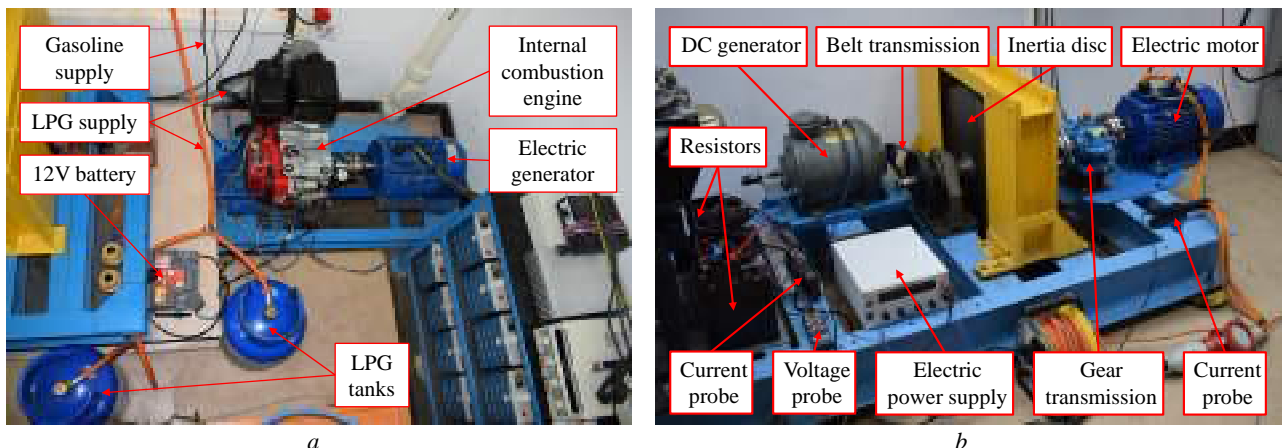Fig. 1. Schematic diagram of laboratory test stand

a

b

Fig. 2. General view of laboratory test stand: *a* – range extender; *b* – electric vehicle powertrain with active load system

The main parameters of the laboratory stand elements are given below:

- Traction motor: Permanent Magnet Synchronous Machine, 3-phase, rated power 15 kW, rated rotational speed 3600 rpm, air cooled, manufactured by KOMEL;
- Electrochemical battery: Li-ion battery pack consisting of 36 prismatic cells (MGL-SPIM23300260) 90 Ah in series connection, nominal voltage 144 V, air cooled;
- Range extender:
- ICE: Honda IGX440 – four-stroke, single-cylinder, spark-ignition, OHC, displacement volume 438 cm^3, cylinder bore/stroke 88 mm/72.1 mm, max power 9.5 kW at 3600 rpm, max torque 29.8 Nm at speed 2500 rpm, carbureted, air cooled;
- Generator: Permanent Magnet Synchronous Machine, 3-phase, rated power 15 kW, rated speed 3600 rpm, air cooled, manufactured by KOMEL;
- Active load: DC generator manufactured by KOMEL, rated power 3.5 kW, rated speed 2850 rpm, separately-excited (from electronic power supply);
- Data Acquisition Unit: ESAM PP/SP in/out signals compiler box with filtration;
- Inertia disc (fly wheel): moment of inertia 6 kg·m^2;
- Gear transmission: ratio 1:2.7;
- Belt transmission: ratio 1:3, belt type 8M-20.

The ICE of the REX worked at a single operating point, selected taking into account the two-dimensional efficiency characteristic (map) determined earlier [14].

The tests were carried out according to the special driving cycle developed by authors (Fig. 3). The cycle is based on ECE 15 and represents city driving conditions.
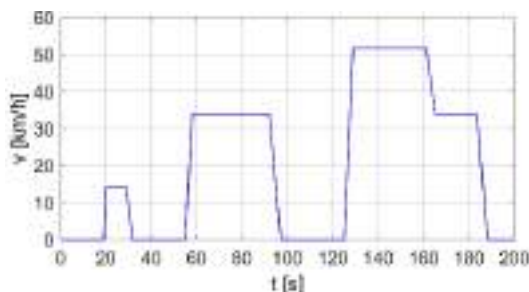
Fig. 3. Special driving cycle used for testing

REX control strategies. In this research three REX control strategies are evaluated:

- strategy 1: Pure electric mode;
- strategy 2: Hybrid mode I;
- strategy 3: Hybrid mode II.

The strategies govern the two states of the REX:

- OFF state, where REX is disabled and no power is delivered to the powertrain from the REX;
- ON state, where REX is enabled and constant power of 2.5 kW is delivered by REX to the powertrain.

These strategies are tested in isolation, meaning for each test only one strategy is used. No switching between the strategies is evaluated.

The first strategy results with pure electric driving. The REX is in OFF all the time during the drive with this strategy scheduled for operation. In real driving conditions, such strategy is suitable when traction motor demand is low and it is critical to not generate any emissions by REX engine. This includes city traffic driving and no pollution zones driving.

Scheduling the second strategy for operation results with hybrid driving, with REX always in ON state. This helps avoiding overcharging and excessive battery charging current. In real driving conditions, such strategy is suitable for high motor power demand and for areas where pollution restriction is not critical. This strategy is suitable for times when battery SOC is running low. Then, it is critical to provide additional energy to the battery, even by running REX when vehicle is stationary.

The third strategy, when scheduled for operation, results with REX changing the state between ON and OFF as requested. In this research, this request is triggered when power demand by the traction motor is greater than zero. In real driving conditions, such strategy is suitable when traction motor demand is moderate to high and SOC is not enough to provide demanded vehicle range in pure electric mode. The driving conditions suitable for this strategy include mixed city (without zero emissions zones) and motorway driving.

Results. Overview. This section presents time series plots of selected operating parameters of the tested powertrain. For AC current and voltage, the measured signals are marked in blue, while the effective values (RMS) – in red. Time series plots of rotational speed, power and current of the traction electric motor were almost the same for each analysed variant of the control strategy, therefore they were presented only in the first case. The power of active load generator (DC generator) results from the resistance to motion, which in turn depends on the speed of the vehicle (i.e. the rotational speed of the traction motor). Hence, for each analysed variant, its time series plot was very similar.

Strategy 1: Pure electric mode. Figures 4–10 show the results obtained for the first control strategy, where REX is turned off during the entire cycle (i.e. «zero emission» mode).
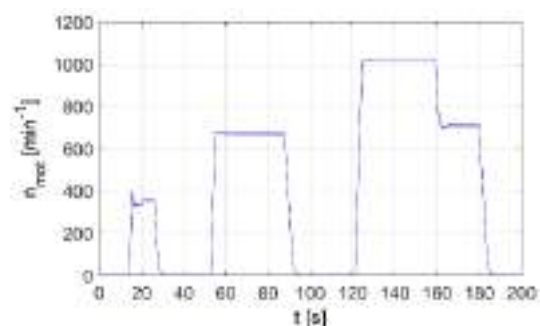

Fig. 4. Electric motor rotational speed for 1st control strategy

The battery current corresponds to the current of the traction motor. The battery power is higher than the power of the traction motor due to energy transmission losses and power electronic converter efficiency, which are variable and depend on the actual operating points. The battery voltage throughout the entire cycle is relatively constant, instantaneous voltage drops are caused by the higher instantaneous current load on the battery. As the battery discharges, the voltage at its

terminals decreases slightly. The power, current and voltage of REX generator equal zero, due to the principle of the first control strategy in which extender generator is turned off. Current peaks occur in dynamic states, i.e. when the vehicle accelerates or when it brakes regeneratively. The battery current peak is positive for acceleration and negative for braking. This means that during acceleration, energy is drawn from the battery, while during recuperative braking the battery is charged.
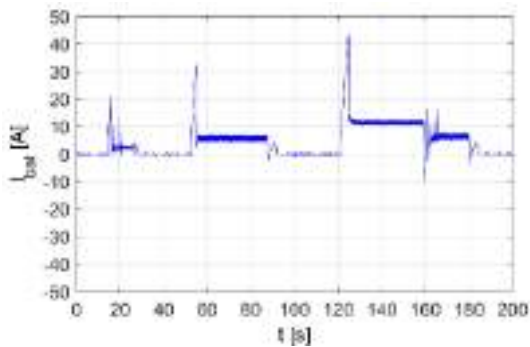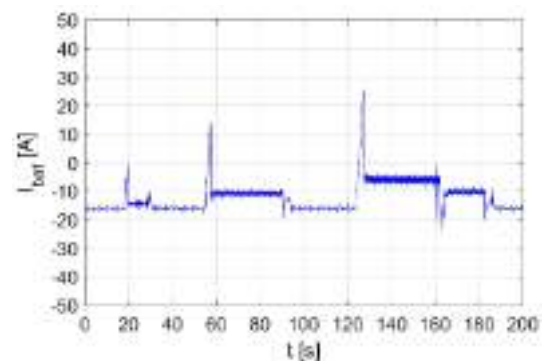

Fig. 5. Electrochemical battery current for 1st control strategy
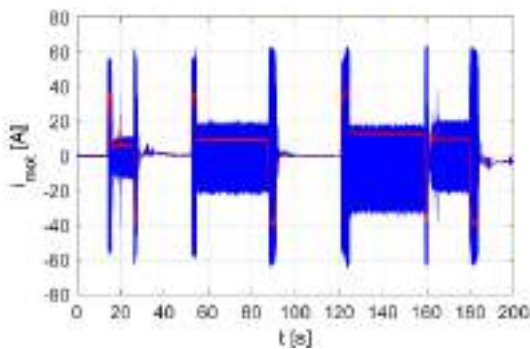
Fig. 6. Electric motor current for 1st control strategy
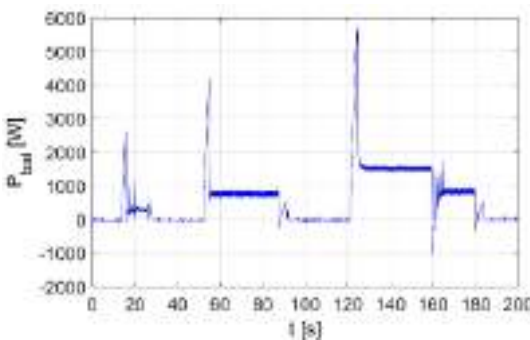
Fig. 7. Electrochemical battery power for 1st control strategy
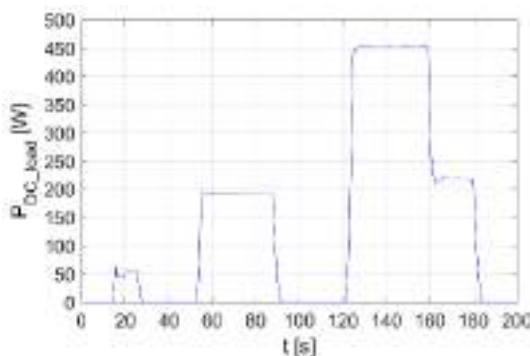
Fig. 8. Active load power for 1st control strategy
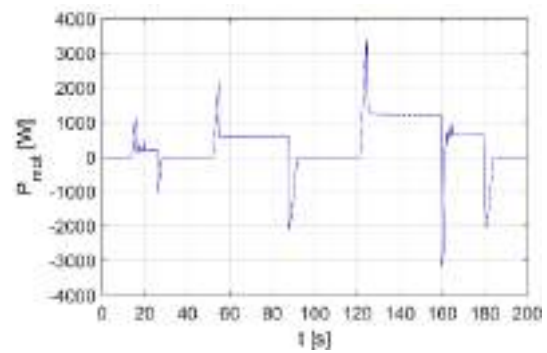
Fig. 9. Electric motor power for 1st control strategy
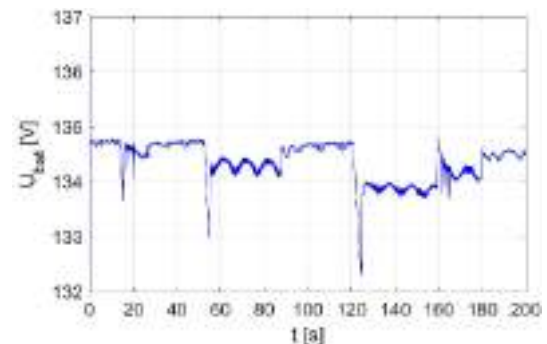
Fig. 10. Electrochemical battery voltage for 1st control strategy

Strategy 2: Hybrid mode I. Figures 11–16 show the results obtained for the second control strategy, where REX is turned on during the entire cycle.

Fig. 11. Electrochemical battery current for 2nd control strategy
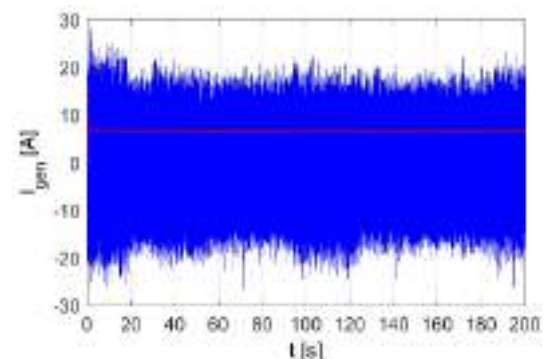
Fig. 12. REX generator current for 2nd control strategy

The surplus power, in relation to the demand resulting from the cycle, recharges the battery. The instantaneous battery current is the sum (excluding losses) of the REX generator instantaneous current and the

traction motor current. In the case of regenerative braking, the battery is charged with current from both the traction motor and the REX generator. In this case, it must be ensured that the maximum battery charging current is not exceeded (depending on the capacity of the battery) or that it is not overcharged, as this may result in permanent damage. The REX generator current and voltage have positive and negative values, which means that AC is generated.
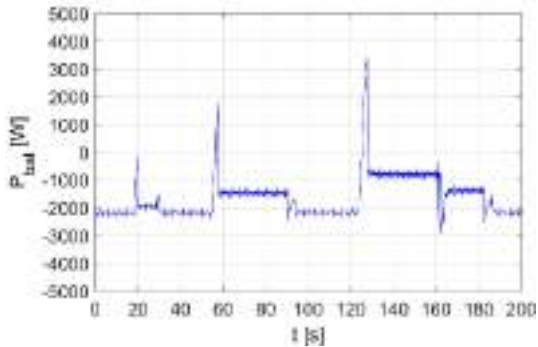

Fig. 13. Electrochemical battery power for 2nd control strategy
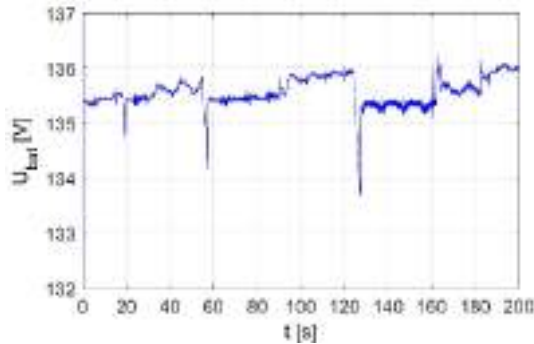
Fig. 14. Electrochemical battery voltage for 2nd control strategy
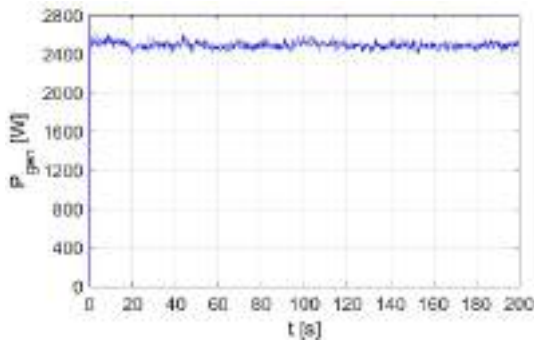
Fig. 15. REX generator power for 2nd control strategy
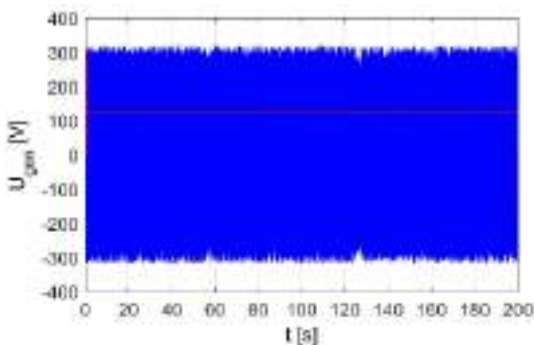
Fig. 16. REX generator voltage for 2nd control strategy

Strategy 3: Hybrid mode II. Figures 17–22 show the results obtained for the third control strategy, where REX is activated in situations of high power demand, determined by the driving cycle.
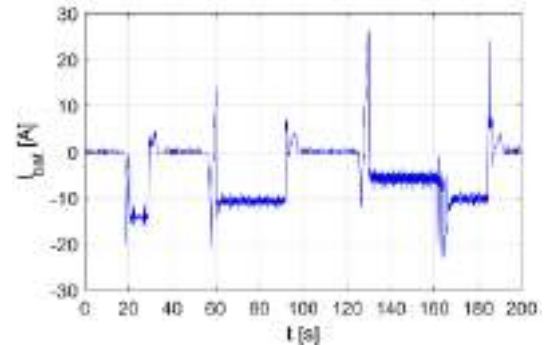

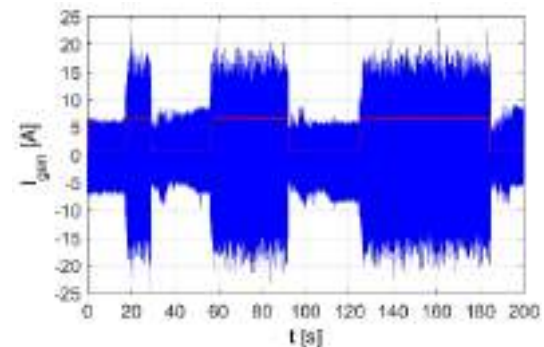Fig. 17. Electrochemical battery current for 3rd control strategy

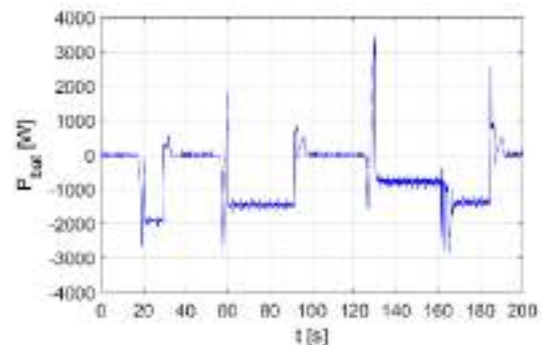Fig. 18. REX generator current for 3rd control strategy

Fig. 19. Electrochemical battery power for 3rd control strategy
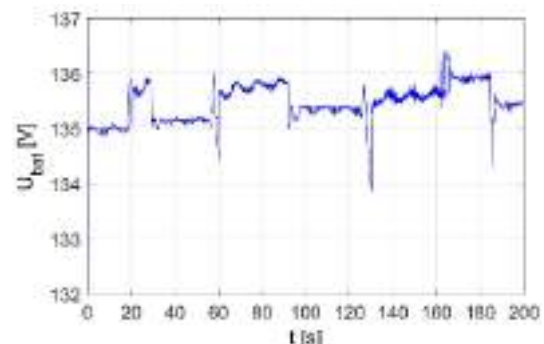

Fig. 20. Electrochemical battery voltage for 3rd control strategy

When REX is turned on, the graphs for battery pack show that the instantaneous current and power values are negative. This means that the power required by the traction motor, necessary for the vehicle to follow the

driving cycle, is lower than the power supplied by REX, hence the battery voltage ends up being higher after the considered driving cycle. If similar test would be carried out, but using a different driving cycle with higher energy demand, expected results would show higher energy consumption, and therefore battery energy staying closer to the same level before and after driving cycle.
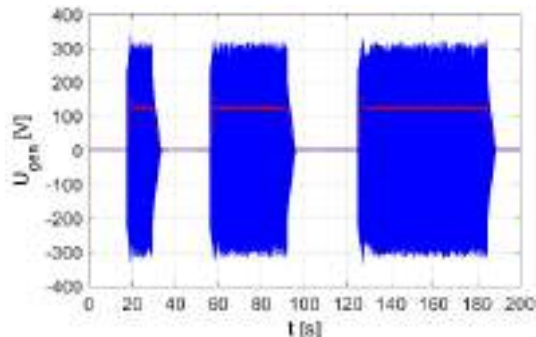

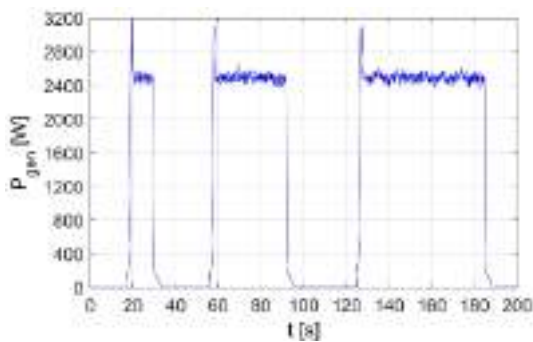Fig. 21. REX generator voltage for 3rd control strategy

Fig. 22. REX generator power for 3rd control strategy

Conclusions.

The control strategy applied to EREV powertrain should ensure first of all:

• avoiding overcharging and excessive battery charging current;

• reduction of battery current in dynamic states with REX support.

Appropriate selection of powertrain components allows for proper choice of control strategy. The selection of components should take into account the power, voltage and current of the traction motor, battery and REX.

The energy balance of the electrochemical battery for the considered control strategies is:

• negative for a purely electric mode, i.e. the SOC level of the battery at the end of the cycle was lower than at the beginning;

• significantly positive for continuous REX operation mode, i.e. the SOC level of the battery at the end of the cycle increased significantly;

• moderately positive for the mode with REX activation only in dynamic states, i.e. the final battery SOC level increased (the battery SOC level at the end of the cycle), although to a lesser extent than for the case of continuous REX operation – the SOC levels of the battery at the beginning and the end of the cycle had close values.

It should be noted that when analyzing the energy balance of the whole powertrain, it is necessary to take into account the fuel consumption of the ICE and its correspondence to the SOC level of the battery. This may be one of the directions for further research.

Furthermore, the energy balance of the whole powertrain largely depends on the proper selection of operating parameters of the primary power source considering the driving cycle. The relationship between the parameters of individual components of the powertrain also plays an important role. For the considered laboratory test stand, the REX power was significantly higher than the average demand for the power of the driving cycle (traction electric motor) itself. The authors see this as limitations to the results obtained so far. It is assumed that further research will take into account the optimization of the parameters of the test stand.

Conflict of interest. The authors declare that they have no conflicts of interest.

REFERENCES
1. Dell R.M., Moseley P.T., Rand D.A.J. Progressive Electrification of Road Vehicles, in *Towards Sustainable Road Transport*, Eds. Cambridge, Academic Press, 2014, pp. 157-192. doi: https://doi.org/10.1016/B978-0-12-404616-0.00005-0.
2. Gis W., Waśkiewicz J., Gis M. Projections of future use of electric cars. *Journal of KONES Powertrain and Transport*, 2015, vol. 22, no. 2, pp. 55-62. doi: https://doi.org/10.5604/12314005.1165395.
3. Singh K.V., Bansal H.O., Singh D. A comprehensive review on hybrid electric vehicles: architectures and components. *Journal of Modern Transportation*, 2019, vol. 27, no. 2, pp. 77-107. doi: https://doi.org/10.1007/s40534-019-0184-3.
4. Chmielewski A., Szulim P., Gregorczyk M., Gumiński R., Mydłowski T., Mączak J. Model of an electric vehicle powered by a PV cell – A case study. *2017 22nd International Conference on Methods and Models in Automation and Robotics (MMAR)*, 2017, pp. 1009-1014. doi: https://doi.org/10.1109/mmar.2017.8046968.
5. Orecchini F., Santiangeli A. Automakers' Powertrain Options for Hybrid and Electric Vehicles, in *Electric and Hybrid Vehicles*, Pistoia G. Ed., Elsevier, 2010, pp. 579-636. doi: https://doi.org/10.1016/B978-0-444-53565-8.00022-1.
6. Bradley T.H., Frank A.A. Design, demonstrations and sustainability impact assessments for plug-in hybrid electric vehicles. *Renewable and Sustainable Energy Reviews*, 2007, vol. 13, no. 1, pp. 115-128. doi: https://doi.org/10.1016/j.rser.2007.05.003.
7. Mansour C., Clodic D. Optimized energy management control for the Toyota Hybrid System using dynamic programming on a predicted route with short computation time. *International Journal of Automotive Technology*, 2012, vol. 13, no. 2, pp. 309-324. doi: https://doi.org/10.1007/s12239-012-0029-0.
8. Naeem H.M.Y., Bhatti A.I., Butt Y.A., Ahmed Q. Velocity Profile optimization of an Electric Vehicle (EV) with Battery Constraint Using Pontryagin's Minimum Principle (PMP). *2019 IEEE Conference on Control Technology and Applications (CCTA)*, 2019, pp. 750-755. doi: https://doi.org/10.1109/CCTA.2019.8920609.
9. Lee W., Jeoung H., Park D., Kim N. An Adaptive Concept of PMP-Based Control for Saving Operating Costs of Extended-Range Electric Vehicles. *IEEE Transactions on Vehicular Technology*, 2019, vol. 68, no. 12, pp. 11505-11512. doi: https://doi.org/10.1109/TVT.2019.2942383.
10. Du J., Chen J., Song Z., Gao M., Ouyang M. Design method of a power management strategy for variable battery capacities range-extended electric vehicles to improve energy efficiency

and cost-effectiveness. *Energy*, 2017, vol. 121, pp. 32-42. doi: https://doi.org/10.1016/j.energy.2016.12.120.

11. Pozzato G., Formentin S., Panzani G., Savaresi S.M. Least costly energy management for extended-range electric vehicles: An economic optimization framework. *European Journal of Control*, 2020, vol. 56, pp. 218-230. doi: https://doi.org/10.1016/j.ejcon.2020.01.001.

12. Chen Y., Zhang Y., Wei C., Li G., Li C. Optimization of extended range electric vehicle energy management strategy via driving cycle identification. *IOP Conference Series: Materials Science and Engineering*, 2020, vol. 793, no. 1, p. 012040. doi: https://doi.org/10.1088/1757-899x/793/1/012040.

13. Yu Y., Jiang J., Min Z., Wang P., Shen W. Research on Energy Management Strategies of Extended-Range Electric Vehicles Based on Driving Characteristics. *World Electric Vehicle Journal*, 2020, vol. 11, no. 3, p. 54. doi: https://doi.org/10.3390/wevj11030054.

14. Lasocki J., Kopczyński A., Krawczyk P., Roszczyk P. Empirical Study on the Efficiency of an LPG-Supplied Range Extender for Electric Vehicles. *Energies*, 2019, vol. 12, no. 18, p. 3528. doi: https://doi.org/10.3390/en12183528.

15. Kopczyński A., Krawczyk P., Lasocki J. Parameters selection of extended-range electric vehicle supplied with alternative fuel. *E3S Web of Conferences*, 2018, vol. 44, p. 00073. doi: https://doi.org/10.1051/e3sconf/20184400073.

16. Kopczyński A., Piórkowski P., Roszczyk P. Parameters selection of extended-range electric vehicle powered from supercapacitor pack based on laboratory and simulation tests. *IOP Conference Series: Materials Science and Engineering*, 2018, vol. 421, p. 022016. doi: https://doi.org/10.1088/1757-899x/421/2/022016.

Jakub Lasocki[1]*, PhD,*
Pawel Krawczyk[1]*, PhD,*
Artur Kopczyński[1]*, MSc, MBA,*
Pawel Roszczyk[1]*, PhD,*
Arkadiusz Hajduga [1]*, PhD, Associate Professor,*
[1] Institute of Vehicles and Construction Machinery Engineering, Warsaw University of Technology,
84, Narbutta Str., Warsaw, 02-524, Poland,
e-mail: jakub.lasocki@pw.edu.pl (Corresponding author),
pawel.krawczyk@pw.edu.pl,
artur.kopczynski@pw.edu.pl,
pawel.roszczyk@pw.edu.pl,
arkadiusz.hajduga@pw.edu.pl

Передплатний індекс: 01216